BRNO UNIVERSITY OF TECHNOLOGY
VYSOKÉ UČENÍ TECHNICKÉ V BRNĚ

FACULTY OF MECHANICAL ENGINEERING
FAKULTA STROJNÍHO INŽENÝRSTVÍ

ENERGY INSTITUTE
ENERGETICKÝ ÚSTAV

SHAPE OPTIMIZATION OF THE HYDRAULIC MACHINE FLOW PASSAGES
TVAROVÁ OPTIMALIZACE PRŮTOČNÝCH ČÁSTÍ HYDRAULICKÝCH STROJŮ

DOCTORAL THESIS
DIZERTAČNÍ PRÁCE

AUTHOR   Ing. Prokop Moravec
AUTOR PRÁCE

SUPERVISOR   doc. Ing. Pavel Rudolf, Ph.D.
ŠKOLITEL

BRNO 2019

ABSTRAKT

Tato dizertační práce se zabývá vývojem optimalizačního nástroje, který je založen na metodě Particle swarm optimization a je poté aplikován na dva typy oběžných kol radiálních čerpadel.

KLÍČOVÁ SLOVA

Tvarová optimalizace, CFD, Particle swarm optimization, PSO, Multi-objective particle swarm optimization, MOPSO, oběžné kolo čerpadla, čerpadlová turbína, čerpadlo s nízkými specifickými otáčkami, Nelder-Mead.

ABSTRACT

This doctoral thesis deals with the development of a shape optimization tool based on a Particle swarm optimization algorithm, which is then applied to two different problems of two radial pump impellers.

KEYWORDS

Shape optimization, CFD, Particle swarm optimization, PSO, Multi-objective particle swarm optimization, MOPSO, pump impeller, pump turbine, low specific speed pump, Nelder-Mead.

PROHLÁŠENÍ

Prohlašuji, že svou dizertační práci na téma „Tvarová optimalizace průtočných částí hydraulických strojů" jsem vypracoval samostatně pod vedením školitele dizertační práce a s použitím odborné literatury a dalších informačních zdrojů, které jsou všechny citovány v práci a uvedeny v seznamu literatury na konci práce.

Brno ....

podpis autora

PODĚKOVÁNÍ

Rád bych poděkoval vedoucímu své dizertační práce panu doc. Ing. Pavlu Rudolfovi, Ph.D. za odborné vedení a konzultace. Dále bych chtěl poděkovat své milé přítelkyni Evě, rodičům za podporu během studia a nakonec i Kubovi a Lukinovi za milý kolektiv v práci.

Brno   . . . .
                                                                      podpis autora

CONTENT

INTRODUCTION

A well-known technical problem called a **shape optimization** has become increasingly popular amongst engineers in various parts of industry or academia in the past few years, primarily thanks to a development of computer technology and a specialized software connected with it. The main goal of every shape optimization process is to provide a shape/size (we can call it **design**) that fulfils given parameters and satisfies chosen constraints.
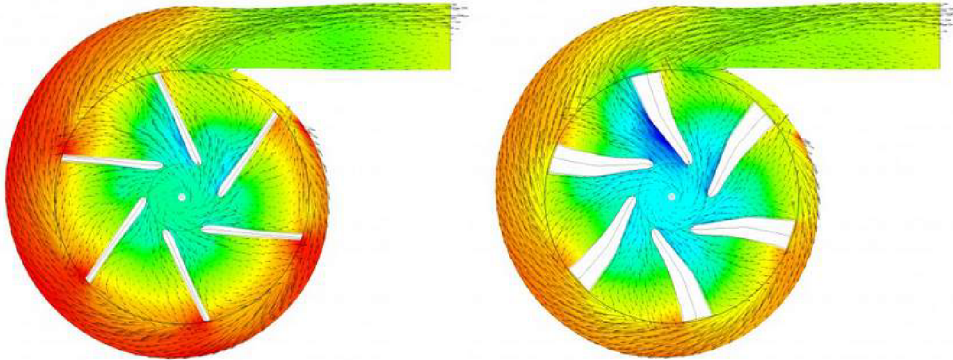

Fig. 1: *Shape optimization: original design (left) vs. optimized design (right)* [70].

Authors in [93] suggest that the final design must be as good as possible in some defined sense, but for a lot of optimization problems is sufficient any feasible improvement of the initial shape (for example fig. 1) - this approach is for our purposes quite adequate and also reasonable. Presented work focuses its full energy mainly on the shape optimization in a field of the hydraulic machinery - to be more accurate in a field of the centrifugal radial pumps. The key question of finding the optimal design of a certain flow part strongly relies on two crucial things: **first** on an accurate numerical simulation of the current flow via Computational Fluid Dynamics (CFD) and **second** on a suitable choice of a proper optimization method or approach. But it must be noted that not every combination of these two prerequisites is a win situation, they must be carefully merged in the most effective way - in terms of a minimizing of a total computational time due to a time-consuming nature of CFD simulations.

The pivotal aim of this work is set to explore a **Particle swarm optimization algorithm** (shortly PSOA) and its possible modifications to create an **optimization tool** for designing a proper shape of chosen radial pump impellers. PSOA is extensively influenced by the social behaviour of miscellaneous animals, such as birds, fish, etc. This method shows convenient and perspective attributes, that could be utilized in the shape optimization of the chosen flow parts in hydraulic machinery, mostly: could be effectively programmed (the PSOA is defined by two basic equations - velocity and position calculations), a great robustness of an optimization search ability (due to a stochastic nature of the algorithm) or an option to a possible computational parallelization (each particle could be investigated separately during one iteration of the algorithm). And together with

Pareto principles, the Particle swarm optimization algorithm could be successfully used in multi-objective shape optimization problems.

The shape optimization tool was applied on a problem of finding the proper **pump turbine** design (grant **TH01020982** - *Zefektivnění akumulace energie a zajištění stability rozvodné sítě rozšířením provozního pásma přečerpávacích vodních elektráren*). This design is supported with both, CFD simulations and with an experiment performed by ČKD Blansko Engineering. Another task, which served as a test case for the future optimization tool, was a problem of finding the proper shape of the very **low specific speed pump** [49], [50].

Both of these types of pumps are characteristic for their rather poor efficiency (especially low specific speed pump), high outlet blade angle, secondary flows (relative eddy in the blade channel) or blocked suction space. So it means that they are very challenging pump types to design and automatic optimization could show new ways how to shape blades properly. Here it should be noted that optimization can not only be a tool for finding the new shape of the pump impeller or turbine runner with improved properties, but can also provide useful information about a relation between geometrical shapes and optimal flow patterns. This information might not be revealed otherwise, since they would be hardly explored using manual shape modifications. Optimization, therefore, offers invaluable feedback about the fluid mechanical aspects of the hydraulic machinery flows, which might improve our understanding of some features underlying the hydraulic machines operation and lead to a substantial improvement of the 1D tools and empirical relations for the fast basic design of pumps or turbines.

The complete doctoral thesis is divided into the six main sections. At the beginning of this thesis will be in short summarized current state of the art of the optimization methods (algorithms, software), which are somehow connected with the hydraulic flow parts and computational fluid dynamics (CFD). Such optimization methods are here separated into three groups, starting with the most basic trial and error method, continuing with the exploitation of the commercial or non-commercial software and ending with utilization of correct optimization algorithms. Following section is a theory section, which covers a basic theoretical basis around the shape optimization, Bézier curves, chosen Particle swarm optimization method and its multi-objective modification. Afterwards, 1D pump design section briefly explains chosen procedures and techniques, which are behind the proper design of the radial pump - such knowledge is then employed for a "starting" design in presented shape optimization problems, which were mentioned above. After all the theoretical background comes the application of the presented shape optimization tool - the case of the shape optimization of the pump turbine impeller and the shape optimization of the very low specific speed pump. Final results from this optimization are compared with the CFD simulations and in the case of the pump turbine are also compared with the measurements performed by ČKD Blansko Engineering.

1 SHAPE OPTIMIZATION COUPLED WITH CFD

A problem of designing the optimal shapes using CFD for practical engineering applications has been a subject of many articles during the last three decades. An effort to reduce computational time of the whole optimization cycle and improve a quality of a final shape (compared to an initial state), enabled a creation of numerous different optimization approaches and methods. There are three fundamental ways, how to achieve a proper design that satisfies chosen parameters and respects limiting aspects of the certain shape optimization problem of the specific hydraulic flow part:

- **Trial and error** method and methods based only on experience in a specific area
- Exploitation of a commercial or non-commercial **software**
- Utilization of the correct **optimization method** and its correct application

Each way could be illustratively transformed into a basic diagram of the shape optimization algorithm (fig. 1.1), where a step called **Optimization environment** could be replaced by the chosen optimization approach.
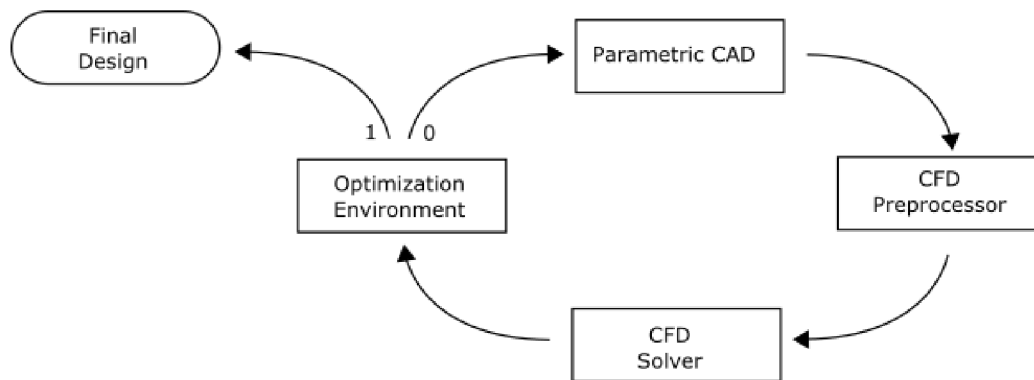
Fig. 1.1*: Basic diagram of the shape optimization coupled with CFD* [108].

All of the mentioned approaches have many representatives with their own advantages and disadvantages and some of the most used ones, which are tightly connected with CFD and the hydraulic flow parts, are summarized in the next three short sections: *Trial and error method* - in sec. 1.1, *Exploitation of a pre-programmed software* - in sec. 1.2 and *Utilization of a correct optimization method and its application* - in sec. 1.3.

1.1 Trial and error method

Trial and error method is the most basic method for a determination of the proper shape of the chosen hydraulic part and is often connected with strong knowledge of a solved problem and with deep underlying experiences in such area. It must be noted that the trial and error method is not presented and used only in the shape optimization field of interest, but it could be generalized on the whole area of the problem-solving. This

method is built on repetition, varied attempts and in the end, it usually finishes with a success (or a premature termination of the algorithm from a side of the user) - fig. 1.2.

Fig. 1.2: *Basic diagram: Trial and error approach* [109].

Application of trial and error method

For example in a problem of designing the proper shape of the centrifugal pump impeller, it is necessary to know, how certain parameters (e.g. β - angle of a blade, number of blades, etc.) of this impeller influences a desi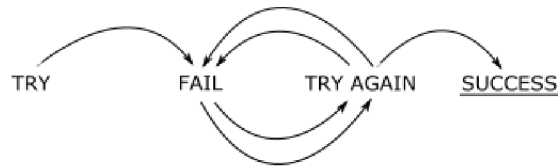gn point of the current pump, which consists of the head, hydraulic efficiency, power or $NPSH_3$ [61]. An engineer starts with a sequence of equations, which leads to a determination of the initial dimensions. Then he assembles n - "test" cases, which substantiate several modifications of these dimensions and "tries luck". After CFD simulations he separates suitable designs from unsuitable ones and explores a correlation between geometrical shapes and optimal flow patterns. Based on this, he modifies the impeller geometry and again CFD simulation must be performed. Such a loop of modifications is repeated until he finds the best feasible solution [61].
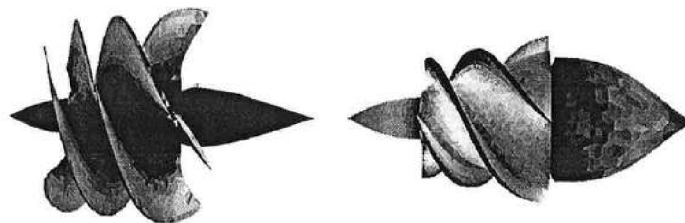
Fig. 1.3: *Initial (left) vs. final (right) design of the blood pump impeller* [13].

Fig. 1.3 shows another example of the trial and error method coupled with CFD - utilization in the designing of the impeller of the blood pump, where on the left side can be seen the initial shape of the impeller and on the right side the final shape, which led to an improvement of the thrombogenic character of the flow (= reduction of the blood clot production). The shape optimization in the field of the axial pumps could be found e.g. in [88] and similar approach, but applied on a bucket of a Pelton turbine, exists in [2].

Conclusion

The main advantage of this approach lies in pure a simplicity (fig. 1.2), but a downside resides in a lack of precision of the final product, mainly due to a manual shape design modification and also great time consumption is a major issue in this method. Trial and error method does not use a full potential, which the whole computational area of a certain problem can offer.

1.2 Exploitation of a pre-programmed softwares

New approaches bountifully emerge with the fast development of the computer performance in the area of the shape optimization. Engineers nowadays can choose from a variety of tools, which are/could be coupled with CFD and can be applied to their current design problem. For example, Fluent **Adjoint solver** (direct implementation in computational fluid dynamics software ANSYS Fluent), **NOMAD** or **EASY** are worth mentioning. These optimization tools have a certain potential and could replace **trial and error** techniques used by engineers e.g. in [2], [13], [61] or [88].

1.2.1 Fluent Adjoint solver

Fluent **Adjoint solver** is a tool implemented within commercial software ANSYS Fluent. It needs a fully converged CFD simulation to provide a sensitivity analysis of a possible shape change of an examined surface area, which strongly depends on a chosen simulation objective - in fig. 1.4 Fluent Adjoint solver outlines with the vectors of the optimal displacement, how to modify a Formula 1 front part to maximize a value of a downforce, which is crucially important for a proper car behaviour on a racing track.
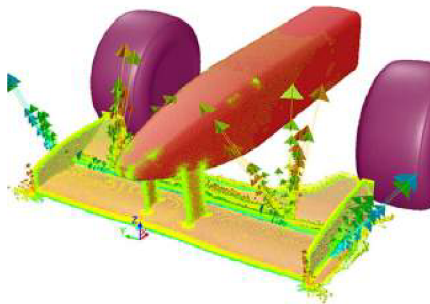
Fig. 1.4: *Aplication of the adjoint solver on the Formula 1 car* [102].

Adjoint solver optimization approach involves a shape modification that goes hand in hand with a mesh morphing. Morphing takes place, when a sensitivity field is calculated (through the adjoint equations; see subsection *Discrete adjoint approach theory*). This morphing procedure has two main functions. First, it smooths the surface sensitivity field and then provides a smooth distortion in the boundary and interior mesh. Adjoint solver creates a rectangular computational volume, which encloses all optimized surfaces that will be later morphed. Control points are then equally distributed in this volume. These points in combination with the mesh coordinates define the proper movement on the surface and in the interior mesh. [62], [94].

Discrete adjoint approach theory
There are two types of the adjoint approaches – continuous and discrete, but Adjoint solver uses only the discrete form. Basic equations, on which is Adjoint solver built, could be found in more detail in [67], [93]. As mentioned above, Adjoint solver needs the fully converged flow simulation, from which the gradients of the objective function are derived.

The gradient G of the objective function $J = J[X_D, Q(X_D)]$ is [67]:

$$G = \frac{dJ}{dX_D} = \frac{\partial J}{\partial X_D} + \frac{\partial J}{\partial Q}\frac{dQ}{dX_D}, \tag{1.1}$$

where X_D is a vector of design variables (in [67] is reduced to scalar), dQ/dX_D is described as flow sensitivities and Q is a vector of conserved flow variables [67]. This gradient could be rewritten in a form [67]:

$$G = \frac{\partial J}{\partial X_D} - \psi^T \frac{\partial R}{\partial X_D}, \tag{1.2}$$

where $R = R[X_D, Q(X_D)]$ is the discretized RANS residual vector, ψ is a vector of adjoint variables and is obtained by solving the linear system of the adjoint equations [67]:

$$\frac{\partial R^T}{\partial Q}\psi = \frac{\partial J^T}{\partial Q}. \tag{1.3}$$

Application of Fluent Adjoint solver
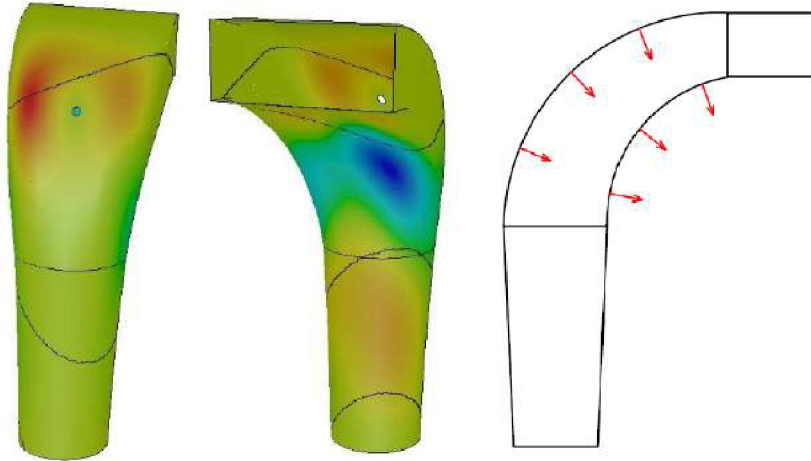
Fig. 1.5: *Aplication of the Adjoint solver on the siphon draft tube* [57].

Chosen applications of the Fluent Adjoint solver in the field of the shape optimization of the certain hydraulic part could be found e.g.: the application on a car duct system in [94] - a problem of a pressure drop minimization in such system; next a maximization of a coefficient of pressure recovery c_p of a turbine diffuser in [62]. Application on more advanced geometry of a siphon draft tube in [57] (once again the problem of the maximization of the coefficient of pressure recovery c_p) - fig. 1.5, where blue and red areas indicate possible shape change of the draft tube surface, which may lead to an improvement of the coefficient of pressure recovery c_p (or its efficiency) of this siphon draft tube. Author in [73] used the Adjoint solver for the shape optimization of a hydraulic valve part in a perspective of the pressure drop minimization.

Conclusion

Among the main advantages of this tool belong: direct implementation in ANSYS Fluent (there is no need for additional software installation); mesh morphing is also presented in Adjoint solver (no need for additional mesher). But on the other hand, there are great disadvantages: first is lack of a useful way to control partial or final shape of any optimized surface - an absence of surface constraints, that fact could lead to a creation of the unmanufacturable designs. Also mesh morphing can deform cell(s) into a state of high skewness and in this state calculation usually cannot continue (new mesh must be created in external mesher) [62], [94]. Another restriction is that the Fluent Adjoint solver only allows you using a $k - \epsilon$ model of turbulence with standard wall function [4].

1.2.2 Evolutionary Algorithms System - EASY

EASY is a licence free optimization tool developed by a group called Parallel CFD and Optimization Unit of the Laboratory of Thermal Turbomachines of the National Technical University of Athens [69].

EASY is capable of finding the optimal solution in the single-objective optimization or solutions in the multi-objective optimization by using Generalized Evolutionary Algorithms. EASY operates with three types of populations: a parent, an offspring and an elite or archival set (in more detail in subsec. 1.3.3). In the multi-objective optimization problems, the Pareto front is utilized for a locating of the optimal solutions [69].

Application of EASY tool

Chosen application of the *EASY* tool could be found in [8] in a problem of the shape optimization of the blades of the Francis turbine or in [101] in the problem of the shape optimization of the bucket of the Pelton turbine - fig. 1.6.

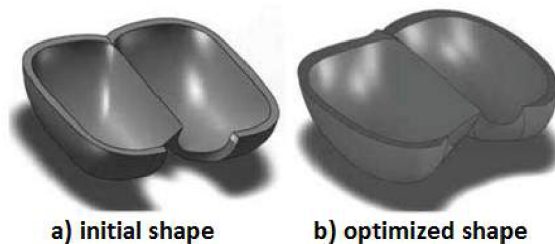a) initial shape   b) optimized shape

Fig. 1.6: *Comparison of the Pelton bucket geometries* [101].

Conclusion

EASY is a licence-free optimization tool and its advantages/disadvantages are tightly linked with quality attributes of evolutionary algorithms (EA) - see subsection 1.3.3.

1.2.3 Nonlinear Optimization by Mesh Adaptive Direct Search - NOMAD

NOMAD tool is a C++ installation of the Mesh Adaptive Direct Search algorithm (**MADS**), which is designed for constrained optimization and uses series of meshes with various sizes [52], [53].

In short the main goal of every iteration of the MADS algorithm is to create a trial point on the mesh, that could improve a current best solution. When such iteration fails to accomplish this improvement, then the next iteration is started on a finer mesh. The main basis of the MADS algorithm are two crucial steps **the search** and **the poll**, which handles creation of a trial mesh points in the close neighbourhood of the best solution (crucial core of MADS) [7], [9], [52], [53].

Description of the MADS algorithm
MADS is an iterative algorithm, which tries to locate an optimum of the function f over Ω (f_Ω) by evaluating f_Ω in the trial points. The algorithm does not need derivatives or approximations of derivatives of function f. Each iteration (denoted by the index k) a finite number of trial points is generated, objective function is evaluated in them and then the function values are compared with the best feasible function value $f_\Omega(x_k)$ found so far [7]. Each trial point lies on the mesh constructed by the equation [7]:

$$M_k = \bigcup_{x \in S_k} \{x + \Delta_k^m D z : z \in \mathbf{N}^{n_D}\}, \tag{1.4}$$

where Δ_k^m is a mesh size parameter, n_D is a finite set of directions and S_k is the set of points, where the objective function had been evaluated by the start of iteration k - fig. 1.7.

Fig. 1.7: *Samples of MADS grids* [52].
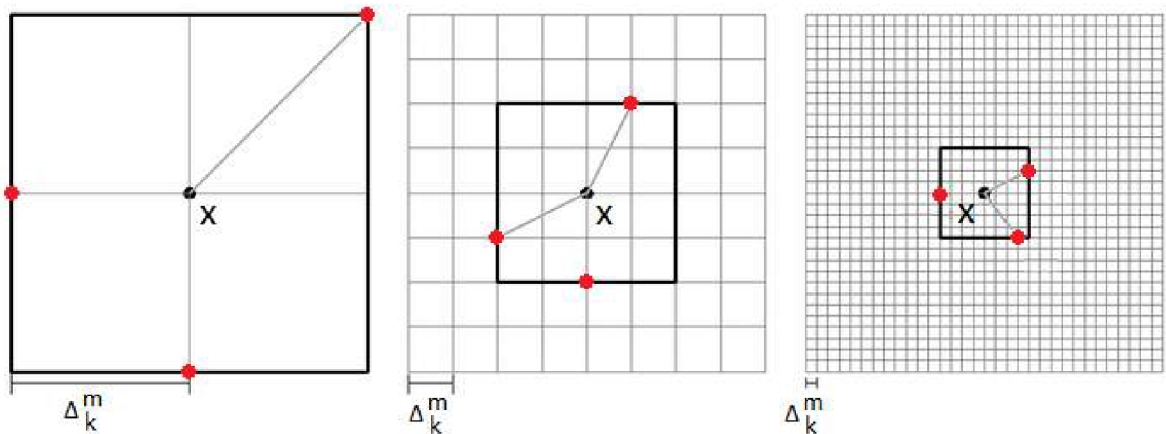
The crucial objective of each iteration is a localization of the trial point with better objective function value than the current best $f_\Omega(x_k)$. Such a trial point is called an *improved mesh point* and the iteration is *successful*. Each iteration is divided into two main parts. First is called **the search** step and it allows evaluation of f_Ω at any finite

number of mesh points. If the search step fails in the improvement of the point with the best value of the objective function, the second step called **the poll** must be invoked before a termination of the current iteration. The poll has a task of a creation of the trial points around the best current solution. When both, the search and the poll fails in generating the improved point, then mesh resolution must be increased [7], [53]. *MADS* algorithm is illustratively summarized by a pseudocode 1.1 [53].

Code 1.1: *MADS pseudocode* [53].

```
 1  initialize x_0 as an initial point
 2  set iteration k=0
 3  while ending criterion is not met
 4    SEARCH application (to find better solution than x_(k))
 5
 6      if SEARCH fails
 7        POLL application (to find better solution than x_(k))
 8      endif
 9
10      if a better solution is found
11        call it x_(k+1) and make coarser mesh
12      else
13        x_(k+1)=x_(k) and refine mesh
14      endif
15
16    update parameters
17    check ending criterion
18    k = k + 1
19  endwhile
```

Application of NOMAD

NOMAD was exploited for example in [8] and [9] for the shape optimization of a Francis turbine runner blade. The optimization cycle in [9] used at the beginning of its run low-fidelity models with a small amount of the design parameters. It created the initial robust shape. In the end of the cycle were used high-fidelity models with more design parameters (for a final precise evaluation). In [100] authors designed microfluidic channels in a way that produces constant strain-rates along the centre of the flow.

Conclusion

NOMAD is the licence-free optimization tool, which lacks graphical user interface, but could be utilized within *Matlab* or *Python*. NOMAD does not need any derivatives of the objective function and is suitable for the single or bi-objective optimization (shows quality imperfections in the multi-objective optimization [52]).

1.3 Utilization of a correct optimization method and its application

1.3.1 Direct methods

Direct methods, such as **Nelder-Mead** or **EXTREM** algorithm, are usually used for the simpler optimization problems. These algorithms are characterized by a fast convergence and a good effectiveness in the final local search [93]. As a member of the direct optimization algorithms should be mentioned also **Response surface method** [31].

1.3.1.1 Nelder - Mead algorithm

Nelder - Mead [66] (NM in short), sometimes known as the Simplex method, is a straightforward algorithm, that does not use any derivatives of the examined function. A method is based on the minimization/maximization of a certain cost function of n variables and the main foundation lies on the comparison of the function values at the $(n+1)$ vertices of the simplex. Every iteration the NM algorithm tries to replace the vertex with the worst value of the examined function with 4 basic steps: reflection, expansion, contraction and simplex reduction [58], [66] - the simplex in 2D problem is a triangle. The main steps of NM algorithm are illustratively shown in fig. 1.8.
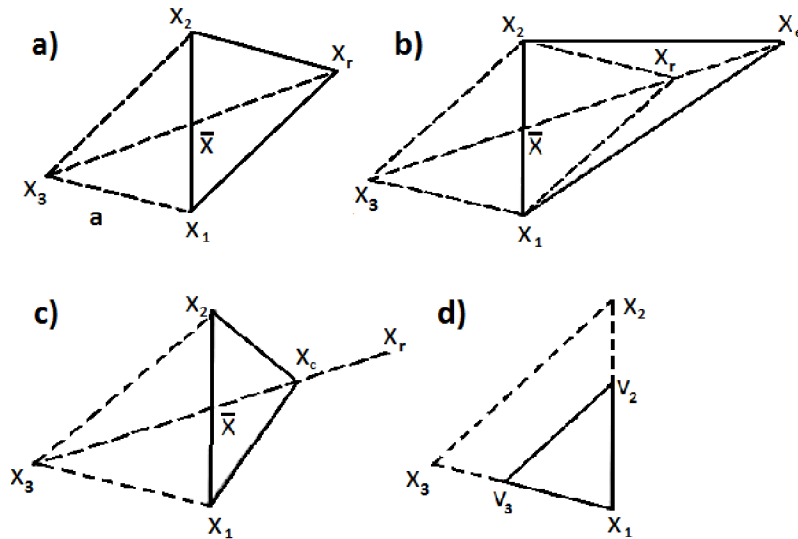

Fig. 1.8: *NM algorithm in 2D: reflection, expansion, contraction and reduction* [58].

Description of the Nelder - Mead algorithm

The first step of the Nelder - Mead algorithm is a formation of the regular simplex with a length side a [58]:

$$x_j = x_1 + pe_j + \sum_{k \neq j} qe_k, \tag{1.5}$$

where x_1 is a specified point (usually specified by a user), e_k is a unit matrix and parameters p and q are defined as [58]:

$$p = \frac{a}{n\sqrt{2}}(\sqrt{(n+1)} + n - 1), \qquad (1.6)$$

$$q = \frac{a}{n\sqrt{2}}(\sqrt{(n+1)} - 1), \qquad (1.7)$$

where n is a dimension of current optimized problem (a number of variables).

Then the vertices of the simplex must be sorted according to the values of the objective function and the vertex with worst value must be found. This worst vertex (vertex x_3 in fig. 1.8) is afterwards reflected around a centroid (average value) of remaining points (first case in fig. 1.8) [58]:

$$x_r = \overline{x} + \rho(\overline{x} - x_{n+1}), \qquad (1.8)$$

where $\overline{x} = \frac{1}{n}\sum_{i=1}^{n} x_i$ is the centroid and $\rho > 0$ is a parameter of the reflection.

If newly reflected vertex improves the value of the worst vertex, it means that this direction is promising and the expansion takes place (second case in fig. 1.8) [58]:

$$x_e = \overline{x} + \eta(x_r - \overline{x}), \qquad (1.9)$$

where $\eta > 1$ is a parameter of the expansion.

But if reflection or expansion fails in the improvement of the vertex with the worst value of objective function, then the contraction (external or internal) must be invoked. External contraction is described by third case in fig. 1.8 and is defined [58]:

$$x_c = \overline{x} + \gamma(x_r - \overline{x}), \qquad (1.10)$$

similarly the internal contraction [58]:

$$x_c = \overline{x} + \gamma(x_{n+1} - \overline{x}), \qquad (1.11)$$

where γ is a parameter of the contraction $(0 < \gamma < 1)$.

If any of the previous steps does not bring the improvement, the simplex reduction must be applied (fourth case in fig. 1.8) [58]:

$$v_i = x_1 + \sigma(x_i - x_1) \quad for \quad i = 1, \ldots, (n+1), \qquad (1.12)$$

where σ is a parameter of simplex reduction $(0 < \sigma < 1)$.
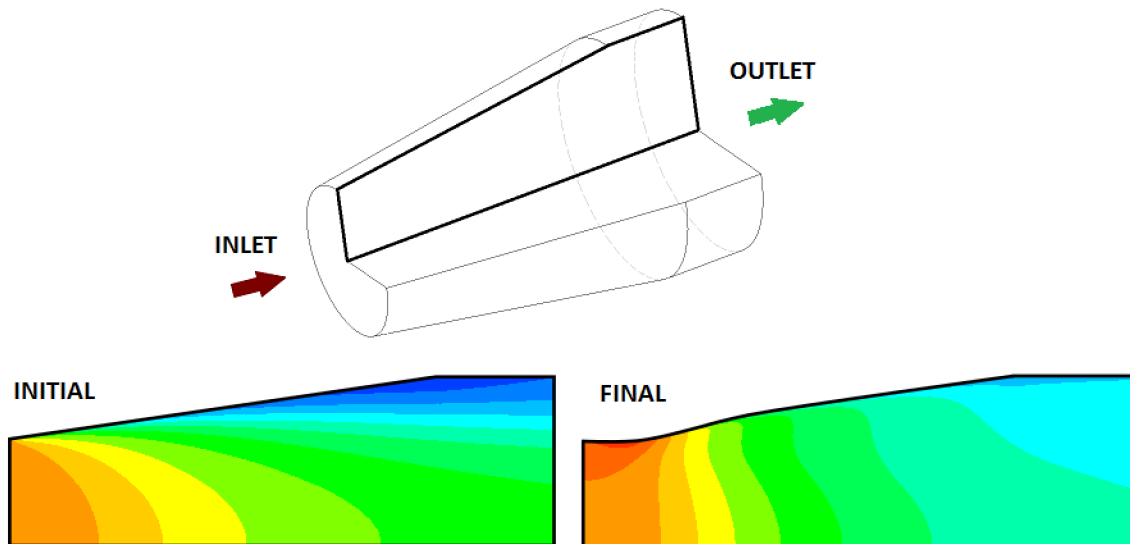
Fig. 1.9: *Aplication of Nelder-Mead algorithm* [32], [62].

Application of the Nelder - Mead algorithm

The application of the Nelder - Mead algorithm in the hydraulic machinery could be e.g.: a diffuser (draft tube) shape optimization problem (fig. 1.9) in a way of maximization of the coefficient of pressure recovery c_p found in [32], [62], [64] or [79].

In [86] authors exploited the Nelder-Mead algorithm in an in-house software to produce a design of the new turbine with the fixed blade runner called a "Mixer"(fig. 1.10).

Fig. 1.10: *CNC machining of "Mixer"(left), installation in the laboratory (right)* [86].

Conclusion

It must be noted that the NM algorithm is usually suited for the minimization/maximization of the functions with $n \leq 10$ variables [48]. It excels in the computational speed and straightforwardness (positive attributes in the local search), but lags behind in the global search of the given problem, mainly thanks to a starting position of the initial simplex and a simplex size (algorithm could be frequently prone to some local optimum).

1.3.1.2 EXTREM algorithm

The algorithm **EXTREM** was introduced in 1982 by H.G. Jacob [38]. This optimization procedure does not use any derivatives of the examined function. Algorithm is based on a directional search - a composition of an one dimensional user search direction, orthogonal direction and their modification [38], [80].

Description of the EXTREM algorithm

EXTREM algorithm could be described on a minimization problem of two variables as follows: it starts with the initial first search direction. Objective function is approximated by a polynomial along this direction (fig. 1.11 through points 1-3 and a starting point c^0). Minimal value of the objective function of this approximation must be found (point 4 in fig. 1.11). Afterwards the search continues in the orthogonal direction and once again this direction is approximated by the polynomial through points 4-6 and once again the minimal value of the objective function along this orthogonal direction must be found (point 7 in fig. 1.11). Next step involves a creation of the new direction using a linear connection between the starting point c_0 and the last found point with the minimal value of the objective function [21]. Algorithm continues in such way until a certain chosen ending criterion is met or until the algorithm termination by the user.
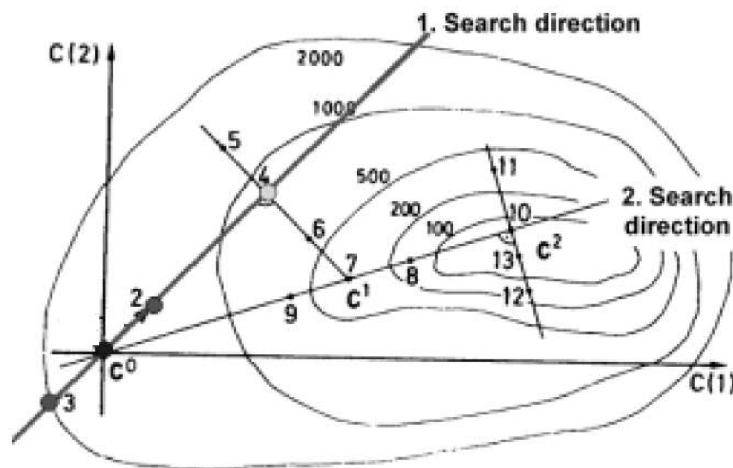
Fig. 1.11: *EXTREM method in 2D* [21], [38].

Application of the EXTREM algorithm

Applications of the *EXTREM* algorithm could be found e.g. in [21] in the problem of the shape optimization of the hydraulic turbine draft tube or in [56], where the algorithm was used for a creation of a low Reynolds number airfoils.

Conclusion

Same case as the Nelder - Mead method, the *EXTREM* algorithm excels in speed, but is frequently trapped in some local optimum.

1.3.1.3 Response surface methodology

Response surface method/methodology (shortly RSM) was firstly reviewed in 1966 by William J. Hill and William G. Hunter [31]. It employs different statistical, mathematical and graphical processes in a way of a developing, predicting, improving or optimizing certain procedures based on data from experiments or numerical simulations [23]. RSM is mentioned in a group of **direct methods** for a reason of the similar way of finding global/local optimum - in short: Nelder-Mead utilizes simplexes, EXTREM uses lines and their modifications and Response surface methodology exploits the approximated response surfaces from acquired data, which come from the experiments or from the numerical simulations.

Description of the response surface methodology

In the optimization process, the engineer is focused on a response y that strongly depends on the controllable input design variables $x_1, x_2, \ldots, x_k$ [65]. The relationship between the response and the input variables is [65]:

$$y = f(x_1, x_2, \ldots, x_k) + \varepsilon, \tag{1.13}$$

where the true aspects of the response function f are usually unknown and often very complicated. The variable ε is a statistical error [65]. The unknown true response function f (eq. 1.13) must be approximated by an appropriate polynomial $\rightarrow$ the RSM employs the **first-order** or **second-order** model. In general, the first-order model is defined according [65] as:

$$\eta = \beta_0 + \sum_{i=1}^{n} \beta_i \cdot x_i, \tag{1.14}$$

where β_0, β_i are regression coefficients, x_i is design variable and η is the approximated response. Figure 1.12 shows the three-dimensional response surface and the two-dimensional contour plot for a case of the **first-order** model [65]:
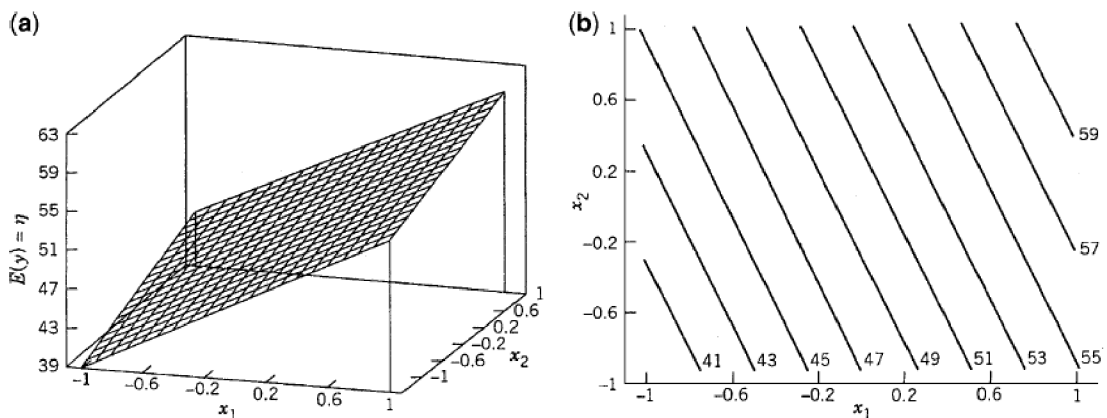
$$\eta = 50 + 8 \cdot x_1 + 3 \cdot x_2. \tag{1.15}$$

Fig. 1.12: *Response surface for the first-order model with contour plot* [65].

If there is an interaction between variables x_1, x_2 in eq. 1.15, the mentioned surface function will change for instance into the form [65]:

$$\eta = 50 + 8 \cdot x_1 + 3 \cdot x_2 - 4 \cdot x_1 \cdot x_2, \tag{1.16}$$

It must be noted that the component $-4 \cdot x_1 \cdot x_2$ brings a slight curvature into the approximated response function - fig. 1.13.
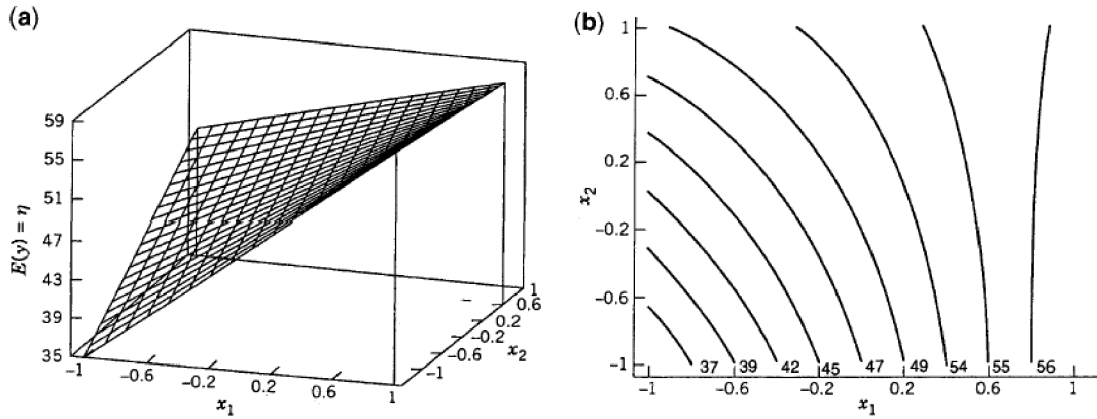
Fig. 1.13: *Response surface for the first-order model with interaction with contours* [65].

In general, the second-order model has the form [65]:

$$\eta = \beta_0 + \sum_{i=1}^{n} \beta_i \cdot x_i + \sum_{i=1}^{n} \beta_{ii} \cdot x_i^2 + \sum_{i<j} \sum_{i=1}^{n} \beta_{ij} \cdot x_i \cdot x_j, \tag{1.17}$$

where β_0, β_i, β_{ii} and β_{ij} are regression coefficients, x_i is design variable and η is the approximated response. Figure 1.14 shows the three-dimensional response surface and the two-dimensional contour plot for the case of the **second-order** model [65]:

$$\eta = 50 + 8 \cdot x_1 + 3 \cdot x_2 - 7 \cdot x_{11}^2 - 3 \cdot x_{22}^2 - 4 \cdot x_1 \cdot x_2. \tag{1.18}$$
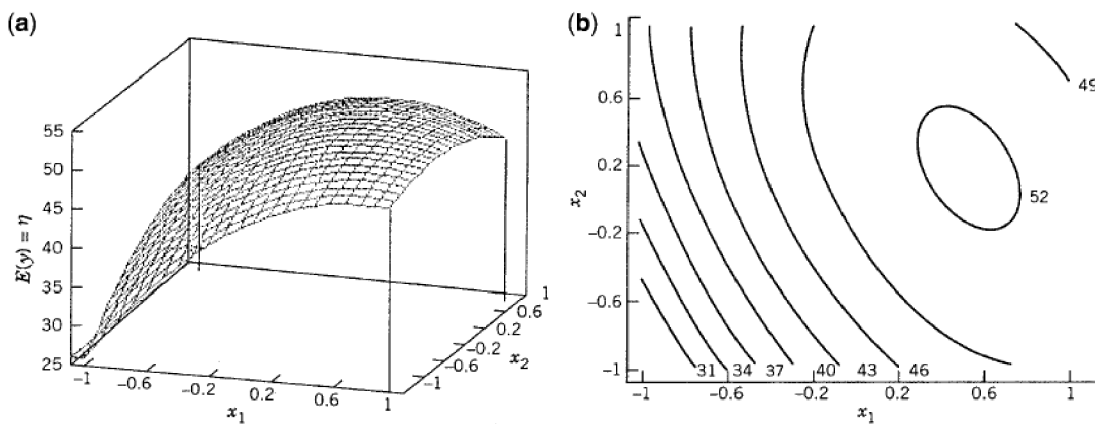

Fig. 1.14: *Response surface for the second-order model with contours* [65].

According to [65], the second-order model is very adaptive, meaning that it could manifest a variety of function forms for the response surface. This model is often used in many practical engineering problems.

It must be noted that from such approximations (fig. 1.12 - 1.14), the optimum could be easily found by an examination of the functions plots. Another important part of RSM is also a proper planing of experimental (or numerical) points/designs - so called experimental **strategies** (designs of experiments $\rightarrow$ **DoE**) - such as full factorial design, central composite design, Box-Behnken design or D-optimal design and many more (in depth described in [23]). These strategies help to locate the optimum by the appropriate choice of the simulations in the near surroundings of the current best design (function value).

Application of the response surface method

Application of RSM is countless across the various parts of the industry. While focusing on the combination of the hydraulic machinery and CFD, these works are worth mentioning: a task of the shape optimization of stator parts in a way of the maximizing efficiency (while minimizing turbine power) in [55] or the shape optimization of the mixed-flow pump with the diffuser for a purpose of finding the proper pump design point [46].

1.3.2   Gradient methods

1.3.2.1   Quasi - Newton methods

The most popular Quasi - Newton method is **BFGS**. It was proposed independently in 1970 by C. G. Broyden [12], R. Fletcher [22], D. Goldfarb [24] and D. F. Shanno [83]. In comparison with a well-known Newton's method, BFGS differs in Hessian evaluation (i.e matrix of second derivations) - does not to be computed directly, approximation is sufficient. In more detail in [59].

Application of the BFGS algorithm

BFGS was for example applied in a problem of a finding proper shape of the hydraulic diffuser [32] or in the shape optimization problem of the adapting pipes in [91] - fig.1.15.
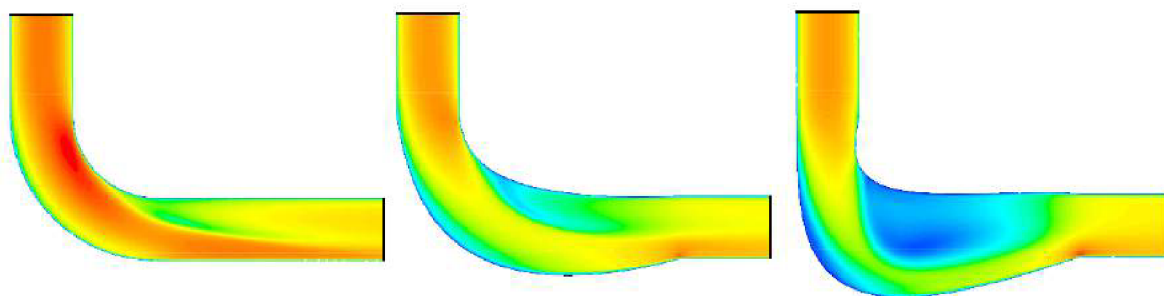

Fig. 1.15: *Initial shape of an elbow in the pipe (far left) vs optimized (right)* [91].

Conclusion

BFGS occasionally suffers of inaccuracies, mainly due to a calculation of partial derivatives in a gradient computation. The magnitude of the total computational time shows similarities, compared to Nelder - Mead method - in a problem of shape optimization of hydraulic diffuser [32] or in [59] (applied on a Rosenbrock test function - mathematical point of view).

1.3.2.2 Adjoint approach

Discrete **adjoint approach** in subsection 1.2.1 was contained inside the commercial software called ANSYS Fluent. But in many occasions commercial software with a limited number of licences is not an option, so engineers programmed adjoint equations (discrete or continuous) via some chosen programming language such as *Python, C++*, etc.. This is plentifully exploited especially in aerodynamic shape optimization problems.

Application of the Adjoint approach

Chosen publication with this type of adjoint application could be found e.g. in: the maximization of a lift (or the minimization of a drag) in an inviscid and viscous flows problems in [44], [45]; an aerodynamic shape optimization of the complete aircraft configuration in [39]; a shape optimization aiming to a reduction of a shock wave in [29] or an airfoil shape optimization in a transonic flow in [25].

1.3.3 Stochastic methods

Robust methods, such as Evolutionary Algorithms (EA) / Genetic Algorithm (GA) or Particle swarm optimization (PSO) and their various modifications, are nowadays extremely popular and exploited in the shape optimization problems, because they offer a lot of convenient features, such as great global search ability or lower tendencies to be trapped in some local optimum.

1.3.3.1 Evolutionary algorithm/Genetic algorithm

Genetic algorithms (GA) were developed in the 60-70s at the Michigan university, where they were used for solving problems in a field of an artificial intelligence [48].

The main idea, which is connected with the EA/GA algorithms is to search for some optimal solutions using an analogy to the evolution/genetic theory. During the iteration of EA/GA algorithm, the genes or the decision variables are treated using various operators, such as selection, mutation, (re)combination or crossover, to create new populations with new sets of modified parameters, that could lead to the improvement of the examined function [93].

Application of Evolutionary algorithm/Genetic algorithms

Utilizations of EA/GA are introduced in e.g.: the shape optimization of the draft tube in [21]; the multi-objective shape optimization of the cetrifugal pump in [81]; the shape optimization of the GAMM Francis turbine runner in [17]. A software using CFD simulations

and evolutionary algorithm with neural networks and surrogate models could be found in [51], where it is used for the shape optimization of the Francis turbine runner. Authors in [99] deeply investigated the problem of finding the proper shape of a pump turbine impeller - they designed a runner with high lean angle of the blade with high hydraulic efficiency (fig. 1.16).
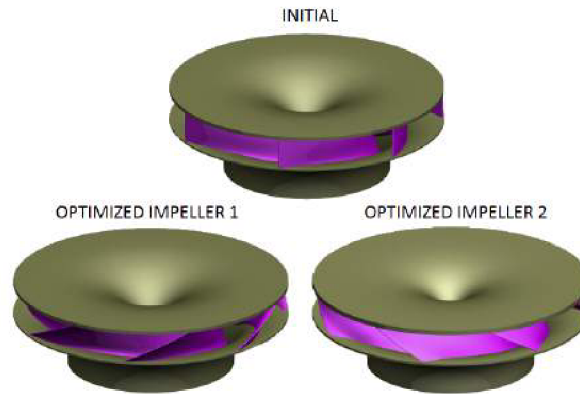
Fig. 1.16: *Pump turbine shape optimization* [99].

Another utilization of the GA algorithm could be found in [54] - a shape optimization problem of a valve shape in a micro cross-flow turbine (fig. 1.17).
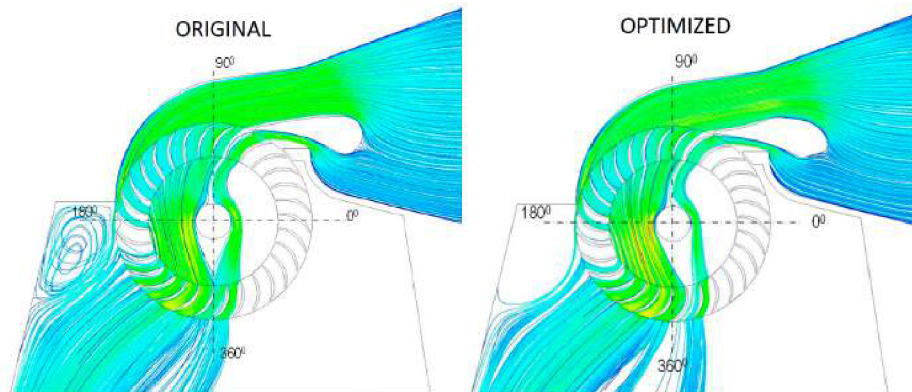
Fig. 1.17: *Valve shape optimization - original and optimized design* [54].

1.3.3.2 Particle swarm optimization
Particle swarm optimization is population based stochastic optimization method developed by J. Kennedy and R. Eberhart [42] in 1995. This method is strongly inspired by the social behaviour of fish schooling, bird flocking or swarming theory in particular. In more detail in section 2.4.

Application of Particle swarm optimization algorithm
Chosen applications of the PSO algorithm in the field of the shape optimization could be found e.g. in [63] or in [64] in the problem of designing the proper shape of the hydraulic turbine diffuser, based on the maximization of the coefficient of pressure recovery c_p.

Exploitation of the PSO algorithm in the axial pump impeller problem is shown in [60]. PSO utilization for the designing of a hull of the ship could be found in [35].

1.3.3.3 Artificial bee colony

Artificial bee colony (ABC) [41] is the latest meta heuristic (stochastic) method that is based on the animal behaviour. It was developed in year 2007 by D. Karaboga and B. Basturk. The algorithm mimics the foraging behaviour of a randomly distributed bee colony, which searches the best source of food (nectar) in the specific target area (clear influence of the Particle swarm optimization). The bee colony is divided into three groups: worker (employed) bees, scout bees and onlooker bees. In the algorithm, the source of food represents some solution of the optimization problem, a quantity of food indicates fitness value of the source and a number of bee workers matches with possible solutions [18].

Application of Artificial bee colony

ABC application in the hydraulic machinery could be found e.g. in the problem of the shape optimization of the centrifugal pump impeller in [18]. Derakhshan et al. also used the Artificial Bee Colony for the designig of the blades of a wind turbine in [19]. Such blades of the wind turbine are shown in fig. 1.18, where the output geometry from ABC optimization and the real manufactured model are compared.
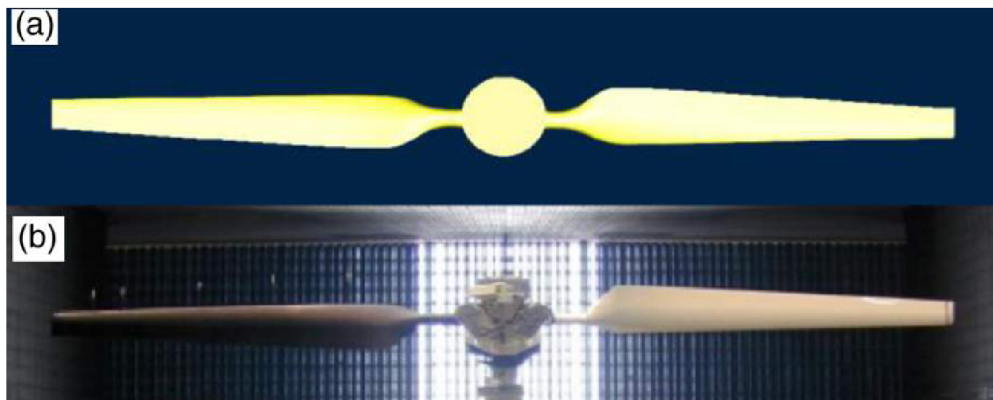
Fig. 1.18*: Impeller of wind turbine - a) output from optimization, b) real model* [19].

Slightly modified ABC algorithm called AsBeC (Artificial super-Bee enhanced Colony) was applied on an airfoil shape optimization problem in the turbomachinery field of the interest, which could be found in [5].

Conclusion for stochastic methods

All of the presented stochastic methods excel in the **robustness** and great **global search**, thanks to the size choice of the optimizing populations and the random population distribution in the whole given computational area. Due to these facts, they have a better chance to find a proper optimum and avoid tendencies to a premature convergence to some local optimum. But it must be mentioned, that the larger populations go hand in hand with the higher **computational time**, so a right and useful compromise must be found,

especially when a certain method is coupled with CFD. So an opportunity open here for a collaboration and a combination of two methods e.g. the robust PSO in a beginning of the optimization algorithm and the fast Nelder - Mead in the end of the algorithm [64].

In this brief conclusion lies a foundation for answering the question: why was the **Particle swarm optimization algorithm** chosen as the basis of the presented optimization tool? The answer could be simply summarized into the following three statements: **robustness**, **global search**, **uncomplicated algorithm**.

2 THEORY

This chapter covers a mathematical basis around the chosen Particle swarm optimization method, which was used for the impeller shape optimization. First mathematical concepts are described, which are tied with the optimization in general (the global and local optimum, the optimization problem), then the main type of a curve for a model parametrization is set - **Bézier curve** is outlined. After that, the main BladeGen definitions are briefly explained and in the end, the basic equations of the Particle swarm optimization and Pareto principles are shown together with basics from CFD.

2.1 Basic mathematical concepts

Global minimum and maximum
Be a function $f : \mathbf{R}^n \rightarrow \mathbf{R}$; $\Omega \subseteq D_f$; $A \in \Omega$. Then [59]:

- f has in a point A global maximum on Ω, when $\forall x \in \Omega$ holds $f(x) \leq f(A)$
- f has in a point A global minimum on Ω, when $\forall x \in \Omega$ holds $f(A) \leq f(x)$

The difference between the local and global minimum is captured in a graphical representation of the function of two variables $f(x, y)$ in fig. 2.1.
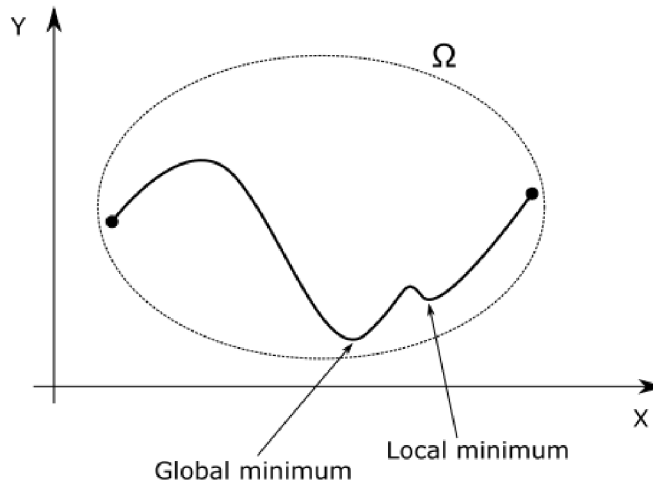
Fig. 2.1: *Global vs. local minimum.*

Optimization problem
The optimization problem (finding a minimum in this paragraph) is a problem of finding such $\mathbf{x}^* \in M$, that for any $\mathbf{x} \in M$ is true [36]:

$$f(\mathbf{x}^*) \leq f(\mathbf{x}); \ \forall \mathbf{x} \in M, \tag{2.1}$$

where the continuous function $f : M \rightarrow \mathbf{R}$ is called an objective function, or a cost function and M is a set of acceptable solutions. If $M = \mathbf{R}^n$, then we talk about an **unconstrained optimization**. In the case, that $\mathbf{x} \in \Omega$, $\Omega \subset \mathbf{R}^n$, optimization changes to a **constrained**, where Ω is called a constraint set or a feasible set [36].

30

General multi-objective optimization problem [15]

General multi-objective optimization problem is a problem of finding such $\mathbf{x}^* = (x_1^*, x_2^*, \ldots, x_n^*)^T$, which satisfies m inequality constraints [15]:

$$g_i(\mathbf{x}) \geq 0; \ i = 1, 2, \ldots, m, \tag{2.2}$$

p equality constraints [15]:

$$h_i(\mathbf{x}) = 0; \ i = 1, 2, \ldots, p, \tag{2.3}$$

and will optimize function [15]:

$$f(\mathbf{x}) = [f_1(\mathbf{x}), f_2(\mathbf{x}), \ldots, f_k(\mathbf{x})], \tag{2.4}$$

where $\mathbf{x} = (x_1, x_2, \ldots, x_n)^T$ is a vector of variables.

2.2 Bézier curves

Bézier curves (fig. 2.2) are famous parametric curves, which are frequently used in various technical areas. Among the founders belong P. E. Bézier and independently on him P. de Casteljau [59].

First degree   Second degree   Third degree
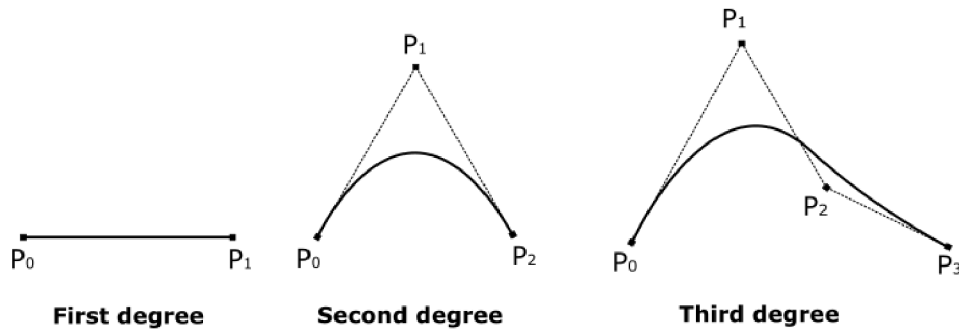
Fig. 2.2: *Bézier curves.*

The general equation of the Bézier curve with $n + 1$ control points P_0, P_1, P_2, $\ldots$, is defined as [59]:

$$Q(t) = \sum_{i=0}^{n} P_i B_i^n(t), \ t \in \langle 0, 1 \rangle, \tag{2.5}$$

where $B_i^n(t)$ are Bernstein polynomials, which serve as a basis for Bézier curve. Bernstein polynomials are defined [59]:

$$B_i^n(t) = \binom{n}{i} t^i (1 - t)^{n-i}. \tag{2.6}$$

The crucial attributes of the Bézier curves are primarily: the first and the last control point are endpoints of the curve; the beginning and the end of the curve is tangent to the first and last section of the control polyline (fig. 2.2); first derivative of the Bézier curve is another Bézier curve (lower degree); position change of one control point causes a shape change of the whole curve [59].

2.3 BladeGen definitions

Two main BladeGen variables M and θ, which are later extensively exploited in the following sections of this doctoral thesis, must be properly explained for a better understanding of several key elements of the presented optimization tool.

M definition

The variable M represents in BladeGen a distance along a meridional curve, which is defined as [4]:

$$dM = \sqrt{dR^2 + dZ^2},\tag{2.7}$$

where R is a radial location and Z is an axial direction.

M-prime definition

The variable M' represents in BladeGen a radius normalized distance along the meridional curve, which is defined as [4]:

$$dM' = \frac{\sqrt{dR^2 + dZ^2}}{r} = \frac{dM}{r},\tag{2.8}$$

where R is the radial location, Z is the axial direction and r is the reference radius.

θ - angle definition

The variable θ - angle represents in BladeGen a rotation around Z axis from X towards Y axis (right hand rule), which is defined as [4]:

$$d\theta = tan(\beta) \cdot dM',\tag{2.9}$$

where β is the angle of the blade and M' the radius normalized distance along the meridional curve.

2.4 Particle swarm optimization algorithm (PSOA)

Particle swarm optimization was introduced by J. Kennedy and R. C. Eberhart in 1995. This method was discovered through a simulation of a simplified social model and focuses its energy on behaviour study of various animals such as fish schooling, bird flocking and swarm theory in particular [42].

The Particle swarm optimization algorithm uses the swarm of particles randomly distributed in a computational area (some problems need a bounded computational area to ensure a meaningful behaviour of the swarm [63]). Individual swarm members exchange crucial information mainly about their velocities (step sizes), positions and values of examined function (fitnesses) [42]. Velocity in PSOA is not a velocity in physical point of view, it represents **only** the size of the potential particle movement.

Every particle in PSOA is handled as a point in n-dimensional space. The i-th particle is $X_1 = (x_{i1}, x_{i2}, \ldots, x_{in})$. The best previous position of any member of the swarm is recorded and is represented as $P_1 = (p_{i1}, p_{i2}, \ldots, p_{in})$ and velocity (step size precisely) is $V_1 = (v_{i1}, v_{i2}, \ldots, v_{in})$. Particle with the best value of examined function (GBEST) is marked by index g (see eq. 2.10) [20], [84].

Generally there are two basic particle swarm optimization concepts [20]:

- **Global best** particle swarm optimization (GBEST model)
- **Local best** particle swarm optimization (LBEST model)

and the crucial difference between these two basic models is in a swarm topology.
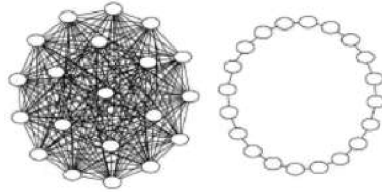

***Fig. 2.3**: GBEST model vs. LBEST model* [43].

In Global best model (fig. 2.3) all particles in the swarm are directly connected to the best value of examined function, but in Local best model (fig. 2.3) is every particle influenced by only a few neighbouring particles – typical number of neighbours is 2 – ring lattice [20].

2.4.1 Global best PSO

In this model is the basic movement of the particles characterized by following equation [20], [84]:

$$v_{in} = w \cdot v_{in} + c_1 \cdot rand() \cdot (p_{in} - x_{in}) + c_2 \cdot Rand() \cdot (p_{gn} - x_{in}), \qquad (2.10)$$

where c_1 and c_2 are positive constants; w is inertia weight, $rand()$ and $Rand()$ are two random vectors from range $(0, 1)$; v_{in} is the velocity (step size) of the i-th particle; x_{in} is a current position of the i-th particle; p_{in} is the best previous position of the i-th

particle (personal best); p_{gn} is the position of the certain particle with the best value of the examined function in the whole swarm (GBEST). It must be noted that the velocity in eq. 2.10 is not the velocity from the physical point of view, it represents possible particle displacement (step size).

Particle positions are afterwards computed according to equation [20], [84]:

$$x_{in} = x_{in} + v_{in}. \tag{2.11}$$

Global best PSO could be summarized by pseudocode 2.1, which is written down bellow.

Code 2.1: *Pseudocode for PSO* [84].

```
 1  initialize swarm position (random)
 2  function evaluation
 3  find GBEST
 4  initialize velocity (with zeroes)
 5
 6  iteration = 1
 7  while iteration < max_iteration
 8      for i=1:no_particles %number of particles
 9          calculate velocity
10          update position
11          function evaluation
12          find GBEST
13          update pbest (personal best)
14      endfor
15    iteration = iteration + 1
16  endwhile
```

2.4.2   Local best PSO

This model differs only in velocity calculation [20], [84]:

$$v_{in} = w \cdot v_{in} + c_1 \cdot rand() \cdot (p_{in} - x_{in}) + c_2 \cdot Rand() \cdot (p_{ln} - x_{in}), \tag{2.12}$$

where p_{ln} is the position of the certain particle with the best value of the examined function in the the specified neighbourhood (LBEST).

It must be noted, that PSO excels in single-objective optimization [63], but in multi-objective optimization must be slightly modified [14], [60]. This modification involves a **Pareto principle** [15] and is further introduced in section 2.5.

2.4.3 Main PSO parameters

Inertia weight w

Authors in [84] introduced **inertia weight w**. This parameter is used to set an equilibrium between the local and global search of the current optimizing swarm. Parameter w could be treated usually by two potential manners: constant [84] or adaptive [6], [85], [98].

Parameters c₁ and c₂

PSO parameter **c₁** stands for a "self-cognition". The main task of **c₁** is to ensure a diversity of the swarm (basically it pushes particles to inspect whole computational area) [42]. On the other hand, PSO parameter **c₂** is a representative of a "social influence". Parameter **c₂** compels the swarm to converge to the current global best solution of the optimizing function [42]. These parameters could be treated once again in two possible ways: constant [42] or adaptive [6], [98].

Population size

Authors in [33] recommend population size between 10 and 40 (this issue was tested in single objective problem, mostly on mathematical functions with several variables). In [63] there were tested populations of five and ten members as the smallest feasible swarms in a single objective problem with two and four variables. A specific size of the swarm cannot be precisely determined, because it strongly relies on a number of variables and on a character of the examined (optimized) problem.

2.4.4 PSO application - mathematical test function

To get a better idea of how the Particle Swarm optimization algorithm works, it is advisable to apply this optimization algorithm to some mathematical test functions. There are a plenty of the test functions with various shapes and with different values and locations of the global optima, such as e.g. **Rosenbrock function** [78] or **Ackley function** [1] (in more detail in [95]). The utilization of the Global best PSOA on Rosenbrock function was examined in a previous work [64], which deals with the combination of the Global best PSO and the Nelder-Mead algorithm in the shape optimization problem. Ackley function (fig. 2.4) was chosen as the testing example for this doctoral thesis. It has the global optimum located in the position $[0,0]/, [x-position, y-position]$ with the functional value equals to 0. Ackley function also posses multiple local optima, which could sufficiently mimic some complicated engineering shape optimization problem.

Examined Ackley function is defined for the two variables x and y as follows [1]:

$$f(x,y) = -20 \cdot exp\left[-0.2\sqrt{\frac{x^2+y^2}{2}}\right] - exp\left[\frac{cos2\pi x + cos2\pi y}{2}\right] + 20 + e. \qquad (2.13)$$

Function limitations were set for practical visualization purposes to $(-6, 6)$ for both, x-axis and y-axis.

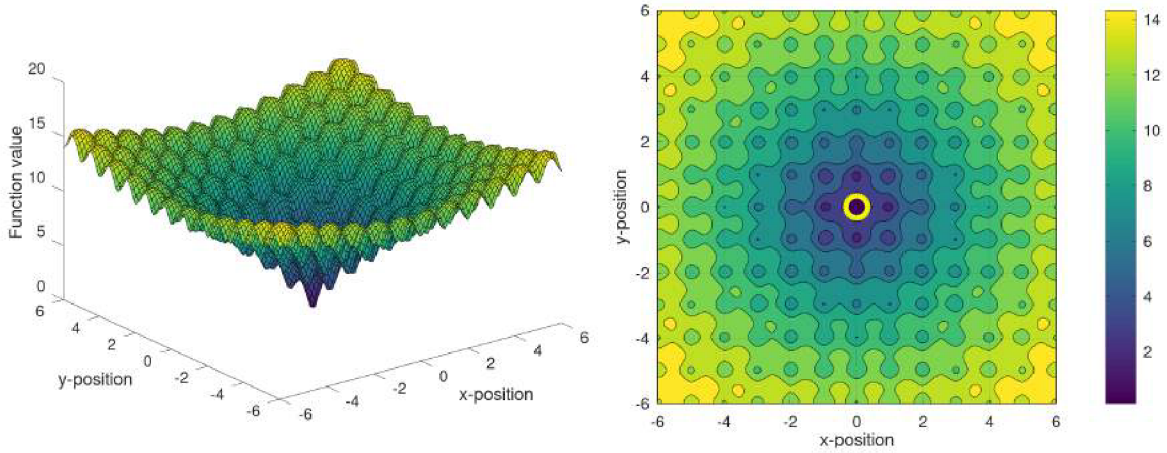**Fig. 2.4**: *Ackley function in 3D and contour plot - visualized by GNU Octave.*

The application of the Global Best version of the Particle swarm optimization algorithm is shown in fig. 2.5. The swarm had 25 individuals with the main parameters - $w = 0.8$ (linear decrease), $c_{1,2} = 2$. Total number of iterations was set to 100.
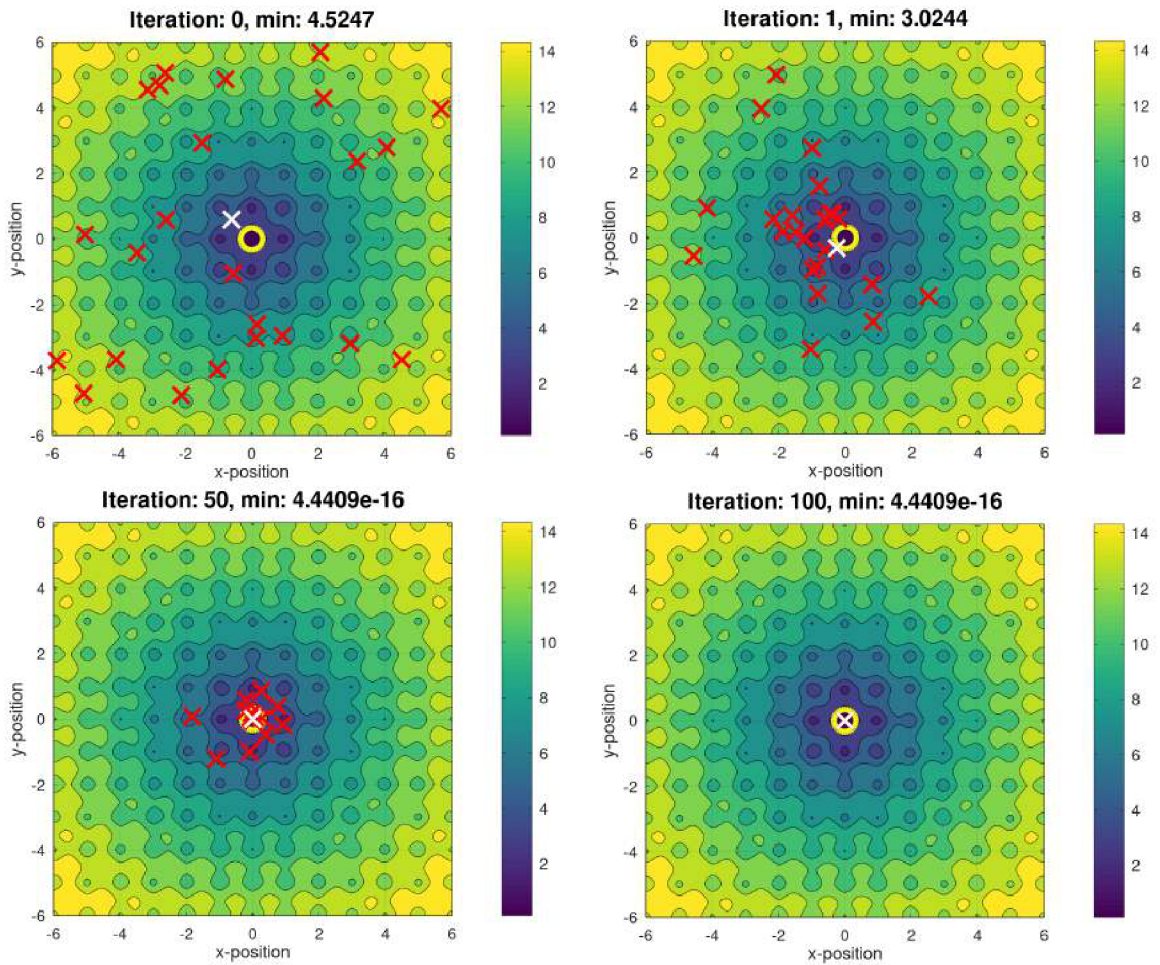

Fig. 2.5: *Global best PSO application - Ackley function.*

The Global best PSOA starts with the randomly generated set of the individuals in the whole given computational area (in fig. 2.5 represented as crosses). The global best individual must be found in every iteration of the optimization algorithm (in fig. 2.5 portrayed by the white cross). Such individual has the lowest functional value of the test function (Ackley function), which is described by the eq. 2.13. The particles move during the run of the algorithm towards the Global best individual and subsequently toward the global optimum, which lies in $[0, 0]$.

An important part of the PSOA is a proper parameter selection (see subsection 2.4.3), namely the inertia weight w, PSO parameters c_1, c_2 and the population size.
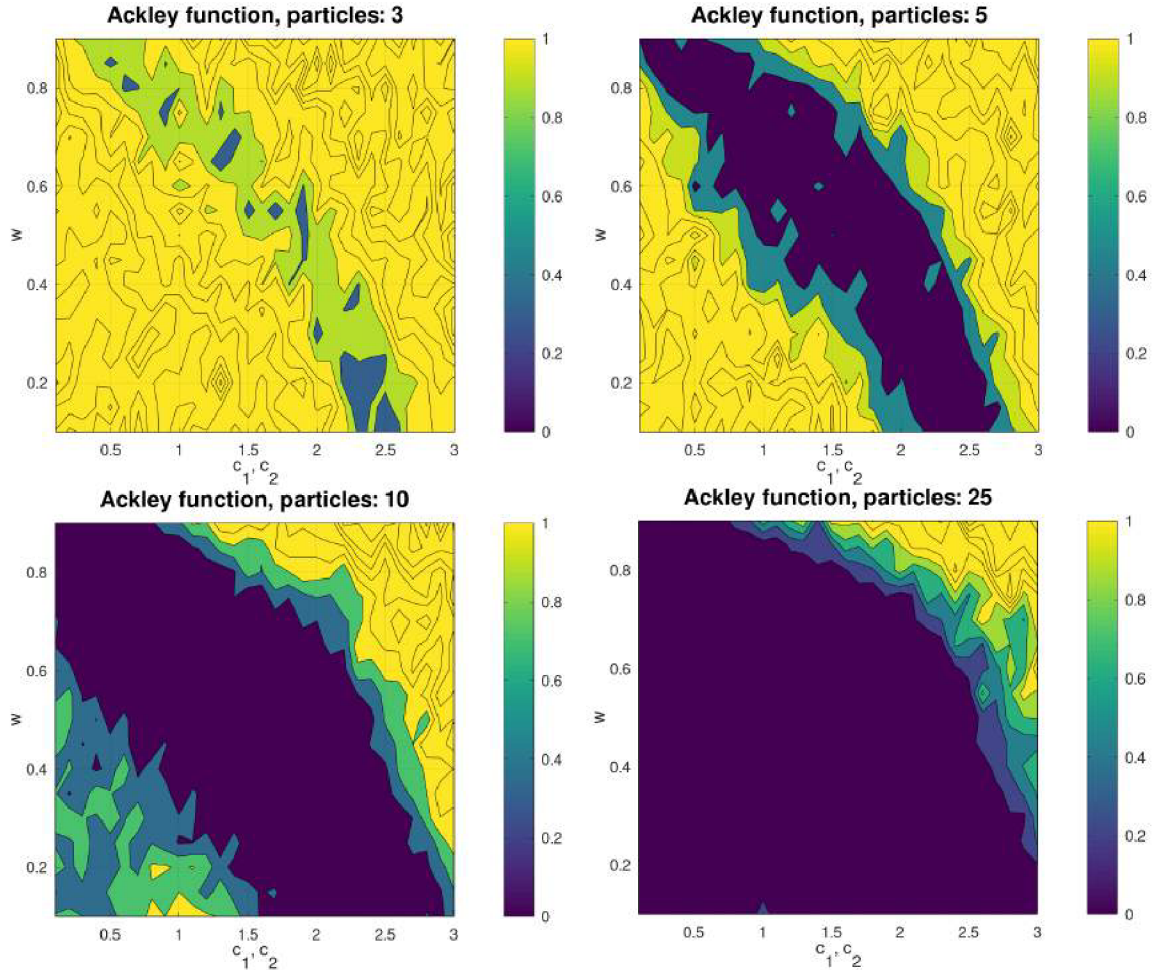

Fig. 2.6: *PSO parameter tuning - Ackley function.*

Figure 2.6 maps suitable/unsuitable sets of mentioned parameters, while thoroughly exploring Ackley function. The inertia weight w was picked from an interval $\langle 0.1, 0.9 \rangle$, on the other hand parameters c_1, c_2 ($c_1 = c_2$) lied in $\langle 0.1, 3 \rangle$. Four population sizes were utilized $(3, 5, 10, 25)$ in 25 different runs (100 iterations) of the Global best PSOA for each combination of w and c_1, c_2 ($c_1 = c_2$). After that, a mean value of the 25 global best individuals (of their functional values) was calculated and subsequently plotted for a purpose of the contour graph creation (fig. 2.6). Such parameter study shows a diagonal valley-like area of the suitable parameter combinations, which get wider with the increase of the population size (dark blue color).

2.5 Multi-objective particle swarm optimization

In [15] authors proposed an approach, in which Pareto dominance is utilized within the Particle swarm optimization algorithm. This approach improved and upgraded algorithm found in section 2.4 in a way of a possible multi-objective optimization. Basically it means, that shape designs are evaluated purely based on two or more objectives - in our case it was hydraulic efficiency and pump head.

2.5.1 Basic concepts [15]

Pareto optimal [15]
A point $\mathbf{x}^* \in \Omega$ is **Pareto optimal** if for every $\mathbf{x} \in \Omega$ and $I = \{1, 2, \ldots, k\}$ either:

$$f_i(\mathbf{x}) = f_i(\mathbf{x}^*); \forall i \in I, \tag{2.14}$$

or there is at least one $i \in I$ such that

$$f_i(\mathbf{x}) < f_i(\mathbf{x}^*). \tag{2.15}$$

Basically, the point $\mathbf{x}^*$ is **Pareto optimal**, if does not exist such $\mathbf{x}$, which would increase some objective without causing concurrent decrease of at least one another objective.

Pareto dominant [15]
A vector $\mathbf{u} = (u_1, \ldots, u_k)$ dominates vector $\mathbf{v} = (v_1, \ldots, v_k)$ ($\mathbf{u} \succeq \mathbf{v}$), if:

$$\forall i \in \{1, \ldots, k\} : u_i \geq v_i \wedge \exists i \in \{1, \ldots, k\} : u_i > v_i. \tag{2.16}$$

Pareto optimal set [77]
The **Pareto optimal set** $\mathcal{P}^*$ is defined as:

$$\mathcal{P}^* = \{\mathbf{x} \in \mathcal{F} | \mathbf{x} \; is \; Pareto \; optimal; \; \mathcal{F} \; is \; feasible \; set \; of \; solutions\}. \tag{2.17}$$

Pareto front [77]
The **Pareto front** $\mathcal{PF}^*$ is defined as:

$$\mathcal{PF}^* = \{f(\mathbf{x}) \in \mathbf{R}^k | \mathbf{x} \in \mathcal{P}^*\}. \tag{2.18}$$

The concepts, which are described above, could be characterized and implemented in bi-objective optimization problem - fig. 2.7.
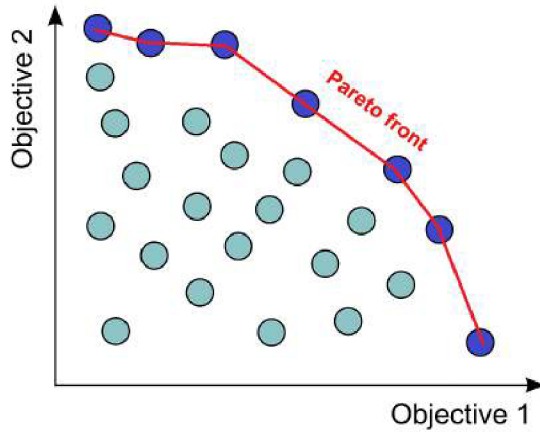
Fig. 2.7: *Schematic representation of Pareto concept in bi-objective problem* [47].

2.5.2   Main algorithm

The fundamental movement of particles for Multi-objective particle swarm optimization (shortly MOPSO) is captured by equation [15]:

$$v_{in} = w \cdot v_{in} + c_1 \cdot rand() \cdot (p_{in} - x_{in}) + c_2 \cdot Rand() \cdot (rep_n - x_{in}), \qquad (2.19)$$

where c_1 and c_2 are positive constants; w is inertia weight, $rand()$ and $Rand()$ are two random vectors from range $(0, 1)$; v_{in} is the velocity (step size) of the $\overline{ith}$ particle; x_{in} is a current position of the ith particle; p_{in} is the best previous position of the $\overline{ith}$ particle (personal best); rep_n is a leader particle selected from an external archive. Particle positions are afterwards computed by rule [15]:

$$x_{in} = x_{in} + v_{in}. \qquad (2.20)$$

External archive
The major task of the external archive (repository) is to keep records of the nondominated solutions, which were found during the optimization cycle [15]. The external repository consists of two main parts: the repository controller and the grid [15].

Repository controller [15]: The controller decides, when a certain solution is suitable for archive or not. Solutions, which are not dominated, are each iteration of the algorithm compared against solutions, which are already stored in external depository. The archive is empty at first, so current solution is accepted at the beginning of the algorithm (case 1 in fig. 2.8). If some new solution is dominated by some member from the external archive, then this solution is automatically discarded (case 2 in fig. 2.8). On the other hand, if none of the solutions stored in the external repository dominates the new solution, then the new solution is placed into the archive (case 3 in fig. 2.8). If there are solutions in the archive that are dominated by the new solution, then these solutions are deleted from the repository (cases 4 in fig. 2.8). Ultimately, if the external archive is full, the adaptive grid procedure must take place (case 5 in fig. 2.8) [15].
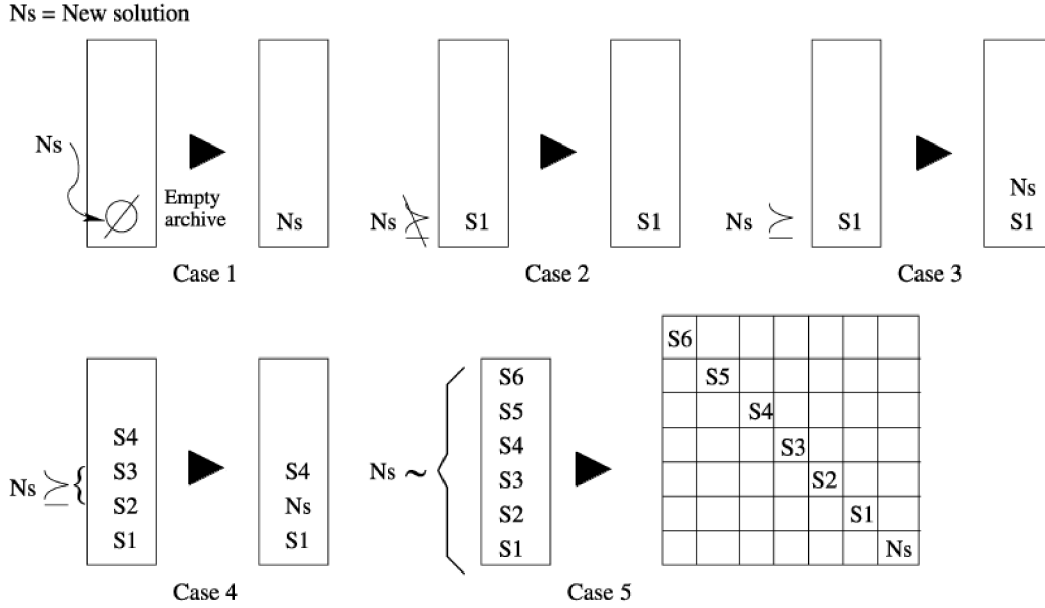
Fig. 2.8: *Archive cases* [15].

Adaptive grid [15]: The grid maintains well-distributed Pareto front - serves in selection of a particle leader and later in a deletion of redundant particles in archive. Simple grid of a constant number of nodes always encloses particles in external archive. This enclosed area is divided by the grid into several rectangle sub areas. Each sub areas with particle(s) are provided by a chosen weight factor. Value of the weight factor is set according to the next algorithm procedure - leader selection or particle deletion.

Leader **rep$_n$** selection [15]: Leader **rep$_n$** is chosen from external repository by a roulette-wheel selection. Every sub area with a particle(s) is provided with the weight factor - sub areas with one particle have greater weight values compared to sub areas with multiple particles.

Particle deletion [15]: Redundant particles are deleted by similar principle, which was used in the leader selection. Sub areas with multiple particles has greater weight factor compared to sub areas with only one particle.

Roulette wheel selection [15]: Roulette wheel selection assigns probability values proportional to a fitness of each individual (particle, design). After that, roulette selects from such distribution - fit individuals get a better chance of being selected, on the other hand less-fit individuals get lower chances. Fitness of each particle is calculated according to chosen function, which will be described in section 4 called *Shape optimization procedure*. The main task of roulette wheel selection is to maintain diversity of the optimization procedure (avoid premature swarm convergence).

MOPSO pseudocode

MOPSO behaviour could be described by following pseudocode 2.2.

Code 2.2: *Pseudocode for MOPSO* [15].

```
1  initialize swarm position (random) and velocities (zero)
2  function evaluation
3  create the external archive and the grid
4
5  iteration = 1
6  while iteration < max_iteration
7      for i=1:no_particles %number of particles
8          select leader from the external archive
9          calculate velocity
10         update position
11         function evaluation
12         mutation**
13         update pbest (personal best)
14      endfor
15    update external archive and external grid
16    iteration = iteration + 1
17  endwhile
```

**Authors in [15] proposed mutation within MOPSO algorithm to maintain the better diversity of the swarm. This operation is a characteristic part of Evolutionary/Genetic algorithms and has an analogy to biological mutation - it alters one or more (or all) particle parameters in a way which could lead to a discovery of the optimal solution.

It must be noted that maintaining "healthy" diversity is an important task in population based algorithms (and in optimization algorithm in general), usually to avoid population stuck in some local (not best) optimum. Diversity brings an opportunity to free population from such local optimum and search on in given computational area.

2.6 Computational fluid dynamics (CFD)

The first indications of Computational fluid dynamics (shortly CFD) are shown in early 70s. Such acronym stands for a combination of numerical mathematics, physics and computer sciences applied to simulate fluid flows in miscellaneous environments using various commercial or non-commercial software [10]. Presented thesis and afterwards optimization software is focusing on commercial package from ANSYS called CFX, which has excellent attributes and advantages in the field of the rotary hydraulic machines.

One of the most used approaches for modelling (simulating) mentioned turbulent flows of the fluid is with an employment of the Reynolds averaged Navier-Stokes equations (RANS in short) or unsteady Reynolds averaged Navier-Stokes equations (URANS) together with specific turbulence model and wall function. But before mentioning URANS equations a concept of Reynolds-averaging must be explained. Such process separates the

variable e.g. v into two parts - the **average** $\overline{v}$ and the **fluctuating** v' (fig. 2.9) with specific matematical rules and conditions around them, see in detail in [3].
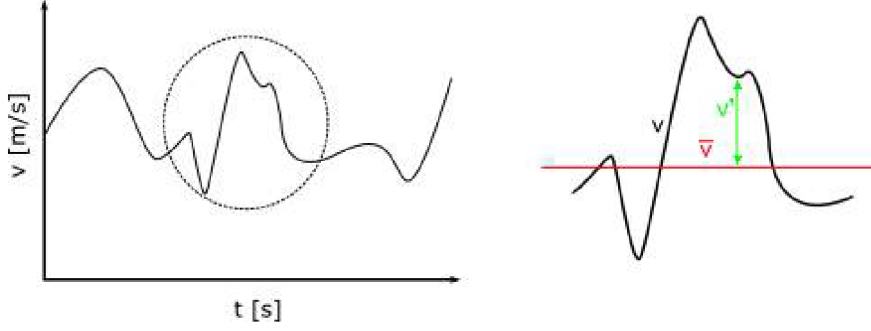

Fig. 2.9: *Average and fluctuating part of the variable* [3].

The unsteady RANS equations (with help of Einstein summation convention) for the flow of a viscous incompressible fluid are written [3]:

$$\frac{\partial \overline{v_i}}{\partial t} + \frac{\partial \overline{v_i}}{\partial x_j}\overline{v_j} = -\frac{1}{\rho}\frac{\partial \overline{p}}{\partial x_i} + \nu\frac{\partial^2 \overline{v_i}}{\partial x_j \partial x_j} - \frac{\partial}{\partial x_j}\left(\overline{v_i' v_j'}\right) + g_i, \tag{2.21}$$

$$\frac{\partial \overline{v_i}}{\partial x_i} = 0, \tag{2.22}$$

where v $[m/s]$ is fluid velocity, p $[Pa]$ is pressure, t $[s]$ is time, ν $[m^2/s]$ is kinematic viscosity, x $[m]$ is position and ρ $[kg/m^3]$ is fluid density and g_i $[m/s^2]$ is external acceleration (gravitational, etc.). By Reynolds-averaging process a **Reynolds stress tensor** appears [3]:

$$\tau_{ij} = \rho\overline{v_i' v_j'}, \tag{2.23}$$

which is in general unknown and makes URANS equations unsolvable. Such problem could be estimated by utilizing Boussinesque hypothesis of a closure problem with employing correct type of the turbulence model.

2.6.1 Turbulence modelling

There are several ways, how to model mentioned Reynolds stress tensor using Boussinesque hypothesis of the closure problem. In this thesis was primarily used a two-equation approach [3]:

$$\overline{v_i' v_j'} = -2v_t\overline{S}_{ij} + \frac{2}{3}\delta_{ij}k, \tag{2.24}$$

where $\overline{S}_{ij} = \frac{1}{2}\left(\frac{\partial \overline{v_i}}{x_j} + \frac{\partial \overline{v_j}}{x_i}\right)$ is the strain-rate tensor, v_t is turbulent viscosity, $k = \frac{1}{2}\overline{v_i' v_j'}$ is turbulent kinetic energy. The most common two-equations models are $k - \epsilon$ (which was utilized in the presented optimization software) and $k - \omega$, in more detail in [3].

The $k - \epsilon$ model shows a stable and numerically robust regime and brings a favourable compromise between the computational accuracy and the global robustness [4].

2.6.2 Computational mesh

Every computational domain must be discretized into smaller geometric shapes in order of a proper application of RANS/URANS equations for the numerical solution by a finite volume method and correct fluid flow capturing. In presented thesis are utilized hexahedral an tetrahedral computational meshes - fig. 2.10.
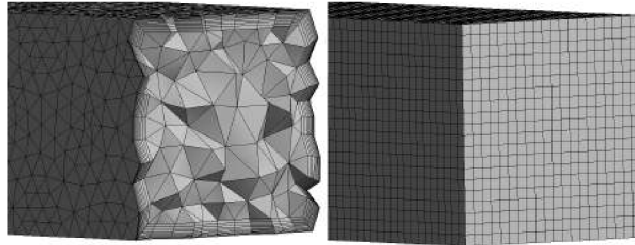

***Fig. 2.10**: Types of utilized computational grids (tetrahedral vs. hexahedral type).*

A lot of fluid flow problems utilized complicated shapes. A generation of structured mesh, which consists of the hexahedral elements, is for such geometries very time expensive and sometimes impossible. This fact is a primary motivation for employing unstructured meshes, which are based on the tetrahedral cells. Other problems of structured mesh application are often mesh quality issues, high number of cells in inappropriate areas. On the other hand structured meshes excel in better computational convergence compared to the unstructured mesh [4].

ANSYS commercial software was used for the mesh creation, namely: ICEM CFD and TurboGrid for the structured computational grids and ANSYS Meshing for the unstructured computational grids.

3 1D PUMP DESIGN

Following text deals with the determination and aftewards the calculation of the main **radial** pump impeller dimensions and outlines the basic terminology, which is connected to such computational process. This chapter utilized and exploited a knowledge and observation mainly from [26], [27], [71], [72], [74], [90] in a strict and complex procedure, which is implemented in presented optimization software.

3.1 Centrifugal radial pump

Pumps are mechanical devices that are used to transport fluids from point A to point B. Pumps are based on a transformation of a mechanical energy (from a motor) to a hydraulic energy, which consists of kinetic and pressure energies. Simple one stage centrifugal pump consists of (fig. 3.1): **1** impeller, **2** shaft, **3** volute (spiral case), **4** suction chamber, **5** pump bearing, **6** stern gland, **7** blade, **8** gasket [71].
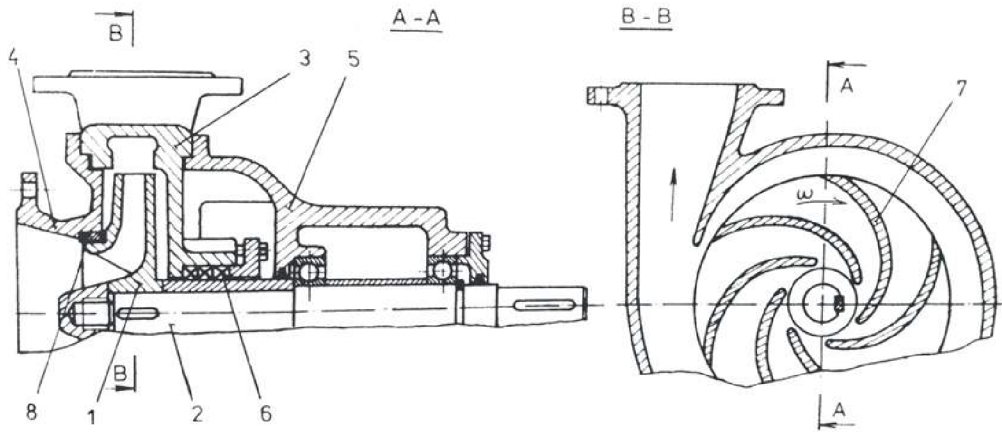

Fig. 3.1: *One stage radial centrifugal pump with volute* [71].

The radial pump impeller is usually described by its **hub**, **shroud** (there are pumps without a shroud → semi open type of impeller) and **blade** with trailing and leading edges - fig. 3.2. Blade experiences high pressure and low pressure states along its length, so from this perspective blade could be divided into a pressure and suction side [26].
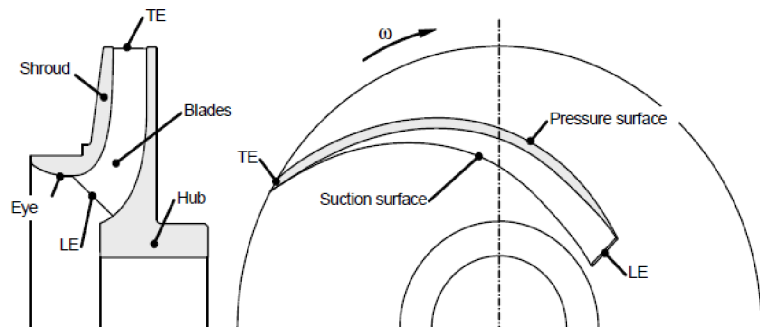

Fig. 3.2: *Pump layout* [26].

44

3.2 Performance data - basic pump parameters and characteristics

The performance data of the radial centrifugal pump (and pumps in general) are defined by seven main variables, namely [26]:

Pump head (Pump specific energy)	$\mathbf{H}$ ($\mathbf{Y}$)	m (J/kg)
Flow rate	$\mathbf{Q}$	m^3/s
Power	$\mathbf{P}$	W
Rotational speed (RPM)	$\mathbf{n}$	min^{-1}
Total efficiency	$\eta_{\mathbf{c}}$	$-$ or $\%$
Critical net positive suction head	$\mathbf{NPSH_3}$	m
Energy dissipation	$\mathbf{D}$	W

When the flow rate Q of the pump changes its value, the head H, the power P and the efficiency η_c or $NPSH_3$ change its value as well. This fact creates main **pump characteristics** as dependencies against the flow rate Q - fig. 3.3.
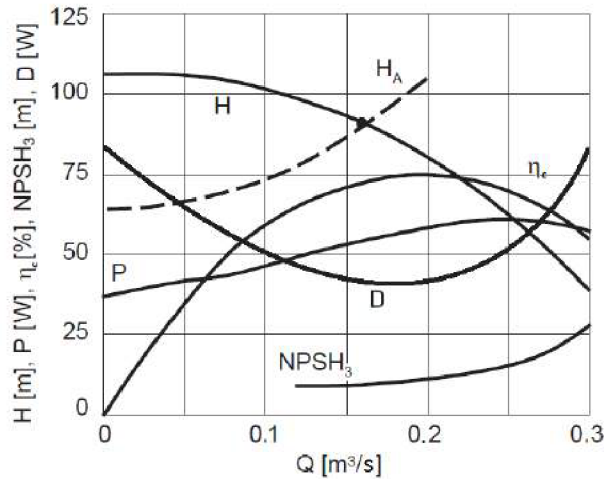

Fig. 3.3: *Pump characteristics with system characteristic H_A* [26].

For our optimization purposes will the total efficiency η_c be substituted by the hydraulic efficiency η_h, where volumetric and disk friction losses are not included. In presented optimization software chosen dependencies will be created only from the three values of the flow rate. Such a restriction is caused by a time-consuming nature of CFD simulations and by limited computational resources of department's cluster KAPLAN, which was employed in the optimization process.

3.2.1 Flow rate

The pump flow rate Q $[m^3/s]$ is defined as a volume of fluid, which the pump delivers to its outlet per a time unit [71].

3.2.2 Pump specific energy / Pump head

The specific energy Y $[J/kg]$ is defined as an energy per mass unit delivered by the pump. Y equals to an increment of the specific energy between the pump inlet and outlet [71]:

$$Y = g \cdot H = Y_2 - Y_0 = \frac{p_2}{\rho} + \frac{v_2}{2} + g \cdot y_2 - \left(\frac{p_0}{\rho} + \frac{v_0}{2} + g \cdot y_0 \right), \qquad (3.1)$$

where H $[m]$ is the pump head, p_2 $[Pa]$ is an average static pressure at the pump outlet, p_0 $[Pa]$ is an average static pressure at the pump inlet, v_2 $[m/s]$ is an average velocity at the pump outlet, v_0 $[m/s]$ is an average velocity at the pump inlet, y_2 $[m]$ is a height at the pump outlet (with respect to some reference point), y_0 $[m]$ is a height at the pump outlet (with respect to some reference point) and g $[m/s^2]$ is a gravitational acceleration and ρ $[kg/m^3]$ is a fluid density. For our purposes was eq. 3.1 reshaped into a form:

$$H = \frac{p_{total,2} - p_{total,0}}{\rho \cdot g}, \qquad (3.2)$$

where $p_{total,2}$ $[Pa]$ is a total pressure at the pump outlet, $p_{total,0}$ $[Pa]$ is a total pressure at the pump inlet. It must be noted that the total pressure is composed of a **static** and a **dynamic** pressures.

To be absolutely complete an **Euler's pump equation** must be added to this section. Euler's pump equation characterizes change of the pump specific energy [27]:

$$\frac{Y_2 - Y_0}{\eta_h} = u_2 \cdot c_{u2} - u_0 \cdot c_{u0}, \qquad (3.3)$$

where η_h $[-]$ is the hydraulic efficiency of the pump, u_2 $[m/s]$ is a circumferential velocity at the impeller outlet, u_0 $[m/s]$ is a circumferential velocity at the impeller inlet, c_{u2} $[m/s]$ a circumferential component of an absolute velocity at the impeller outlet and c_{u0} $[m/s]$ a circumferential component of an absolute velocity at the impeller inlet.

3.2.3 Power

The power P $[W]$ is defined as a ratio of a useful power and the total efficiency η_c $[-]$ (in more detail in sec. 3.4.3) [71]:

$$P = \frac{\rho \cdot Q \cdot Y}{\eta_c}, \qquad (3.4)$$

where ρ $[kg/m^3]$ is the fluid density, Q $[m^3/s]$ is the flow rate, Y $[J/kg]$ is the pump specific energy.

3.2.4 Energy dissipation

The energy dissipation D $[W]$ is derived from a calculation of the hydraulic efficiency η_H $[-]$ [27]:

$$D = \rho \cdot Q \cdot Y \cdot \frac{1 - \eta_H}{\eta_H}, \tag{3.5}$$

where ρ $[kg/m^3]$ is the fluid density, Q $[m^3/s]$ is the flow rate, Y $[J/kg]$ is the pump specific energy.

3.3 Unfavourable phenomena in centrifugal pumps

As it was already been mentioned, in the shape optimization process within the pump machinery, the engineer must find the proper design that satisfies chosen parameters and respects limiting aspects of the explored problem. But in such process there are certain flow phenomena, which negatively influence correct behaviour of the pump - particularly negatively effect the hydraulic efficiency and the pump head. The main unfavourable phenomena inside the centrifugal radial pump (and in pumps in general) are summarized in following three sections.

3.3.1 Secondary flow

Secondary flow negatively affects the main pump characteristics (fig. 3.3) and can also cause a noise or even vibrations. Such flow could be divided by a location in the pump into the three groups: at pump's inlet/outlet - fig. 3.4; inside the flow channel of the impeller - fig. 3.5 and the secondary flow outside the impeller - e.g. in the volute.
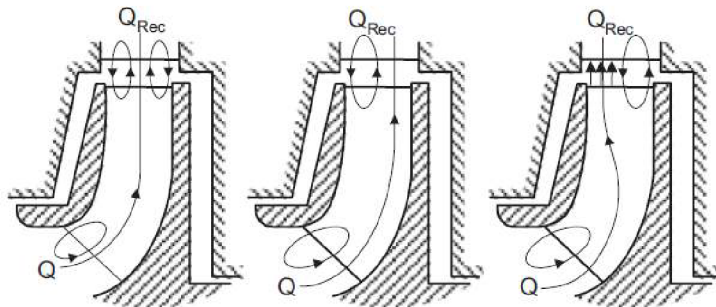

Fig. 3.4: *Flow recirculation* [26].

Fig. 3.4 describes an effect called **recirculation**, which can occur at impeller inlet or outlet. During the recirculation at pump's inlet the liquid always flows back on a streamline near shroud (outer streamline) from the impeller to the suction chamber. The rate of the recirculation increases with the flow rate reduction. It must be noted that a useful way of an accurate prediction of such phenomenon has not been found yet [26].

The recirculation could also develop at the impellers outlet with a direction from the stator (static domain) into the impeller (moving domain). An interaction between the

stator and the impeller brings an immoderate flow deceleration, which leads to a creation of the recirculation [26].
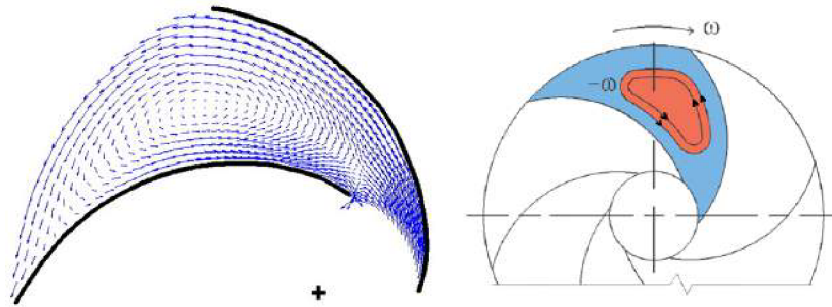

Fig. 3.5: *Secondary flow in the impeller* [28], [37].

The uneven pressure and velocity distribution in the flow channel of the centrifugal pump impeller generates a local vortex that rotates in an opposite direction than the impeller rotation (fig. 3.5). This secondary flow occurs especially in the low specific speed pumps or by using the pump in non-optimal regimes. The local swirl (fig. 3.5) results in a decreasing of a value of the β_2 angle, which leads to a change of the specific energy (pump head) of the pump according to eq. 3.3 [61].

The secondary flow in the simple centrifugal radial pump with the volute can occur also near a volute's tongue (cutwater) - mainly due to a non-optimal values of the flow rate.

3.3.2 Flow separation

The secondary flow in the centrifugal radial pump is not the only unfavourable phenomenon that affects the pump head and efficiency. Among others belong an effect called **flow separation** (in more detail e.g. in [76] - fig. 3.6). The separation of the flow occurs in the locations, where the liquid flows around a solid obstruction - the blades in the pump impeller. As a result of the flow separation (and the blade thickness) is a change of the pump's flow cross-section, which leads to a velocity change and afterwards change of a pressure distribution inside the pump's flow channel [61].
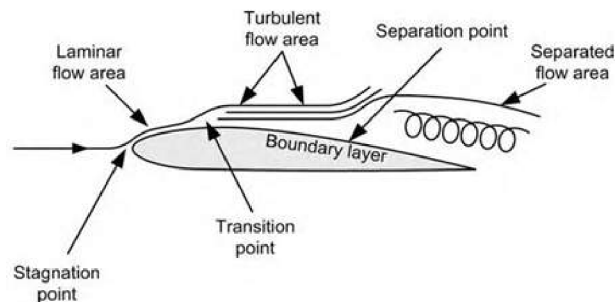

Fig. 3.6: *Flow separation near blade profile* [103].

48

3.3.3 Cavitation

Cavitation is a phenomenon characterized by a formation and afterwards implosion of cavitation bubbles (**cavitas**) in the liquid [68] - fig. 3.7. Bubble, which is filled with vapour, is formed when the static pressure in a flow decreases its value to the vapour pressure due to high velocities in current stream. Vapour cavity implodes as soon as is moved into the regions, where the static pressure is higher than the vapour pressure (this could be in the flow stream or on the walls of blades or shroud/hub). A development of the cavitation causes changes of the head and efficiency of the pump, creates noise and vibrations and even cavitation erosion [26].
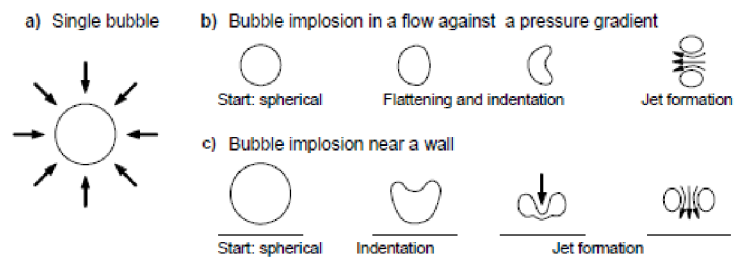

Fig. 3.7: *Cavitaion bubble (cavity implosion)* [26].

Cavitation erosion (fig. 3.8) of material takes place only when the hydrodynamic cavitation intensity (HCI) surpasses the cavitation resistance (CR) of the material for a certain period of time. Hydrodynamic cavitation intensity is dependant on the current flow (and flow attributes), on the other hand cavitation resistance is strictly material quantity. The term hydrodynamic cavitation intensity is utilized for the totality of the implosion energy of all cavities [26].

Fig. 3.8: *Cavitaion erosion* [104].

3.4 Design methods and variables

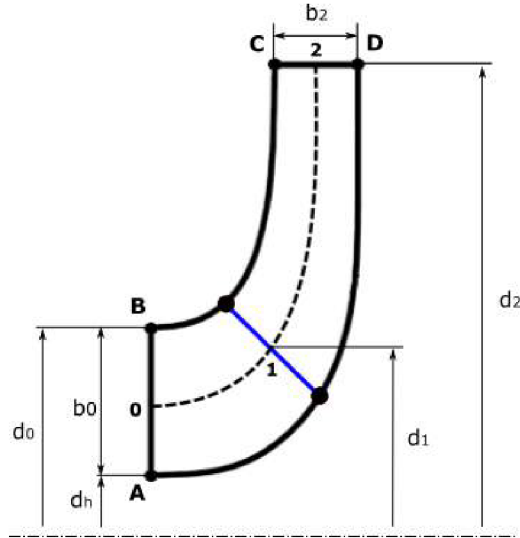### 3.4.1 The fundamental pump dimensions

Fig. 3.9: *Main pump dimensions* [26], [87].

The position and size of the pump impeller is ensured and described by its main dimensions - fig. 3.9 - points A, B, C, D are defined in our case by the user by using an interactive dialogue menu (fig. 4.2), so from this perspective, the optimization procedure needs only the diameter d_1 $[m]$, which is exploited for the computation of the inlet angle β_1 $[^o]$ and outlet angle β_2 $[^o]$.

3.4.2 Specific speed

According to the value of the chosen specific speed (n_s, n_b, n_q), an initial shape of the pump impeller could be simply determined - fig. 3.10. It must be noted that presented optimization procedure focuses only on the **radial** type of the pump impellers - first two impeller shapes in fig. 3.10.
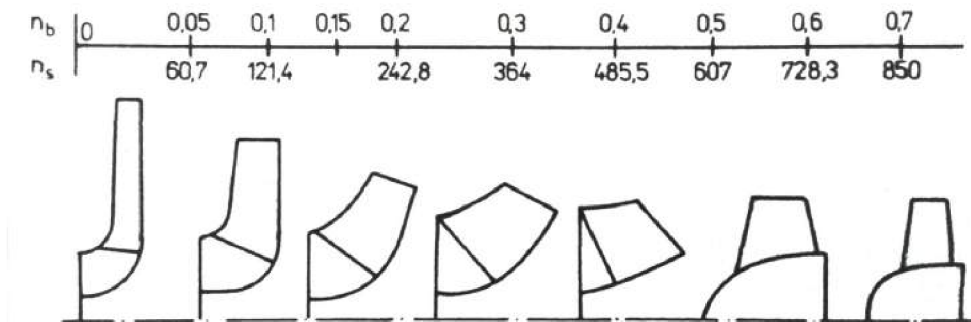

Fig. 3.10: *Types of the impellers* [71].

Let's start with the most common specific speed n_s $[1/min]$, which is defined [16], [27]:

$$n_s = 3.65 \cdot n \cdot \frac{Q^{0.5}}{H^{0.75}}, \tag{3.6}$$

where n $[1/min]$ is a rotational speed (RPM), H $[m]$ is the pump head and Q $[m^3/s]$ is the flow rate. It must be noted that some literature and its particular equations use the specific speed n_b $[1/min]$, which is determined [27],[71]:

$$n_b = n \cdot \frac{Q^{0.5}}{(g \cdot H)^{0.75}}, \tag{3.7}$$

where n $[1/s]$ is the rotational speed, g $[m/s^2]$ the gravitational acceleration, H $[m]$ is the pump head and Q $[m^3/s]$ is the flow rate. Gülich, on the other hand, uses the volume specific speed n_q $[1/min]$ defined as [26]:

$$n_q = n \cdot \frac{Q^{0.5}}{H^{0.75}}, \tag{3.8}$$

where n $[1/min]$ is the rotational speed, H $[m]$ is the pump head and Q $[m^3/s]$ is the flow rate. Gülich also uses a suction specific speed, which depends on a critical value of the net positive suction head [26]:

$$n_{ss} = n \cdot \frac{Q^{0.5}}{(NPSH_3)^{0.75}}, \tag{3.9}$$

where n $[1/min]$ is the rotational speed, Q $[m^3/s]$ is the flow rate and $NPSH_3$ $[m]$ is the critical value of $NPSH$, usually determined from a set of experiments. For our purposes an estimated value is sufficient [68]:

$$NPSH_3 = \sigma_b \cdot H \cdot n_b^{4/3}, \tag{3.10}$$

where H $[m]$ is the head of the pump, n_b $[1/min]$ is the specific speed determined by eq. 3.7 and σ_b $[-]$ is a constant.

3.4.3 Hydraulic efficiency

The crucial part of the 1D design is an estimation of the **hydraulic efficiency** η_H $[-]$. Such task could be performed by several methods. Presented optimization procedure utilized an **average value** of four different approaches described in following sections.

Erhart's diagram and its approximation [74]
The total pump efficiency η_c $[-]$ could be determined from a knowledge of the given flow rate Q $[l/s]$ and specific speed n_s $[1/min]$ (or n_b $[1/min]$) by using Erhart's diagram (fig. 3.11). The hydraulic efficiency η_H $[-]$ is afterwards computed [71]:

$$\eta_H = \sqrt{\eta_c} - (0.02 \div 0.04), \tag{3.11}$$

51

where the value 0.02 is for the large sized pump impellers, 0.03 is for the medium sized and 0.04 usually for the smaller pump impellers. This approach has its own limitations - it is suited for the flow rates $Q \ [m^3/s] \in \langle 0.004, 10 \rangle$ and the specific speeds $n_s \ [1/min] \in \langle 25, 1000 \rangle$.
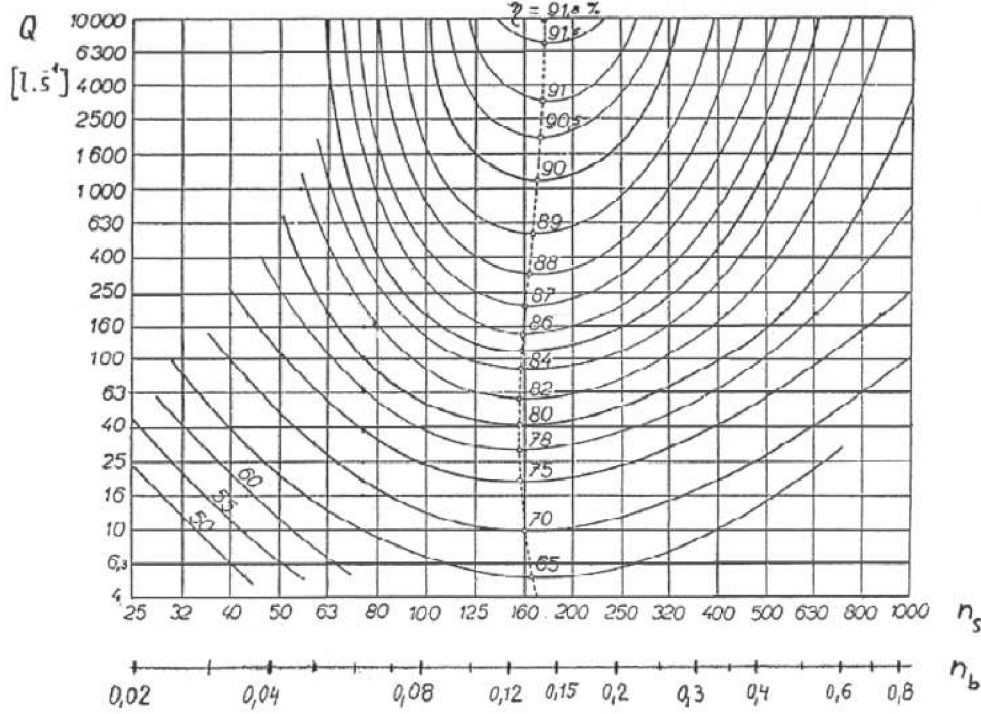

Fig. 3.11: *Erhart's diagram* [96].

In the presented optimization software it is quite challenging to capture the Erhart's diagram properly, thus an alternative approach using empirical equations, which could describe the Erhart's diagram with a deviation $\pm 0.6\%$, is utilized [71]:

$$\eta_H = \sqrt{\eta_c} - (0.02 \div 0.04),$$

where the total efficiency $\eta_c \ [-]$ is defined as [74]:

$$\eta_c = x \cdot (1000 \cdot Q)^y \cdot (3 + \log Q)^z, \tag{3.12}$$

where $Q \ [m^3/s]$ is the flow rate and variables $x \ [-], y \ [-], z \ [-]$ are set according to following three rules [74]:

$$x = 0.5374 + 5.2431 \cdot n_b - 39.0474 \cdot n_b^2 + 94.9523 \cdot n_b^3, \tag{3.13}$$

$$y = -exp\left[(1.8818 + 0.2650 \cdot \ln n_b)^{-6.331} - 3.2826\right], \tag{3.14}$$

$$z = exp\left[(1.9602 + 0.2760 \cdot \ln n_b)^{-7.665} - 0.9489\right], \tag{3.15}$$

where $n_b \ [1/min]$ is the specific speed - eq. 3.7. It must be noted, that this so-called approximation is valid for flow rate in a range $Q = 0.01 \div 10 \ [m^3/s]$ and specific speed in a range $n_b = 0.05 \div 0.125 \ [1/min]$.

Peck's approach [72]

In [72], Peck outlined another way for the calculation of the hydraulic efficiency η_H [−]:

$$\eta_H = \left(100 - K_h \cdot \left(\frac{60 \cdot Q \cdot 219.969}{3.28084 \cdot \sqrt{H}}\right)^{-0.25}\right) \cdot \frac{1}{100}, \qquad (3.16)$$

where K_h [−] is a constant (with value 25 for the big pump impellers, 35 for the medium sized and 40 usually for the smaller pump impellers), Q [m^3/s] is the flow rate and H [m] is the pump head. This equation is not limited in terms of the flow rate or the pump head [72].

Paciga's approach [71]

Equation 3.11 is utilized in this approach in a following way [71]:

$$\eta_H = \sqrt{\eta_c} - (0.02 \div 0.04)$$

where the total efficiency η_c [−] is defined as [71]:

$$\eta_c = \sqrt{\left[\left(\frac{Q}{0.048}\right)^{0.083} + (0.722 + \log(n_b)^3\right]^{0.5}} - \xi, \qquad (3.17)$$

where Q [m^3/s] is the flow rate, n_b [$1/min$] is the specific speed, ξ [−] is a constant (with value $\langle 0.18, 0.2 \rangle$ for the single stage pump with the volute; $\langle 0.2, 0.23 \rangle$ for the multiple stage pump). This equation is valid for the flow rate $Q < 0.65 \ m^3/s$ and the specific speed $0.04 < n_b < 0.33$.

Gülich's approach [26]

The hydraulic efficiency η_H [−] is in [26] computed for the radial pumps (valid for the flow rate $Q \geq 0.005 \ m^3/s$ and the specific speed $n_q \leq 100 \ 1/min$) as follows:

$$\eta_H = 1 - 0.055 \cdot \left(\frac{Q_{ref}}{Q}\right)^m - 0.2 \cdot \left(0.26 - \log \frac{n_q}{25}\right)^2 \cdot \left(\frac{Q_{ref}}{Q}\right)^{0.1}, \qquad (3.18)$$

where Q [m^3/s] is the flow rate, $Q_{ref} = 1 \ m^3/s$ is the referential flow rate, n_q [$1/min$] is the specific speed (eq. 3.8) and m [−] is an exponent defined as [26]:

$$m = 0.08 \cdot a \cdot \left(\frac{Q_{ref}}{Q}\right)^{0.15} \cdot \left(\frac{45}{n_q}\right)^{0.06}, \qquad (3.19)$$

where Q [m^3/s] is the flow rate, $Q_{ref} = 1 \ m^3/s$ is the referential flow rate, n_q [$1/min$] is the specific speed (eq. 3.8) and a [−] is a variable defined as [26]:

$$a = \begin{cases} 1 & : Q \leq 1 \ m^3/s \\ 0.5 & : Q > 1 \ m^3/s. \end{cases}$$

3.4.4 Blade angle β_1 (inlet blade angle)

The calculation of the β_1 angle for the middle streamline is based on one crucial condition: a **shockless** (shockfree) fluid entry on the blade's leading edge. Such condition deforms a velocity triangle into a form described by fig. 3.12.
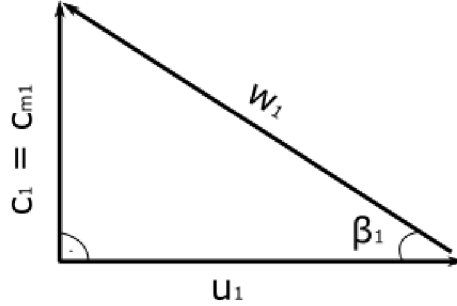

Fig. 3.12: *Velocity triangle at pump's leading edge* [27].

First computational approach [71] (Paciga + Strýček + Gančo's approach)
The angle β_1 is determined from fig. 3.12 using a trigonometric function [71]:

$$\beta_1 = arctg\left(\frac{c_{m1}}{u_1}\right) = arctg\left(\frac{c_{m1}}{\pi \cdot d_1 \cdot n}\right), \tag{3.20}$$

where c_{m1} $[m/s]$ is the meridional velocity defined by eq. 3.21, d_1 $[m]$ is the diameter (see fig. 3.9) defined by eq. 3.23, n $[1/s]$ are revolutions per second. The meridional velocity c_{m1} is calculated [71]:

$$c_{m1} = k_{m1} \cdot \sqrt{2 \cdot g \cdot H}, \tag{3.21}$$

where g $[m/s^2]$ is the gravitational acceleration, H $[m]$ is the requested pump head and k_{m1} $[-]$ is a constant specified by following quasi-empirical equation [71]:

$$k_{m1} = 0.12 + 0.5617 \cdot (8.23723e^{-4} \cdot n_s - 0.041)^{0.8}, \tag{3.22}$$

where n_s $[1/min]$ is the specific speed defined by eq. 3.6. The diameter d_1 $[m]$, which characterizes the proper position of the leading edge of the blade, is defined as [71]:

$$d_1 = \sqrt{\frac{d_0^2 + d_h^2}{2}} + K \cdot \left(d_0 - \sqrt{\frac{d_0^2 + d_h^2}{2}}\right), \tag{3.23}$$

where d_0 $[m]$ and d_h $[m]$ are the diameters entered by the user (see figures 3.9 and 4.2), K $[-]$ is a constant once again defined by a quasi-empirical equation [71]:

$$K = 0.59 + 0.47 \cdot cos(n_b \cdot 1255\ ^o), \tag{3.24}$$

where n_b $[1/min]$ is the specific speed defined by eq. 3.7.

Second computational approach [90] (Strýček + Gančo's approach)

This approach differs from the methodology found in [71] in k_{m1} and K determination. These two constants are obtained from a diagram captured in fig. 3.13, which depicts their dependencies on the specific speed n_s [$1/min$].
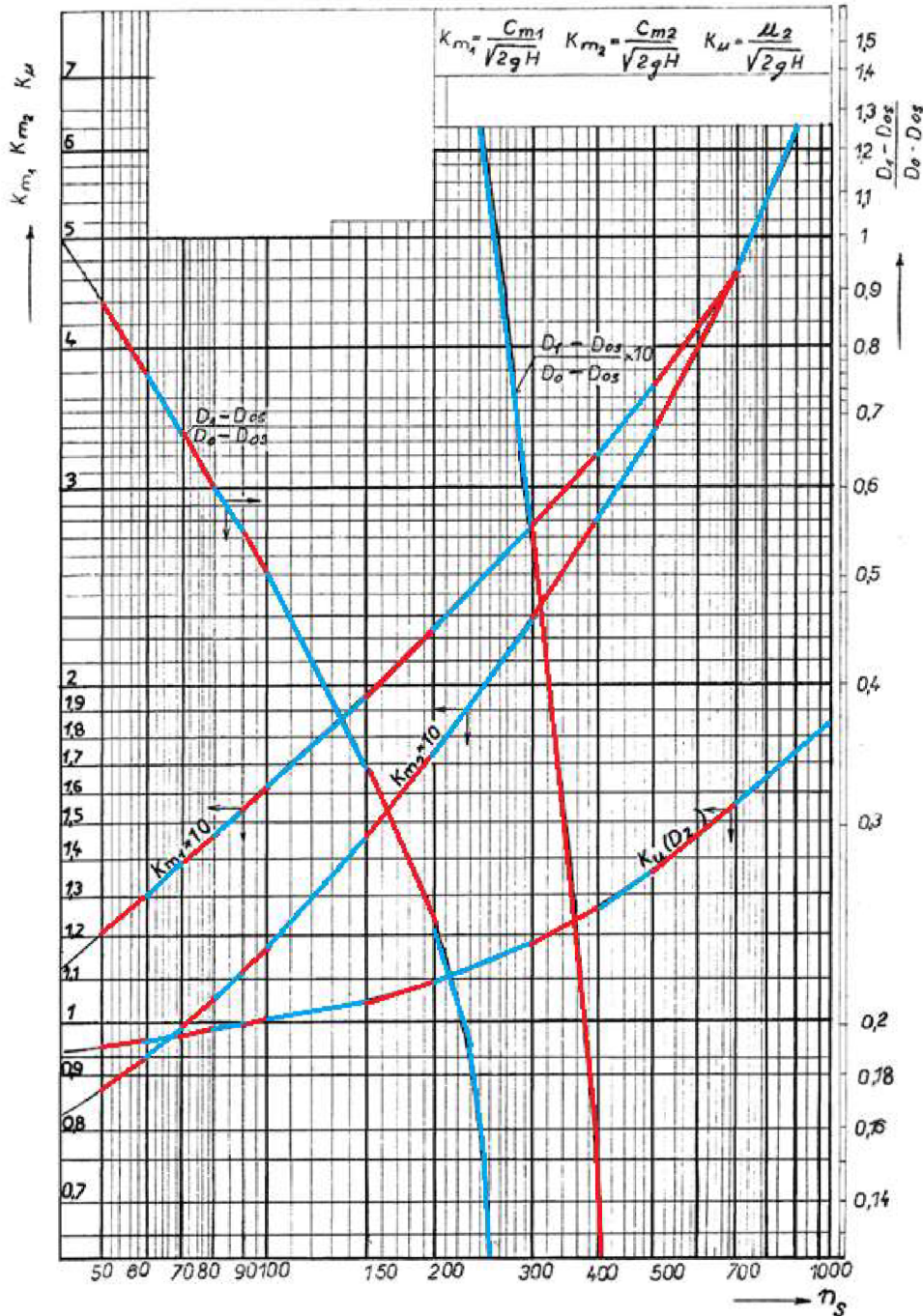

Fig. 3.13: *Diagram for constants K, k_{m1} and k_{m2} [90].*

Diagram (fig. 3.13) was in the presented optimization cycle transformed piece by piece (red and blue lines) into the form of a pseudocode, which shape optimization algorithm uses.

Third computational approach [26] (Gülich's approach)

To match previous approaches, the eq. 3.20 and the shockless fluid entry must be utilized:

$$\beta_1 = arctg\left(\frac{c_{m1}}{u_1}\right) = arctg\left(\frac{(0.8 \div 0.9) \cdot c_{m,Gulich}}{\pi \cdot d_1 \cdot n}\right), \tag{3.25}$$

where $c_{m,Gulich}$ $[m/s]$ is the meridional velocity characterized by eq. 3.26, n $[1/s]$ are the revolutions per second and d_1 $[m]$ is the diameter computed from eq. 3.29. The meridional velocity $c_{m,Gulich}$ $[m/s]$ is in [26] determined:

$$c_{m,Gulich} = \frac{2 \cdot Q_{loss}}{\pi \cdot (d_{1,Gulich} - d_{shaft}) \cdot d_1}, \tag{3.26}$$

where Q_{loss} $[m^3/s]$ is the flow rate with the volumetric losses (eq. 3.27), b_0 $[m]$ is the width at pump inlet (fig. 3.9). In the beginning of the diameter d_1 computation is equation for the flow rate with volumetric losses Q_{loss} $[m^3/s]$ [26]:

$$Q_{loss} = Q + Q \cdot \frac{a}{n_q^{0.6}}, \tag{3.27}$$

where Q $[m^3/s]$ is the requested flow rate, a $[-]$ is the constant defined by the same way as in eq. 3.19, n_q $[1/min]$ is the specific speed computed from eq. 3.8. Next step includes a calculation of the flow coefficient φ_1 $[-]$ [26]:

$$\varphi_1 = \left(\frac{125}{n_{ss}}\right)^{2.2} \cdot \left(\frac{n_q}{27}\right)^{0.418}, \tag{3.28}$$

where n_q $[1/min]$ is the specific speed defined by eq. 3.8 and n_{ss} $[1/min]$. The diameter d_1 is determined in a following way [26]:

$$d_1 = \frac{d_{1,Gulich} + d_{shaft}}{2}, \tag{3.29}$$

where d_{shaft} $[m]$ is the diameter of the pump shaft defined by eq. 3.31 and $d_{1,Gulich}$ $[m]$ is defined [26]:

$$d_{1,Gulich} = 2.9 \cdot \left[\left(\frac{Q_{loss}}{n \cdot \varphi_1 \cdot k_n}\right) \cdot \left(1 + \frac{\varphi_1}{tg\ \alpha_1}\right)\right]^{1/3}, \tag{3.30}$$

where Q_{loss} $[m^3/s]$ is the flow rate with the volumetric losses, n $[1/min]$ are the revolutions per minute, k_n $[-]$ is a blockage caused by the hub, φ_1 $[-]$ is the flow coefficient (eq. 3.28) and α_1 $[^o]$ an angle of a possible inlet pre-rotation. The shaft diameter according [26] is determined:

$$d_{shaft} = 3.65 \cdot \left(\frac{P_{max}}{n \cdot \tau_{al}}\right), \tag{3.31}$$

where n $[1/min]$ are the revolutions per minute, τ_{al} $[Pa]$ is a material shear stress (strongly depends on the shaft material) and P_{max} $[W]$ is a maximal power [26]:

$$P_{max} = \frac{\rho \cdot Q \cdot g \cdot H}{\eta_{c,Gulich}}, \tag{3.32}$$

where ρ $[kg/m^3]$ is the fluid density, Q $[m^3/s]$ is the flow rate, g $[m/s^2]$ is the gravitational acceleration and $\eta_{c,Gulich}$ $[-]$ is the total pump efficiency estimated from following three equations [26]:

$$\eta_{c,Gulich} = 1 - 0.095 \cdot \left(\frac{Q_{ref}}{Q}\right)^m - 0.3 \cdot \left(0.35 - \log_{10}\frac{n_q}{23}\right)^2 \cdot \left(\frac{Q_{ref}}{Q}\right)^{0.05}, \tag{3.33}$$

$$m = 0.1 \cdot a \cdot \left(\frac{Q_{ref}}{Q}\right)^{0.15} \cdot \left(\frac{45}{n_q}\right)^{0.06}, \tag{3.34}$$

where Q $[m^3/s]$ is the flow rate, $Q_{ref} = 1\ m^3/s$ is the referential flow rate, n_q $[1/min]$ is the specific speed defined by eq. 3.8 and a $[-]$ is a variable [26]:

$$a = \begin{cases} 1 & : Q \leq 1\ m^3/s \\ 0.5 & : Q > 1\ m^3/s. \end{cases}$$

3.4.5 Blade angle β_2 (outlet blade angle)

First computational approach [27]
First of all a meridional velocity c_{m2} $[m/s]$ must be computed as an **average value** from three following aproaches. The velocity is dependent on a k_{m2} constant defined by [27] [71], [90]:

$$c_{m2} = k_{m2} \cdot \sqrt{2 \cdot g \cdot H}, \tag{3.35}$$

where g $[m/s^2]$ is the gravitational acceleration, H $[m]$ is the requested pump head and k_{m2} $[-]$ is a constant specified by following three ways, first [27]:

$$k_{m2} = -0.001809 + 0.001213 \cdot n_s - 1.8 \cdot 10^6 \cdot n_s^2, \tag{3.36}$$

where n_s $[1/min]$ is the specific speed (eq. 3.6). Second [71]:

$$k_{m2} = 0.077 + 1.41 \cdot (8.23723 \cdot 10^4 \cdot n_s - 0.041)^{1.2}, \tag{3.37}$$

where n_s $[1/min]$ is the specific speed (eq. 3.6). And the last way, how to determine the constant k_{m2} is by utilizing the diagram fig. 3.13 [90]. The calculation of the β_2 angle leads to an employment of the **Euler's pump equation** in form of the iterative process, which ends when the requested pump head is found [27]:

$$H = \frac{\eta_H}{g} \cdot \left(\kappa_w \cdot u_2^2 - \frac{c_{m2}}{tg\ \beta_2} \cdot u_2\right), \tag{3.38}$$

where H $[-]$ is the pump head, η_H $[-]$ is the hydraulic efficiency, c_{m2} $[m/s]$ is the meridional velocity (eq. 3.35), g $[m/s^2]$ is the gravitational acceleration, u_2 $[m/s]$ is the circumferential velocity (eq. 3.40)and κ_w is a Waisser correction for a finite number of blades [27]:

$$\kappa_w = 1,01 - \frac{0.395 + 0.457 \cdot sin\ \beta_2}{\sqrt{z}}, \tag{3.39}$$

where β_2 [^{o}] is the blade angle at outlet, z [$-$] is the number of blades. The circumferential velocity mentioned above is calculated:

$$u_2 = \pi \cdot d_2 \cdot n, \qquad (3.40)$$

where d_2 [m] is the outlet diameter and n [$1/s$] are the revolutions per second.

Second computational approach [71]

Paciga [71] in the Euler's pump equation employed the impeller widths b_1, b_2. Such equation must be also solved iteratively to obtain the requested head H [m]:

$$H = \frac{\eta_H}{g} \cdot \left(\kappa_w \cdot u_2^2 - \frac{Q}{\pi \cdot d_2 \cdot b_2 \cdot \varphi_2 \cdot \sqrt{tg \ \beta_2 \cdot tg \ \beta_1}} \cdot \sqrt[4]{\frac{b_2}{b_1}} \cdot \sqrt{\frac{\varphi_2}{\varphi_1}} \cdot u_2 \right), \qquad (3.41)$$

where H [$-$] is the pump head, η_H [$-$] is the hydraulic efficiency, g [m/s^2] is the gravitational acceleration, u_2 [m/s] is the circumferential velocity (eq. 3.40), κ_w is the Waisser correction for the finite number of blades (eq. 3.39), d_2 [m] is the outlet diameter, β_1 [^{o}] is the inlet angle, β_2 [^{o}] is the outlet angle, φ_1 [$-$] is a constatnt from a range $0.75 \div 0.85$, φ_2 [$-$] is a constatnt from a range $0.9 \div 0.95$, b_2 [m] is the outlet width and b_1 [m] is the width around pump's leading edge [71]:

$$b_1 = \frac{Q + Q \cdot (0.03 \div 0.05)}{\pi \cdot c_{m1} \cdot d_1}, \qquad (3.42)$$

where Q [m^3/s] is the flow rate, c_{m1} [m/s] is the meridional velocity (from eq. 3.21) and d_1 [m] is the diameter, which is related to the proper position of the leading edge.

Third computational approach [26]

Gülich [26] also uses an iterative process to obtain the β_2 angle, but in the most advanced and complex way:

$$H = \frac{\eta_H \cdot u_2^2}{g} \cdot \left\{ \gamma - \frac{Q_{loss}}{\pi \cdot d_2 \cdot b_2 \cdot u_2 \cdot tan \ \beta_2} \cdot \left[\tau_2 + \frac{\pi \cdot d_2 \cdot b_2 \cdot d^* \cdot tan \ \beta_2}{A_1 \cdot tan \ \alpha_1} \right] \right\}, \qquad (3.43)$$

where H [$-$] is the pump head, η_H [$-$] is the hydraulic efficiency, u_2 [m/s] is the circumferential velocity (eq. 3.40), g [m/s^2] is the gravitational acceleration, γ [$-$] is a slip factor (eq. 3.46), d_2 [m] is the outlet diameter, b_2 [m] is the outlet width, β_2[^{o}] is the outlet angle, τ_2 [$-$] is a blade blockage (eq. 3.47), d^* [$-$] is a dimensionless diameter (eq. 3.45), α_1 [^{o}] is the angle of possible fluid pre-rotation at inlet and A_1 [m^2] is an area defined [26]:

$$A_1 = \frac{\pi \cdot d_1 \cdot (d_{1,Gulich} - d_{shaft})}{2}, \qquad (3.44)$$

where d_1 [m] is the diameter defined by eq. 3.29, $d_{1,Gulich}$ [m] is the diameter defined by eq. 3.30 and d_{shaft} [m] is the shaft diameter defined by eq. 3.31. The dimensionless diameter d^* [−] is determined according [26] as:

$$d^* = \frac{\sqrt{0.5 \cdot \left(d_{1,Gulich}^2 + (1.25 \cdot d_{1,Gulich})^2 \right)}}{d_2},$$ (3.45)

where d_1 [m] is the diameter defined by eq. 3.29, $d_{1,Gulich}$ [m] is the diameter defined by eq. 3.30 and d_{shaft} [m] is the shaft diameter defined by eq. 3.31. The **slip factor** is defined according to [26]:

$$\gamma = 0.98 \cdot \left(1 - \frac{\sqrt{\sin \beta_2}}{z^{0.7}} \right),$$ (3.46)

where β_2 [º] is the outlet angle, z [−] is the number of blades. The **bBlade blockage** is computed from [26]:

$$\tau_2 = \left(1 - \frac{\Delta \cdot z}{\pi \cdot d_2 \cdot \sin \beta_2 \cdot \sin \lambda} \right)^{-1},$$ (3.47)

where Δ [m] is the blade thickness, z [−] is the number of blades, d_2 [m] is the outlet diameter, β_2 [º] is the outlet angle and λ [º] is an angle of a blade inclination (see fig. 3.14).
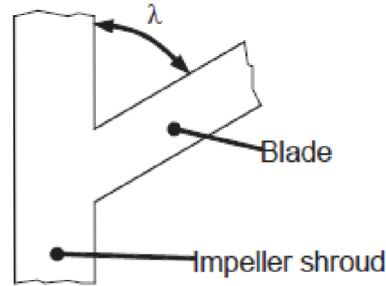

Fig. 3.14: *Blade inclination* [26].

4 SHAPE OPTIMIZATION PROCEDURE

The presented shape optimization tool will find its most suitable application in the area of the **centrifugal radial pump** impellers.

4.1 Master code

Under a concept of the **master code** are hidden lines of a very complex code, compiled within Matlab programming language (using free licence software GNU Octave), which has the significant role in the shape optimization algorithm. This code calls and handles the MOPSO algorithm, which is described in sec. 4.1.2, an impeller modeller mentioned in sec. 4.1.3, a mesh generator characterized in sec. 4.1.4 and a CFD solver remarked in sec. 4.1.5 - all steps are summarized in the algorithm diagram in fig. 4.1. Every software in all these steps works in a so-called **batch mode** - a software run in a Windows/Linux background without any graphical user interface. This run is handled via text scripts, which are in more detail described in following sections.
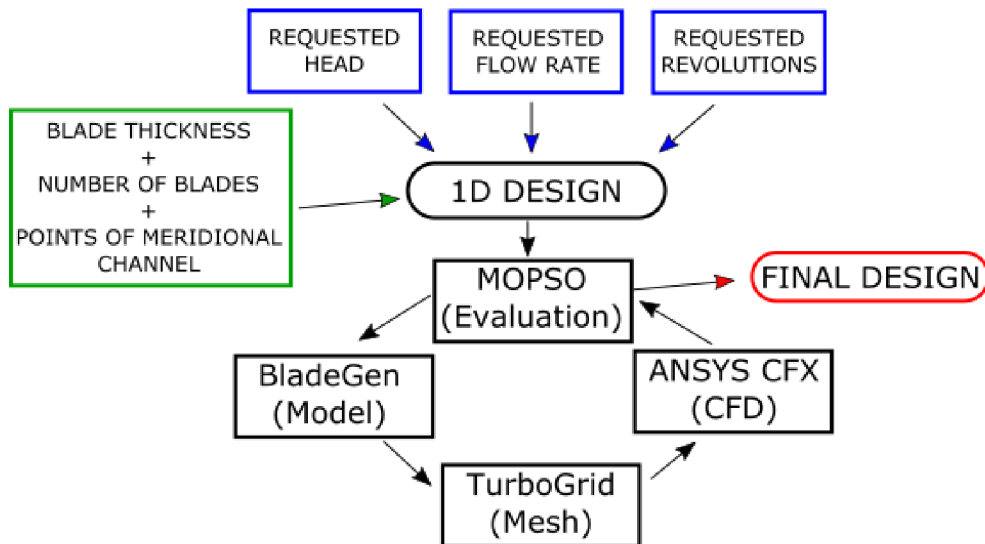

Fig. 4.1: *Diagram of the optimization loop.*

4.1.1 Software input

It must be noted, that the optimization algorithm needs some initial design to begin with. This starting 1D design is based on the empirical relations - in detail described in sec. 3. The optimization software requires namely: points **A** [mm], **B** [mm], **C** [mm], **D** [mm] in R-z coordinate system, which characterize the size and position of the meridional flow channel (fig. 4.2); the number of blades **z** [-], the blade thickness **e** [mm] on the three main streamlines (hub, middle, shroud); the requested head **H** [m]; the requested flow rate **Q** $[m^3/s]$ and the requested rotational speed (RPM) **n** [1/min]. These pump parameters are assigned via software's graphical interface - *Pump info...* window in fig. 4.2.
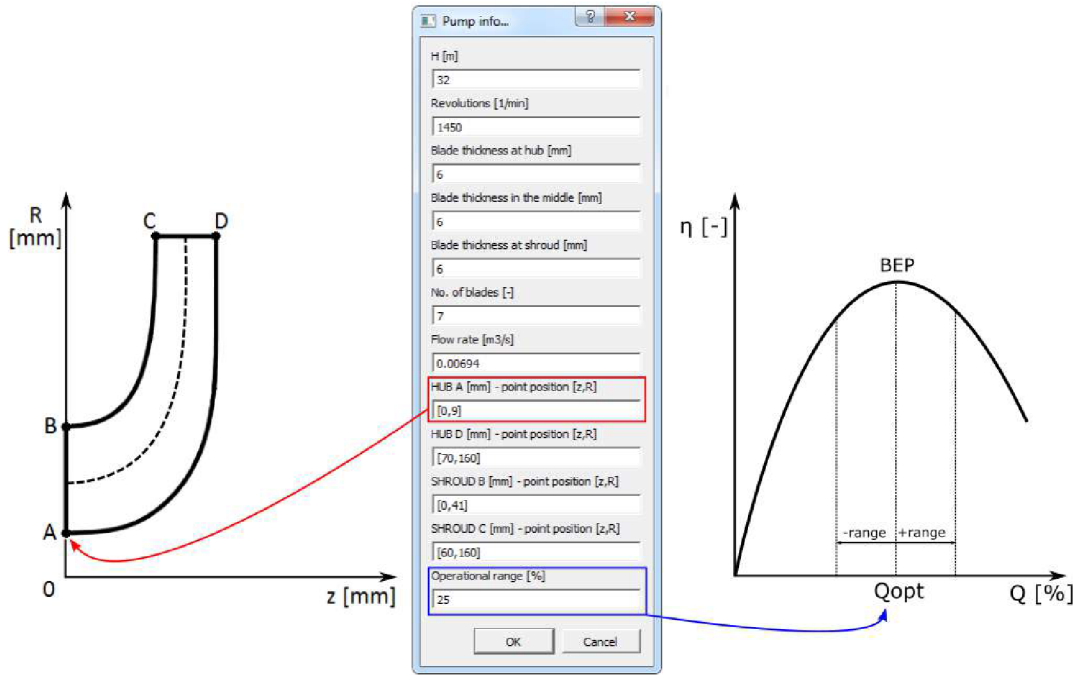
60

Fig. 4.2: *Position and size of the meridional flow channel + operational range.*

Another important input parameter is the reasonable choice of the pump's operational range (fig. 4.2 - right). Customers want in many occasions to have guaranteed pump operational range with the highest possible efficiency together with required head, so for this reason was an option **Operational range** implemented within the presented optimization tool.

The crucial dimensions, which are computed by the optimization software (based on the empirical study in sec. 3) are β_1 [°] angle of the blade at inlet, β_2 [°] angle of the blade at outlet and the diameter d_1 [mm]. It must be noted that the diameter d_1 served only for the determination of β_1 angle and did not have another job in the shape optimization procedure.

4.1.2 MOPSO

A leading role of the optimization cycle is proper optimization method. In this case the MOPSO (in more detail in sec. 2.5) with Pareto principles and several modifications was utilized in the problem of designing the proper shape of the pump impeller.

MOPSO parameters

The multi-objective particle swarm optimization needs several key parameters (sec. 2.4), which significantly influence the behaviour of the swarm and also a behaviour of the optimization cycle itself. These parameters are summarized in a simple table below - some parameters were inspected in the previous researches [63] and [64].

Tab. 4.1: General MOPSO settings.

Name	Value
Population size	10
Repository size	40
Grid size	15
Inertia weight w	0.2 (linear decrease)
Parameter c_1 and c_2	2

The parameters summarized in the table 4.1 can be altered by the user via the first part of the interactive input window called *MOPSO + NM info...* (fig. 4.3).
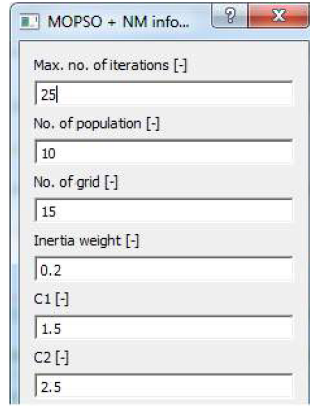

Fig. 4.3: *MOPSO parameters.*

Optimization objectives and evaluation function

Every optimization method or algorithm is driven by a chosen optimization objective(s). In the presented shape optimization procedure are chosen these: the hydraulic efficiency η_H, the pump head H and the static relative pressure on the blade. These three objectives together with shape penalties, which ensure the creation of suitable designs, formed the **evaluation function** f. The main task of the function f and its **minimal** value is to select the "best" design from the external archive (the best in the meaning of what is the best for the user and his parameter input).

$$f = weight_H \cdot \left| 1 - \frac{H_{opt}}{H_{req}/const_H} \right| + weight_\eta \cdot (3 - \eta_{H,-} - \eta_{H,opt} - \eta_{H,+}) +$$
$$+ weight_{surf} \cdot (1 - C_{pressure}) + pen_{shroud} + pen_{hub} + 0.2 \cdot pen_\theta + pen_{HQ}, \quad (4.1)$$

where H_{opt} $[m]$ is the current value of pump head acquired from CFD; $\eta_{H,-}$ $[-]$ is the hydraulic efficiency acquired from CFD in the operating point on the left from pump optimum; $\eta_{H,opt}$ $[-]$ is the hydraulic efficiency acquired from CFD in the pump optimum; $\eta_{H,+}$ $[-]$ is the hydraulic efficiency acquired from CFD in the operating point on the right from the pump optimum. The rest of the variables are described in a following text.

Weights $weight_H$, $weight_\eta$ and $weight_{surf}$: A magnitude of each weight sets a partial goal in the optimization procedure. For example with the higher value of the $weight_H$ is swarm strongly influenced by the change of the pump head H, on the other hand remaining objectives are suppressed. The weights can be entered into the optimization algorithm by the user via the third part of the interactive input window called *MOPSO + NM info...* (fig. 4.4).
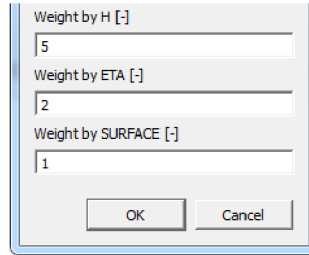

Fig. 4.4: *Computational weights.*

Constant $const_H$: The presented optimization procedure uses only one periodical flow channel, which means that the additional parts of pump such as the diffuser, volute or distributor are neglected. The fluid, which passes through the neglected parts, is affected by losses. These losses decrease value of the pump head and efficiency, so to balance this problem, requested value of the pump head must be boosted by a chosen constant $const_H = \mathbf{0.975}$. Such value is based on the research in [11], where authors determined the difference between the head of the impeller and the head of the impeller with the volute to approximately 3%.

Variable $C_{pressure}$: The blade experiences the low pressure states on its suction side, so from this perspective the blade must be checked for the critical values of this pressure for a possible manifestation of the cavitation.
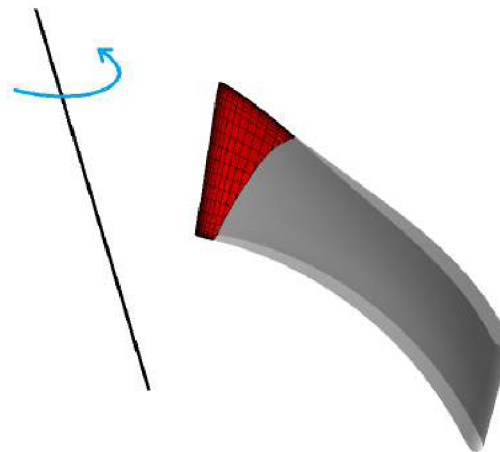

Fig. 4.5: *Surface pressure check on the blade of the impeller.*

Thus, the variable $C_{pressure}$ $[-]$ is defined as a ratio between the area of the blade

$S_{pressure}$ $[m^2]$ with the static relative pressure equal and lower than a chosen value $(-\,75000\ Pa)$ (red area in fig. 4.5) and the total area of the blade S_{blade} $[m^2]$:

$$C_{pressure} = \frac{S_{pressure}}{S_{blade}}. \tag{4.2}$$

It must be noted that the variable/penalty $C_{pressure}$ $[-]$ does not necessary exclude the pump designs with the low values of the static pressure on the blade, it only penalizes them significantly.

Penalties pen_{hub} and pen_{shroud}: A key role of the penalties pen_{hub} and pen_{shroud} is to penalize the deformed shapes of the Bézier curves - fig. 4.6.
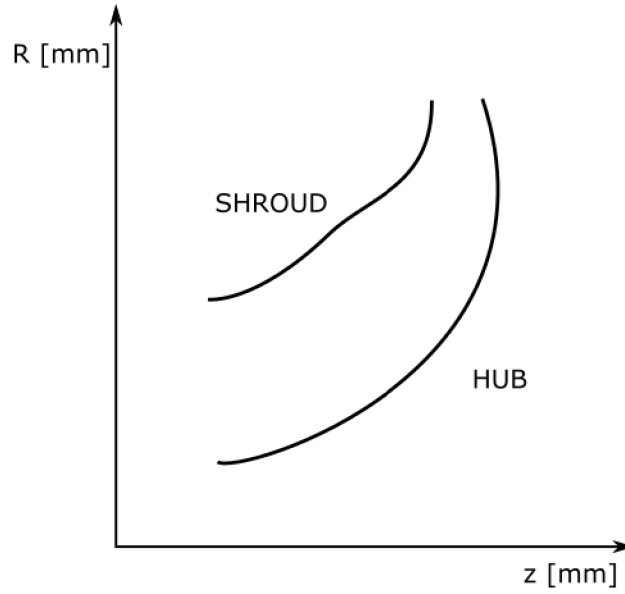
Fig. 4.6: *The deformed shapes of the Bézier curves in the meridional view.*

In the meridional view, the Bézier curves outline the shape of hub and shroud. Such curve could and is divided by n-points (fig. 4.7, n = **1000**). Let's focus on the hub first - penalty pen_{hub} is computed form a knowledge of each point, which is characterized by set of coordinates $(z_{i,hub}, R_{i,hub})$:

$$pen_{hub} = 0.01 \cdot \sum_{i=1}^{n} A_{i,hub} + 0.01 \cdot \sum_{i=1}^{n} B_{i,hub}, \tag{4.3}$$

where $A_{i,hub}$ and $B_{i,hub}$ are defined according following rule:

$$z_{i,hub} - z_{i-1,hub} \begin{cases} < 0, \ \Rightarrow A_{i,hub} = 1; \ i = 1, \ldots, n. \\ > 0 \ \Rightarrow A_{i,hub} = 0; \ i = 1, \ldots, n. \end{cases}$$

And:

$$R_{i,hub} - R_{i-1,hub} \begin{cases} < 0, \ \Rightarrow B_{i,hub} = 1; \ i = 1, \ldots, n. \\ > 0 \ \Rightarrow B_{i,hub} = 0; \ i = 1, \ldots, n. \end{cases}$$

Penalty pen_{shroud} is calculated similarly only using the Bézier curve, which defines shroud:

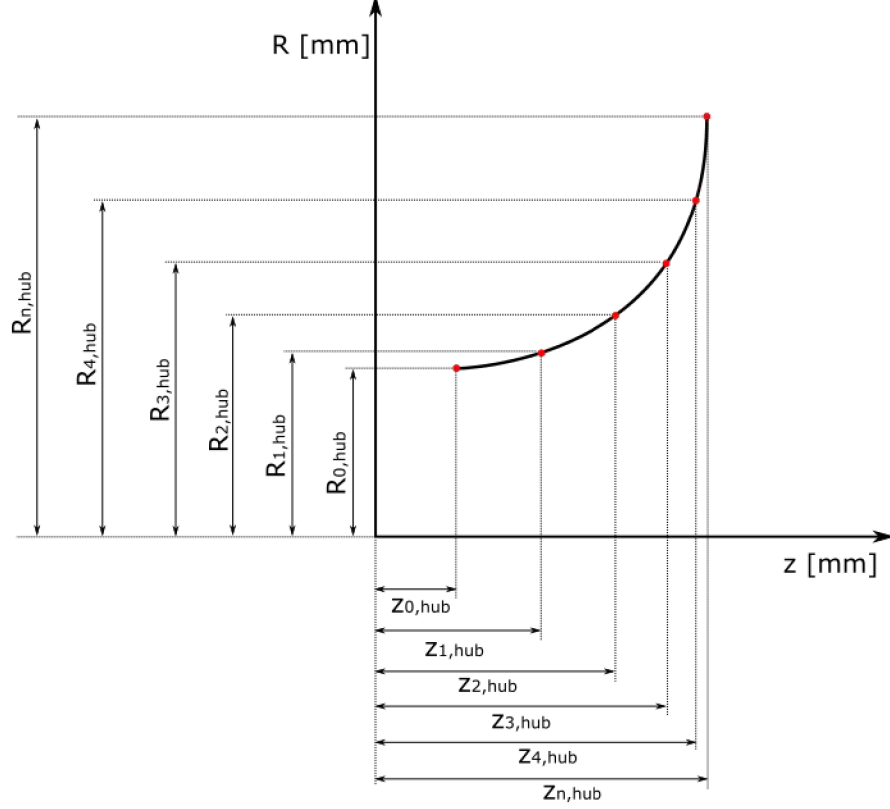$$pen_{shroud} = 0.01 \cdot \sum_{i=1}^{n} A_{i,shroud} + 0.01 \cdot \sum_{i=1}^{n} B_{i,shroud}. \tag{4.4}$$

Fig. 4.7*: Hub or shroud curve dividing.*

Penalty pen_{θ}: Another type of the computational penalty must be set to avoid the creation of the deformed blade shapes at the impeller outlet (trailing edge deformation) - pen_{θ}. Such trailing edge deformations make usually the hydraulic design unmanufacturable. Generally, there are four main deformations, which could be observed during the hydraulic design procedure, namely - c), d), e), f) in fig. 4.8.

To successfully treat this deformation problem a value of a variable θ-angle (wrap angle) - see eq. 2.9, which corresponds with the three main streamlines (near the hub, in the middle and near the shroud) must be extracted from the BladeGen tool. To be more precise, the value of θ-angle in the end of each streamline - let's called them θ_{shroud}, θ_{middle}, θ_{hub}. It must be noted that such θ-angle extraction from the BladeGen tool is done in the batch mode via a script, which tells the BladeGen to focus and to export only the θ-angle to the simple text file. Mentioned text file is afterwards utilized within the master code, which is described in the section above.
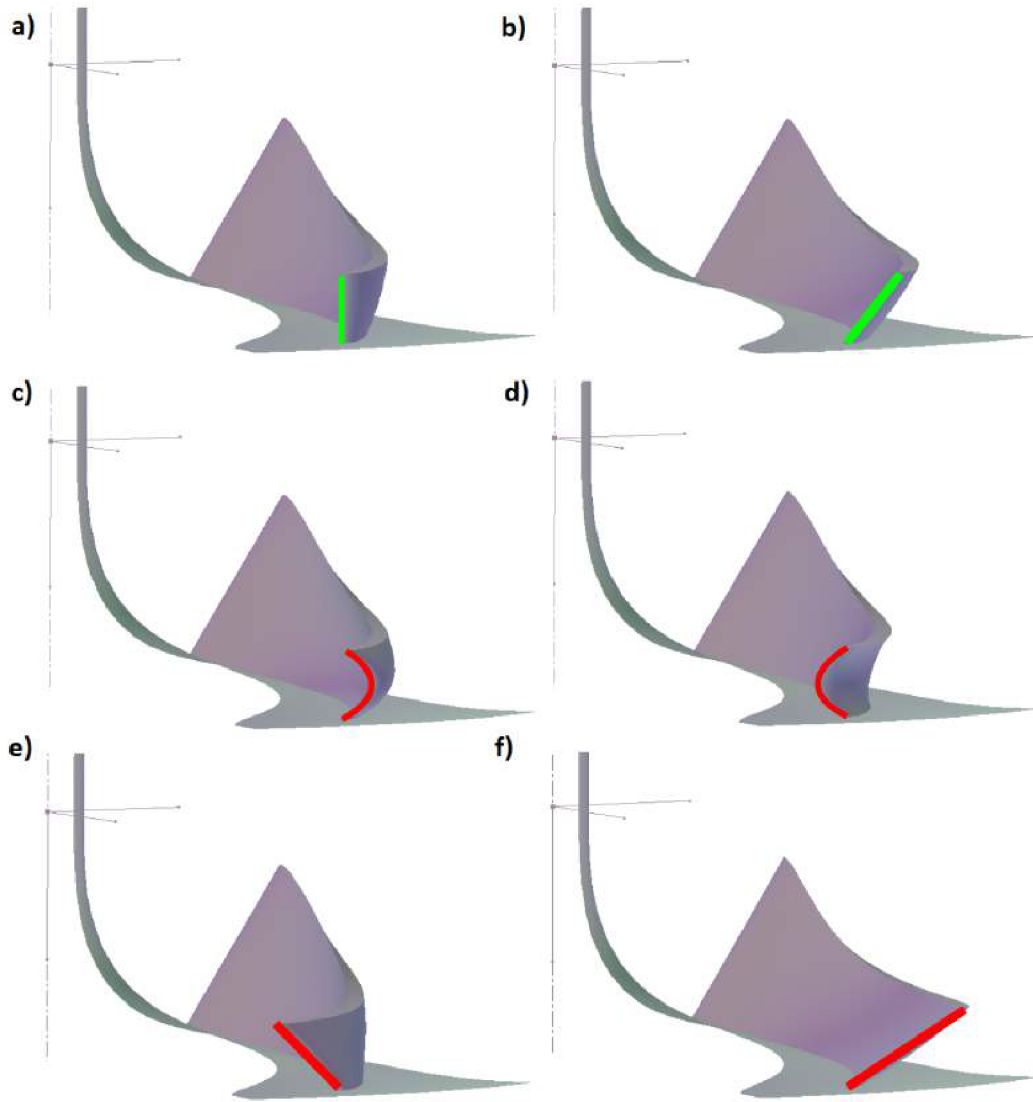
Fig. 4.8: *Suitable vs. deformed designs - the trailing edge perspective.*

Case **a)** - fig. 4.8: **Suitable** blade design - a large number of pumps are manufactured like this. Occurs when the values of θ-angles are equal:

$$\theta_{shroud} = \theta_{middle} = \theta_{hub}. \tag{4.5}$$

Case **b)** - fig. 4.8: **Suitable** blade design - reduces pressure pulsation of the pump [27]. Occurs when:

$$\theta_{shroud} < \theta_{middle} < \theta_{hub} \wedge \theta_{middle} - \theta_{shroud} \leq \theta_{critical} \wedge \theta_{hub} - \theta_{middle} \leq \theta_{critical}, \tag{4.6}$$

where value of $\theta_{critical}$ was set to **10°**.

Case **c)** - fig. 4.8: **Unsuitable** deformed blade design, which occurs when:

$$\theta_{shroud} > \theta_{middle} \wedge \theta_{middle} < \theta_{hub}. \tag{4.7}$$

Case **d)** - fig. 4.8: **Unsuitable** deformed blade design, which occurs when:

$$\theta_{shroud} < \theta_{middle} \wedge \theta_{middle} > \theta_{hub}. \tag{4.8}$$

Case **e)** - fig. 4.8: **Unsuitable** deformed blade design

$$\theta_{shroud} > \theta_{middle} > \theta_{hub}. \tag{4.9}$$

Case **f)** - fig. 4.8: **Unsuitable** deformed blade design, which occurs when:

$$\theta_{shroud} < \theta_{middle} < \theta_{hub} \wedge \theta_{middle} - \theta_{shroud} > \theta_{critical} \wedge \theta_{hub} - \theta_{middle} > \theta_{critical}, \tag{4.10}$$

where value of $\theta_{critical}$ was set to **10°**.

For cases a) and b) $pen_\theta = \mathbf{0}$, on the other hand for cases c), d), e), and f) has pen_θ value equal to **1**.

Penalty pen_{HQ}: A key role of this penalty is to penalize the pump impeller designs, which create a H-Q instability in the chosen working range - fig. 4.9. It means that, if the head value in the operating point on the left from the optimal flow rate has the smaller value than in the optimal flow rate, the current design shows signs of the instability. This penalty has only two values: if the instability is present $pen_{HQ} = \mathbf{1}$, otherwise $pen_{HQ} = \mathbf{0}$.
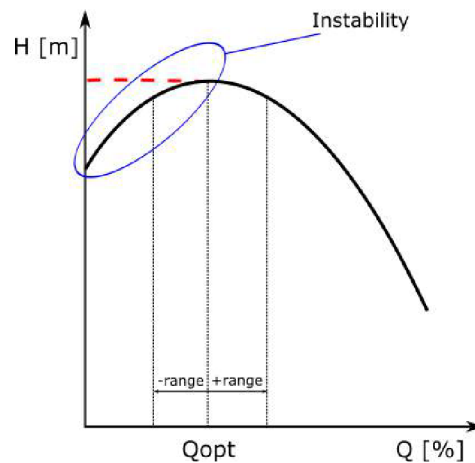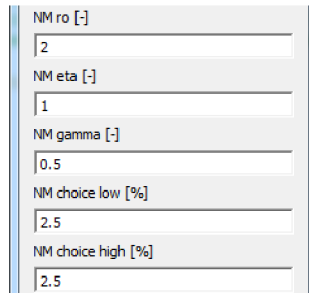

Fig. 4.9: H-Q instability.

Nelder-Mead modification and swarm diversity restart

An idea of a combination of two optimization algorithms, namely **Particle Swarm Optimization** and **Nelder-Mead algorithm**, was explored in [64]. This idea was transformed and modified into this optimization procedure and afterwards applied on the key element of the MOPSO algorithm - on the external archive, where Pareto dominant designs are stored. Basically, an area of specific dimensions (set by the user - fig. 4.10) is created around the best design in the archive, which is determined by eq. 4.1. If another designs (two or more) are located in such area, the Nelder-Mead algorithm is applied on them in a task of the improvement of the design with the worst value of the evaluation function (eq. 4.1). Only one iteration of the Nelder-Mead algorithm is investigated (all procedures, such as the reflection, contraction, expansion and simplex reduction are investigated at once). This modification brings another type of the diversity of the swarm and afterwards of the optimization algorithm.

Fig. 4.10: *NM parameters.*

A final improvement of the swarm diversity is by a so called "**restarting**" of the current swarm (could be compared to the mutation mentioned above in the MOPSO section, which is plentifully exploited in EA/GA). A restart concept is defined as a creation of the completely new swarm with random parameters (identical procedure takes place at the beginning of MOPSO algorithm). But it must be noted that this restart procedure does **NOT** replace current swarm at all cost, just only if a newly restarted particle improves the current one. This procedure takes place every **third** iteration of the MOPSO algorithm.

Two different types of swarm restart are thoroughly implemented inside the optimization algorithm and while iteration goes on, they'll alternate between each other. **First** restart utilizing the whole given computational areas for changing parameters such as the β angles or the position of the control points of the Bézier curves.

On the other hand, the **second** type of the restart exploits a simple fact of the equation 3.20, which serves for the proper determination of the inlet blade angle β_1 on the middle streamline. In this equation, the value of β_1 strongly relies on the value of the circumferential velocity u_1, which depends on the diameter $d_1 \rightarrow$ higher velocity $u =$ smaller inlet β angle. So from this perspective it is adequate to have for the inlet values of the β angle increasing magnitudes, meaning that β angle near the shroud has the lowest value and near the hub has the highest value (fig. 4.11). The outlet values of the β_2 angle for this type of restart have identical magnitudes (fig. 4.11).
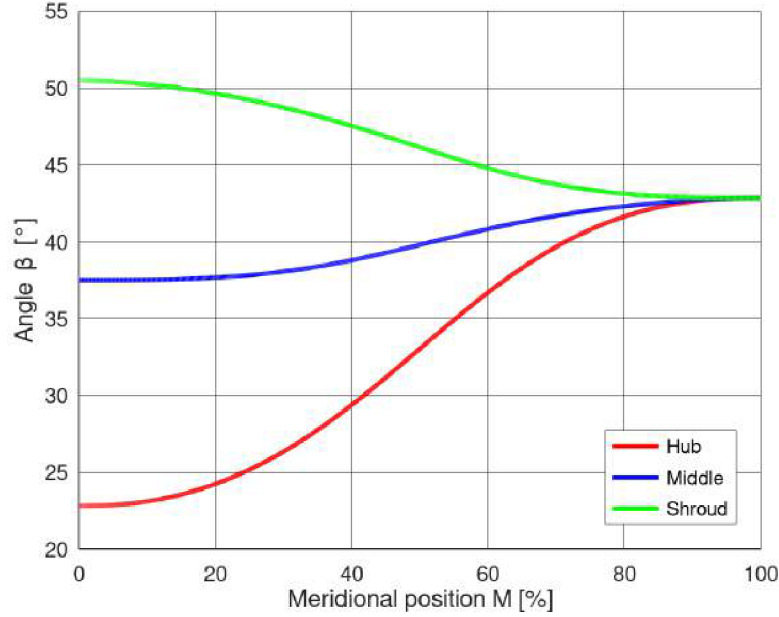
Fig. 4.11: _Second type of the restart: the β - angle along the blade._

4.1.3 Parametric model

The most effective way, how to create a specific design of the centrifugal radial pump impeller, is by using the commercial ANSYS software package with a specialized tool **BladeGen**. BladeGen (running in the batch mode) could be controlled via a text script file *.bgi*. The crucial parameters of the pump impeller could be defined in such file, namely: β - the angle of the blade (inlet/outlet angles); the blade thickness; the shape of a meridional flow channel (with the Bézier curves or splines) or the position of a leading edge and its form. The shape of each impeller is in the presented thesis (optimization tool) parametrized in three main steps: the meridional parametrization, the blade parametrization and the leading edge parametrization. It must be noted that the operating limits (boundaries) of the parametric model are **first** developed around data from empirical equations (see section 3) and later during the optimization run around the best suitable design proposed by the function f (see equation 4.1) $\rightarrow$ the floating operational boundaries.

Meridional parametrization

First, the meridional flow channel must be parametrized. This fact is done by exploitation of the **Bézier curves** with **five** control points - fig. 4.12. On the hub (and of course on the shroud) two points A and D (B and C for shroud) are fixed and characterize the position and size of the meridional flow channel, the rest of them are responsible for the **shape**.
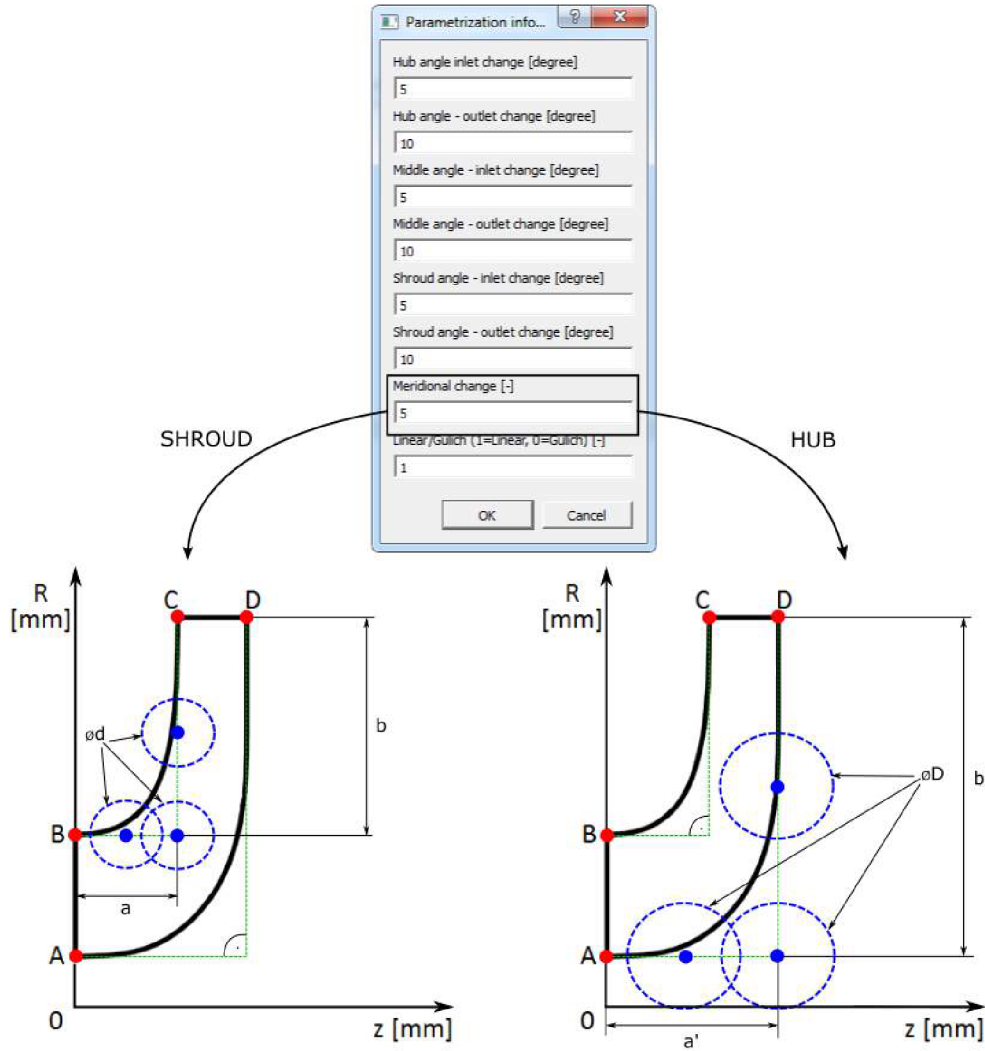
Fig. 4.12: *Meridional parametrization.*

The initial position of the shroud free control points (**circle centres**) is created in following way: a perpendicular line at a point **B** to width b_1 must be constructed. Another perpendicular line at a point **C** to width b_2 is put together. These two perpendicular lines intersect at one of the free control points (let's call this point **Int**). If a midsection of newly created intersection point Int and point B is made, it'll set another initial position of the free control point. Finally, a midsection of point Int and point C creates the last center of a restriction circle. Such construction process is similar for the hub curve. Free control shroud points can move in such restriction circles (fig. 4.12) with the diameter d $[mm]$ defined as:

$$d = \frac{L_{shroud,ini}}{M_{change}}, \tag{4.11}$$

where $L_{shroud,ini}$ $[mm]$ is a length of the shroud curve in the initial state (fig. 4.12); M_{change} $[-]$ is a constant defined by the user (fig. 4.12). Analogously for the hub is the

diameter D [mm]:

$$D = \frac{L_{hub,ini}}{M_{change}}, \tag{4.12}$$

where $L_{hub,ini}$ [mm] is a length of the hub curve in the initial state (fig. 4.12); M_{change} [$-$] is a constant defined by the user (fig. 4.12).

Leading edge parametrization

The shape and the position of the leading edge is ensured by the Bézier curve with three control points. Two of them are partially fixed on the shroud and hub curve - fig. 4.13. Fixation on the shroud is set from 2.5% to 30% of the shroud curve length, on the other hand fixation on the hub is set from 15% to 50% of the hub curve length. Such values are not permanently set and could be alternate for user purposes, but only with a change of some specific lines in mentioned **master code**.
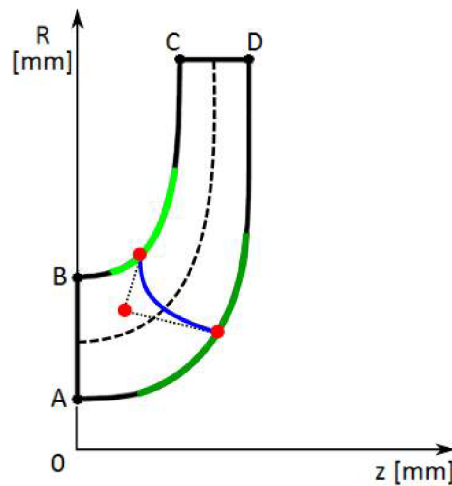

Fig. 4.13: *Leading edge parametrization.*

Blade parametrization

Two main methods of the proper blade modelling are implemented in this optimization software - first, the linear change of β angle along the length of the blade (M [%] - fig. 4.14 left) and second, the Gülich's approach [26] with an inflection point in the β angle development (fig. 4.14 right). The linear change of β angle supposed to be energy-efficient solution [27].

Before anything else, the β_1 and β_2 angles must be computed from knowledge of the empirical equations in section 3 and then a working range is constructed around these values. Magnitudes of these working ranges are obtained from the interactive *Parametrization info...* window - fig. 4.14.

The β angle change with the inflection point is according to Gülich [26] suitable for the designs, which try to avoid possible cavitation on the blades of the impeller. Once again β_1 and β_2 must be computed, afterwards the working ranges around these values are constructed. Then the Bézier curve with six controls points is put together. Two new

parameters h_1 and h_2 emerged - fig. 4.14 right. Those parameters characterize a distance of the second control point from the first one and a distance between the fifth and the last control point. Maximal value for h_1 and h_2 is set to **30%** of the length of blade on the current streamline.
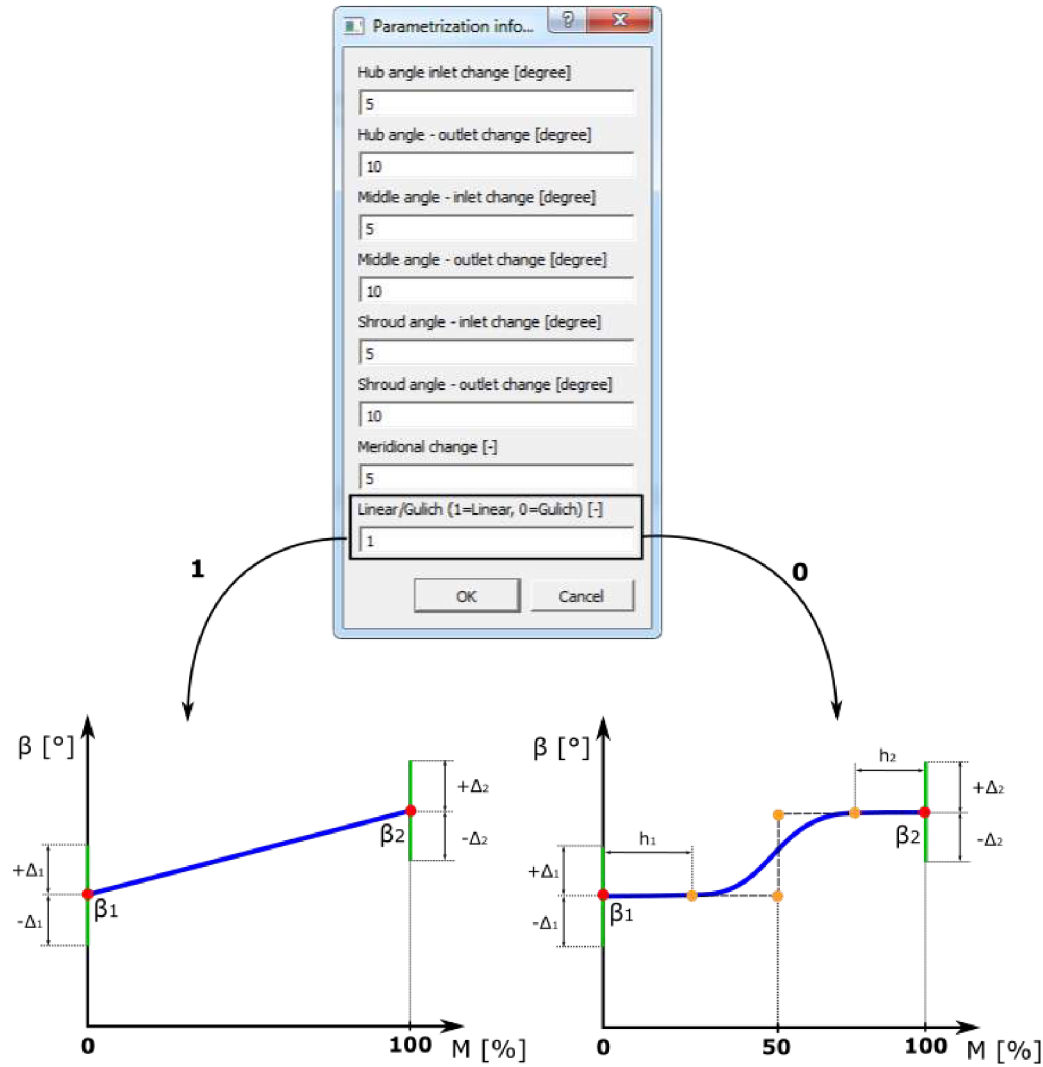

Fig. 4.14*: Blade parametrization.*

4.1.4 Computational mesh

The mesh generation is ensured by a tool called **TurboGrid** (also belongs in the commercial ANSYS product package). TurboGrid excels in the meshes for rotational machines and it is tightly connected with the **BladeGen** output. This software is also handled and managed by a text script file called **replay** (basically, replay is a simple record of actions, which were executed during the mesh creation in TurboGrid). One periodical flow channel was used, with hexahedral elements and higher mesh resolution near walls. Total element count did not exceed **250k cells**.
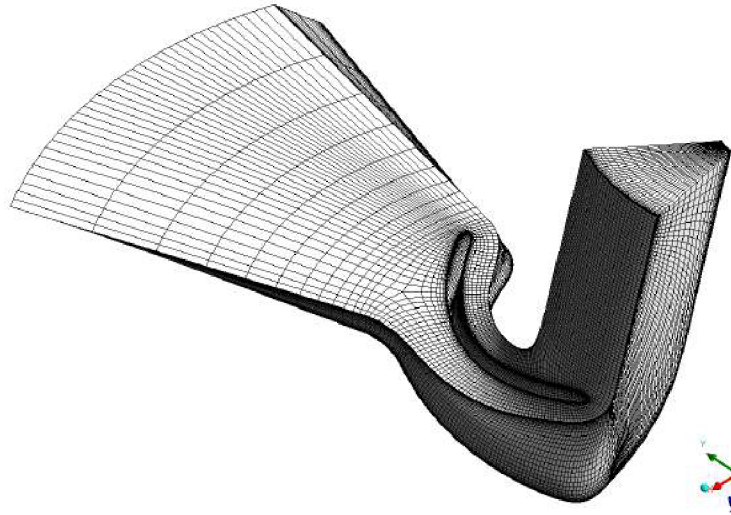

Fig. 4.15: *Computational mesh of the one periodical flow channel.*

Negative volume detection

Important step in presented computational hierarchy is a procedure called **negative volume detection**, which is performed by **ICEM CFD**. This procedure takes place right after the generation of the computational mesh and has a task of revealing deformed mesh cells inside the computational domains. This phenomenon is strongly connected with the unsuitable impeller designs, where some mesh cells collapsed inside each other - this fact results in the error, which leads to a software crash of the CFX solver. So, if the procedure Negative volume detection finds such mesh, it will immediately delete this mesh, to avoid possible ANSYS license and cluster space blocking.

4.1.5 CFD simulation

A proper CFD simulations were handled via commercial software **ANSYS CFX**. ANSYS CFX stands out in the area of CFD simulations connected with the rotational hydraulic machines like pumps, turbines etc. Every numerical calculation was performed as a **steady** simulation with a frozen rotor model used on interfaces, which connected static and rotational domains. As boundary conditions served a zero static relative pressure at the domain inlet and a constant mass flow at the outlet. It must be noted that CFD simulations were performed for three different mass flows, which corresponded with the working

operational range set by the user at the beginning of the optimization cycle. General solver settings are described in the table below.

Tab. 4.2: General solver settings.

Name	Value
Turbulence numerics	High resolution
Advection scheme	High resolution
Number of iterations	8000 iterations
Turbulence model	K-epsilon
Double precision	Enabled
Flow medium	Water

4.1.6 Computational (working) domains
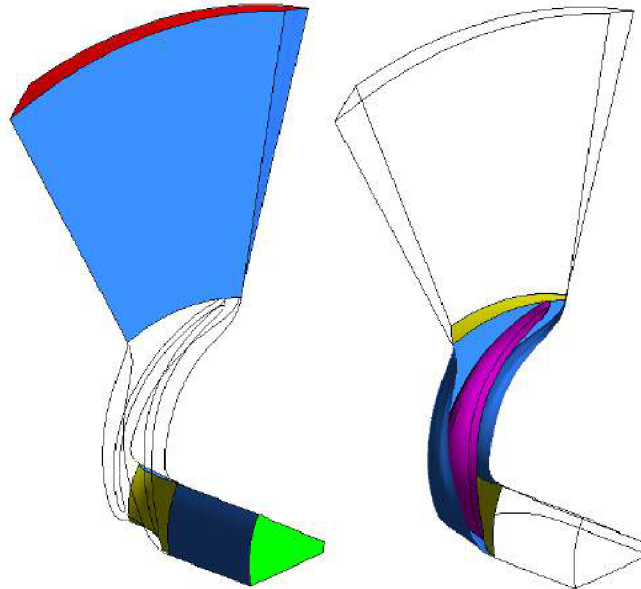
Fig. 4.16: Computational (working) domains of the radial impeller case.

A periodical flow channel was selected for a significant total computational time reduction - see fig. 4.16. This periodical flow channel consists of three main working regions: inlet, rotational passage with the blade and outlet. On the left and right side of the channel are prescribed periodical interfaces, which substitute the rest of the optimized impeller.

Static domains (absolute domains)
The static domain of the computational impeller case consists of two parts - the inlet region and the outlet region (fig. 4.16 left). In between those parts there is the rotational region with the blade, shroud and hub of the pump. Every region must be connected with another one with proper interfaces - the **frozen rotor** was chosen in our optimization

problem for its computational stability. The inlet boundary condition takes place in the inlet region and is characterized by the zero relative pressure and is represented as a green surface in fig. 4.16 (name in expressions - *REGION:INBlock INFLOW*). Outlet region contains outlet boundary condition, which was set as mass flow and is portrayed as a red area in fig. 4.16 (name in expressions - *REGION:OUTBlock OUTFLOW*).

A rotating domain (relative domain)

The rotational domain is outlined in fig. 4.16 right. A dominant part of this domain is the blade (purple color - name in expressions - *BLADE*), than the hub (name in expressions - *Passage HUB*) and the shroud (name in expressions - *Passage SHROUD*). This passage revolves with revolutions n and is the primary contributor to final parameter values (H,η_H).

4.1.7 Results evaluation

Two crucial monitors must be set in every simulation case with the impeller design in it - the first one is for the pump head H and the other for the hydraulic pump efficiency η_H. The monitors are dependent on expressions, which are composed in CFX as follows:

```
TORQUE
(torque_z()@BLADE+torque_z()@Passage HUB
+torque_z()@Passage SHROUD)*numberofblades
```

```
PUMP HEAD
(massFlowAve(Total Pressure)@REGION:OUTBlock OUTFLOW-
massFlowAve(Total Pressure)@REGION:INBlock INFLOW)/(997*g)
```

```
HYDRAULIC EFFICIENCY
((massFlowAve(Total Pressure)@REGION:OUTBlock OUTFLOW-
massFlowAve(Total Pressure)@REGION:INBlock INFLOW)*
numberofblades*(massFlow()@REGION:INBlock INFLOW/997))/
(2*pi*torque*(revolutions/60))
```

After successful termination of the CFD simulation in ANSYS CFX a result file (***res**) is always created. The result file contains a history of chosen monitors. Values of these monitors are bound with iterations of the CFD calculation. This fact is exploited further in a way of the correct design case evaluation - the last 2000 iterations are extracted from the final result file (***res**) and afterwards a mean values of the pump head H and the hydraulic efficiency η_H are calculated.

Computational parallelization

One of the most important advantage of PSO (MOPSO) algorithm is that the necessary CFD simulations could be redistributed to multiple workers. This fact is transformed into a batch calculation using a department cluster called **KAPLAN** and a simple **shell** script file - it means that the all designs are sent for the CFD simulations at once → significant savings in the total computational time.
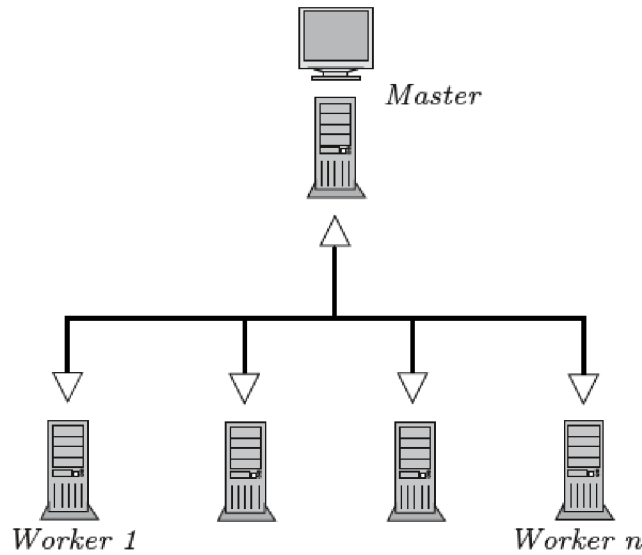
Fig. 4.17: *Computational parallelization* [93].

The computational parallelization can be simply described by a diagram displayed in fig. 4.17. Master is a local computer with the master code and ANSYS package software. A main task of the master computer is to create the impeller models (designs), computational mesh, prepare impeller cases in CFX-pre and perform postprocessing. The CFD simulations takes over KAPLAN computational cluster with **1+13** computational nodes (one main node with 32 cores and 13 nodes each with 8 cores). The most suitable (maximal) computational distribution of the CFD simulations is: 8 cases for the main node (each simulation occupies 4 cores) and for nodes 1-12 only two simulations (once again each simulation occupies 4 cores) → **ten particles** of the MOPSO algorithm (node no. 13 will serve as an observation node on the cluster with no CFD simulations on it).

5 TOOL APPLICATION

Presented optimization software, which employs MOPSO and NM algorithms and procedures, possesses an output graphical interface, which is divided into the five pump property windows - described by fig. 5.1.
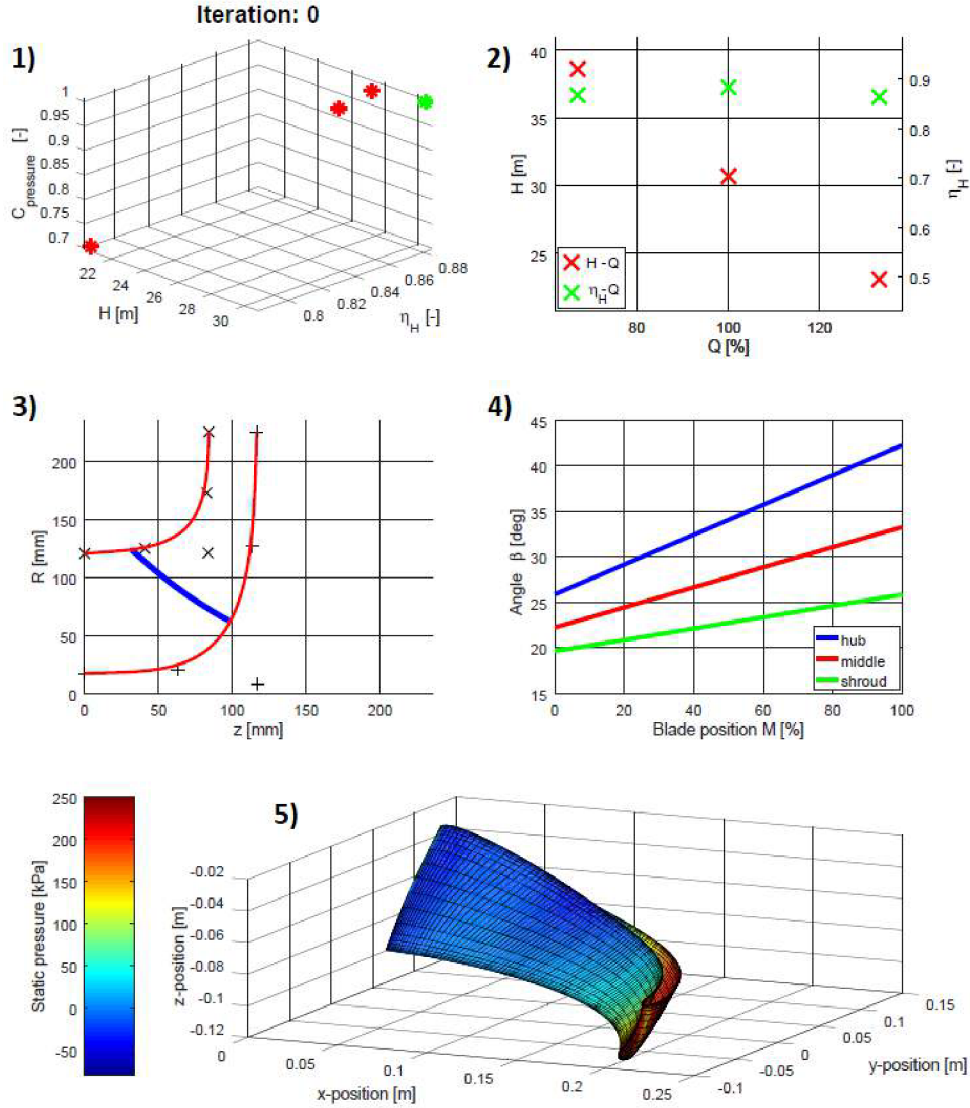

Fig. 5.1: *Software layout.*

Window 1) shows during the optimization procedure the Pareto front with the selected best design (green color). The pareto front consists of the pump head H, the hydraulic efficiency η_H and the operational constant $c_{pressure}$ (all three variables are acquired from the CFD simulations). The best design is established by the evaluation function f defined by eq. 4.1. **Window 2)** outlines two main performance characteristics, namely: $H - Q$ (red color) and $\eta_h - Q$ (green color) in three operation points. These dependencies belong to the current best design. **Window 3)** has a task of presenting the Bézier curves of the pump meridional flow channel (red color) and the leading edge (blue color) of the current best design. **Window 4)** describes the β angle development along the length of the blade. Such development is captured on the three main streamlines - near the hub (blue), near

the shroud (green) and on the middle streamline (red). Plotted β-curves belong to the current best design. **Window 5)** demonstrates the current best shape of the pump blade together with the static pressure distribution.

5.1 Pump turbine

The first main task for the presented optimization software is a problem of finding the proper shape of the **pump turbine** impeller (grant **TH01020982** - *Zefektivnění akumulace energie a zajištění stability rozvodné sítě rozšířením provozního pásma přečerpávacích vodních elektráren*). Such impeller (and the hydraulic machine itself) works in pump and turbine modes, so it must be noted that in the presented thesis the shape optimization was done only for the **pump mode** of the pump turbine.

5.1.1 Pump turbine assembly

This section covers a basic description of the pump turbine system/hydraulic machine (see fig. 5.2 and 5.3), which operated both as the turbine for generating energy, and in the reverse as the pump for transporting fluid (water).
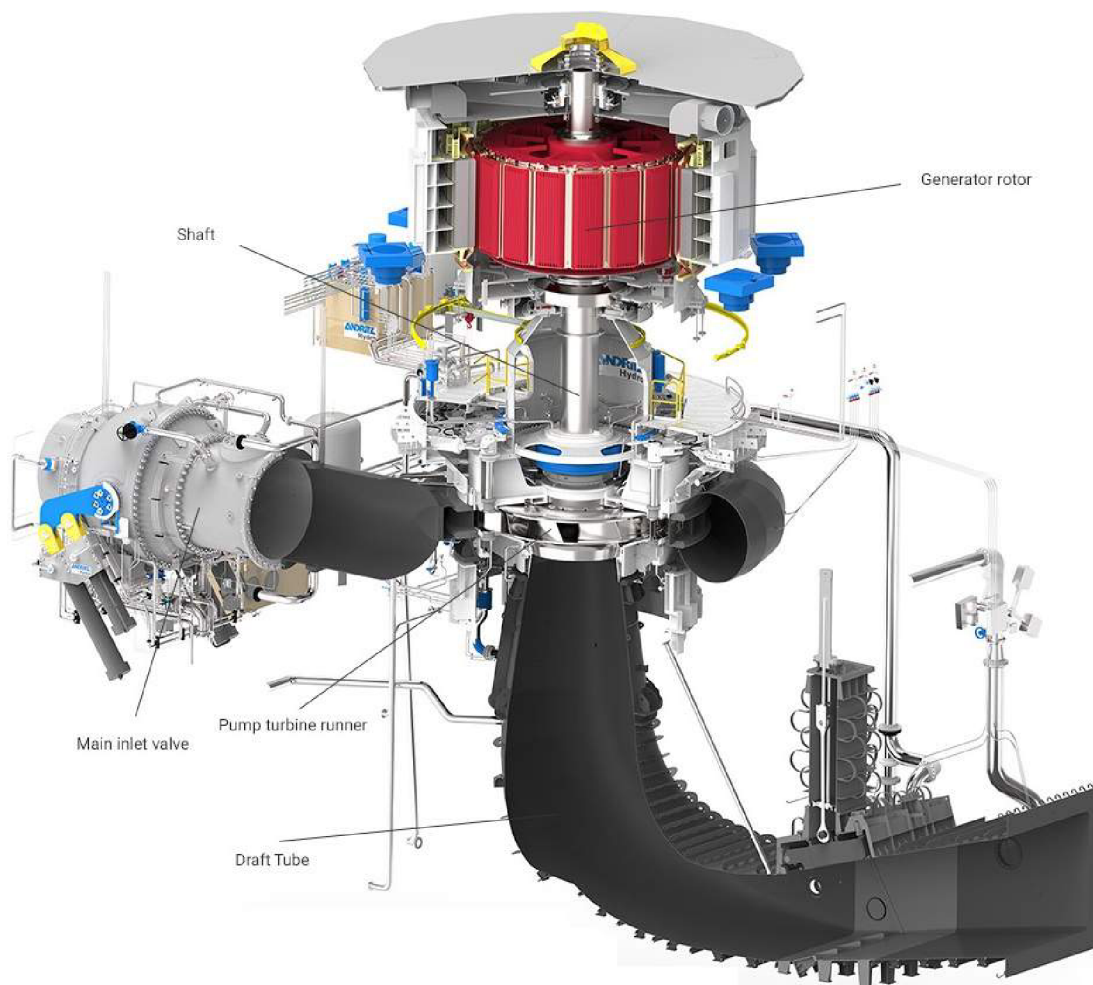

Fig. 5.2: *Pump turbine in power plant in Hebei Province, China - Andritz* [105].

In the pump mode fluid flows from the draft tube through the impeller to the spiral case (volute), in the turbine mode is the other way around. The pump turbine is usually composed of the five main hydraulic parts [30]:

Draft tube - supplies fluid to the inlet of the impeller (pump mode) or converts the kinetic energy of the flow to the pressure energy (turbine mode).

Spiral case (volute) - converts the kinetic energy of the flow to the pressure energy (pump mode) or ensures an uniform flow distribution at the stay vanes (turbine mode).
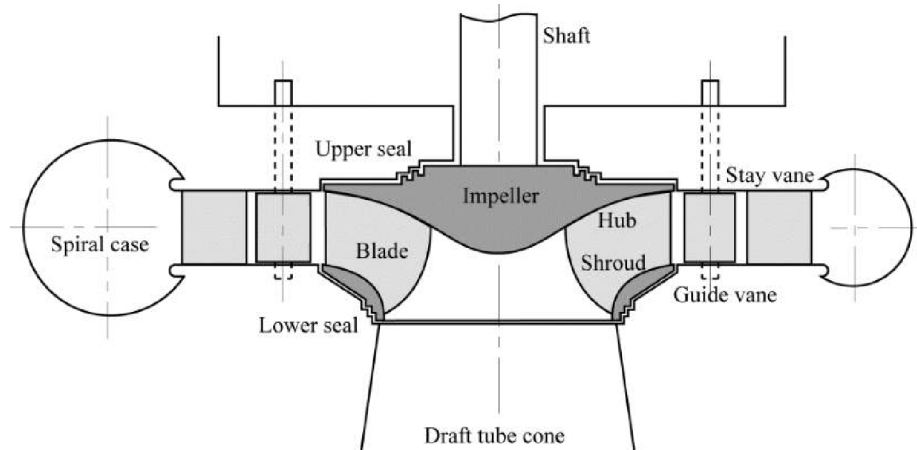
Fig. 5.3: *Pump turbine* [30].

Impeller - converts the mechanical energy from a motor to the hydraulic energy (pressure and kinetic) (pump mode) or converts the hydraulic energy of the flow into the mechanical energy (turbine mode).
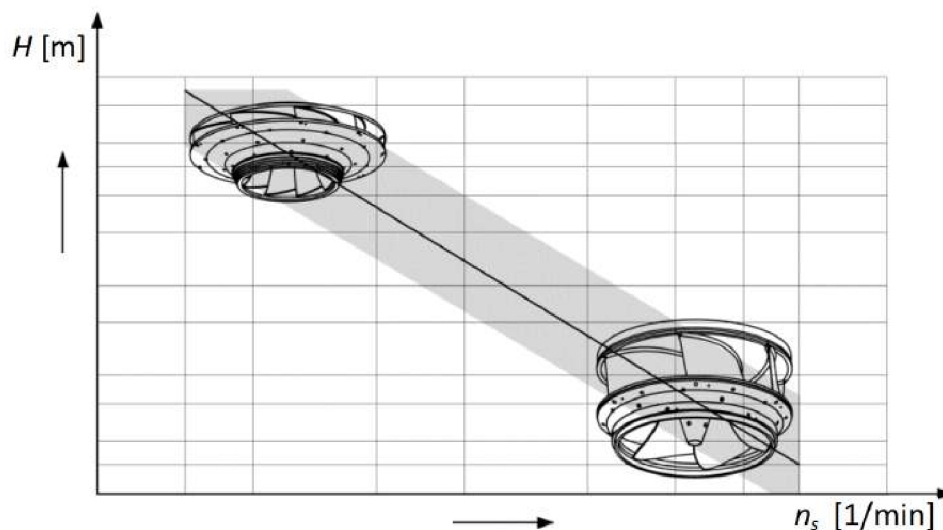

Fig. 5.4: *Pump turbine impeller type* [30].

The main shape and also the size of the pump turbine impeller is fundamentally dependant

on the required head and the flow rate (fig. 5.4). Usually, the high head pump turbines with the low specific speed manifest by a narrow shape of the impeller channels at the inlet section. On the other hand the impellers for the low heads and with the high specific speeds are characterized by the large impeller channels width at the inlet section [30].

Guide vanes - different openings ensure the different values of the flow rate. The vanes leads the flow from the impeller to the stay vanes and spiral case (volute) (pump mode) or from the stay vanes to the impeller and afterwards to the draft tube (turbine mode).

Stay vanes - ensure a proper structural integrity of the spiral case (volute) and lead the flow to the spiral case (pump mode) or to the guide vanes (turbine mode).

5.1.2   Requested and given parameters

Requested pump turbine parameters and crucial **optimization parameters** represents table 5.1 [75], [92]. Such table contains values for the prototype impeller and also scaled values for the model impeller, which was measured by **ČKD Blansko Engineering** (ČBE) (section 5.1.5) [75], [92].

Tab. 5.1: *Requested and shape optimization pump turbine parameters* [75], [92].

	Prototype	Model
Pump head H $[m]$	435	34.77
Flow rate Q $[m^3/s]$	26.9	0.181
RPM n $[1/min]$	600	1100

The shape of the pump turbine impeller was also strictly constrained with the dimensional restrictions - table 5.2. Once again, mentioned table 5.2 contains values for the prototype impeller and also scaled values for the model impeller.

Tab. 5.2: *Dimensional constraints* [75], [92].

	Prototype	Model
Inlet diameter d_0 $[mm]$	1560	240.58
Outlet diameter d_2 $[mm]$	2918	450
Inlet width b_0 $[mm]$	670	103.32
Outlet width b_2 $[mm]$	210	32.39
Number of blades z $[-]$	9	9

Presented dimensional constraints firmly set the size of the impeller. This fact means that **size** was **NOT** under the process of the shape optimization. Altogether, **three** impellers were optimized. They are called in following sections: **Design A**, **Design B** and **Design C**.

5.1.3 CFD simulation

The unsteady (URANS) simulations were utilized for the purpose of data correlation between the measurements (section 5.1.5) and CFD simulations. The computational grids of all pump turbine domains such as the distributor (guide vanes), the impeller and the draft tube were built in ICEM CFD and TurboGrid as fully **hexahedral**, only the spiral case (volute) was meshed in ANSYS meshing as **tetrahedral** with the prismatic layers near walls (fig. 5.5).
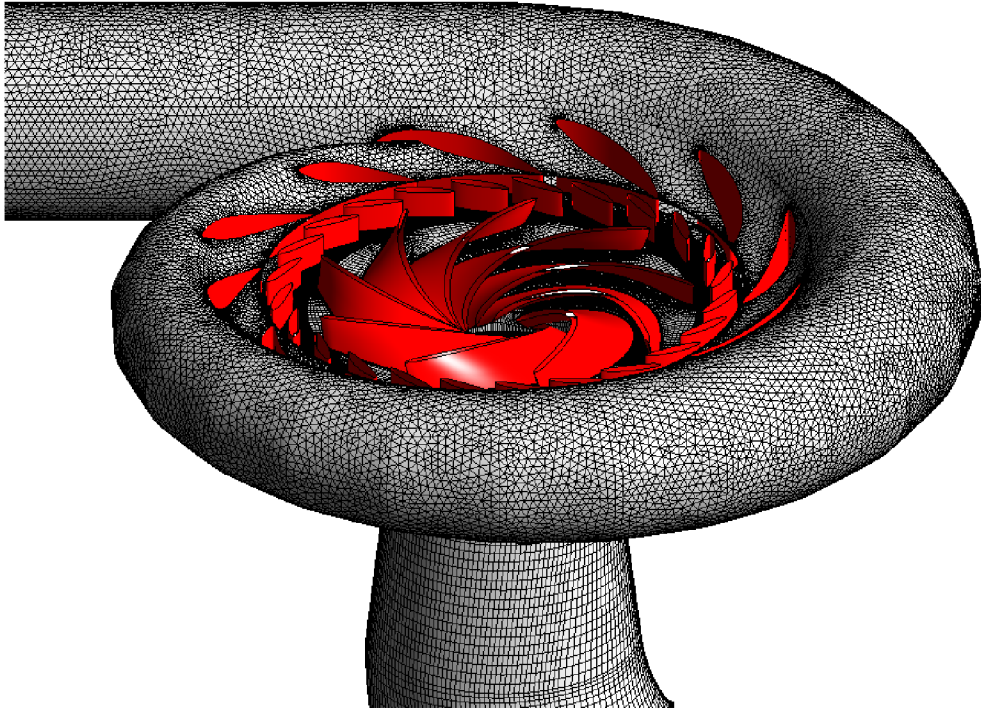

Fig. 5.5: *Sample of the computational mesh.*

Informations about mentioned computational meshes for the pump turbine CFD model are transparently summarized in following table 5.3.

Tab. 5.3: *Mesh overview.*

	Type	Number of elements
Spiral case	Tetrahedral	≈ 1600000
Guide vanes	Hexahedral	≈ 2000000
Impeller	Hexahedral	≈ 900000
Draft tube	Hexahedral	≈ 1100000

The CFD calculations were done in the commercial software **ANSYS CFX** using standard k-ϵ model of turbulence. The "High Resolution" option was selected for the advection scheme, "Second Order Backward" for the transient scheme and "High Resolution" for turbulence numerics. Chosen time step corresponds to 3° of the pump turbine impeller

revolution. Each time step had **5** inner iterations. As a domain initialization served steady simulation (RANS) with mixing planes between relative and absolute computational domains. The requested variables (velocity, pressure, etc.) for the evaluation of the pump head H and the hydraulic efficiency η_H were averaging from the last **10** whole revolutions of the pump impeller. Locations of the pressure taps were identical compared to the measurement performed by ČKD Blansko (see section 5.1.5 - fig. 5.59). For a proper $NPSH_3$ determination, a two-phase calculation (water / vapour) with Rayleigh-Plesset cavitation model with the value of a saturation pressure 3170 Pa (25 ^oC) [97] was utilized. The change of the pump head in $NPSH_3$ determination was inspected over the **6** whole revolutions of the pump turbine impeller.

Complete pump turbine model

As was mentioned, the basic pump turbine system consists of four main parts, namely: spiral case (volute) **(1)**, guide vanes (distributor) **(2)**, impeller **(3)** and draft tube **(4)** - fig. 5.6. The RANS and URANS simulations were performed only for the **pump mode**, which is simply described by the yellow arrows in fig. 5.6.
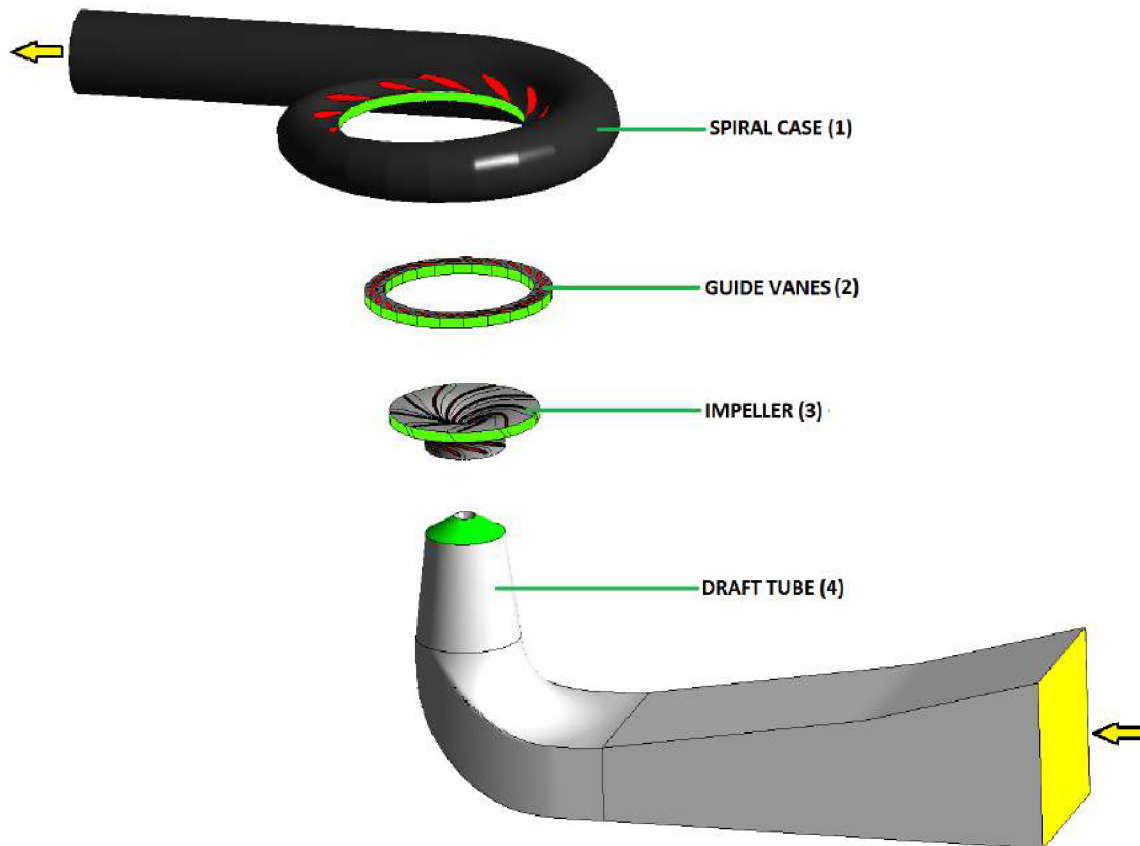

Fig. 5.6*: CFD model of the pump turbine.*

Following four subsections will describe each individual domain inside the complete pump turbine CFD model, with relevant boundary conditions and corresponding domain interfaces.

Spiral case (volute)

The spiral case (volute) belongs into a group of absolute computational domains. The tetrahedral mesh with the prismatic layers near the stationary walls was utilized for this domain. The spiral case includes the outlet boundary condition, which was portrayed by a yellow area (fig. 5.7) and characterized by the mass flow rate (tab. 5.4).
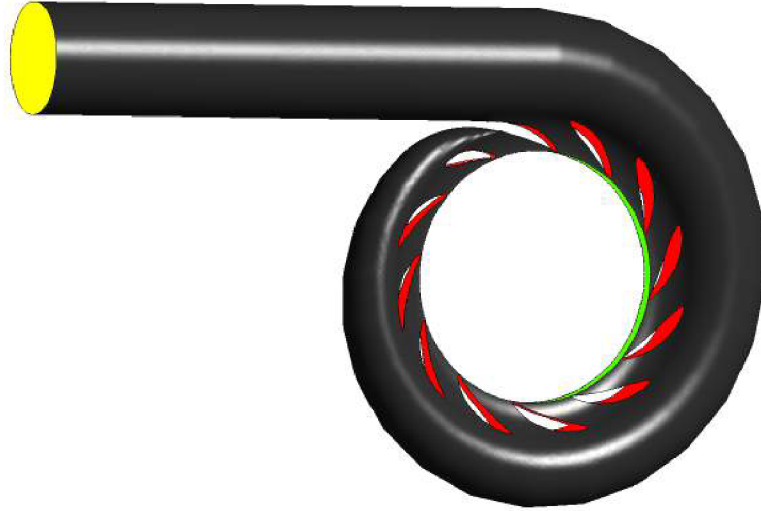

Fig. 5.7: *Model of the spiral case.*

The main performance characteristics were constructed from six operating points (**OP1 ÷ OP6**), the $NPSH_3$ curve was compiled from three operation points (**COP1 ÷ COP3**) - tab. 5.4. The mass flow rate Q_m $[kg/s]$ was computed from a selected value of the flow rate Q $[m^3/s]$ and a value of the water density, which was measured by ČBE and afterwards averaged for a purpose of CFD simulations ($\rho = 997.9407$ kg/m^3):

$$Q_m = \rho \cdot Q. \tag{5.1}$$

Tab. 5.4: *Values of the flow rate for simulated operation points (OP).*

	Flow rate Q $[m^3/s]$	**Mass flow rate** Q_m $[kg/s]$
OP1	0.05	49.897
OP2	0.1	99.794
OP3	0.15	149.691
COP1	0.155	154.681
OP4/**COP2**	0.181	180.627
COP3	0.195	194.598
OP5	0.2	199.588
OP6	0.25	249.458

Figure 5.7 also displays domain interface between the spiral case and the guide vanes (distributor) with a green area and also blades (stay vanes) as walls with red areas.

Guide vanes

As was mentioned, the main task of the guide vanes is to control the turbine. The CFD simulations were performed only for one fixed opening, which had value $a_0 = 20\ mm$.
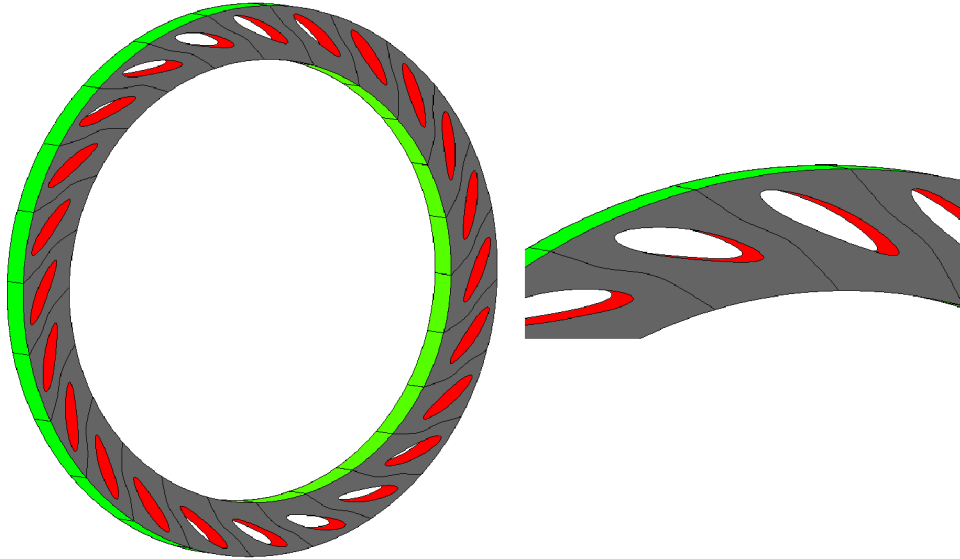

Fig. 5.8: *Model of the guide vanes.*

The guide vanes belong to the absolute computational domain, which has two interfaces towards to the spiral case (volute) and the impeller (green areas in fig. 5.8). The fixed blades of the distributor are portrayed by the red color.

Pump turbine impeller

All pump impeller designs (A, B, C) were utilized in the relative computational domain - fig. 5.9. The domain spins with the model RPM ($n = 1100\ 1/min$ - tab. 5.1) and has two domain interfaces (**transient rotor stator**) towards the guide vanes and the draft tube (once again portrayed with the green color).
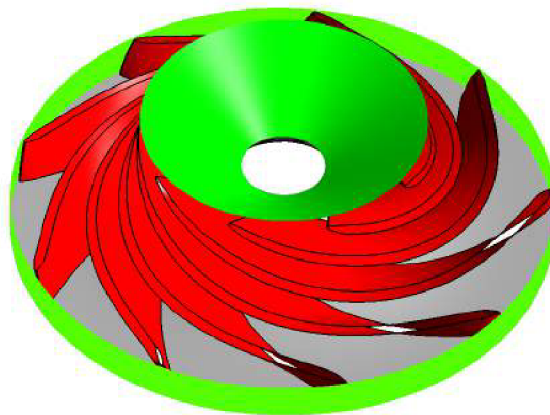
Fig. 5.9: *Pump turbine impeller.*

Draft tube

The draft tube (absolute domain) includes the inlet boundary condition portrayed by the zero static relative pressure (yellow area in fig. 5.10). This domain also contains the domain interface (green area) toward to the impeller and also small portion of the impeller hub, which rotated in the same direction and with same RPM as the impeller.
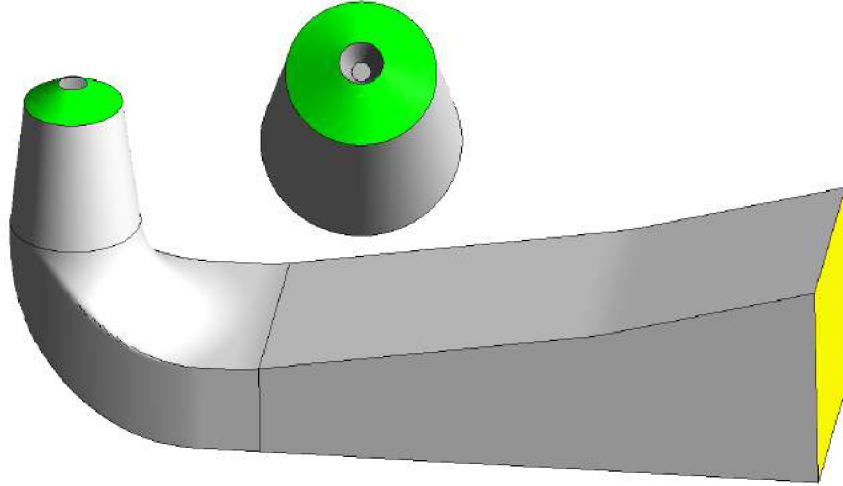

Fig. 5.10*: Draft tube model.*

It must be noted that for the $NPSH_3$ determination was **NOT** chosen the zero relative pressure as the inlet boundary condition. The static pressure always started at value **250000 Pa** and was slowly decreased towards the point of the crucial head change. Such high inlet pressure ensured cavitation-free start for the all examined operational points.

Wall y+ overview

For a proper and stable behaviour of the default $k - \epsilon$ model of turbulence and the numerical simulation in general in ANSYS CFX, it is recommended to have wall $y+ \; [-]$ in a range $30 < y+ < 300$. For this fact was constructed table 5.5 with wall $y+ \; [-]$ overview of every computational domain in the optimal flow rate $Q = 0.181 \; m^3/s$.

Tab.*5.5**: Wall y+ overview.*

	Area-average value of $y+ \; [-]$
Draft tube	≈ 46
Impeller Design A	≈ 79
Impeller Design B	≈ 84
Impeller Design C	≈ 83
Guide vanes	≈ 11
Spiral case (volute)	≈ 48

5.1.4 Impeller designs

5.1.5.1 Design A

This design (let's call it the **design A**) differs from the rest of the optimized designs in two crucial things: it was made by the early stage of the presented optimization software and utilized input from an another in-house optimization software based on the quasi-potential flow [75], [89]. Such input set a fixed shape of the meridional flow channel and laid a foundation for a characteristic form of the β angles along the length of the blade (fig. 5.20). The β angle was parametrized on the three streamlines (near the hub, shroud and on the middle streamline) in six different locations $\Rightarrow$ **18** modified parameters. The maximal β angle change was set in each location to the value 2.5^o.

Early stage of the optimization procedure utilized PSOA (with five particles) and its Global Best modification. The Pareto principles were **NOT** used and each design was evaluated according a simple rule $\Rightarrow$ a task of the **minimization** of following equation:

$$f = weight_1 \cdot |1 - \frac{H_{CFD}}{H}| + weight_2 \cdot |1 - \eta_{H,CFD}|, \tag{5.2}$$

where $weight_1$ $weight_2$ $[-]$ are optimization weights (with chosen value $= 1$), H $[m]$ is the requested pump head, H_{CFD} $[m]$ is the current pump head from the CFD simulation and $\eta_{H,CFD}$ $[-]$ is the current hydraulic efficiency from the CFD simulation.

Design A was optimized as the single periodical flow channel with the frozen rotor interfaces between relative and absolute domains. It must be also mentioned that the impeller was set into the whole computational domain of the pump turbine - with the spiral case (fig. 5.7), draft tube (fig. 5.10) and guide vanes (fig. 5.8). The shape optimization was stopped by the user after six iterations - swarm grouped in a very close non-moving area (fig. 5.11).
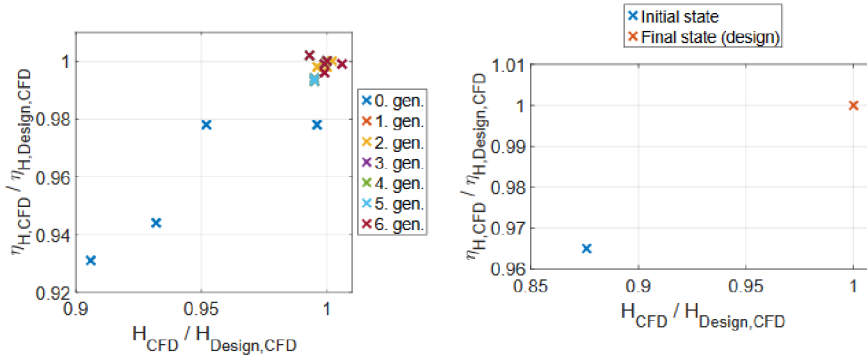

Fig. 5.11: *Swarm behaviour and result difference between used methods* [75], [92].

Fig. 5.11-left also shows a progressive movement of PSOA particles towards some best solution, fig. 5.11-right compares hydraulic qualities of the in-house software based on the quasi-potential flow (input or initial design) and a final state accomplished by the PSOA. It must be noted that this design was as the only one manufactured and also measured by ČKD Blansko Engineering (section 5.1.5).

Impeller properties

Following table shows the hydraulic efficiencies and the β angles of the design A compared to the quasi-empirical methods vividly described in section 3. Mentioned efficiencies are linked only to the impeller, so without the draft tube, spiral case and distributor. The β angles were evaluated only on the **middle streamline**.

Tab. 5.6: *Computed pump turbine parameters - design A.*

	Design	1. method	2. method	3. method	4. method
Hydr. efficiency η_H [%]	93.7907	89.506 [74]	90.950 [72]	88.954 [71]	92.925 [26]
Inlet angle β_1 [^{o}]	29.67	18 [71]	21 [90]	14 [26]	-
Outlet angle β_2 [^{o}]	43.64	26 [27]	25 [71]	38 [26]	-

The best estimation of the hyd. efficiency of the pump impeller shows Gülich's approach [26] (tab. 5.6). When comparing β_2 of the design A and results from the quasi-empirical equations, once again the Gülich's estimation [26] shows the most convenient match. The angle β_1 of the design A extremely differs from all 1D computational approaches.
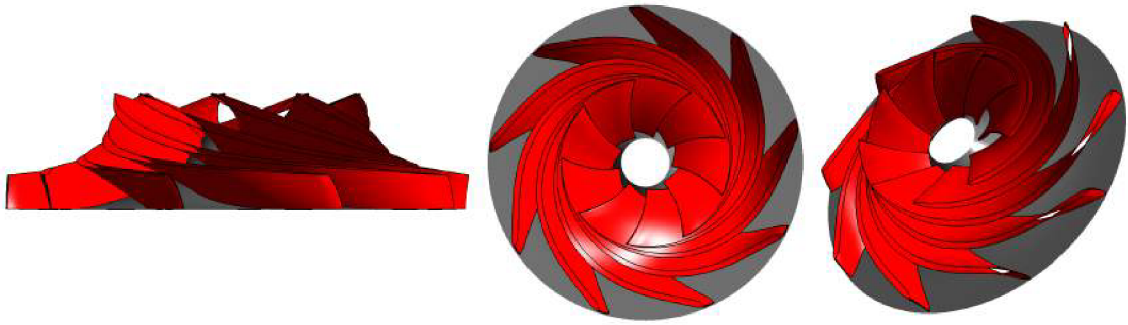
Fig. 5.12: *Impeller - design A.*

The basic shape of the design A is described by fig. 5.12 in three different views. Such design is remarkable by its high values of the outlet angle β_2 and blades with a "lying" shape - fig. 5.13 (mainly thanks to a β angle behaviour along the length of the blade - fig. 5.20).
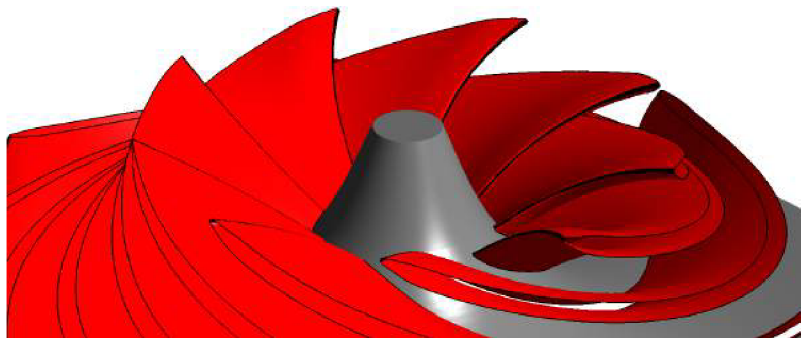

Fig. 5.13: *Impeller - design A - leading edge detail.*

Pump characteristics

Figures 5.14, 5.16 and 5.17 show comparison between the ČBE measurement (black color, see section 5.1.5) and the CFD simulations (red color). All requested values of the pump head (tab. 5.7) are coloured green and are defined by following table.

Tab. 5.7: *All requested head values (RHV) for the pump turbine model.*

	Flow rate Q $[m^3/s]$	Head H $[m]$
RHV1	0.168	35.97
RHV2	0.181	34.77
RHV3	0.194	33.57

The comparison was done for one selected guide vane opening $a_0 = 20\ mm$ (fig. 5.14). The pump head is well predicted around the requested head values, but for the flow rate $Q = 0.1\ m^3/s$ a large underestimation is observed. Focusing on a point defined by flow rate $Q = 0.05\ m^3/s$ - a large overestimation is noticeable. It must be noted that the head values acquired from the CFD simulations are without disk friction and volumetric losses → this fact is mentioned by "without losses"in fig. 5.14
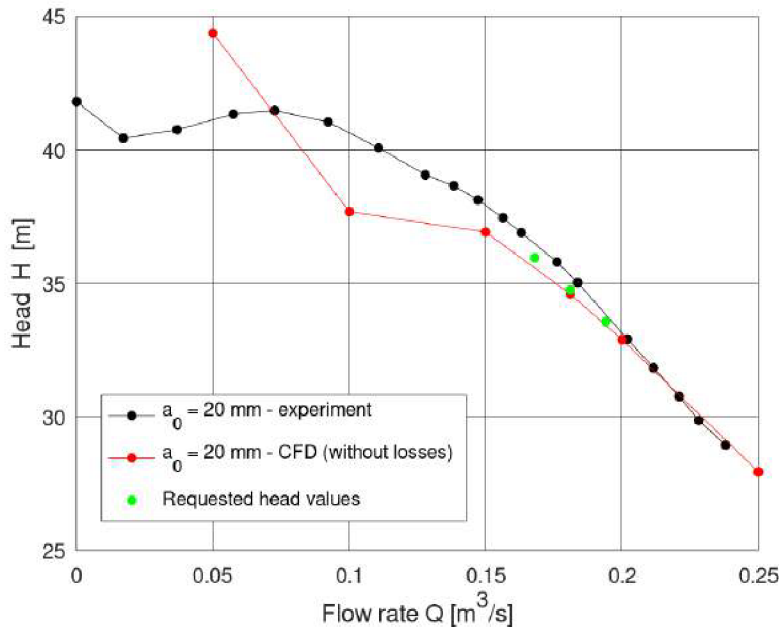
Fig. 5.14: *H − Q characteristics: design A.*

The head underestimation/overestimation phenomena might be caused by a very complex flow in the non-optimal flow regimes. For the flow rate $Q = 0.05\ m^3/s$ an extremely swirling flow (fig. 5.15) could be found in the whole computational domain. It must be noted that such complex flow is hard to capture and to simulate with the two equation turbulence model so another model could be used.
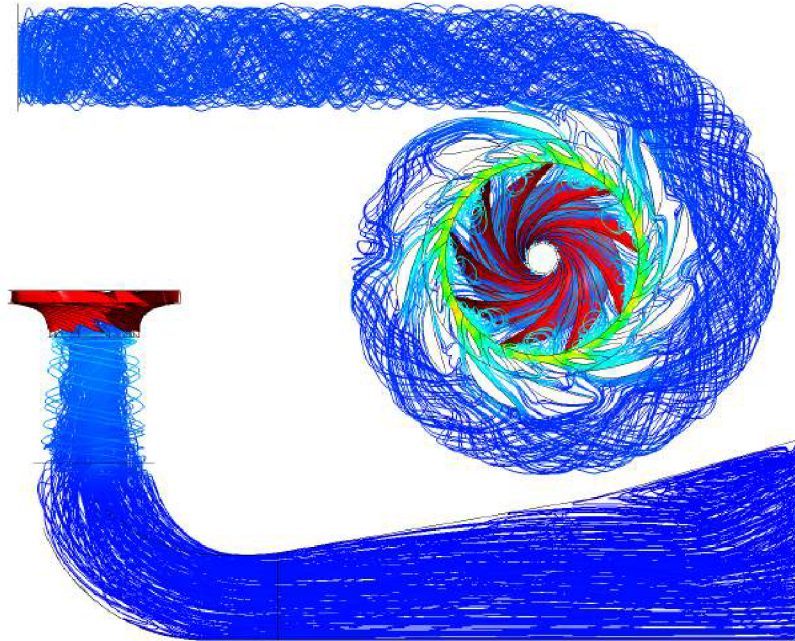
Fig. 5.15: *Streamlines $Q = 0.05 \ m^3/s$: design A.*

The pump efficiency (fig. 5.16) is predicted well in almost all points, where CFD simulations were performed. The only exception was a point defined by the flow rate $Q = 0.05 \ m^3/s$, in which the value from the numerical simulation was underestimated compared to the ČBE measurement. Once again, the efficiency values are NOT including the disk and volumetric losses.
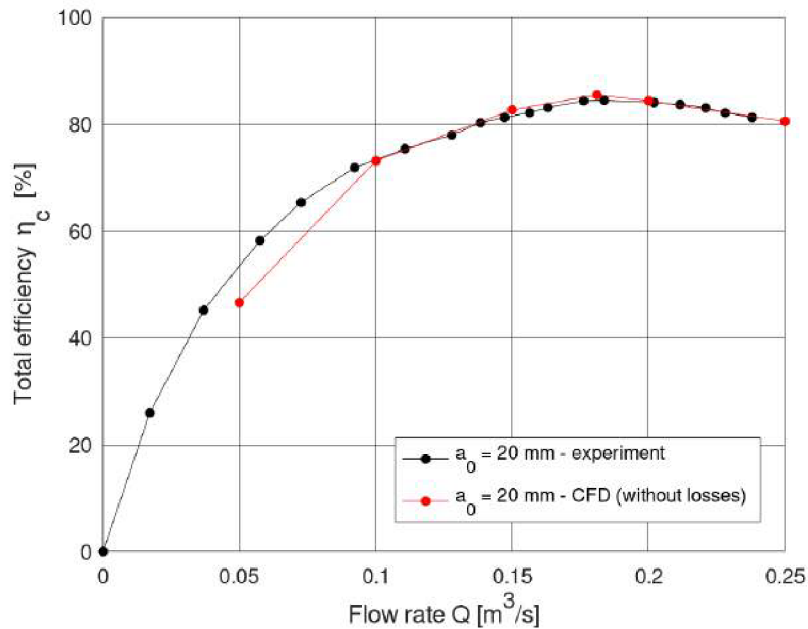

Fig. 5.16: *$\eta_c - Q$ characteristics: design A.*

The last pump characteristic is dependency of the critical net positive suction head $NPSH_3 \ [m]$ on the flow rate $Q \ [m^3/s]$ (fig. 5.17).

89
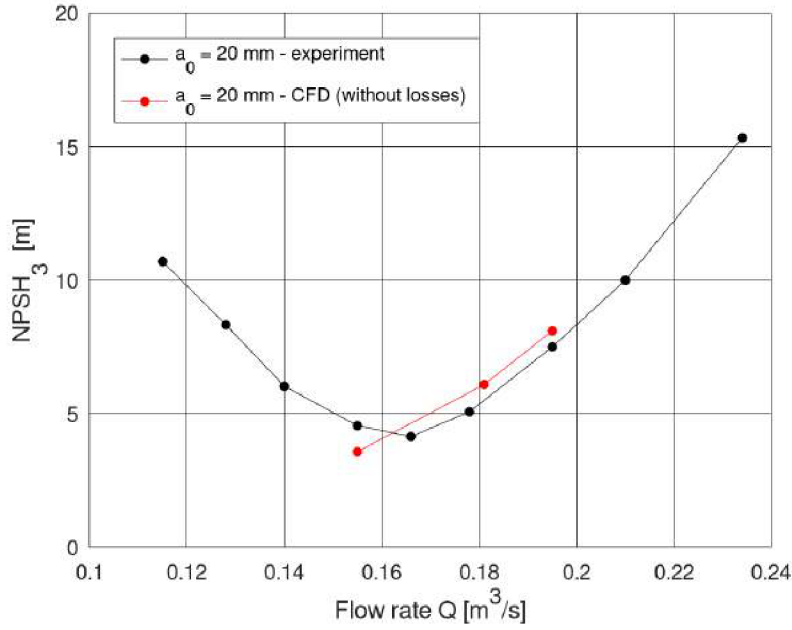
Fig. 5.17: $NPSH_3 - Q$ *characteristics: design A.*

The $NPSH_3$ curve (fig. 5.17), which is based on the two-phase numerical simulations, is evaluated identically as in the ČBE measurement - the static pressure on the domain's inlet is slowly decreased in time and a change of the pump head H [m] under 97 % its value is investigated. From an intersection of the blue and red curve (fig. 5.18), the critical value of the inlet pressure is found and afterwards $NPSH_3$ is calculated.
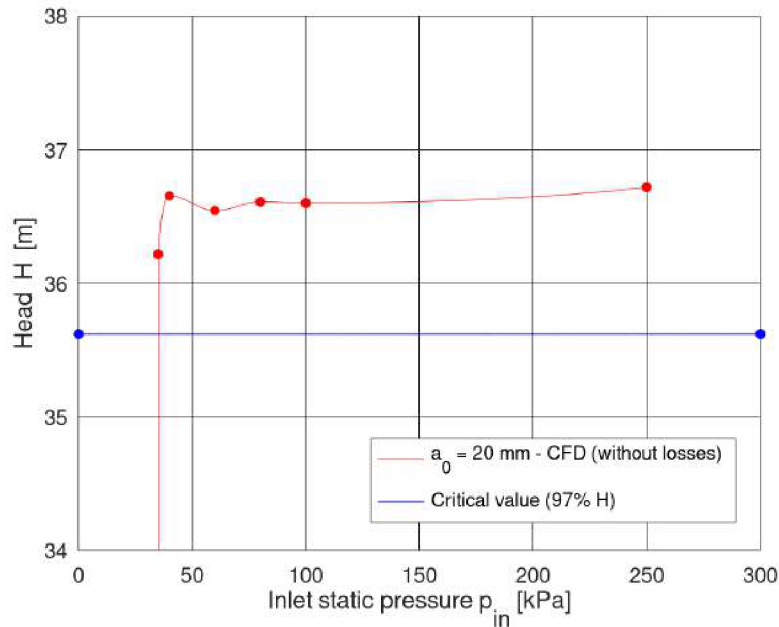

Fig. 5.18: $H - p_{in}$ *dependency for flow rate* $Q = 0.155 \ m^3/s$: *design A.*

It must be noted that figures 5.14, 5.16 5.17 compared the values from the measurement (black color) and from the CFD simulations (red color), where the volumetric losses and the disc friction losses are not included. Such losses lower the magnitudes of the observed variables and could be roughly estimated by the empirical equations found e.g. in [26] ([61]) or by including additional flow domains into the numerical simulations, which unfortunately leads to a significant increase of the computational time.
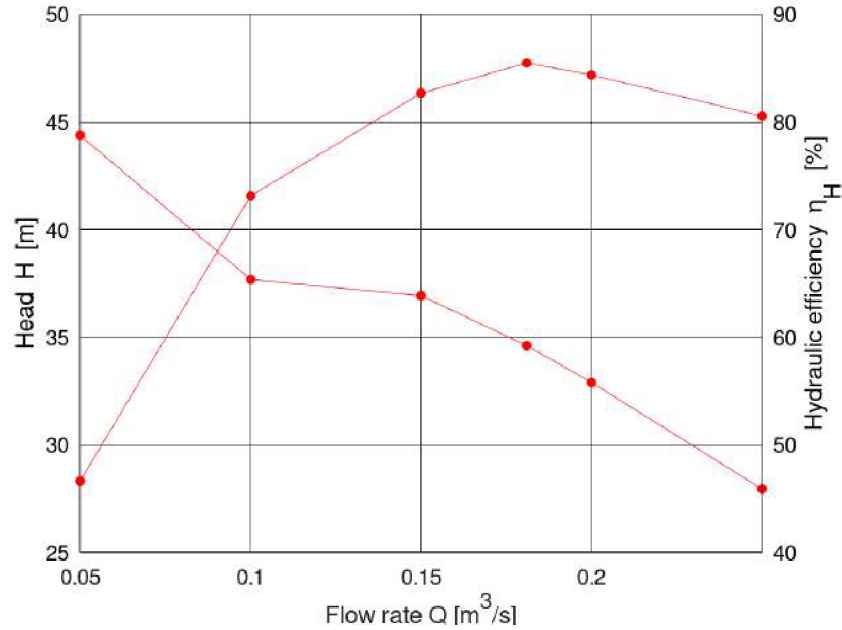

Fig. 5.19: $\eta_H - Q$ *and* $H - Q$ *characteristics: design A.*

Design A must be examined also from the highest hydraulic efficiency point of view. Such efficiency must be located in the design point (in the point, in which the shape optimization was performed) - in this case is the point characterized by flow rate $Q = 0.181 \ m^3/s$. Design A successfully achieved the highest efficiency in mentioned design point prerequisite.
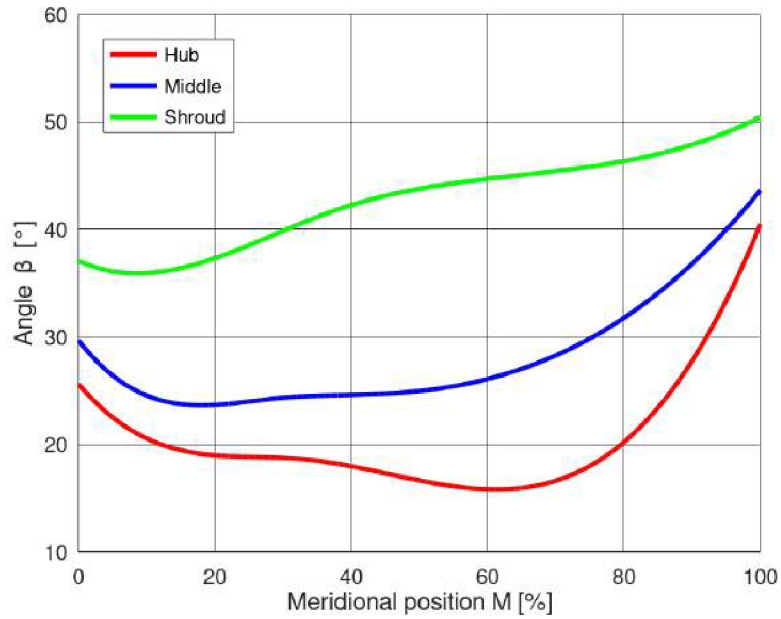
Pressure and velocity distributions inside the impeller

Fig. 5.20: *Angle β - design A.*

The β angle behaviour of the design A (fig. 5.20) results in the inverse static pressure distribution on the blade near the leading edge - the suction side of the blade has higher static pressure than the pressure side (fig. 5.21).
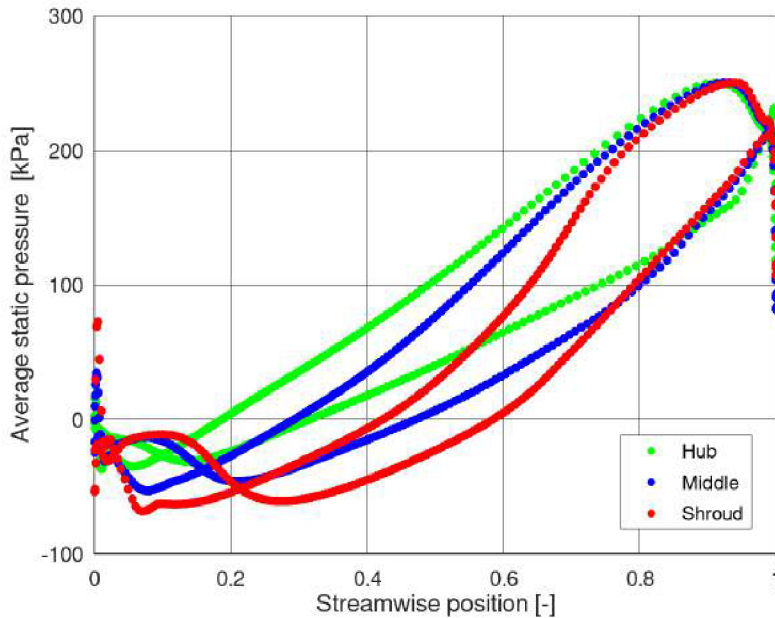

Fig. 5.21: *Blade loading - optimal Q.*

Let's inspect an average static pressure and average velocity distribution of the design A in the meridional and a blade-to-blade point of view. Starting with the meridional point of view: the optimized design A manifests with the higher velocity values in a middle section of the pump shroud, which caused significant pressure drop in such observable area (fig. 5.22).
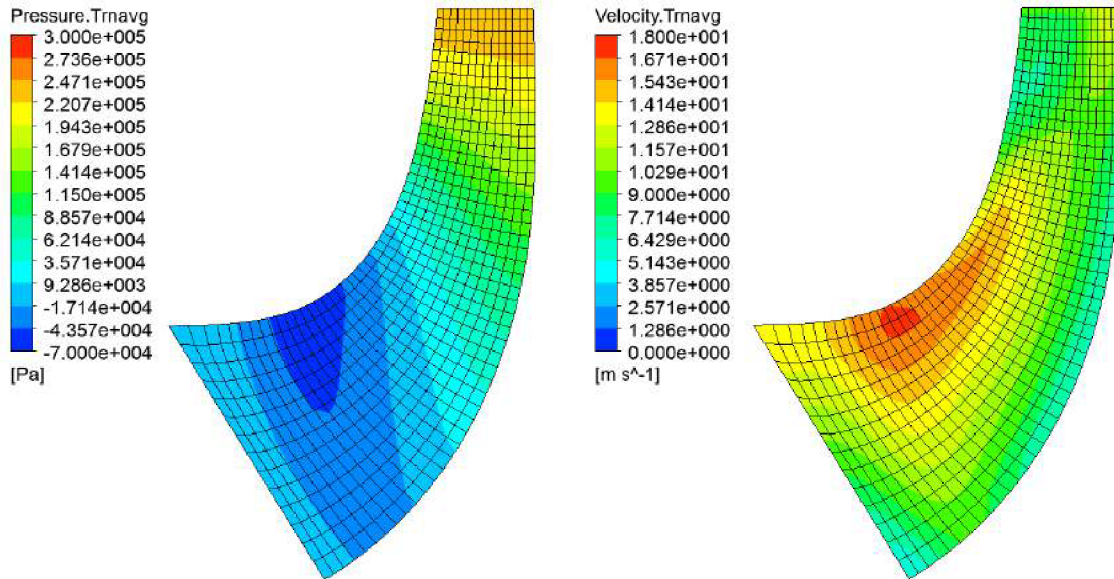

Fig. 5.22: *Average static pressure and velocity distribution - optimal Q.*

Following figure (fig. 5.23) displays the static pressure distribution in the blade-to-blade view in three locations of presented design A - near the hub, in the middle of the impeller and near the shroud. The inlet part of the suction sides of the blades experiences a high pressure drop. It is noticeable primarily near the shroud of the impeller, this fact is captured by a dark blue color in fig. 5.23. Sudden pressure drop is very dangerous and could lead to the creation of cavitation bubbles, if the static pressure reaches its critical value.
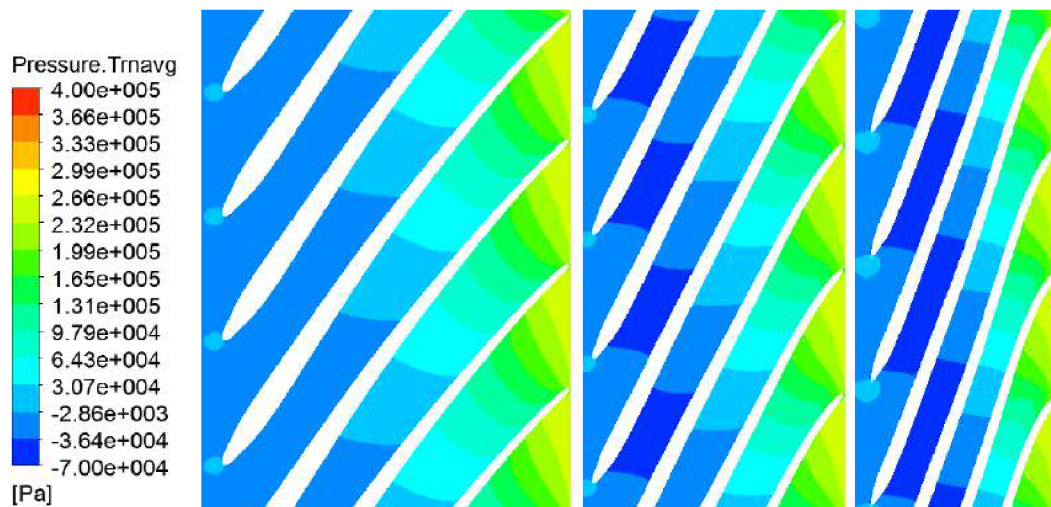

Fig. 5.23: *Average static pressure distribution (hub, middle, shroud) - optimal Q.*

An important part of the flow examination of each design is an investigation of the correct fluid flow at the blade's leading edge $\rightarrow$ **shockless fluid entry**. For this purpose are created and drawn velocity vectors in a blade-to-blade view in three main locations - near the hub (fig. 5.24), in the middle of the impeller (fig. 5.25) and near the shroud (fig. 5.26). It must be noted that the velocity vectors could also reveal possible fluid recirculation, which leads to the head and efficiency decrease.
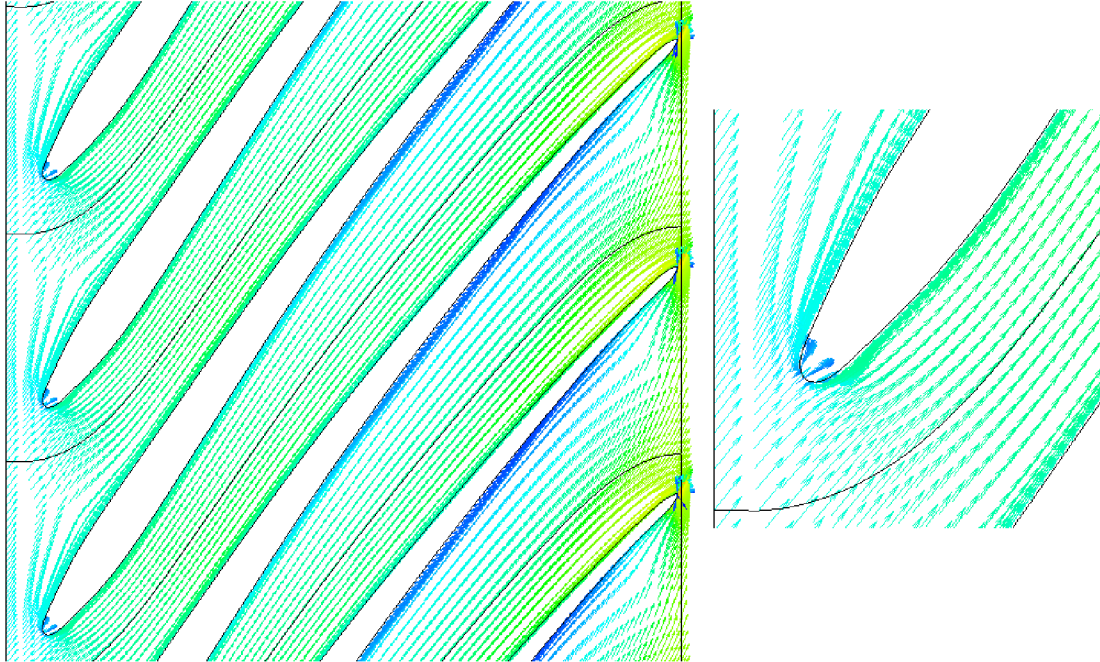

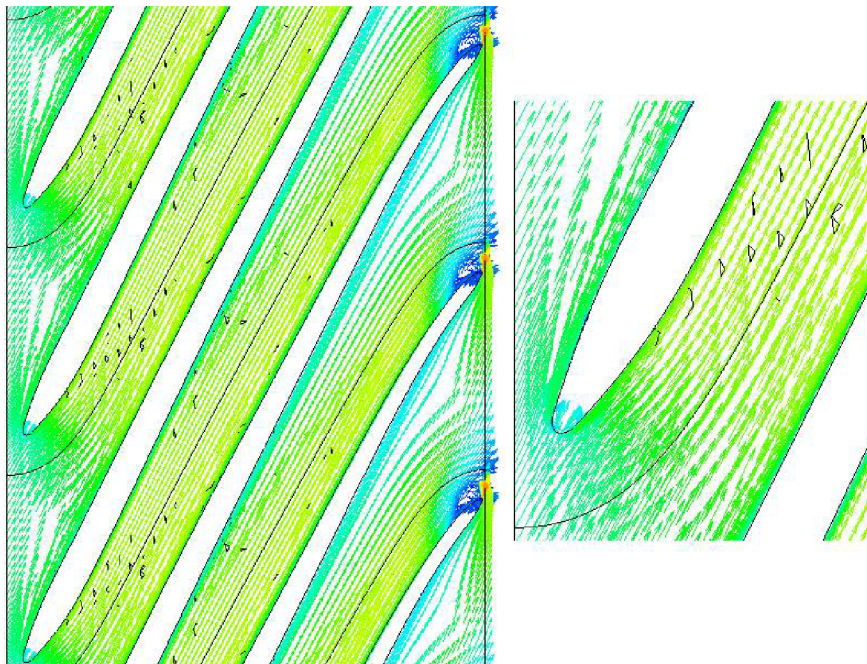**Fig. 5.24**: *Average velocity vectors near leading edge (hub) - optimal Q.*

Fig. 5.25: *Average velocity vectors near leading edge (middle) - optimal Q.*
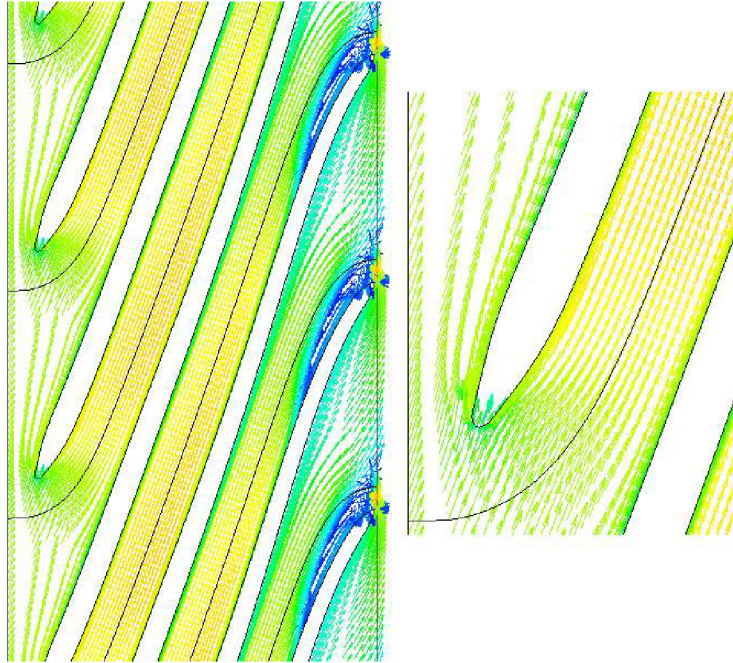
Fig. 5.26: *Average velocity vectors near leading edge (shroud) - optimal Q.*

Blue vectors (fig. 5.25, 5.26, which are located near the trailing edge of the blade, indicate certain areas with the fluid recirculation caused by the specific shape of the blade - the blades of the design A are strongly deformed in the outlet area towards the shroud, mainly for a proper achievement of the pump head. The sudden shape change of the blades creates the flow separation, which is described in sec. 3.3.
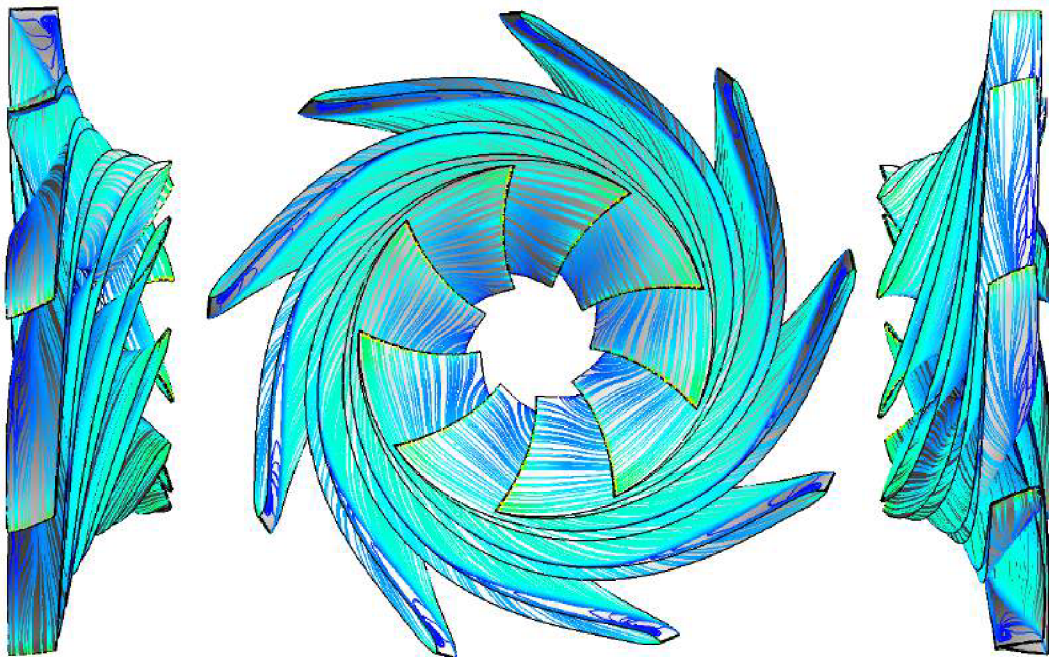
Surface streamlines
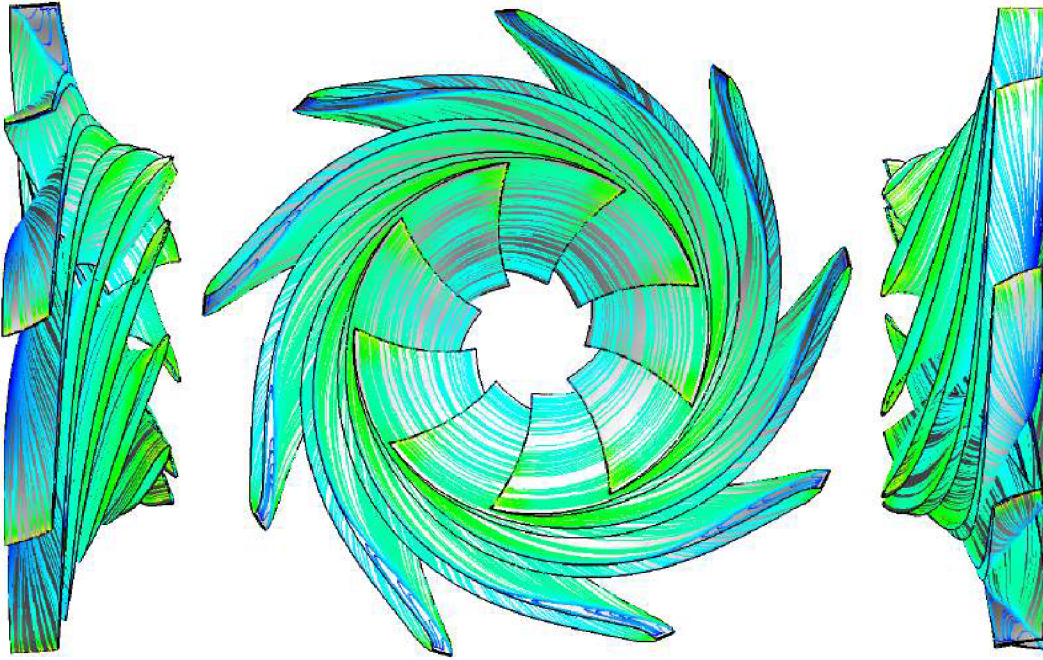

Fig. 5.27: *Surface streamlines - $Q = 0.1 \ m^3/s$.*

Fig. 5.28: *Surface streamlines -* $Q = 0.181 \ m^3/s$ *(optimal flow rate).*
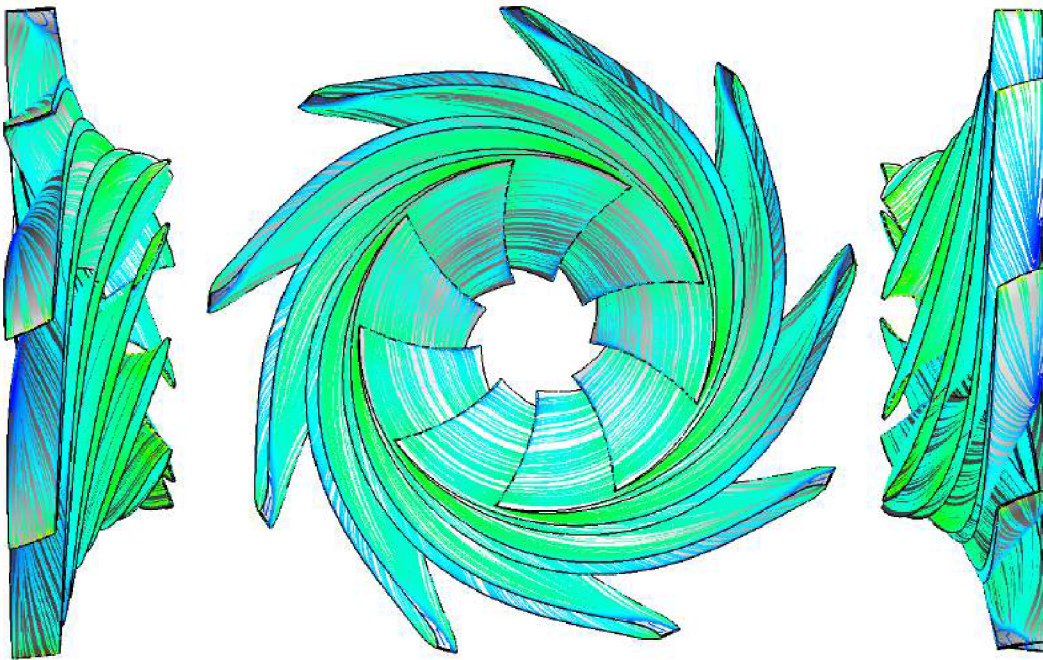
Fig. 5.29: *Surface streamlines -* $Q = 0.25 \ m^3/s$.

Figures 5.27-5.29 capture the fluid behaviour on the blades of the design A in three flow regimes - in $Q = 0.1 \ m^3/s$, $Q = 0.181 \ m^3/s$ (optimum) and $Q = 0.25 \ m^3/s$. Figure 5.28 confirms recirculation passages near the shroud at blade's outlet, which were uncovered by the velocity vectors in figures 5.25 and 5.26. As it was mentioned, the fluid recirculation decreases the values of the hydraulic efficiency and the pump head, so such phenomenon must be suppressed as much as possible in the shape optimization process.

5.1.5.2 Design B
Impeller properties

Table 5.8 shows the hydraulic efficiencies and the β angles of the design B compared to the quasi-empirical methods described in section 3. Mentioned efficiencies are linked only to the pump turbine impeller, so without the draft tube, spiral case and distributor. The β angles were evaluated only on the middle streamline.

Tab. 5.8: *Computed pump turbine parameters - design B.*

	Design	1. method	2. method	3. method	4. method
Hydr. efficiency η_H [%]	94.9468	89.506 [74]	90.950 [72]	88.954 [71]	92.925 [26]
Inlet angle β_1 [^{o}]	20.35	18 [71]	21 [90]	14 [26]	-
Outlet angle β_2 [^{o}]	56.66	26 [27]	25 [71]	38 [26]	-

The best estimation of the hydraulic efficiency of the pump turbine impeller shows Gülich's approach [26] (table 5.8). When comparing β_2 of the design B and the results from the quasi-empirical equations, once again Gülich estimation [26] shows the most convenient match. The angle β_1 of the design B was estimated as best by the method found in [90].
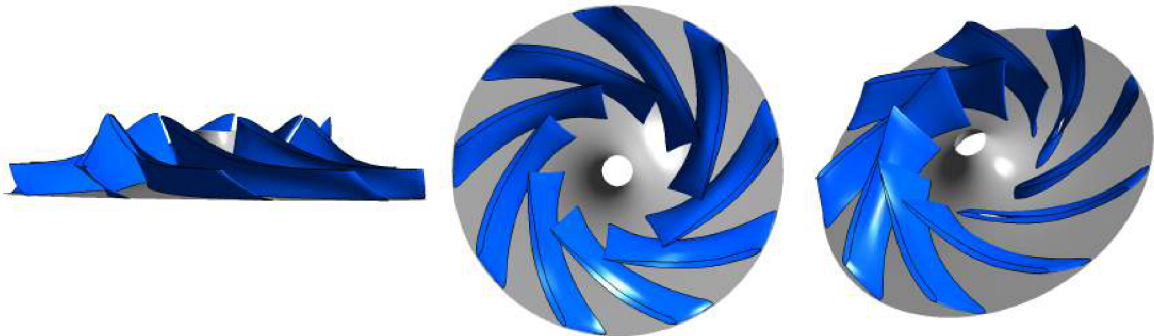

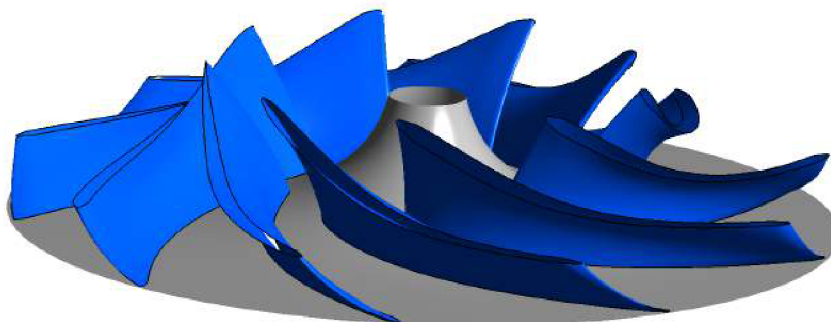
Fig. 5.30: *Impeller - design B.*

Fig. 5.31: *Impeller - detail of design B.*

Design B is geometrically characteristic for its short blades (see fig. 5.30) and highly sloped trailing edge, which has a slight curvature (fig. 5.31).

Pump characteristics

The highest hydraulic efficiency point of the design B is subtly offset towards the higher values of the flow rate (fig. 5.32). Interesting fact of this design is that it misses the huge head overestimation in the point $Q = 0.05 \ m^3/s$ (fig. 5.32, 5.33) compared to the design A or C. Once again, the values of the pump head and the efficiency are not affected by the volumetric and the disk friction losses.
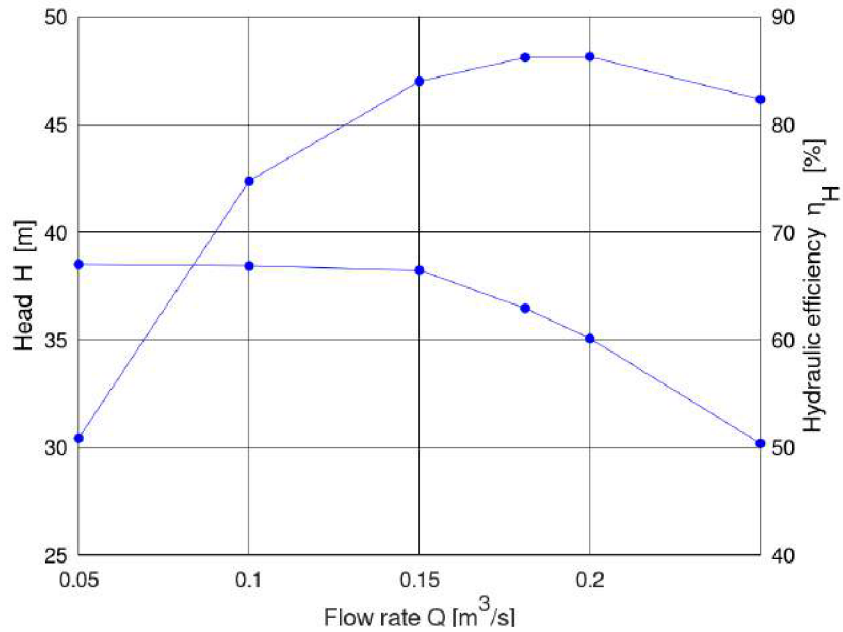
Fig. 5.32: $\eta_H - Q$ and $H - Q$ characteristics: design B.
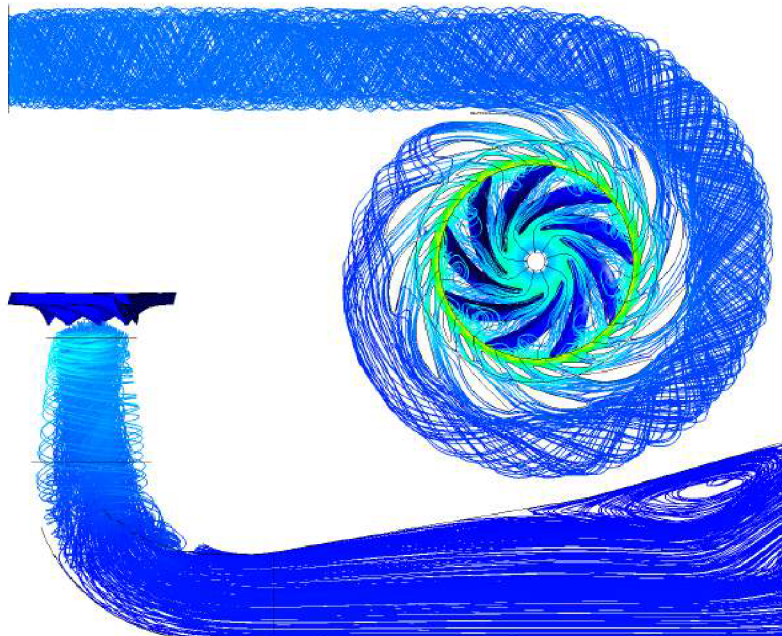
Fig. 5.33: Streamlines $Q = 0.05 \ m^3/s$: design B.

Pressure and velocity distributions inside the impeller

The Design B investigated the pure linear development of the β angles along the length of the blades (fig. 5.34).
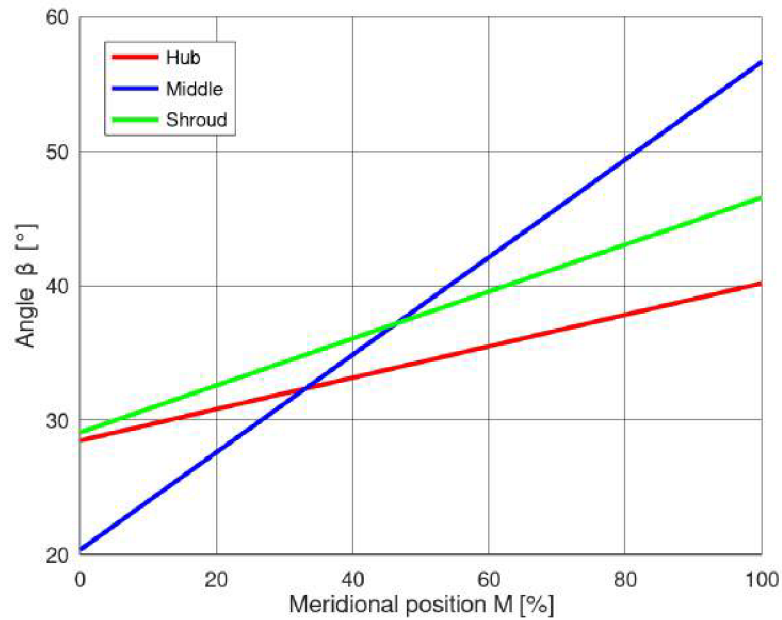
Fig. 5.34: *Angle β - design B.*

The β angle behaviour results in the "normal" pressure distribution on the pump blades. The suction side has lower values than the pressure side (fig. 5.35).
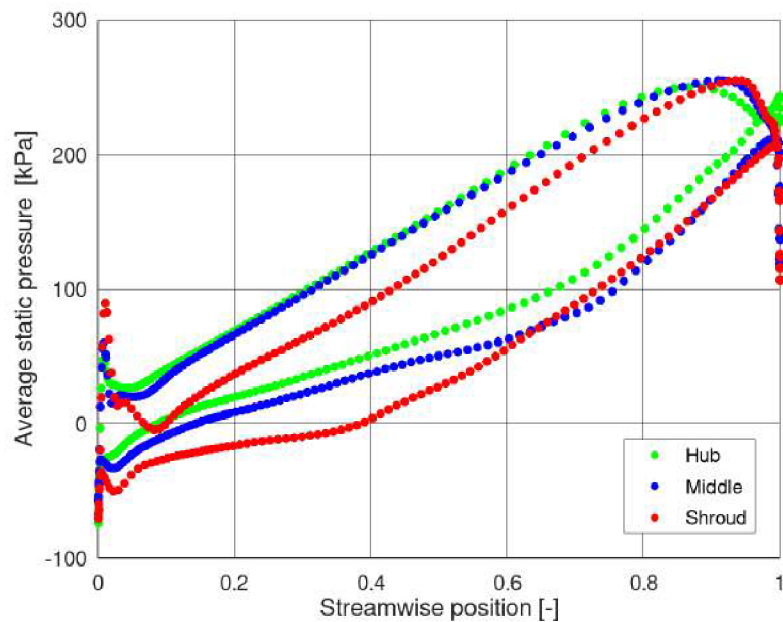
Fig. 5.35: *Blade loading - optimal Q.*

99

Focusing on the meridional point of view: the optimized design B presents with the slightly higher averaged velocity values in inlet section near the pump shroud and lower averaged velocity values near the pump hub (fig. 5.36). The average static pressure change is remarkable by a gradual transition from the low values of the pressure (impeller inlet) to the higher values, which are located at the impeller outlet - fig. 5.36.
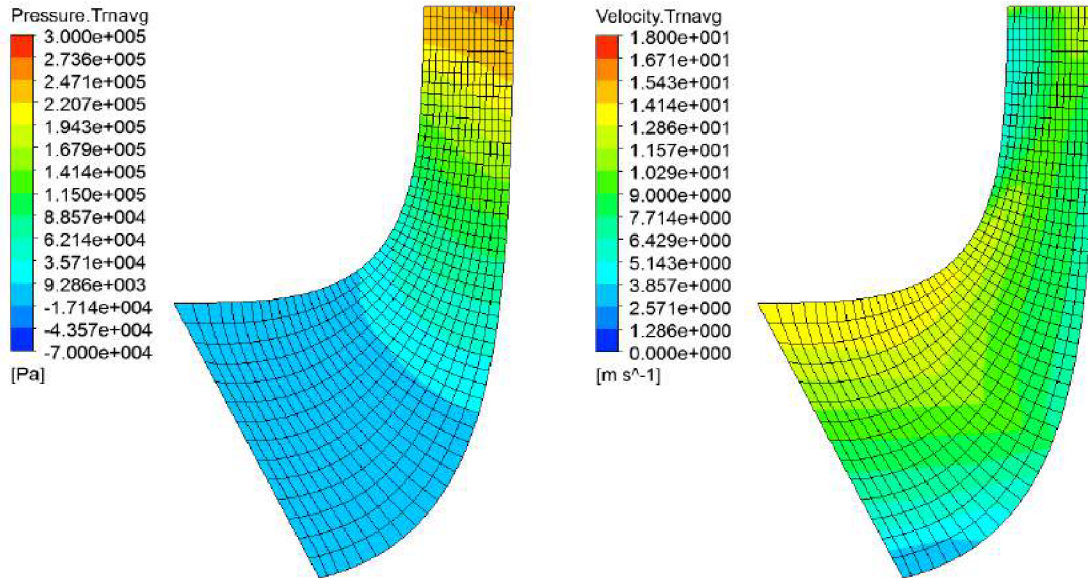
Fig. 5.36: *Average static pressure and velocity distribution - optimal Q.*

Following figure (fig. 5.37) displays the average static pressure distribution in the blade-to-blade point of view in the three main locations of the design B - near the hub, in the middle of the pump turbine impeller and near the shroud. A critical place of this design is located near the shroud on the suction side of the blade (at the beginning) - there is a small low pressure spot (dark blue color in fig. 5.37). Such sudden pressure drop is very dangerous and could lead to the creation and afterwards the manifestation of the cavitation bubbles, if the static pressure reaches its critical value.
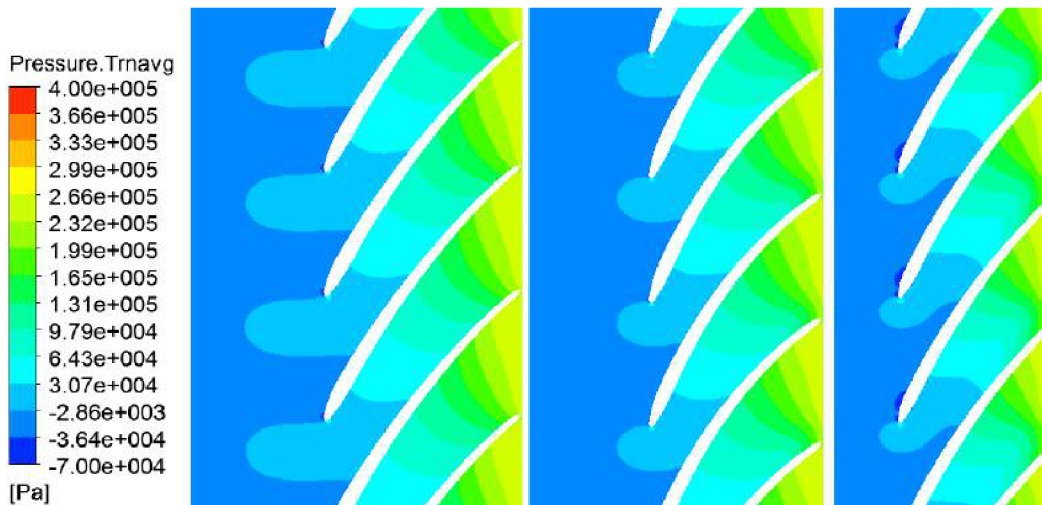
Fig. 5.37: *Average static pressure distribution (hub, middle, shroud) - optimal Q.*

Next figures examine the correct water flow inside the design B impeller, namely near the hub (fig. 5.38), in the middle of the impeller (fig. 5.39) and near the shroud (fig. 5.40).
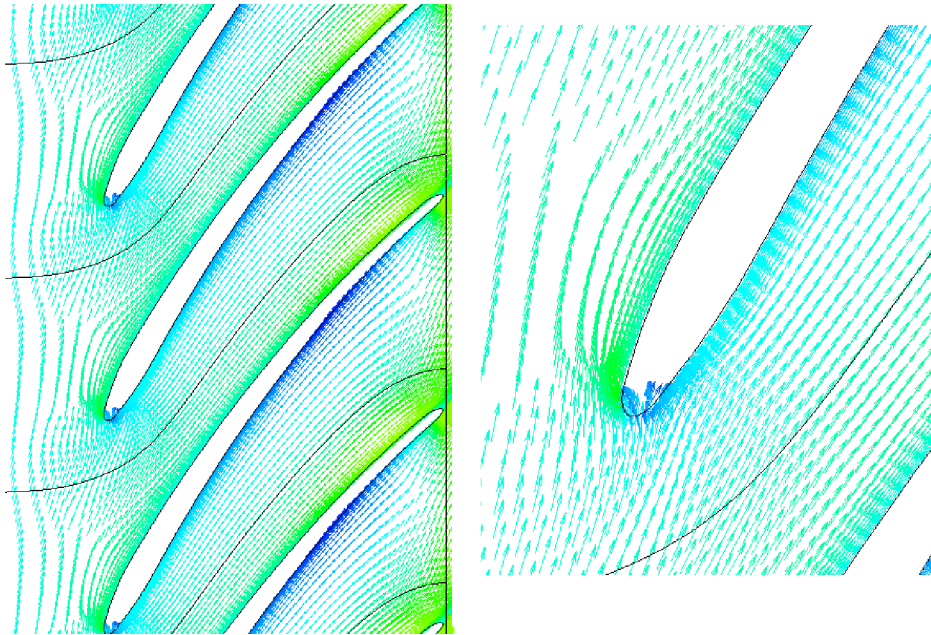
Fig. 5.38: *Average velocity vectors near leading edge (hub) - optimal Q.*

The velocity vectors around the blade tip at the impeller's hub shows a massive fluid shock - fig. 5.38 (detail look). Such water shock leads to the unsuitable flow patterns along the length of the blade - hand in hand with the pump turbine head and efficiency decrease. The velocity vectors in the middle section of the pump turbine impeller (fig. 5.39) reveal starting fluid recirculation in the end of the blade at its suction side.
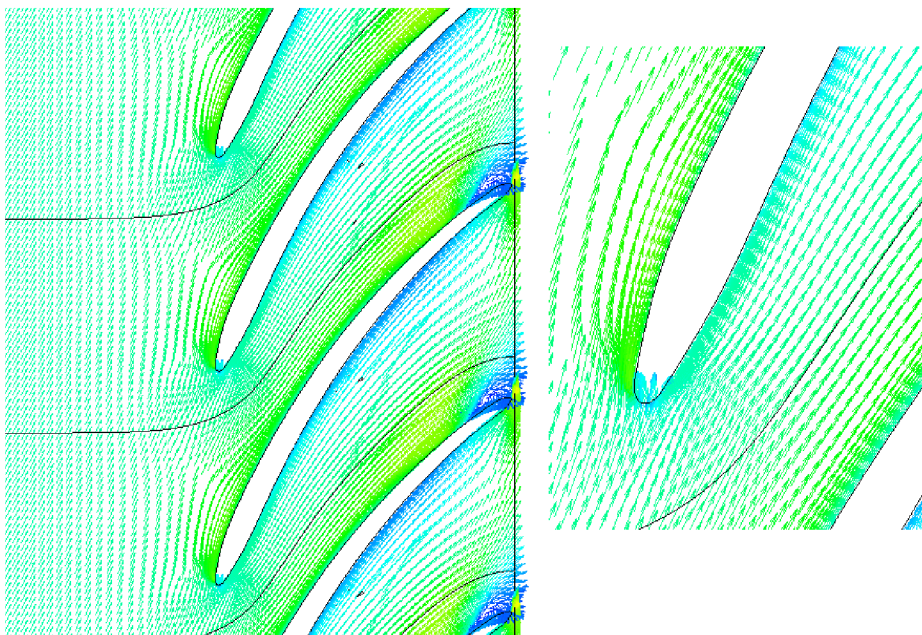
Fig. 5.39: *Average velocity vectors near leading edge (middle) - optimal Q.*

Fig. 5.40 displays continuing water recirculation in the end of the blade at the suction side. Such recirculation occupies and blocks larger area than in the middle section (fig. 5.39). From the perspective of the shockless fluid entry - middle section shows signs of the mild water shock at blade's tip, on the other hand water in the shroud section is remarkable for its flawless entry.
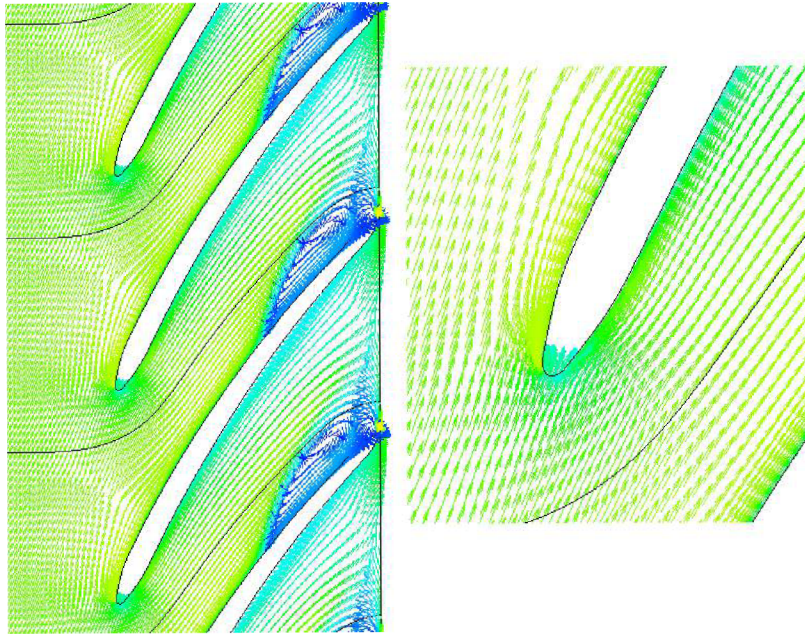
Fig. 5.40: *Average velocity vectors near leading edge (shroud) - optimal Q.*

Surface streamlines
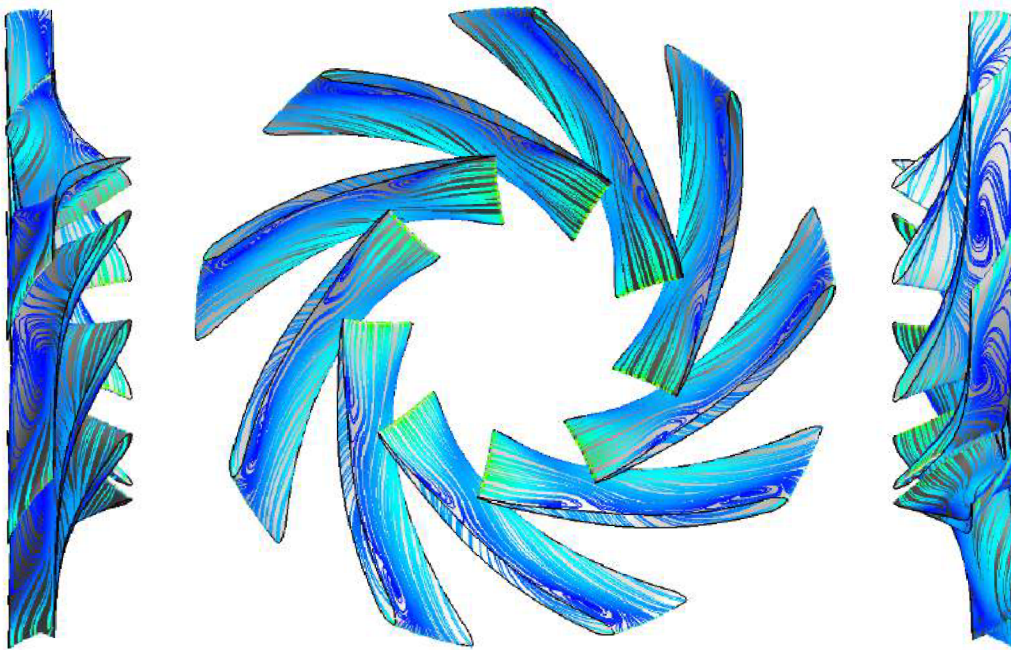
Fig. 5.41: *Surface streamlines - Q = 0.1 m³/s.*
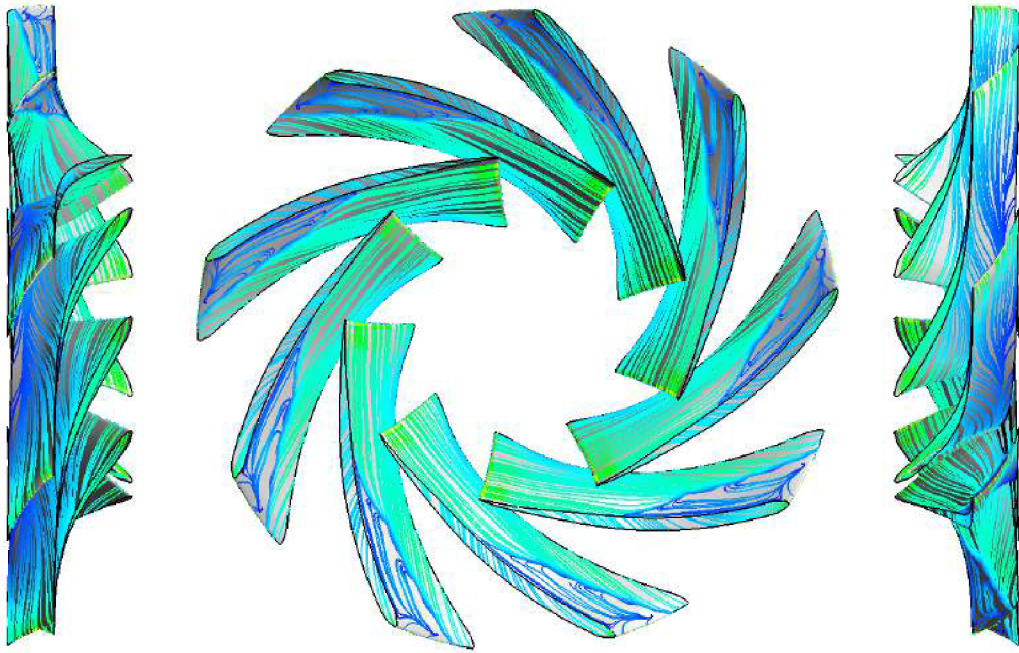
Fig. 5.42: *Surface streamlines - Q = 0.181 m^3/s (optimal flow rate).*
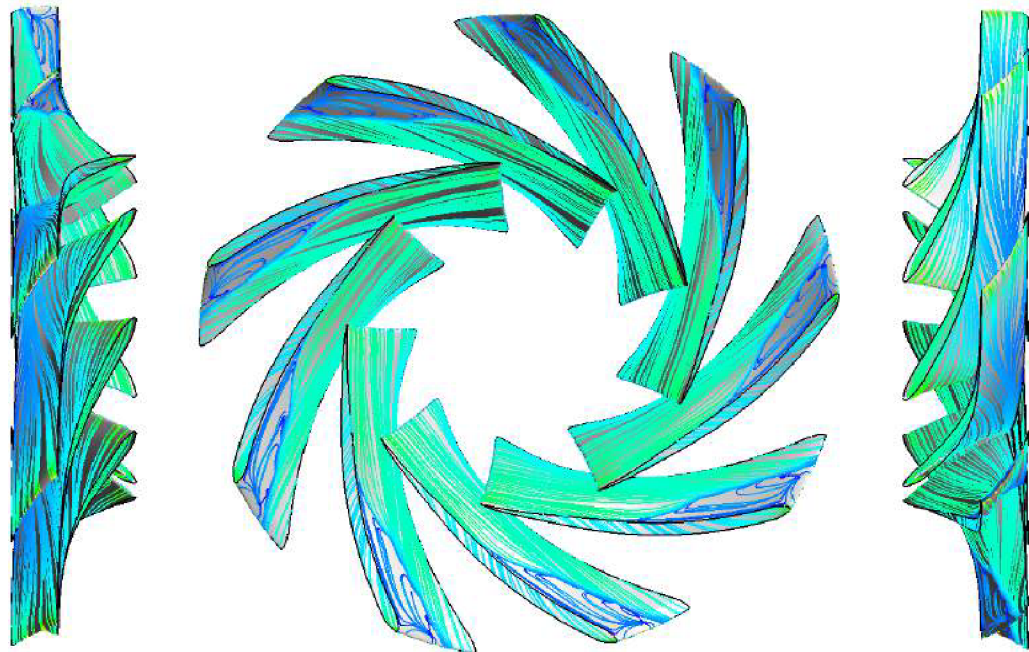
Fig. 5.43: *Surface streamlines - Q = 0.25 m^3/s.*

Figures 5.41-5.43 capture the fluid behaviour on the blades of the optimized design B in three chosen flow regimes - in $Q = 0.1\ m^3/s$, $Q = 0.181\ m^3/s$ (optimum) and $Q = 0.25\ m^3/s$. Figure 5.42 confirms recirculation passages near the shroud at blade's outlet, which was uncovered by the velocity vectors in figures 5.39 and 5.40. Such recirculation also propagates itself into the higher (fig. 5.43) and lower (fig. 5.41) values of the flow rate. This phenomenon is probably caused by the insufficient length of the blade, which goes hand in hand with the inadequate water guiding inside the pump impeller.

5.1.5.3 Design C

Table 5.9 shows the hydraulic efficiencies and the β angles of the design C (fig. 5.44) compared to the quasi-empirical methods described in section 3. Mentioned efficiencies are linked only to the pump turbine impeller, so without the draft tube, spiral case and distributor. The β angles were evaluated only on the middle streamline.

Tab. 5.9: *Computed pump turbine parameters - design C.*

	Design	1. method	2. method	3. method	4. method
Hydr. efficiency η_H [%]	96.859	89.506 [74]	90.950 [72]	88.954 [71]	92.925 [26]
Inlet angle β_1 [^{o}]	37.5	18 [71]	21 [90]	14 [26]	-
Outlet angle β_2 [^{o}]	42.83	26 [27]	25 [71]	38 [26]	-

The best estimation of the hyd. efficiency shows Gülich's approach [26] (tab. 5.9). When comparing β_2 of the design C and the results from the quasi-empirical equations, once again Gülich's estimation [26] shows the most convenient match. The angle β_1 of the design C extremely differs from all 1D computational approaches found in sec. 3.
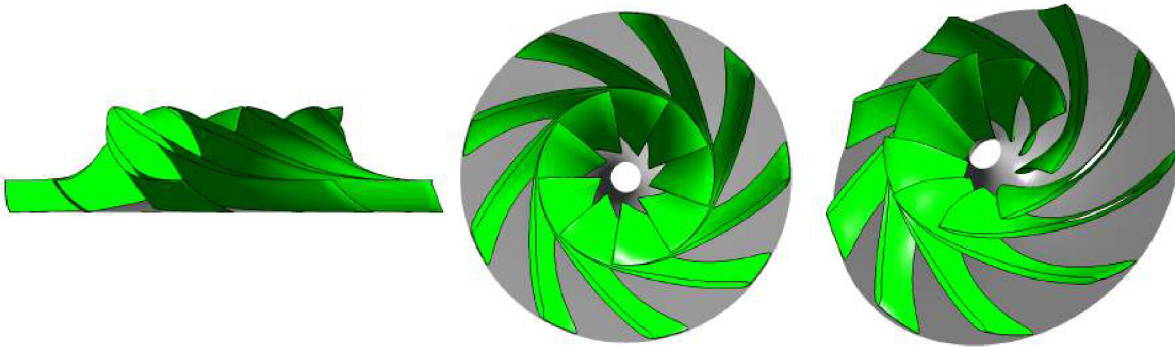
Fig. 5.44: *Impeller - design C.*

The length of the blades of the design C offers compromise between the long shape of the design A and the short shape of the design B. A possible geometrical fault of the design lies in the trailing edge, which is formed by the slight curvature (same as in design B) - fig. 5.45.
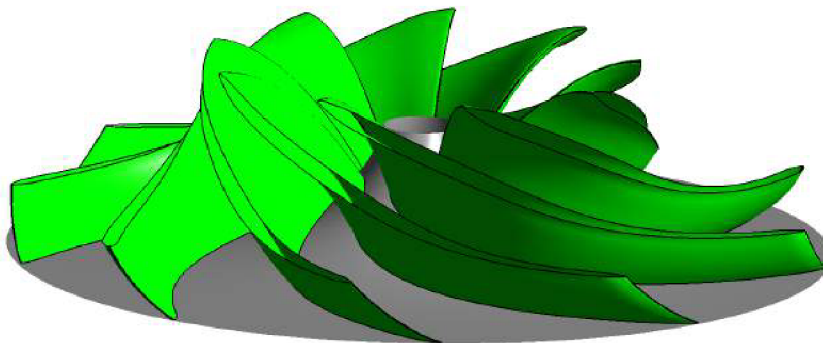
Fig. 5.45: *Impeller - detail of design C.*

Pump characteristics

The highest hydraulic efficiency point of the design C is subtly offset towards the higher values of the flow rate (fig. 5.46). Once again the unsuitable phenomenon towards lower values of the flow rate could be observed in design C simulations (fig. 5.46 and 5.47).
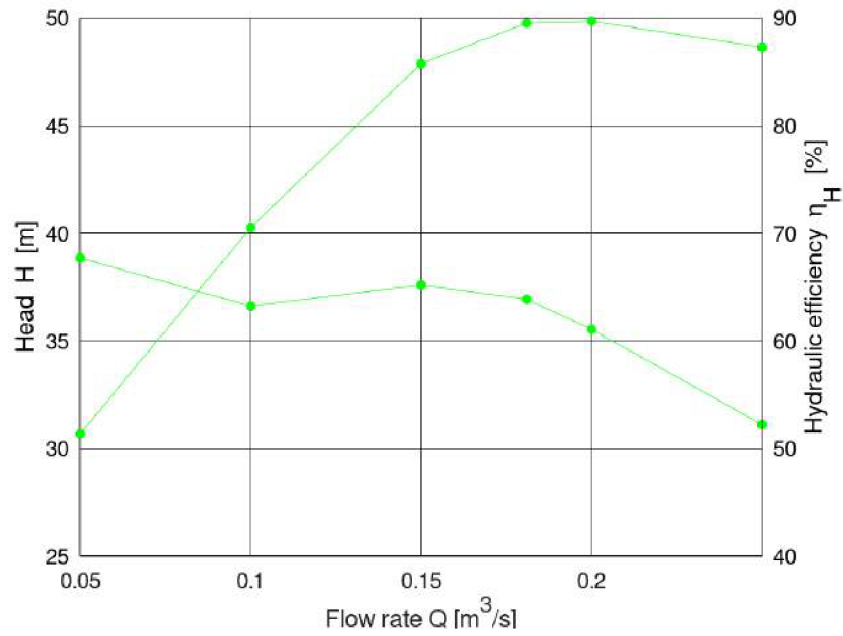
Fig. 5.46: $\eta_H - Q$ and $H - Q$ characteristics: design C.
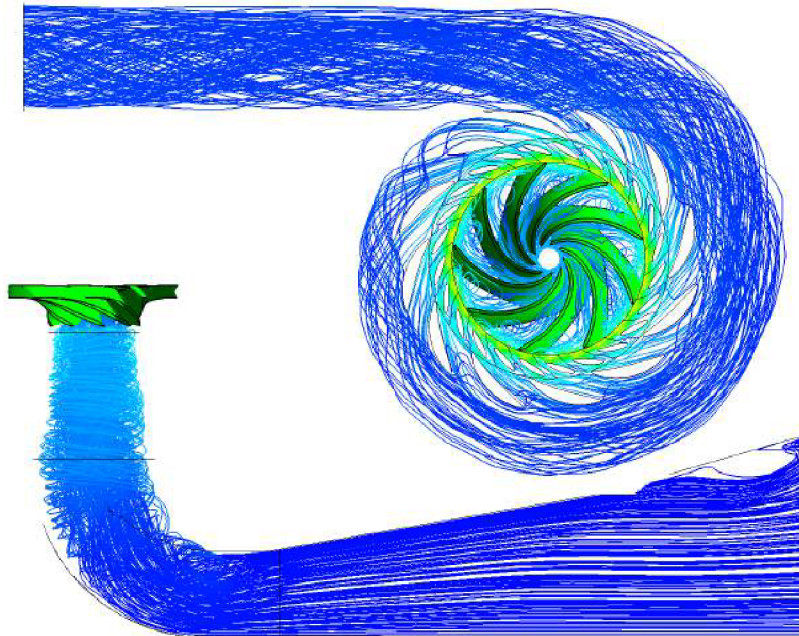
Fig. 5.47: Streamlines $Q = 0.05 \ m^3/s$: design C.

Pressure and velocity distributions inside the impeller

Design C investigated the development of β angles with inflection point along the length of the blade (fig. 5.48).
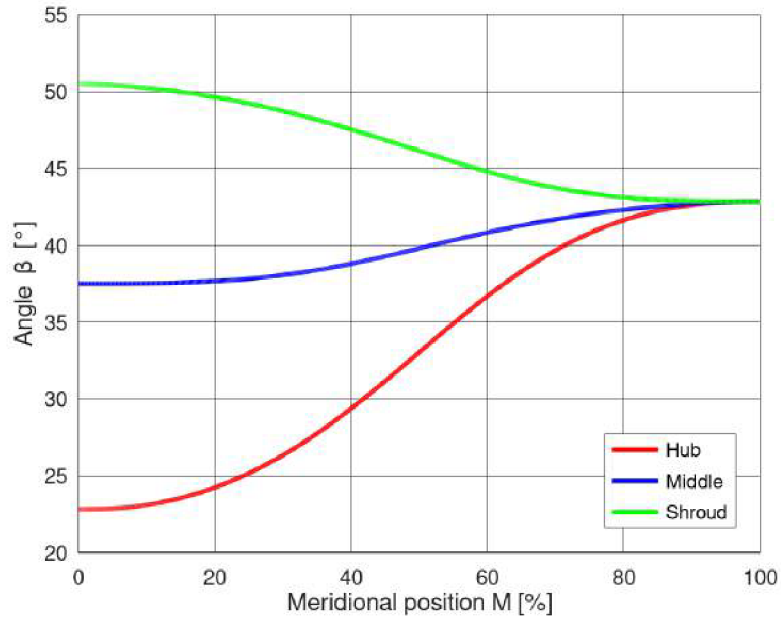
Fig. 5.48: *Angle β - design C.*

The β angle behaviour results in the "normal" pressure distribution on the pump blades. The suction side has the lower values than the pressure side (fig. 5.49).
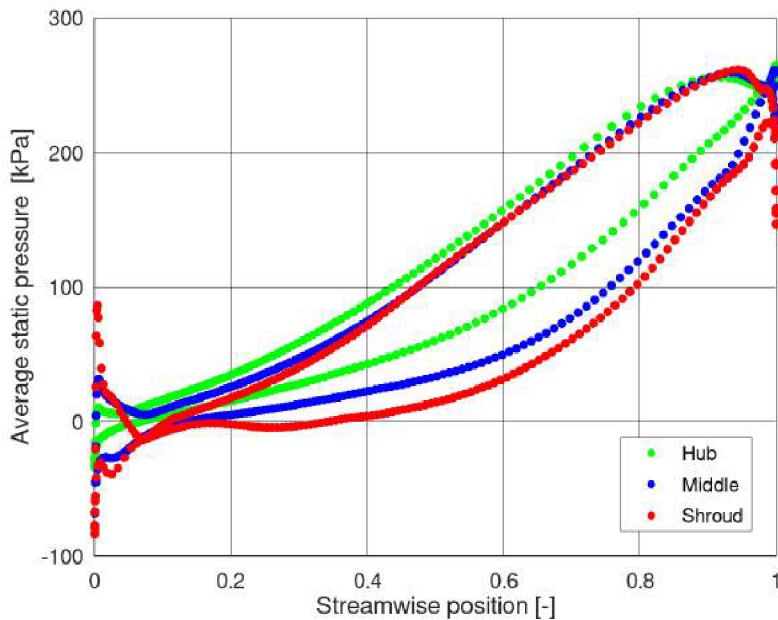
Fig. 5.49: *Blade loading - optimal Q.*

106

The design C has slightly higher average velocity values in the inlet section near the pump shroud (fig. 5.50) and the low velocity value areas near the hub (also in inlet area). The pressure change is remarkable by a gradual transition from the low values of the static pressure (impeller inlet) to the higher values, which are located in the impeller outlet - fig. 5.50 - same behaviour as in the design B.
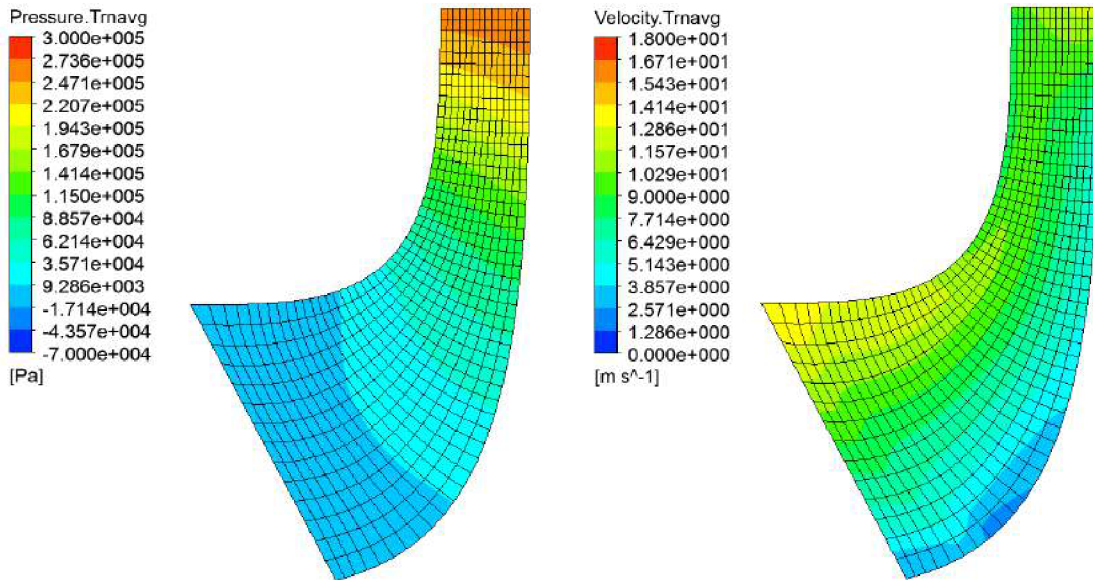
Fig. 5.50: *Average static pressure and velocity distribution - optimal Q.*

Following figure (fig. 5.50) displays the average static pressure distribution in the blade-to-blade view in three main locations of the optimized design C - near the hub, in the middle of the impeller and near the shroud. The critical places are located in the middle and near the shroud section on the suction side of the blade (at the beginning) - there are high pressure drop spots (dark blue are in fig. 5.51). Sudden pressure drop is very dangerous and could lead to the creation of cavitation bubbles, if the static pressure reaches its critical value.
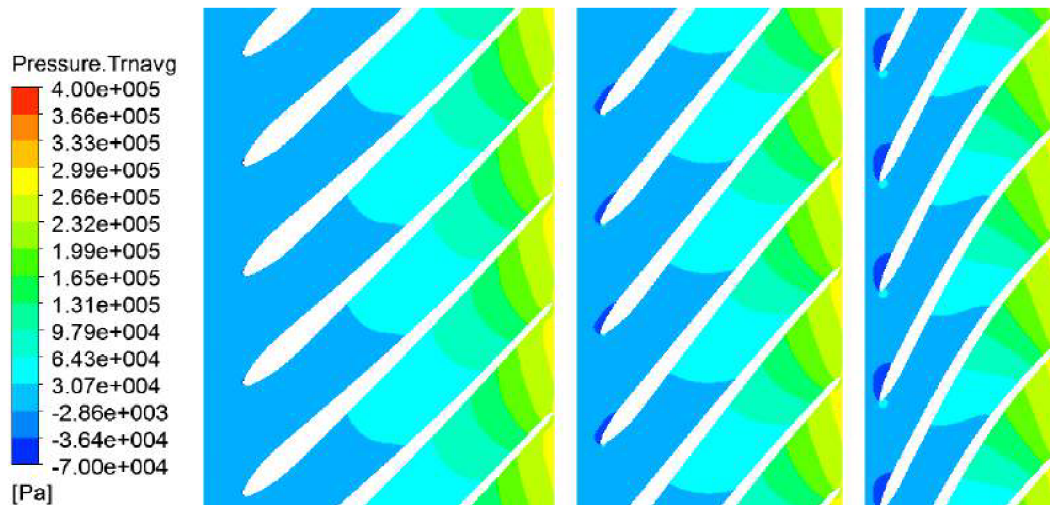
Fig. 5.51: *Average static pressure distribution (hub, middle, shroud) - optimal Q.*

Next three figures examine the correct water flow inside the optimized design C impeller, namely near the hub (fig. 5.52), in the middle of the poump turbine impeller (fig. 5.53) and near the shroud (fig. 5.54).
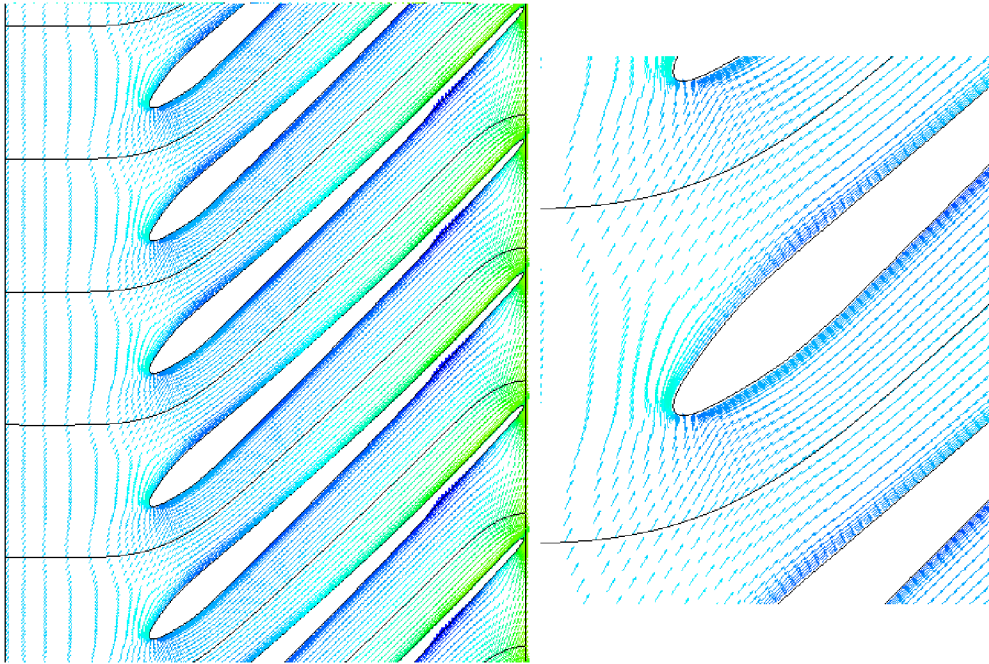
Fig. 5.52: *Average velocity vectors near leading edge (hub) - optimal Q.*

The velocity vectors around the blade tip at the impeller's hub shows a mild fluid shock - fig. 5.52. Such water shock could lead to the unsuitable flow patterns along the length of the blade hand in hand with the pump turbine head and efficiency decrease.
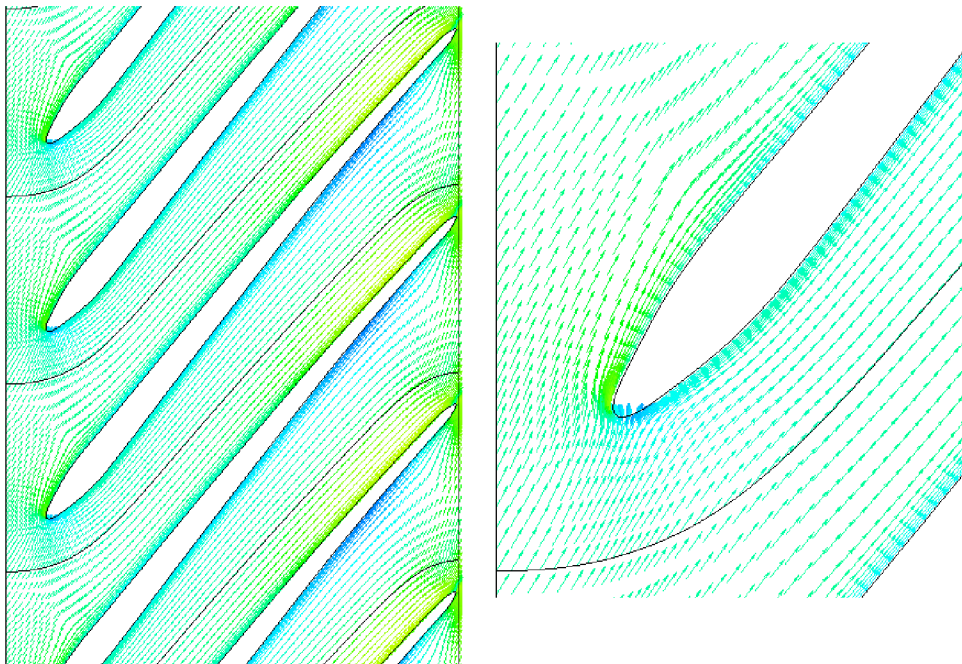
Fig. 5.53: *Average velocity vectors near leading edge (middle) - optimal Q.*

Mentioned mild fluid shock is also slightly noticeable in the middle section view of the pump turbine impeller - fig. 5.53). Fig. 5.54 displays initial water recirculation in the end of the blade at the suction side (very small area, defined by dark blue vectors). From the perspective of the shockless entry - the shroud section is remarkable for the flawless water entry.
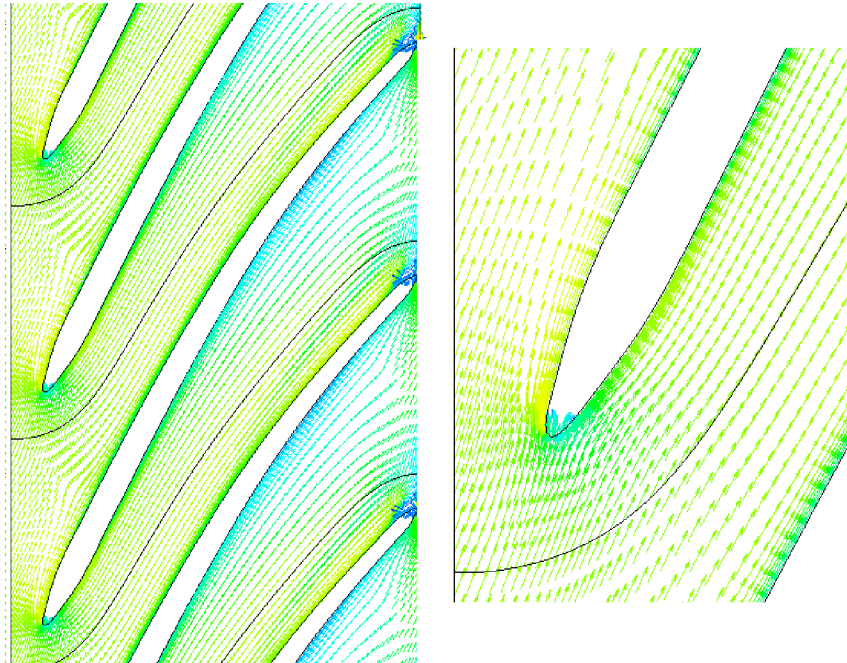
Fig. 5.54: *Average velocity vectors near leading edge (shroud) - optimal Q.*

Surface streamlines
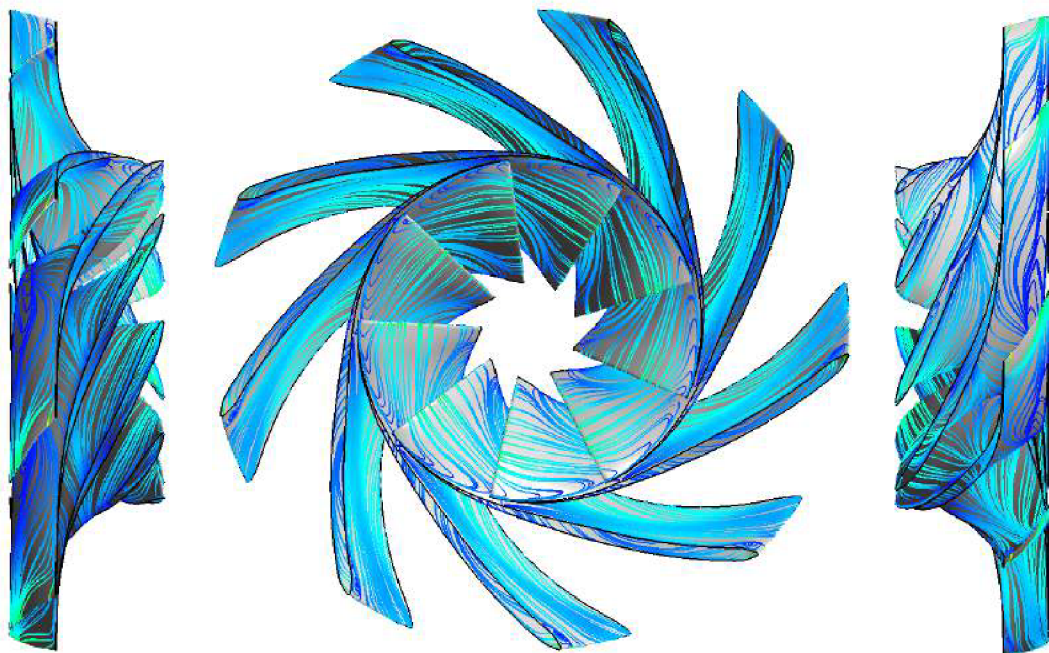
Fig. 5.55: *Surface streamlines - $Q = 0.1\ m^3/s$.*
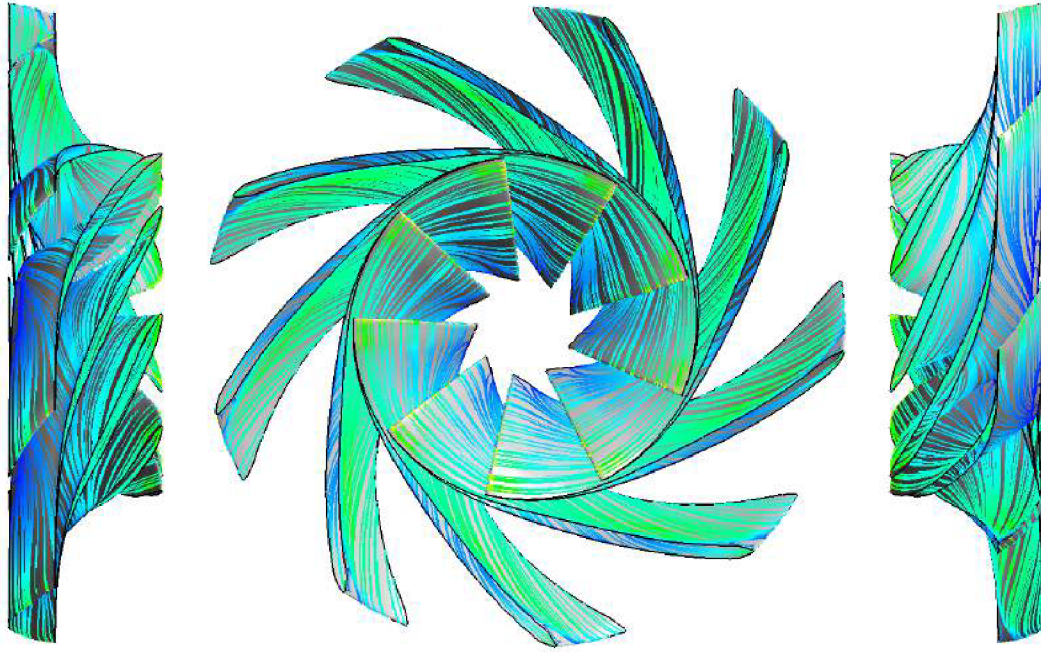
Fig. 5.56: *Surface streamlines - Q = 0.181 m^3/s (optimal flow rate).*
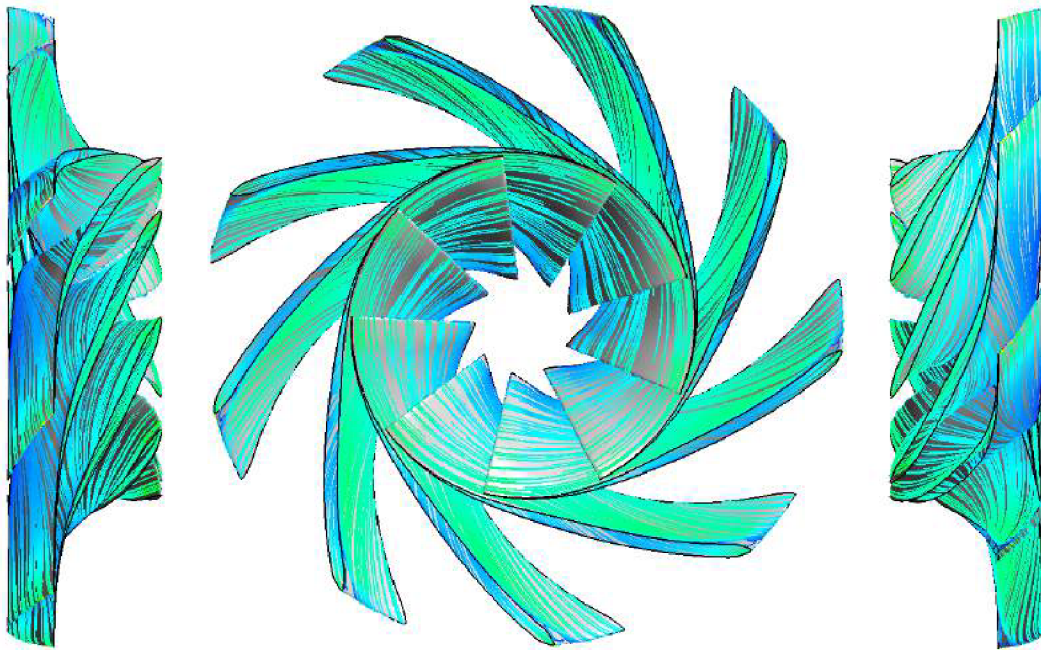
Fig. 5.57: *Surface streamlines - Q = 0.25 m^3/s.*

Figures 5.55-5.57 capture the fluid behaviour on the blades of the design C in three chosen flow regimes - in Q = 0.1 m^3/s, Q = 0.181 m^3/s (optimum) and Q = 0.25 m^3/s. No recirculation passages could be seen in the optimal (fig. 5.56) and the over optimal flow regimes (fig. 5.57). On the other hand, under optimal regime (fig. 5.55) shows signs of water recirculation on the blades (and afterwards in the pump's flow passages), which has negative impact on the pump's head and the hydraulic efficiency. Globally, the design C has the best surface streamlines among the all optimized designs.

5.1.5 ČBE Measurement

Design A was manufactured (fig. 5.58) and subsequently measured in **ČKD Blansko Engineering** (shortly ČBE) in grant collaboration **TH01020982** - *Zefektivnění akumulace energie a zajištění stability rozvodné sítě rozšířením provozního pásma přečerpávacích vodních elektráren.*

Fig. 5.58: *Impeller model* [92].

Figure 5.59 shows the location of the pressure taps in the pump turbine measurement. These location were afterwards utilized in the comparative CFD simulations. The inlet static pressure was measured in **12** location (cross-section **F-F**), the outlet pressure was measured in **4** different places (cross-section **B-B**).
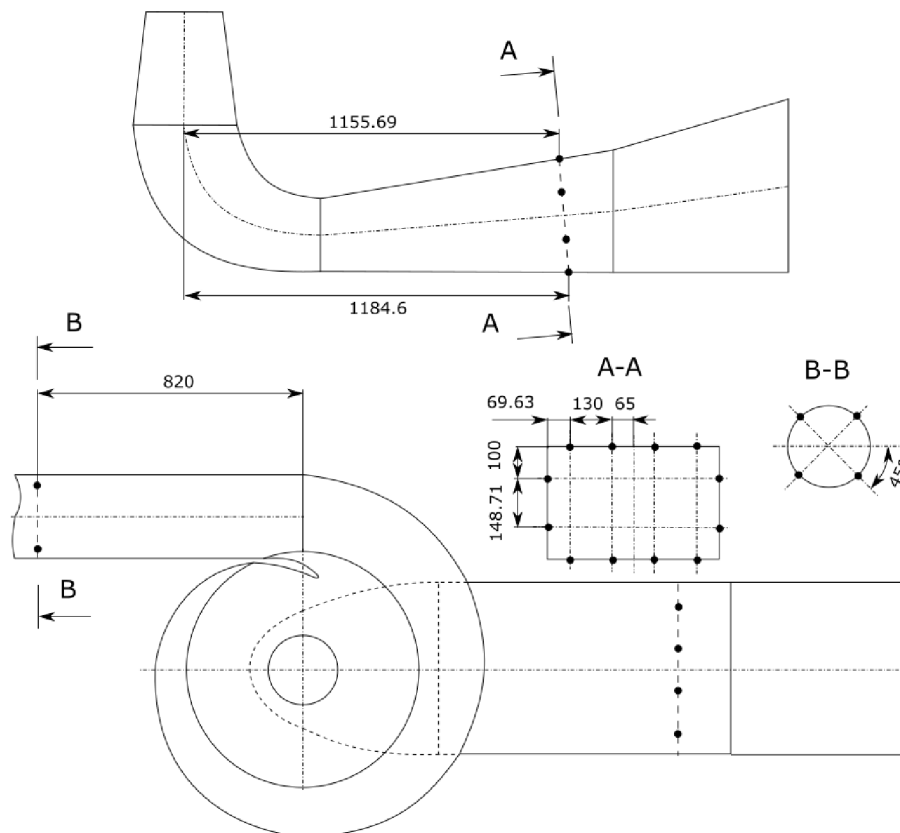
Fig. 5.59: *Pressure taps locations* [92].

Main performance characteristics [92]

Experiments were performed for four different openings of the guide vanes: 18 mm, 20 mm, 22 mm, 24 mm. For comparative CFD simulations was chosen opening $a_0 = 20\ mm$ (**black** curves in figures 5.60, 5.61 and 5.62).
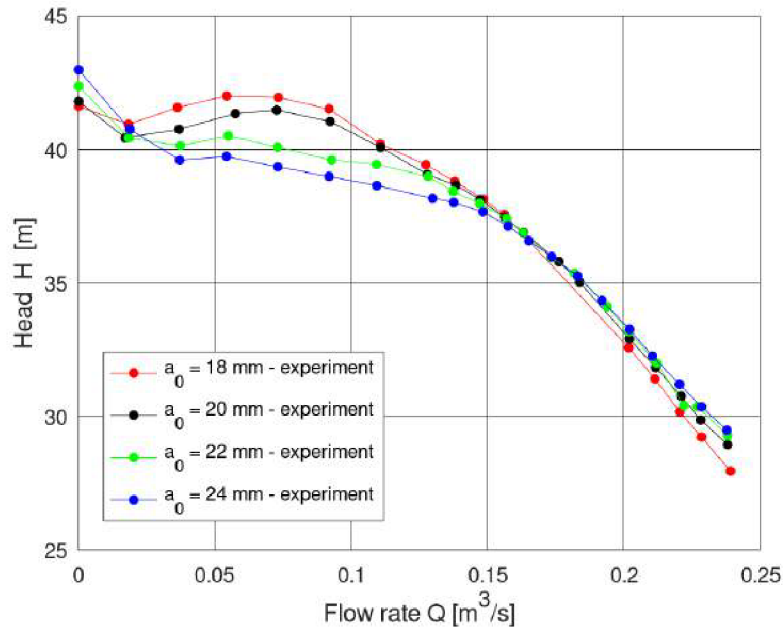
Fig. 5.60: *H-Q dependencies - experiment* [92].
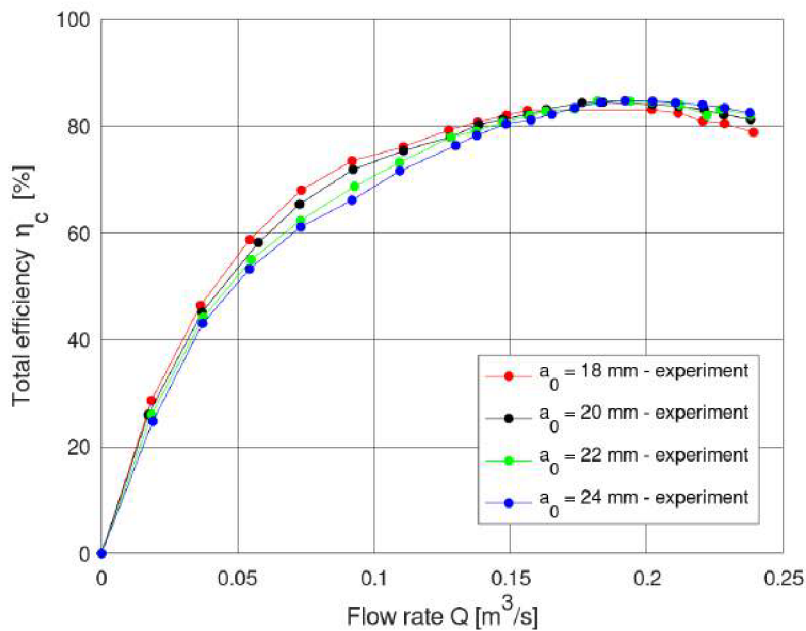
Fig. 5.61: η_c-*Q dependencies - experiment* [92].

The flow regimes for all openings show instabilities in $H - Q$ dependencies towards to the zero value of flow rate, on the other hand $\eta - Q$ dependencies show wide operation range with high values of efficiency around BEP/requested points. The last main pump characteristic, which was measured and examined by ČBE, was $NPSH_3$ dependency on the pump flow rate (fig. 5.62).
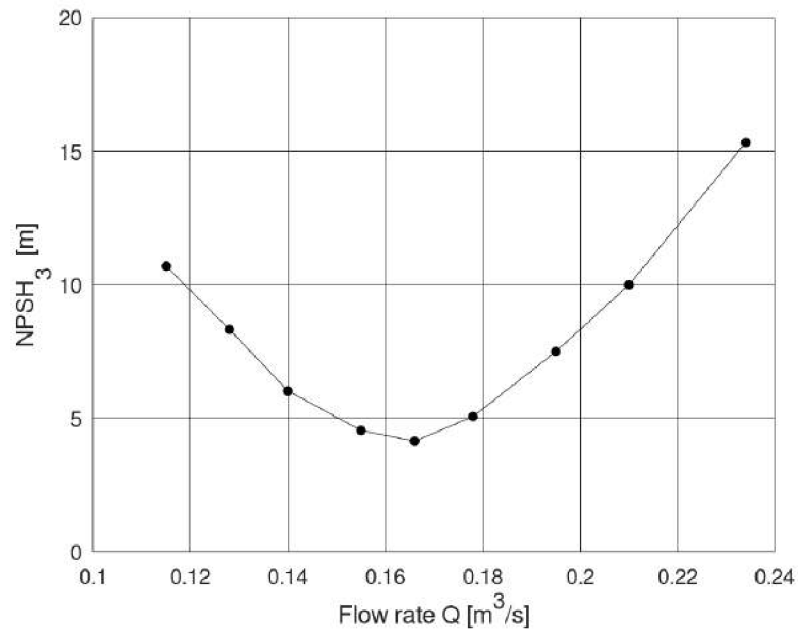
Fig. 5.62: $NPSH_3$-Q dependency - experiment [92].

The $NPSH_3$ curve of the Design A has a common parabolic shape, with the lowest point located to the left from the optimal flow rate, which is characterize by $Q = 0.181 \; m^3/s$ (fig. 5.62).

5.1.6 Complete results and design comparison

Three different geometries of the pump turbine impeller were created as the output of the shape optimization tool based on the Particle swarm optimization, namely: **Design A** (portrayed in this section by the red color) - this design was made in the collaboration with the OFIVK in-house software based on the quasi-potential flow [89], **Design B** (displayed by the blue color) and **Design C** (coloured by green). These designs are compared in following subsections on the geometrical, performance characteristic and the flow patterns base in a way to uncover basic differences and their possible advantages or disadvantages.

Geometrical comparison

First, the geometrical comparison must take place. In fig. 5.63 are all three impeller designs drawn over one another to reveal the main shape and length differences. The red design A is remarkable by the longest blades, on the other hand, blue design B is distinguished by the shortest blade's length. In the middle lies green design C, with the compromisable impeller blade's length.
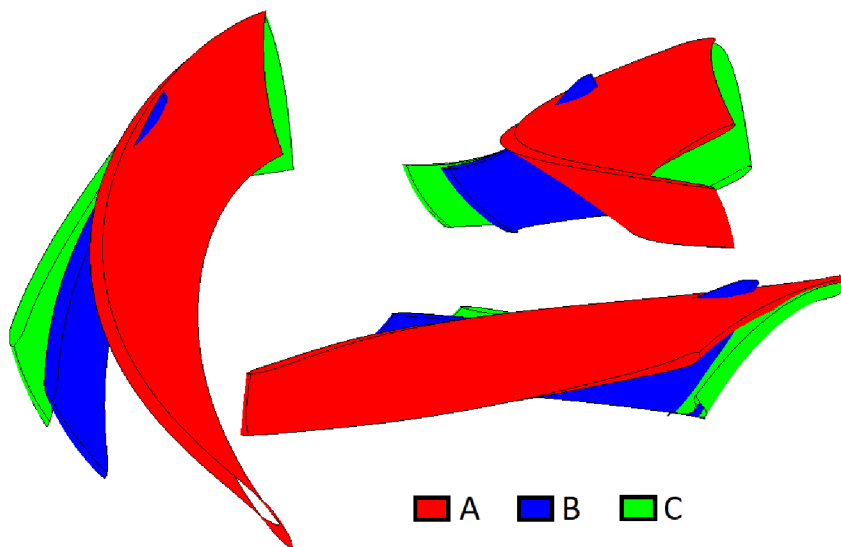
Fig. 5.63: *Design comparison - blade perspective.*

It should be noted that the suitable length of the blade has a key role in a right fluid (water) guiding in the impeller and consequently in the correct behaviour of the pump. This means that the long shaped blades are very convenient for water directing in the pump rotational passages, but the area of blades causes higher hydraulic losses due to greater wall-water interaction and thereby sheer stress. Such losses are one of the main contributors to the pump head and hydraulic efficiency decrease. On the other hand, short blades must deal with a larger "pressure shock" on blade's length compared to the longer blades. With high values of pressure on one side of the blade goes hand in hand low pressure areas on the other side - such areas could initiate the formation of cavitation bubbles.

The length of the blade can be also visualised by the θ-angle (the **wrap angle**) in the meridional point of view. This fact is captured in fig. 5.64, where the design A is on the left side, design B is in the middle and design C is on the right side.
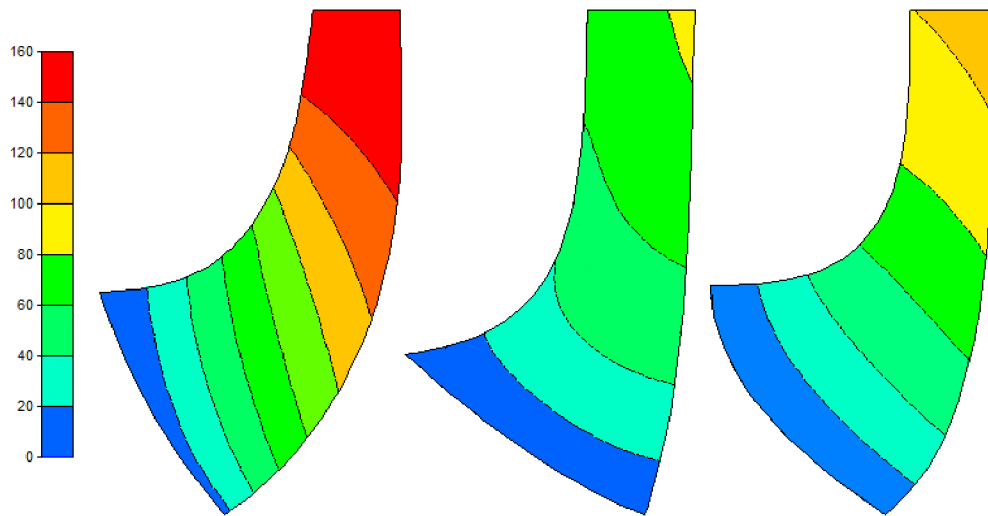
Fig. 5.64: *Design comparison - θ-angle perspective.*

Fig. 5.64 confirms visual blade's lengths of the designs in fig. 5.63. Design A has the highest value of θ-angle, which equals up to 160°. On the other hand, design B is characterized with the lowest highest value only up to 100°. The most convenient θ-angle development along the blade shows **design C** - with highest value of hydraulic efficiency in the design point $Q = 0.181 \ m^3/s$ (tab. 5.11) and advantageous values of $NPSH_3$ (fig. 5.70). A change of the θ-angle of the design C tries to copy (imitate) the leading edge of the blade, such imitation positively influences the flow inside the pump turbine impeller.

The last geometrical comparison is focused on the β angle, to be more precise on the inlet and outlet values (tab. 5.10) and the global shape along the blade, which is shown in fig. 5.65. This pump parameter had a crucial part in the proper blade shaping process appearing in the presented shape optimization tool.

Tab. 5.10: *Inlet/outlet β angle comparison.*

	Design A	Design B	Design C
Hub	37.06/50.43	29.09/46.56	50.5/42.83
Middle	29.67/43.64	20.35/56.66	37.5/42.83
Shroud	25.61/40.48	28.48/40.18	22.81/42.83

As was mentioned, design A was founded on the output from the OFIVK in-house optimization software based on the quasi-potential flow [89]. This design is characteristic with the most complicated shape of the β angle along the blade. The angle near the hub (red color, first figure in fig. 5.65) decreases its value at the beginning (around the leading edge) and afterwards continues almost linearly. On the other hand, β angle in the middle

streamline and near shroud could be compared to a quadratic function - a valley-like development with inlet β_1 on one side and outlet β_2 on the other side.

Design B explores the pure linear change of the β angle. Such change should be energy efficient with uniform pressure distribution [27].
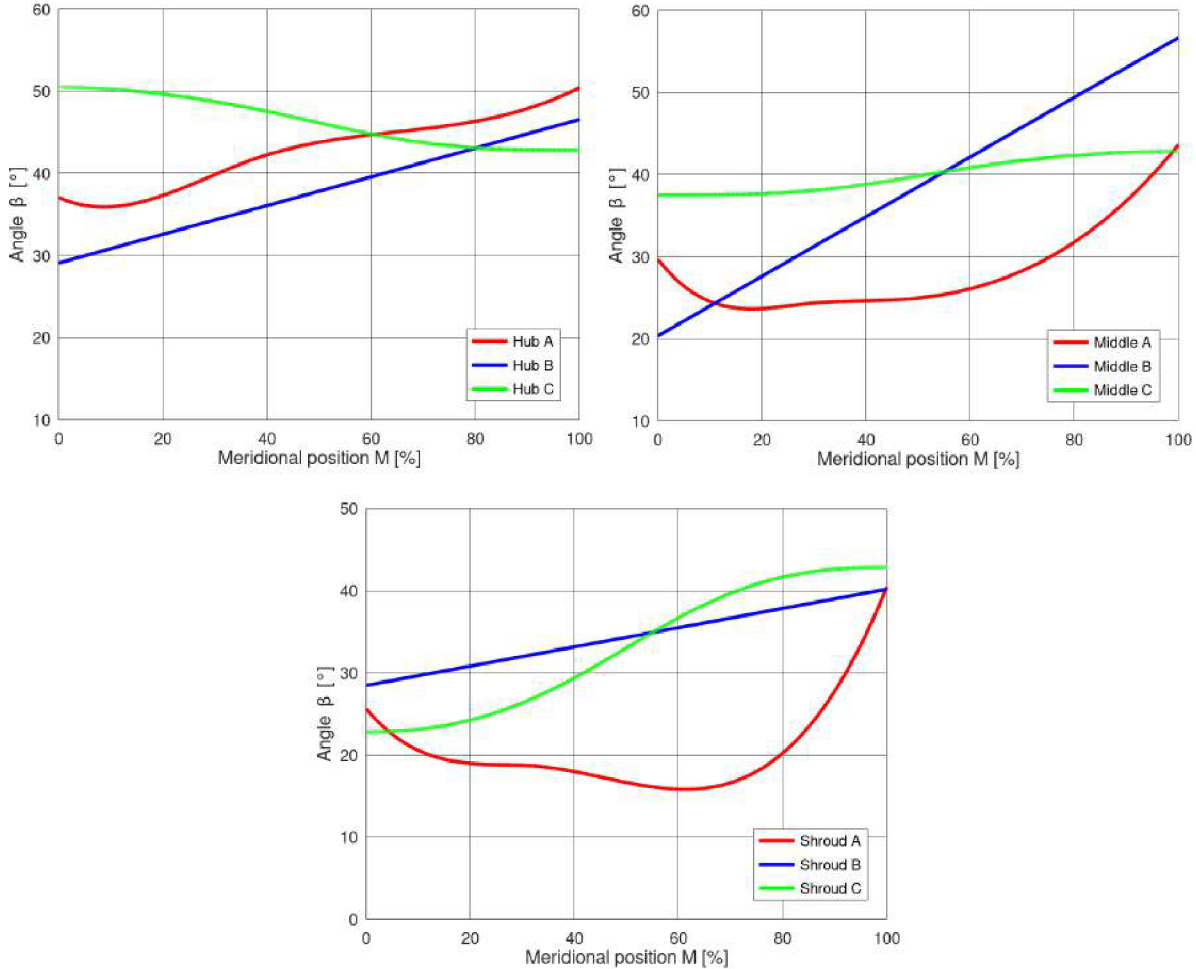
Fig. 5.65: β angle comparison.

Design C goes in a way, which was mentioned in Gülich [26]. The β angle development along the length of the blade has the inflection point. This inflection point provides the slow β change at inlet and outlet of the blade, which decreases pressure loading in these locations. Such decrease shows a positive influence on $NPSH_3$ curve [26]. Almost constant β angle near trailing edge is also favourable for impeller trimming.

From the exact value point of view, all impeller designs show quite high values of inlet/outlet β angles (tab. 5.10) - especially outlet β angle, which predominantly lies in interval $20^o - 35^o$ for radial centrifugal pumps [26], [71]. But it must be also mentioned that high values of the outlet β angle are caused by the small magnitude of the outlet width b_2, which has a key role in the determination of β_2.

Going back to the figures 5.60 and 5.61, there are not any abnormal instabilities in the performance characteristics of the design A. Only saddle like instability in $H-Q$ curve,

which is primarily caused by the distributor. From this point of view and in this case, the high values of *beta* angles does show stable behaviour during the pump run.

Performance characteristics and cavitation qualities comparison

Previous subsection brings information about the shapes of optimized impellers, but without a suitable comparison with the main performance characteristic, such as $\eta_H - Q$ or $H - Q$, is quite useless, so table 5.11 and figures 5.66 - 5.70 summarize acquired data from the URANS CFD simulations of the optimized designs A,B and C.

Table 5.11 compares values of all pump turbine designs in the design point described by the flow rate $Q = 0.181 \ m^3/s$. Design A, which was measured by ČKD Blansko Engineering served as a reference model.

Tab. 5.11: *Computed pump turbine parameters in $Q = 0.181 \ m^3/s$.*

	Design A	Design B	Design C
Hydr. efficiency η_H [%]	85.5/100 %	86.24/ + 1.22 %	**89.54/ + 4.72 %**
Pump Head H [m]	**34.92/100 %**	36.46/ + 4.41 %	36.93/ + 5.76 %
Power P [W]	**61877/100 %**	64605/ + 4.41 %	65438/ + 5.75 %
Energy dissipation D [W]	10493/100 %	10308/ - 1.76 %	**7644/ - 27.15 %**

Both, design B and design C outperformed design A in the hydraulic efficiency delivered by the CFD simulations (tab. 5.11), projected in numbers by 1.22 % (**B**) and 4.72 % (**C**), respectively. Globally, the widest range (in requested flow rates - see tab. 5.7) of the high hydraulic efficiency values belongs to the green **design C** - fig. 5.66.
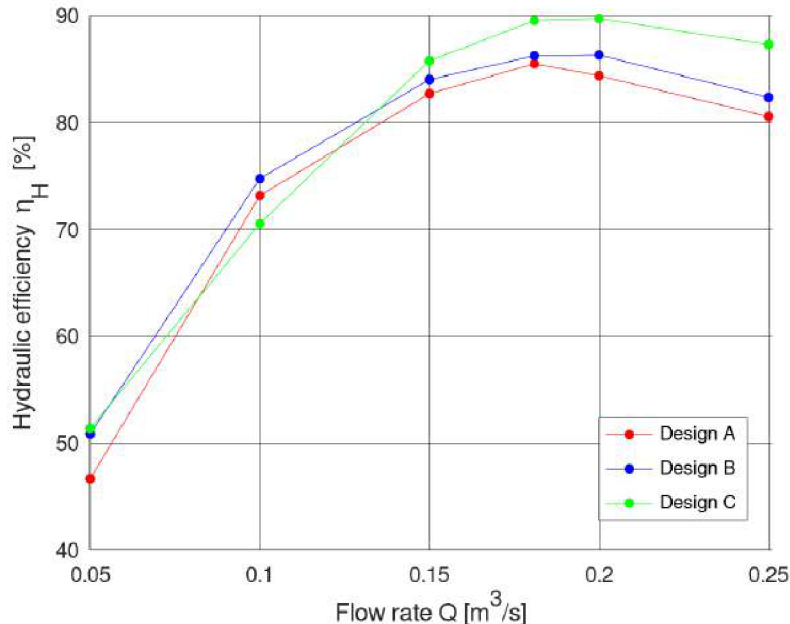
Fig. 5.66: *$\eta_H - Q$ characteristics comparison.*

Unfortunately only **design A** has the highest value of the hydraulic efficiency in the

crucial design point characterized by the flow rate $Q = 0.181\ m^3/s$. Design B and C has the optimum slightly shifted to the right in a way of higher values of the flow rate.

Another important variable, which was closely observed, was the pump head $H\ [m]$. Fig. 5.67 shows comparison between achieved designs and once again all data came from the URANS CFD simulations. In such figure are also marked requested pump head values (portrayed by black crosses) - it is noticeable that only **design A** managed to reach these values, both design B and design C exceeded e.g. required point defined by the flow rate $Q = 0.181\ m^3/s$ by 4.41 % and 5.76 %, respectively.
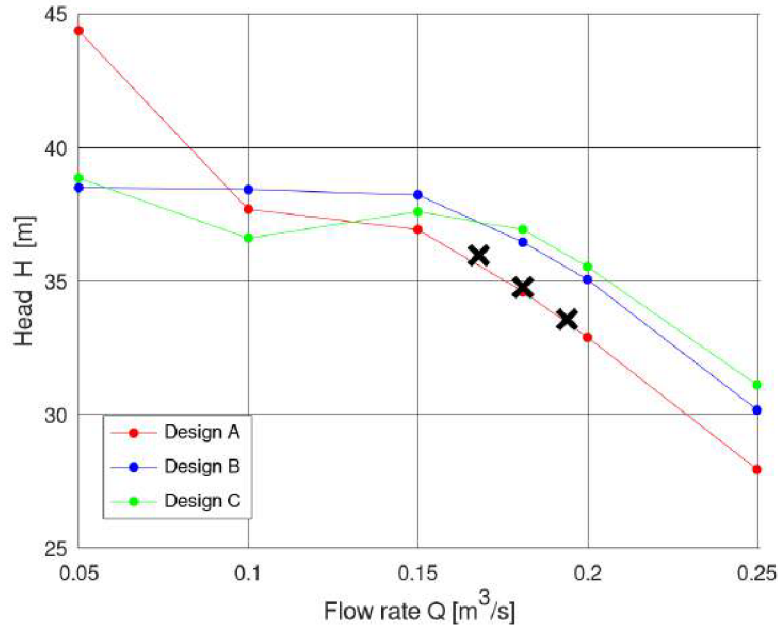
Fig. 5.67: _H − Q characteristics comparison._

It must be mentioned that the interesting phenomenon was found, while evaluating pump heads, especially in region $Q < 0.15\ m^3/s$. Usually (without any flow instabilities) head of the centrifugal pump has the highest value in the zero flow rate and with a discharge increase slowly lower its magnitude (when the distributor (guide vanes) is presented mild saddle-like instability is common in regimes with the low value of the flow rate - it could be seen in the measurement of ČKD Blansko Engineering displayed by fig. 5.14). But the URANS CFD simulations can not detect such "normal" head behaviour towards zero flow rate and huge head overestimations/underestimations are registered. It is possible that the chosen two equation model of turbulence (default k-ϵ in this case) does not properly catch and simulates very turbulent and dissipative flow regimes in complicated flow paths of the pump distributor and impeller, which goes hand in hand with the low values of the flow rate.

118

The next important pump performance characteristic is the power - flow rate dependency (fig. 5.68), which has in the field of the radial centrifugal pumps almost linear form [26], with the lowest value of the power located in the zero flow rate and the highest value in the maximal pump flow rate. All optimized designs shared similar power - flow rate curves, they crucially differ from the optimal flow rate $Q = 0.181 \ m^3/s$ to maximal observed discharge, where the lowest power values in such interval has design A and the highest design C.
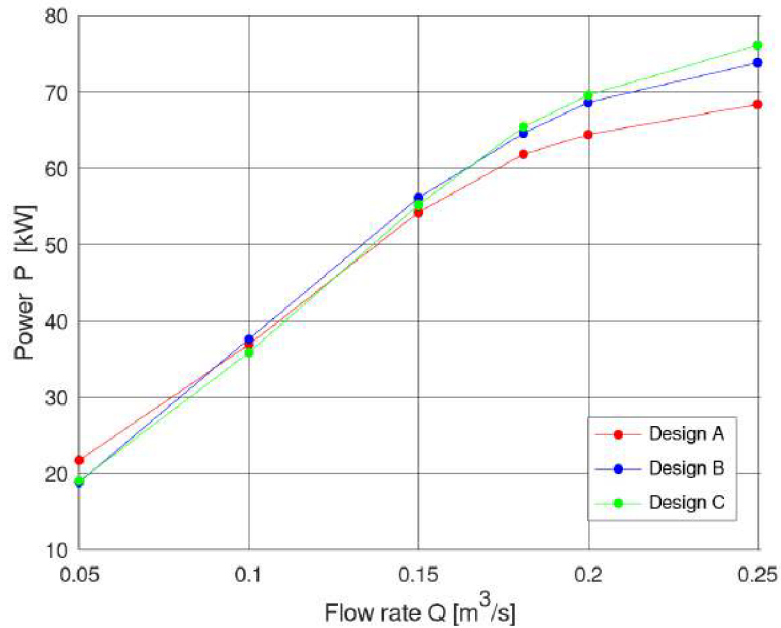
Fig. 5.68: $P - Q$ *characteristics comparison.*
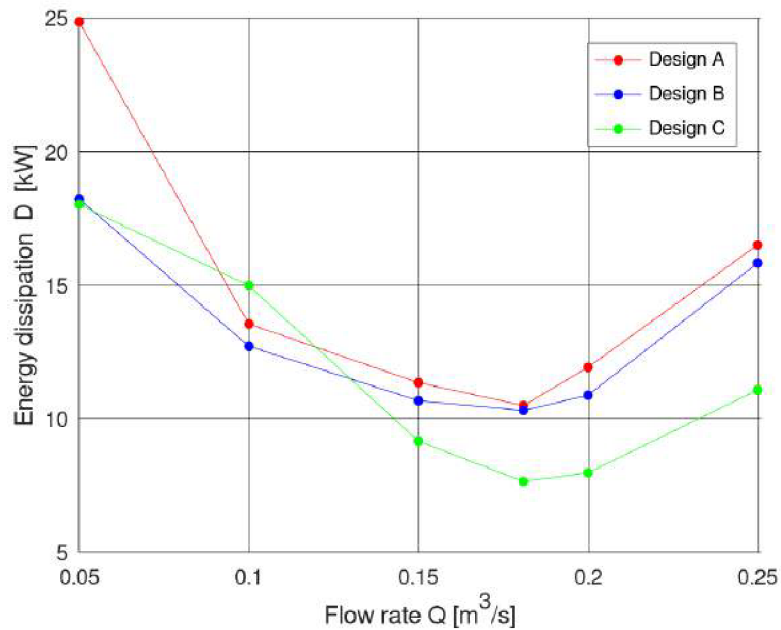
Fig. 5.69: $D - Q$ *characteristics comparison.*

119

The energy dissipation shows an amount of energy of flowing liquid dissipated (converted into a another type of energy, thanks to the hydraulic losses) in the current operation point of the pump. So lower the value of D $[W]$ is, then higher values of the hydraulic efficiency must be. All designs show the lowest point in the optimal design point described by flow rate $Q = 0.181\ m^3/s$, but interesting fact that only design A has the maximal hydraulic efficiency η_H in it (fig. 5.69).

The last compared pump characteristic is the $NPSH_3 - Q$ dependency, which has a crucial role in the proper determination of cavitation qualities of the optimized designs - lower the value of the $NPSH_3$ $[m]$ is, then the better performance without cavitation is expected inside the pump turbine system. The most important values of the $NPSH_3$ were examined in three different flow rates, in $Q = 0.155\ m^3/s$, $Q = 0.181\ m^3/s$ (optimal flow rate) and $Q = 0.195\ m^3/s$ (fig. 5.70).
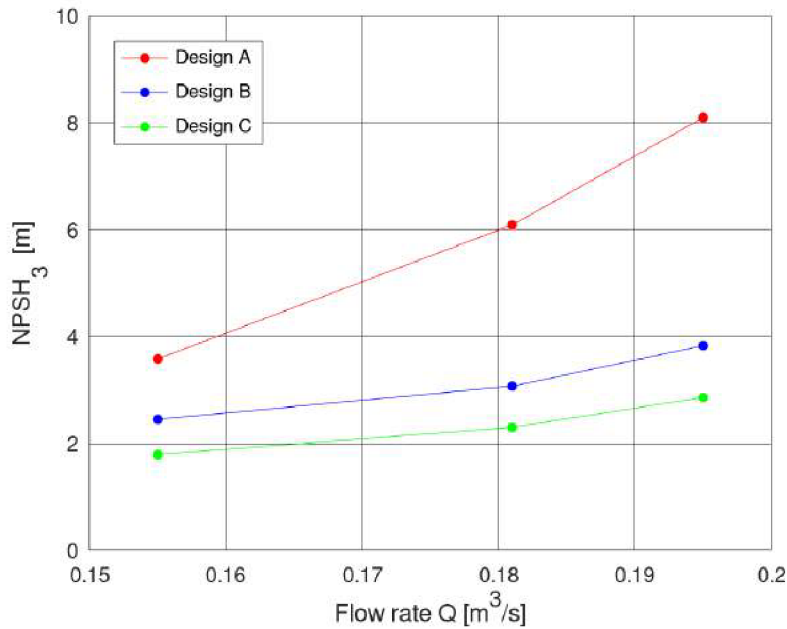
Fig. 5.70: $NPSH_3 - Q$ characteristics comparison.

When comparing $NPSH_3$ in optimal flow rate, designs B and C strongly outperformed design A and almost double reduced the value of $NPSH_3$ in such point (from $6\ m$ to $3\ m$ in the case of design B and almost to $2\ m$ in the case of design C - fig. 5.70). Examined points on the left from the optimal flow rate and also on the right are in cases of design B and C below values of design A. Globally, design A shows the worst $NPSH_3$ values in three explored operational points, with minimum shifted towards smaller flow rate and radical $NPSH_3$ increase with discharge $Q = 0.195\ m^3/s$. On the other hand, **design C** excels in the $NPSH_3$ field of examination, with the wide range of the lowest achieved values.
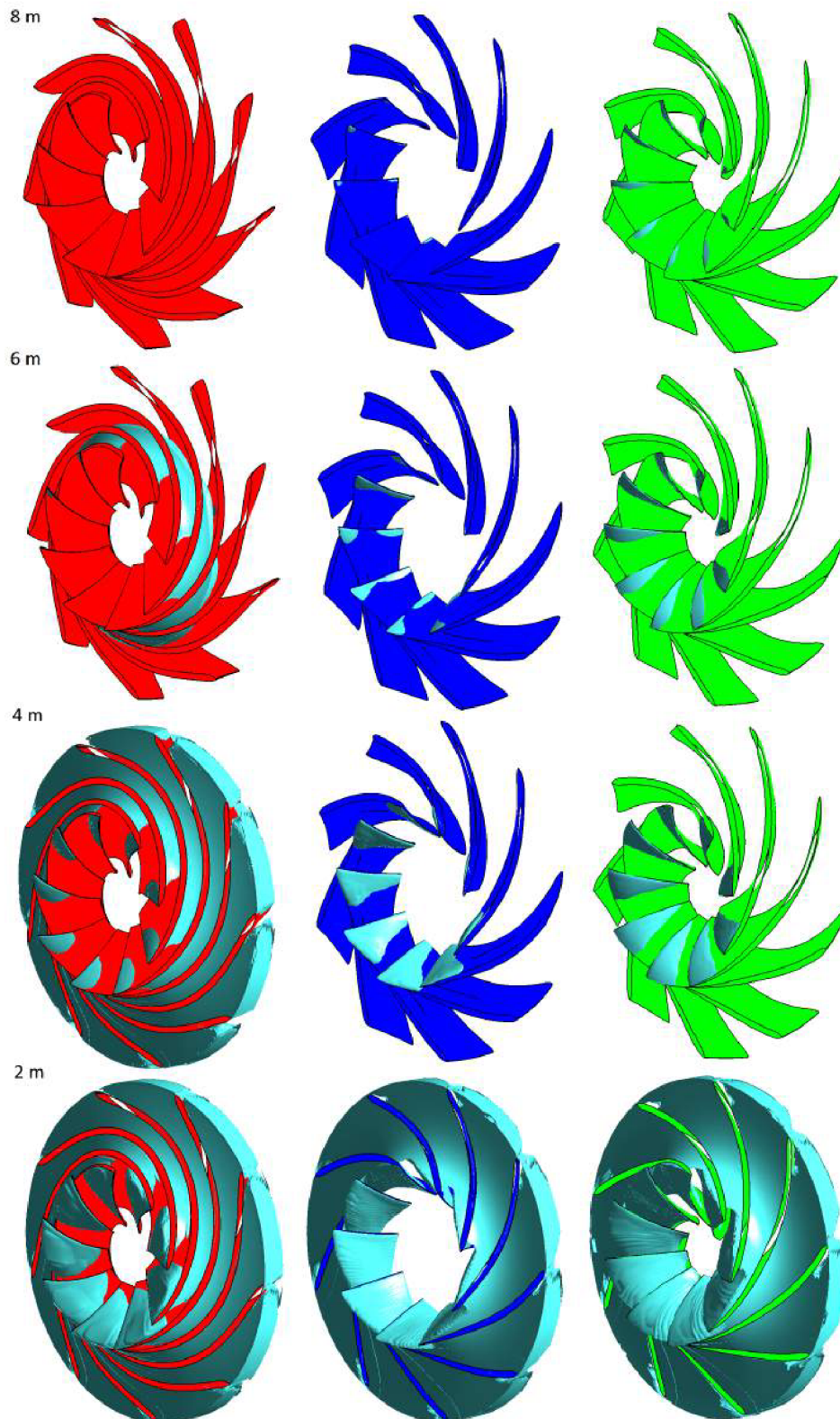
Fig. 5.71: *Water vapour inside impellers (optimal Q) - design comparison.*

Focusing on fig. 5.71, it displays the formation of the water vapour inside optimized impellers (in the optimal flow rate) based on the overpressure in inlet boundary condition, which is in mentioned fig. 5.71 characterized by the heights - 8 m, 6 m, 4 m and 2 m.

Both, design B (blue) and design C (green), shows the initial source of the cavitation bubbles near the leading edge area of the suction part of the blade. Contrarily, the water vapour developed in design A further along the length of the blade in the middle of the flow passage.

The cavitation goes hand in hand with the lowest static pressure on the blade, with the blade loading and also with overall pressure distribution inside the meridional flow channel. The lowest static pressure near hub has blue design B, on the other hand, design C achieved this fact on the middle streamline and also near shroud (fig. 5.72). It must be said that during designing of the radial pump impeller, it is crucial to avoid blade loading, which posses design A, where pressure and suction side of the blade almost switched their roles - this design has the worst $NPSH_3$ values in all observed computational points.
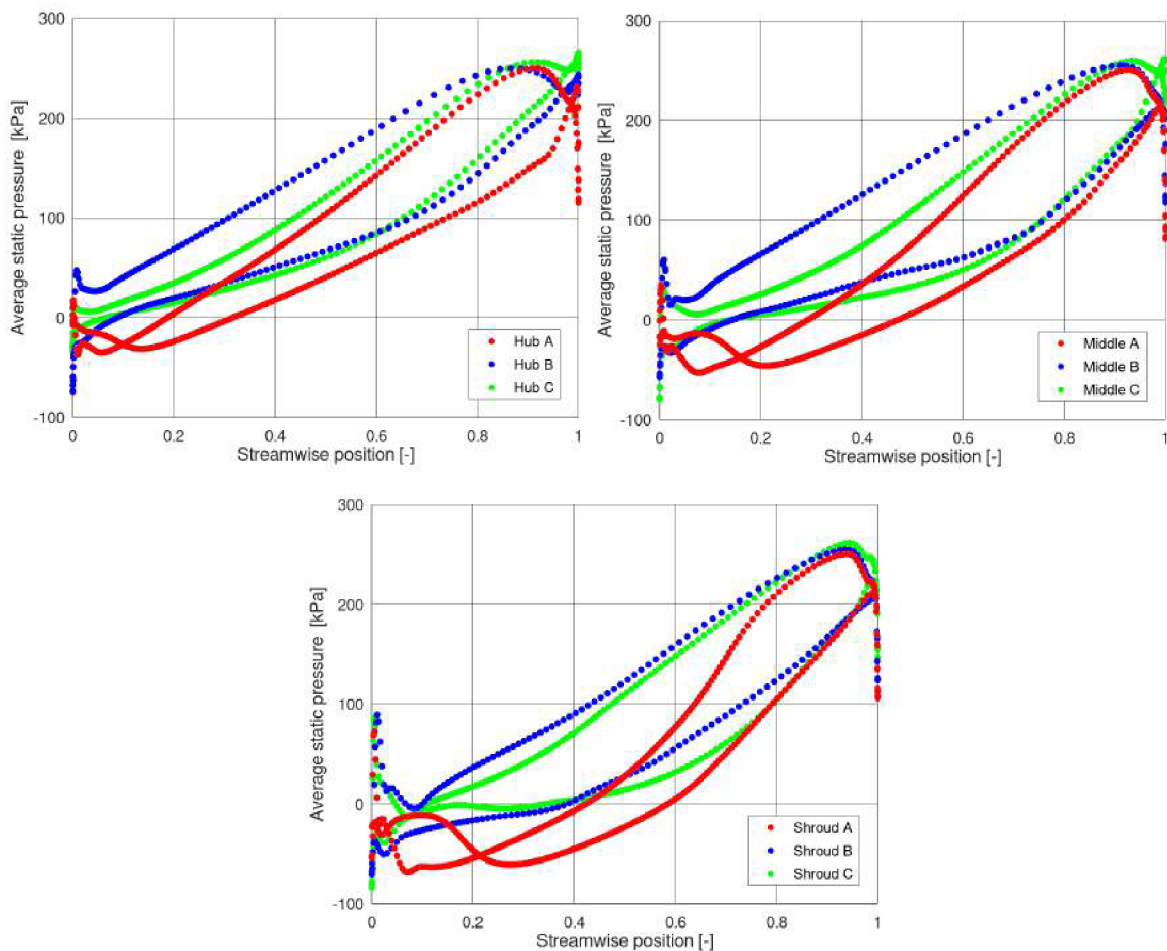
Fig. 5.72: _Blade loading - design comparison (optimal Q)._

Figure 5.73 compares the average static pressure inside the pump flow passage from the meridional point of view, with the order: on the left design A, in the middle design B and on the right side design C. The measuring scale (legend) was set the same for all optimized designs, from the static pressure interval $\langle -7 \cdot 10^4 \ Pa, \ 3 \cdot 10^5 \ Pa \rangle$.

Only the design A shows the significant pressure drop in the meridional flow channel (in meridional point of view), which is portrayed by the dark blue color in fig. 5.73 located near

122

impeller's inlet towards to the shroud - comparing with the achieved $NPSH_3$ values, such pressure drop (low pressure values) negatively affected the optimized design A. Design B and C demonstrate the gradual pressure change from the low values (impeller inlet) to the higher values near the pump impeller outlet. This gradual change without any distinct pressure instabilities shows perspective and favourable attributes in the hydraulic efficiency and also in the $NPSH_3$ dependencies.
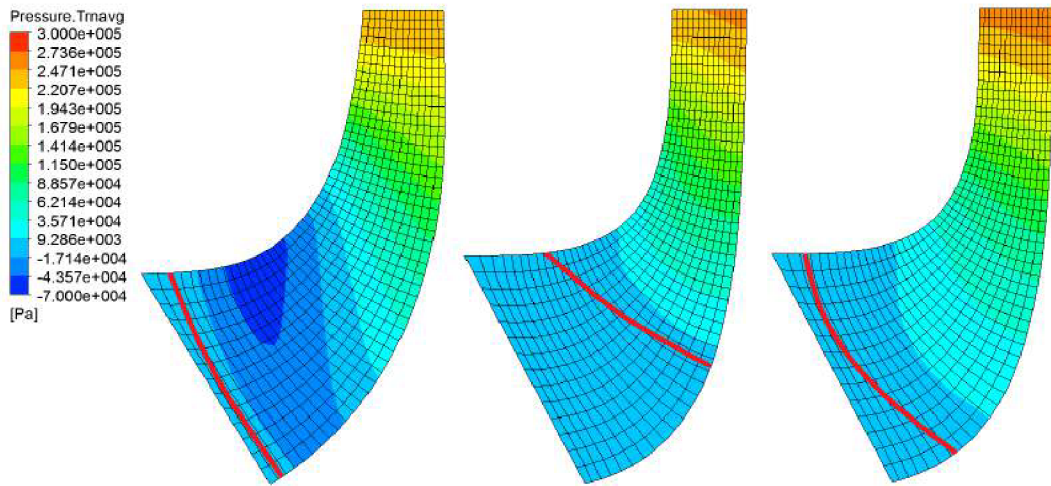
Fig. 5.73: *Meridional flow channel - static pressure comparison (optimal Q).*

While comparing the water vapour volume fraction of the design A in fig. 5.71 and the pressure distribution of the design A in fig. 5.73, it is strongly noticeable that the sudden pressure drop near the shroud is the main contributor in the early vapour manifestation during the $NPSH_3$ determination.

Overall flow patterns comparison

Following figures 5.74, 5.75 and 5.76 capture the flow in the optimum inside the pump turbine model with the optimized impellers.
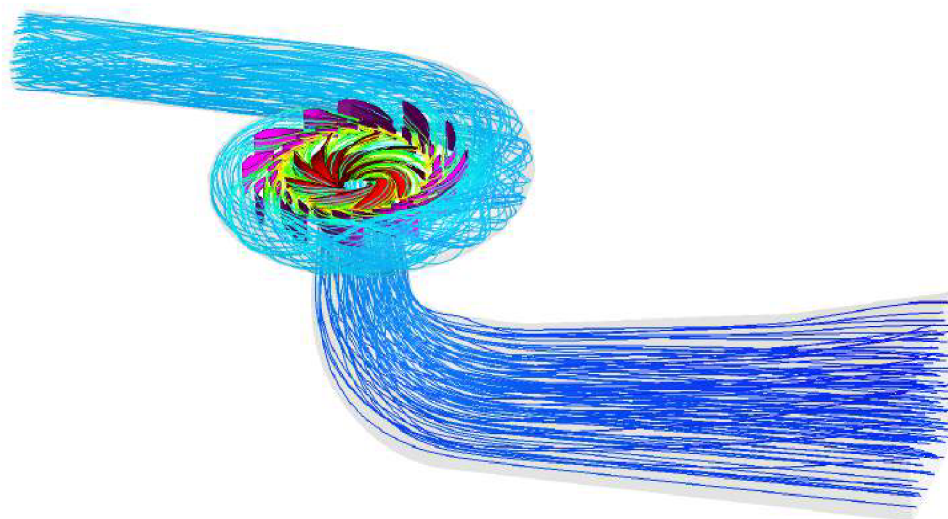
Fig. 5.74: *Streamlines of average velocity (optimal Q) - design A.*

123
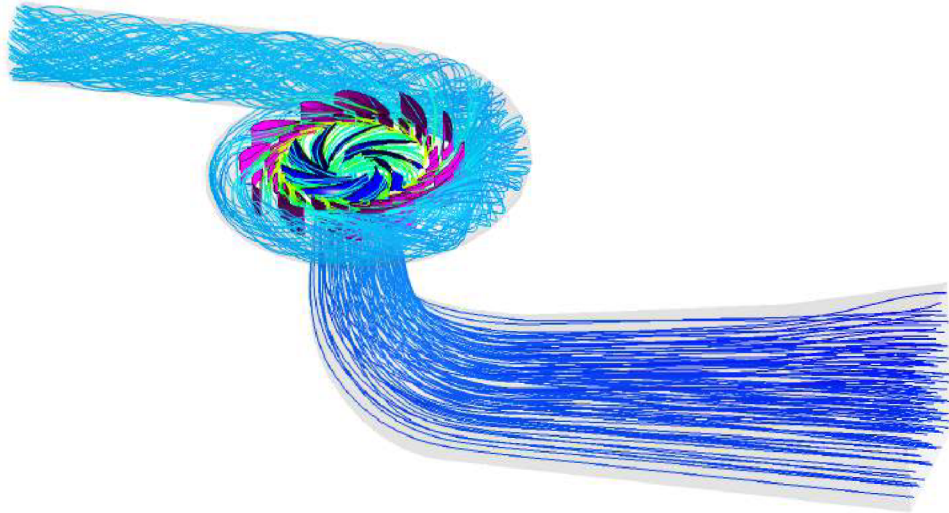
Fig. 5.75: *Streamlines of average velocity (optimal Q) - design B.*
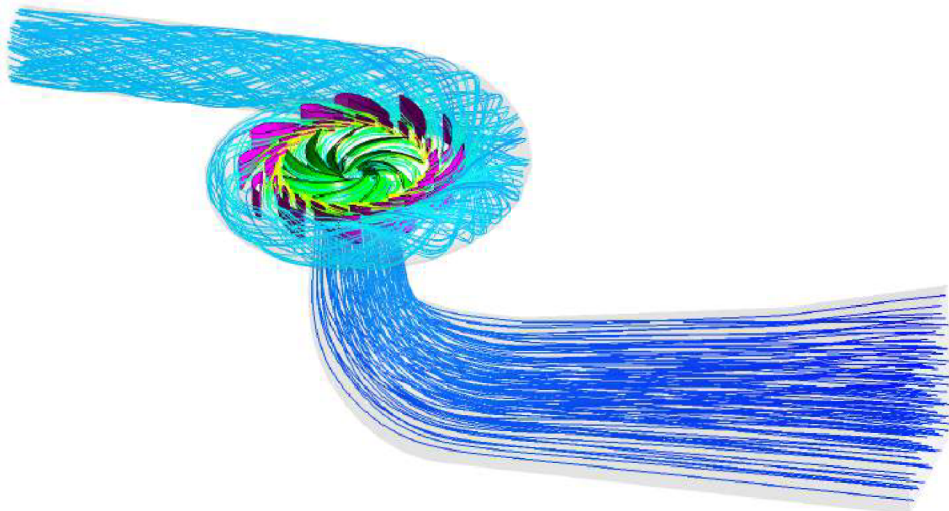
Fig. 5.76: *Streamlines of average velocity (optimal Q) - design C.*

From the streamline point of view, Design A shows narrower streamlines in the outlet section of the model compared to design B and C.

MOPSO and operational parameters comparison

Another possible comparison is in a way of the initial settings of the presented shape optimization tool (= settings, which the user enters into the interactive dialogue menus right before the shape optimization). Some of these adjustments crucially influenced the final shape of the pump turbine impeller and strongly affected the tool behaviour during the shape optimization process.

From this section is excluded the design A, which was made in the collaboration with the OFIVK in-house shape optimization software based on the quasi-potential flow [89] and utilized very early state of the presented optimization tool. This early stage tool

modified the β angle shape along the length of the blade on three streamlines in six main locations = 18 modified parameters. This was done only for the optimal flow rate ($Q = 0.181\ m^3/s$) and in the whole system of the pump turbine hydraulic machine (including the spiral case, draft tube and guide vanes).

Table 5.12 summarized the initial main MOPSO/NM settings. Both design B and C share identical values of these adjustments, which are based on the previous researches found in [63], [64].

Tab. 5.12: *MOPSO parameters comparison.*

	Design B	Design C
Population size	10	10
Grid size	15	15
Repository size	40	40
Inertia weight w	0.2 (linear decrease)	0.2 (linear decrease)
Parameter c_1 and c_2	2	2
Parameter $weight_H$	6	6
Parameter $weight_\eta$	2	2
Parameter $weight_{surf}$	3	3
Parameter ρ (NM)	2	2
Parameter η (NM)	1	1
Parameter γ (NM)	0.5	0.5

The main differences between the design B and C are presented in the initial design settings (user settings of the shape optimization tool described by *Parametrization info...* window), which are catalogued via tab. 5.13.

Tab. 5.13: *Design parameters comparison.*

	Design B	Design C
Changing model parameters	22	28
Shroud angle - inlet change	10	20
Middle angle - inlet change	10	20
Hub angle - inlet change	10	20
Shroud angle - outlet change	15	5
Middle angle - outlet change	15	5
Hub angle - outlet change	15	5
Meridional change	30	150

From the highest value of the hydraulic efficiency and the lowest value of $NPSH_3$ in the optimal flow rate defined by $Q = 0.181\ m^3/s$, it is recommended to choose the software settings according to the values of the design C, with the widest possible change of the inlet blade angle and the narrowest possible change of the outlet blade angle. The meridional change, which controls global shape of the meridional flow channel, supposed to be in the interval $\langle 30, 150 \rangle$.

Archive data comparison

The last design comparison is focused on the key element of the MOPSO optimization algorithm - **the archive**, where suitable impeller designs are stored.
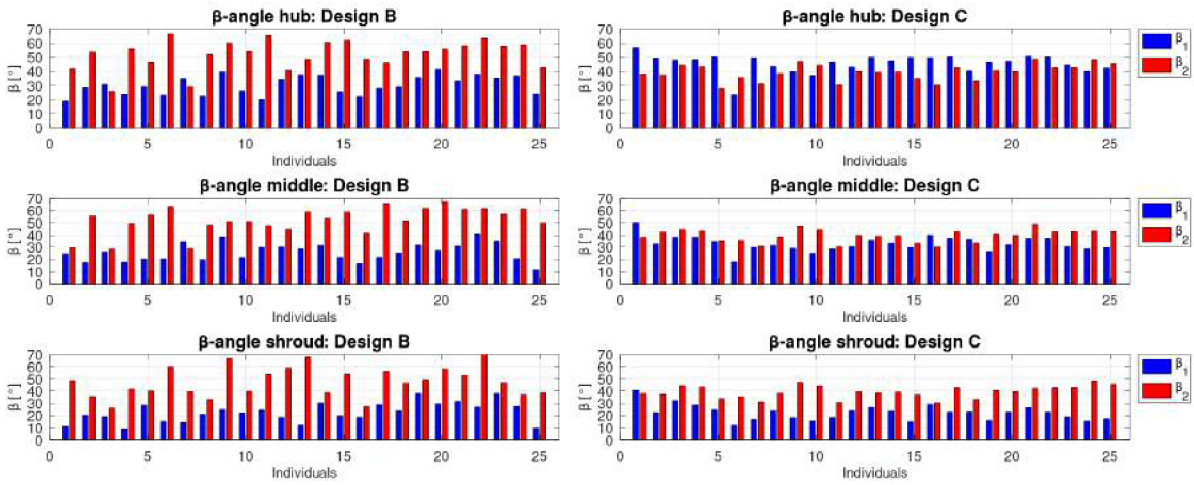
Fig. 5.77: *Blade angle comparison in archives.*

All individuals from the archive of the design B optimization run (fig. 5.77 left) show a dominant behaviour (trend) of the outlet angle β_2. The angle β_2 has larger magnitude on all investigated streamlines than the inlet angle. On the other hand, the archive members of the design C optimization run (fig. 5.77 right) strongly differs on hub and on the middle streamline. On the streamline near the hub the trend of the angle magnitudes is opposite comparing to the archive individuals of the design B. The β angle values on the middle streamline is quite mixed - some cases have the inlet angle bigger, some smaller - there is not a common/noticeable trend of the angle values.

Next step of the archive comparison is a focus on the two main pump parameters, which were investigated during the shape optimization - the hydraulic efficiency and head. The design B archive has slightly higher values of the pump head but lacks a consistency and higher magnitudes of the hydraulic efficiency of the design C run (fig. 5.78).
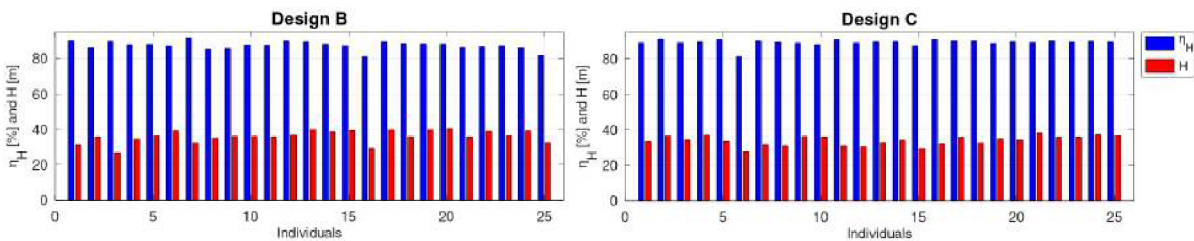
Fig. 5.78: *$\eta_H - H$ comparison.*

Pump turbine - partial conclusion

Three different types of pump turbine impeller designs were created (optimized) using the modified PSO/MOPSO optimization algorithm implemented in the presented shape optimization tool. In the previous sections and subsections were these designs portrayed by the red (**design A**), blue (**design B**) and green color (**design C**). Such designs have own advantages and disadvantages and the following text tries to briefly summarize them and afterwards deduces important conclusions, why is one design more suitable than the other one in the chosen **pump mode** only regime. The crucial task of the shape optimization tool was to design the proper impeller of the pump turbine to achieve the **wide range** of the high hydraulic efficiency in the requested flow rates together with the required head values and good hydraulic qualities related to the cavitation. The size of the impeller was **NOT** included under the process of the shape optimization - inlet and outlet diameters and also inlet and outlet widths were firmly set due to the unchanging geometries of the draft tube and the guiding vanes flow domains.

Presented optimization tool extensively utilized the **Multi-objective particle swarm optimization algorithm** enhanced by the **Pareto principles** and the commercial **ANSYS** software package, which was controlled and handled by the so-called **master code** - lines of the complex code with the MOPSO algorithm written in **MATLAB** programming language and compiled using free licensed **GNU Octave** software. For the impeller model creation was exploited **BladeGen** tool, the mesh was prepared in **TurboGrid** (tightly bonded with BladeGen) and pre-processing, post-processing and own CFD RANS simulations were done in **ANSYS CFX**, which excels in the flow capturing inside the hydraulic rotary machines. All mentioned tools from the ANSYS family were handled by the simple text files, which used only one periodical flow channel of the pump turbine impeller and run in so-called **batch mode** = software run without the graphical interface. Following three designs critically differ from the geometrical point of view in modelling (shaping) blades - design A follows the path, which was found by another optimization tool; design B utilized the pure linear change of the β angle and the design C was inspired by the knowledge from Gülich in [26]. It must be also mentioned that the **Bézier curves** were frequently utilized within presented optimization tool for their favourable attributes, to properly shape the meridional flow channel, the leading edge of the blade and in case of the design B also to correctly form the β angle along the length of the blade. The shape optimization tool and afterwards the optimization MOPSO algorithm employed **TEN** particles in their process/run together with the chosen end restriction, which was set to the total number of iterations → **25 iterations**.

Design A has the longest and the most complicated shape of the blade, which is closely connected with the β angle development from the leading edge to the trailing edge of the blade. This development was based on the output from the in-house shape optimization software [89] and set a huge limitation for a possible change - basically, the PSO algorithm (very early stage of the optimization tool) worked only in the close surroundings of the initial form of the blade and the distinctive shape change was not an option. Final β angle shape along the length of the blade near the shroud could be compared to the linear change, on the other hand, on the middle streamline and near the hub the β angle shape

remotely resembles the quadratic function. Design A has high hydraulic efficiency, but the lowest from all optimized designs. It fulfils requested pump head values (it did not overestimate them as the design B and design C). From the $NPSH_3$ point of view is design A in the end of the line of the optimized impellers with the highest (= the worst) magnitudes in the observed flow regimes. For the next comparison, let's set this design as the **unsuitable** one and compares it with chosen **suitable** design C.

Design B plentifully explored the linear change of the β angle on all three examined streamlines (near the shroud, in the middle and near the hub). This linear change of the β angle is the simplest one using only the inlet and outlet values of the β angles. Such change should be according to [27] energy efficient. Design B is characteristic for the shortest blade length among the all optimized impellers. In all performance characteristics and also in the $NPSH_3 - Q$ dependency lies this design in the middle - between the design A and C. But from a visual point of view this design could NOT be recommended due to unnaturally lying and short shape of the blades.

Design C utilized the inflection point in the β angle development mentioned in [26]. Such inflection point was created by the Bézier curves and ensures the gradual change of the β angle at the blade's inlet mainly for the reducing blade loading in such area and also for the outlet, which could be fully explored in the blade trimming. This design excelled in the hydraulic efficiency point of view, with the highest possible achieved values and with the widest range of the highest efficiency in the requested operational points. Design C also has the lowest values of $NPSH_3$ in the observed flow rates. Where this design falls behind is in the requested pump head magnitudes in the requested flow rates - it overestimated them. Such fact could be corrected by the user/engineer by decreasing the magnitude of the β_2, which is the main contributor in the proper pump head achievement.

Suitable/unsuitable design comparison

So, why is one pump impeller design suitable and another one not? These brief paragraphs will try to show and bring some insight into this subject, while comparing the chosen unsuitable **design A** and the suitable **design C**.

Let's start with the development of the β angle along the length of the blade. From the comparative CFD simulations arises, that the engineer should avoid modelling blades with the extremely crooked shapes of the β angle developments, such as in **design A** (figure 5.20). It creates the unstable flow patterns in the flow passages of the radial centrifugal pump, mainly the local eddies near the blades (fig. 5.24 - 5.26 and fig. 5.27 - 5.28) and the sudden static pressure drops inside the flow channel (fig. 5.23). These mentioned unstable flow phenomena strongly and negatively influence the main performance characteristics of the radial pump. Local eddies (depends on the position inside of the pump's flow passage) affect the hydraulic efficiency and pump head - usually the hydraulic efficiency is decreased by the formation of the local flow recirculation anywhere in the flow channel, and if local eddy is presented near trailing edge of the blade, it affects the value of the outlet β angle, which is the main contributor in the proper pump head achievement. The sudden and radical pressure drops are projected into the $NPSH_3 - Q$ dependency (fig. 5.70) - where design A has the highest (= the worst) values of achieved $NPSH_3$.

128

With the β angle development goes hand in hand the blade loading. From this point of the view, design A has the most unusual blade loading of the all optimized designs (fig. 5.72) - the suction and the pressure side of the blade almost switch their roles near the leading edge, meaning that the suction side had the higher static pressure values than the pressure side and also the overall average static pressure values near leading edge area are lower in the case of the design A, than the rest of the optimized design. On the other hand, the **design C** exploited the approach with the inflection point in the middle of each parametrized streamline. This modification was done by utilizing high degree Bézier curves, while modelling blades in the BladeGen tool. Mentioned inflection points ensured the moderate change of the β angle in the leading edge area and of course in the trailing edge area as well. According to Gülich [26], the mild change in the beginning of the blade will quite positively influence the cavitation attributes of the current impeller - this fact was successfully confirmed by numerical simulations united in fig. 5.70, where the design C came as a winner with the lowest possible $NPSH_3$ values of the all optimized designs. The subtle change of the β in the trailing edge area is beneficial in the blade (impeller) trimming (change of the outlet diameter) - if the impeller is already manufactured, it could be reused for the different operating conditions such as the smaller heads. Design C also excels in the highest values and in the widest range of the highest values of the hydraulic efficiency in requested operational points. One defect of this impeller is that it overestimated requested heads in chosen flow rate regimes, but it could be improved by the engineer by the slight outlet β angle decrease. The important conclusion comes from the perspective of the proper modelling of the β angle - it is crucial to avoid extremely crooked shapes. A way of the simple shapes is a key, but it is very important to make a mild change of the angle near the leading edge - it reduces some of the blade loading, which is afterwards transformed into the favourable values of $NPSH_3$ and also must inlet β angles must be **NOT** forgotten - angle values must be sorted from the hub to the shroud in the descending order.

From a brief evaluation of the shape of the blade in the blade-to-blade view (view, in which is the blade transformed/projected into the developed cylindrical surface area), it is strongly recommended to avoid the radical shape change as in the design A (fig. 5.23) located near the trailing edge in the middle/near the shroud region of the impeller. Such change leads to the unsuitable flow patterns in the flow channel accompanied by the formation of the local eddies. The shape change in the blade-to-blade view should be gradual as much as possible - see design C in fig. 5.51.

When the suitable β angle development is outlined, then the proper length of the blade must be set as well. Let's quickly employ the design B to this debate too and choose the right length, which will form favourable flow patterns in the radial centrifugal pump impeller. The long shaped blades usually guide water well in the flow passages of the pump, but with the length increase goes hand in hand the increase of the area of blade $\rightarrow$ higher hydraulic losses due to the greater wall-water interaction. On the other hand, very short blades produce smaller losses, but often must deal with the higher level of the blade loading. The design A possesses the longest length of the blade among all optimized designs - with the maximal value of the θ-angle (wrap angle) equals to 160°; the design B is on the other end of the spectrum with the shortest blades, with the maximal value of

the θ-angle equals to 100°. Both, the design A and the design B belong into a group with the unsuitable θ-angles $\rightarrow$ in this case (the pump turbine impeller in the pump mode = the centrifugal radial pump impeller) the proper shape of the impeller should possess the maximal value of the θ-angle from the interval $\langle 100^o, 160^o \rangle$ - preferably from the middle of this interval, such as design B with 120°. When focusing on the fig. 5.64, the change of the θ-angle is also crucially important - it looks, that the development of the angle, which tries to imitate the shape of the leading edge, is promising.

The last major difference between the so-called suitable and unsuitable design lies in the meridional point of view, to be more accurate in the average static pressure development inside the meridional flow channel. It is recommended to have once again a gradual change of the average static pressure from the low values, which are located near impeller inlet, to the high values, which are presented near impeller outlet (see design C in fig. 5.73). Such pressure change positively influences the hydraulic efficiency and also the $NPSH_3$ dependency.

To summarize the previous four paragraphs: from the comparative CFD simulations (and also from the measurements) emerge, that it is crucially recommended to make blades of the radial pump impeller **as simple as possible**. The extremely crooked shapes show the inconvenient flow patterns inside the impeller, which leads to the lower values of the hydraulic efficiency and the higher values of the $NPSH_3$. The **mild change** of the β angle near the leading edge is also crucially promising (on all streamlines) - it reduces some of the blade loading, which positively reflects in $NPSH_3$ dependency. With the proper shape of the blade goes hand in hand the **gradual change** of the average static pressure in the meridional flow channel, this fact is also very important in the process of designing the radial pump impeller.

5.2 Low specific speed centrifugal pump

The (very) low specific speed centrifugal pumps are widely used in various parts of industry, such as a pharmacy, an oil industry and even in a space engineering to deliver heterogeneous fluids in small amounts into the relatively high heads. This operating environment goes hand in hand with some unfavourable flow phenomena, which negatively influence the proper run of these mentioned pumps [40].

Rather poor hydraulic efficiency is characteristic for the low specific speed centrifugal pumps, mainly due to the major secondary flows (local eddies) inside the pump's flow channels (fig. 5.79).

Fig. 5.79: *Local eddies in the radial low specific speed pumps* [34].

This fact has a major role in the hydraulic losses increase and also in the decrease of the outlet β angle, which is the crucial contributor in proper achievement of the requested head. The lower hydraulic efficiency is not the only problem connected with the low specific speed pumps, also the pressure fluctuations and structural vibrations play a huge role here and must not be forgotten.
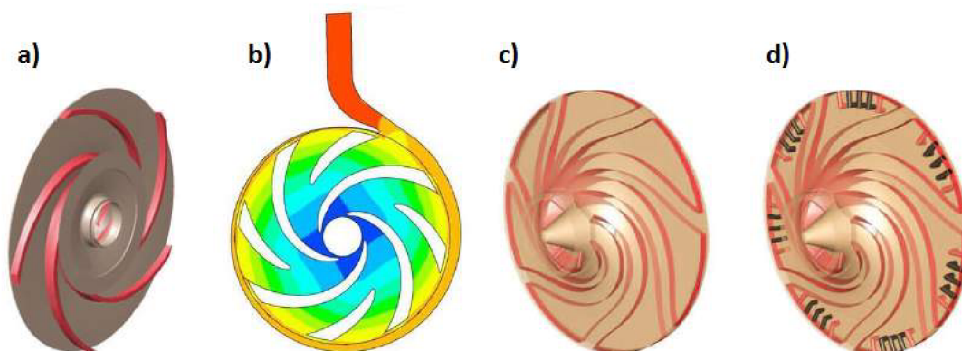
Fig. 5.80: *Designs of low specific speed pump* [34], [49], [50].

Several various pump modifications, which tried to reduce mentioned local eddies inside the flow channels, pressure fluctuations or structural vibrations, appeared in past few years - fig. 5.80 [34], [49], [50].

Figure 5.80 type a) demonstrates a classical type of the blades used in the centrifugal pump designs, which will be utilized and inspected in this part of the doctoral thesis; fig. 5.80 type b) shows an employment of the splitter blades (= shorter blades, which are iserted in the middle of the pump's flow channel to ensure proper fluid guiding) [34]; fig. 5.80 type c) displays design with thick trailing edges, which have a role in a narrowing of the flow channel (smaller flow area in the channel = higher relative velocity → lower probability of the local eddy formation) [49], and fig. 5.80 type d) also shows the thick trailing edges but with the recirculation channels [50].

As it was mentioned above, the so-called "classical" approach of the blade modelling was exploited in the following subsections of this thesis. But before a discussion about the optimized design and the comparative CFD simulations, the two main chapters must be properly clarified - the performance characteristics and the disk friction losses, which have a key role in a main differences between the low specific radial centrifugal pump impeller and the radial centrifugal impeller mentioned and utilized in section 5.1.

5.2.1   Disk friction losses

Disk friction losses in the centrifugal radial pump are produced by the front and rear shrouds of the impeller, which revolve in the water as hydraulically smooth or rough disks [26].

A participation of the disk friction losses in the power consumption of the centrifugal radial pump decreases exponentially with increasing specific speed. With the low specific speed pump, the disk friction is the primary cause of the loss: for the pump with $n_q = 10 \, \mathrm{min}^{-1}$ and $Re = 107$ - the disk friction is approximately 30 % of the useful power of the impeller [26].

The disk friction losses are dependent on the following parameters [26], [27]:
- Reynolds number Re $[-]$
- Average mean roughness of the rotating disk/casing wall Ra $[\mu m]$
- Axial sidewall gap s $[m]$
- Shape of the casing and size of the impeller sidewall gap.

Calculation (estimation) of the disk friction losses for optimal low rate [27]
First, the Reynolds number Re $[-]$ must be calculated from a following equation [27]:

$$Re = \frac{r_2^2 \cdot 2 \cdot \pi \cdot n}{\nu},\tag{5.3}$$

where r_2 $[m]$ is the outlet impeller radius, n $[s^{-1}]$ are revolutions per second and ν $[m^2 \cdot s^{-1}]$ is a kinematic viscosity.

The axial sidewall gap s $[m]$ is afterwards computed from a knowledge of the magnitude of the Reynolds number Re $[-]$ [27]:

$$s = \frac{2.97 \cdot r_2}{Re^{0.34}},\tag{5.4}$$

where r_2 $[m]$ is the outlet impeller radius.

The next step includes a determination of a roughness coefficient k_z $[m]$ [27]:

$$k_z = 4.5 \cdot 10^{-6} \cdot Ra^{0.97}, \qquad (5.5)$$

where Ra $[\mu m]$ is an arithmetic mean roughness of the impeller disks. And then the calculations of loss coefficients for the hub γ_1 $[-]$ and the shroud γ_2 $[-]$ take place [27]:

$$\gamma_1 = \frac{1}{\left[3.8 \cdot log\left(\frac{d_2}{2 \cdot k_z}\right) - 2.4 \cdot \left(\frac{2 \cdot s}{d_2}\right)^{0.25}\right]^2}, \qquad (5.6)$$

and [27]:

$$\gamma_2 = \frac{1}{\left[3.8 \cdot log\left(\frac{d_0 + \Delta_{shroud}}{2 \cdot k_z}\right) - 2.4 \cdot \left(\frac{2 \cdot s}{d_0 + \Delta_{shroud}}\right)^{0.25}\right]^2}, \qquad (5.7)$$

where d_0 $[m]$ is the inlet impeller diameter, d_2 $[m]$ is the outlet impeller diameter, k_z $[m]$ is the roughness coefficient (eq. 5.5), s $[m]$ is the axial sidewall gap (eq. 5.4) and Δ_{shroud} $[m]$ is the thickness of the shroud.

A power dissipation caused by the hub of the impeller is [27]:

$$P_{z1} = \frac{1}{4} \cdot \gamma_1 \cdot \rho \cdot (2 \cdot \pi \cdot n)^3 \cdot \left(\frac{d_2}{32}\right)^5, \qquad (5.8)$$

where γ_1 $[-]$ is the loss coefficient (eq. 5.6), ρ $[kg \cdot m^{-3}]$ is the fluid density, n $[s^{-1}]$ are revolutions per second, d_2 $[m]$ is the outlet impeller diameter. Analogically for the shroud [27]:

$$P_{z2} = P_{z1} - \frac{1}{4} \cdot \gamma_2 \cdot \rho \cdot (2 \cdot \pi \cdot n)^3 \cdot \left(\frac{d_0 + \Delta_{shroud}}{32}\right)^5, \qquad (5.9)$$

where Δ_{shroud} $[m]$ is the thickness of the shroud.

A total power dissipation P_z $[W]$ is afterwards computed [27]:

$$P_z = P_{z1} + P_{z2}, \qquad (5.10)$$

where P_{z1} $[W]$ is the power dissipation caused by the hub (eq. 5.8) and P_{z2} $[W]$ is the power dissipation caused by the shroud (eq. 5.9). Finally, a relative disk loss v $[\%]$ could be estimated from a ratio between the total power dissipation and the theoretical power of the pump [27]:

$$v = \frac{P_z}{P_{th}} = \frac{P_z}{\frac{Q \cdot H \cdot \rho \cdot g}{\eta_c}}, \qquad (5.11)$$

where P_z $[W]$ is total power dissipation (eq. 5.10), Q $[m^3 \cdot s^{-1}]$ is the requested flow rate, H $[m]$ is the requested pump head, ρ $[kg \cdot m^{-3}]$ is the fluid density, g $[m \cdot s^{-2}]$ is the gravitational acceleration and η_c $[-]$ is the total pump efficiency.

Tab. 5.14: *Used pump parameters for disk friction losses computation.*

	Value
Average mean roughness Ra $[\mu m]$	1.6
Shroud thickness Δ_{shroud} $[m]$	0.01
Total efficiency η_c $[-]$	0.45 (fig. 3.11)
Fluid density ρ $[kg \cdot m^{-3}]$	997
Kinematic viscosity ν $[m^2 \cdot s^{-1}]$	$1e^{-6}$
Inlet diameter (original design) d_0 $[m]$	0.425

For the requested pump parameters, such as the head, RPM, the flow rate and the outlet diameter, which are summarized in tables 5.15, 5.16 and the additional pump constraints depicted in the table 5.14 is the relative disk loss $\upsilon \approx \mathbf{27}$ %.

5.2.2 Effects of the impeller outlet angle on the pump head

In the case of the low and the very low specific speed centrifugal pumps, the outlet angle can be considerably larger than the basic recommendation e.g. in Gülich [26]. Such high value of angle deforms shape of the blade (fig. 5.81) and consequently change a shape of the theoretical head values (fig. 5.82).
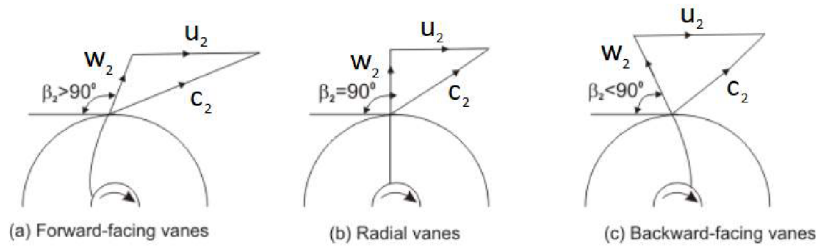
Fig. 5.81: *Outlet blade angles - different pump settings* [106].
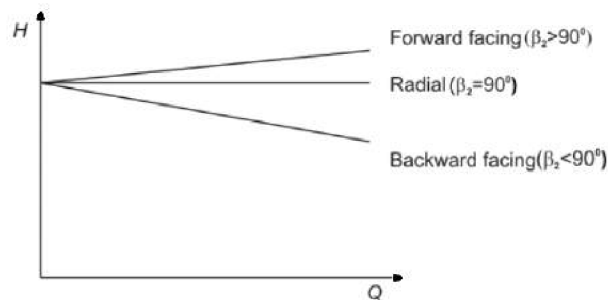
Fig. 5.82: *Theoretical head values* [82].

5.2.3 Requested and given parameters

The main requested low specific pump parameters represents table 5.15. Such table contains values for the prototype impeller, which was designed and afterwards measured in a hydraulic laboratory of **Viktor Kaplan department of Fluid Engineering** (shortly OFIVK) of Brno University of Technology [49], [50].

Tab. 5.15: *Requested pump parameters* [49], [50].

	Prototype
Pump head H $[m]$	32
Flow rate Q $[m^3/s]$	0.00694
RPM n $[1/min]$	1450

Requested pump parameters are utilized in equation 3.6 to properly determine pump's specific speed n_s $[min^{-1}]$:

$$n_s = 3.65 \cdot n \cdot \frac{Q^{0.5}}{H^{0.75}}$$
$$n_s = 3.65 \cdot 1450 \cdot \frac{0.00694^{0.5}}{32^{0.75}}$$
$$n_s = 33 \ min^{-1}.$$

For the additional understanding of the term "low specific speed" pump are computed the values of the differently evaluated specific speeds, namely: $n_b = 0.027 \ min^{-1}$ (eq. 3.7) and $n_q = 9 \ min^{-1}$ (eq. 3.8).

Design constraints

The shape and the position of the pump impeller were strictly constrained with the dimensional restrictions united in the table 5.16.

Tab. 5.16: *Dimensional constraints* [49], [50].

	Prototype
Outlet diameter d_2 $[mm]$	320
Outlet width b_2 $[mm]$	10
Number of blades z $[-]$	7

Presented dimensional constraints once again firmly set the size of the pump impeller. This fact means that size was **NOT** under the process of the shape optimization, only the shape was.

5.2.4 CFD simulations

An unsteady (URANS) simulations were utilized for the purpose of data correlation of CFD simulations between presented designs. The computational grids of the low specific speed pump impellers were created in commercial TurboGrid software as fully **hexahedral**. Inlet domain and spiral case were meshed in ANSYS meshing as **tetrahedral** with the high resolution prismatic layers towards the walls (fig. 5.83, 5.84).
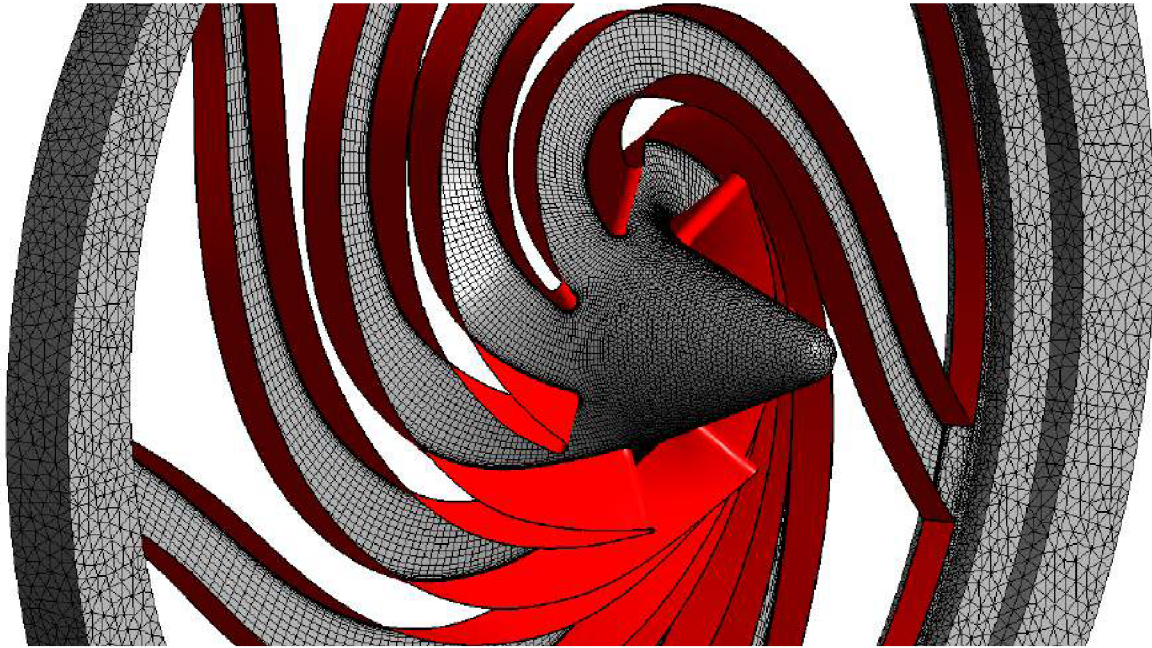
Fig. 5.83: *Sample of the computational mesh.*

The CFD calculations (RANS and URANS) were done in commercial software **ANSYS CFX** using standard k-ϵ model of turbulence. The k - ϵ turbulence model was chosen as in previous case of the pump turbine impeller, mainly due to the robust and stable behaviour during CFD simulations. The "High Resolution" option was selected for the advection scheme, "Second Order Backward" for the transient scheme and "High Resolution" for turbulence numerics. Chosen time step corresponds to 3° of the pump impeller revolution. Each time step had **5** inner iterations. As a domain initialization for URANS cases served steady simulation (RANS) with mixing planes between relative and absolute computational domains. Requested variables (velocity, pressure, etc.) for evaluation of pump head H and hydraulic efficiency η_H were averaging from last **10** whole revolutions of the pump impeller. $NPSH_3$ values was **NOT** evaluated in this case.

Complete model

The complete computational domain of the low specific speed centrifugal pump consists of the inlet tube (**1**) (with a certain part of the hub = nut), pump impeller (**2**) and the spiral case/volute (**3**) - all mentioned parts are captured in fig. 5.84.
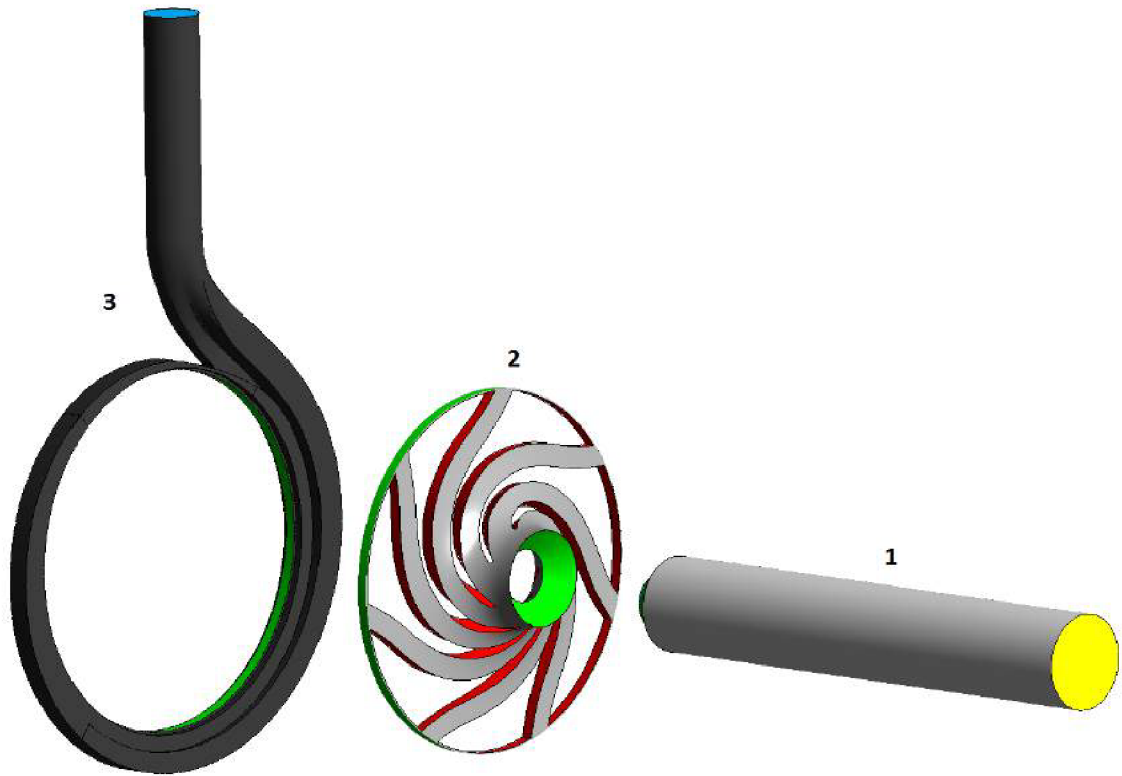
Fig. 5.84: *Complete CFD domain of low specific speed centrifugal pump.*

The inlet tube (**1**) is the absolute non-moving domain, with the nut (fig. 5.85), which rotated in the same direction and with the same RPM as the impeller. This computational domain contains inlet boundary condition (portrayed by the yellow surface in fig. 5.84, 5.85), which was characterized by the **zero** relative static pressure.
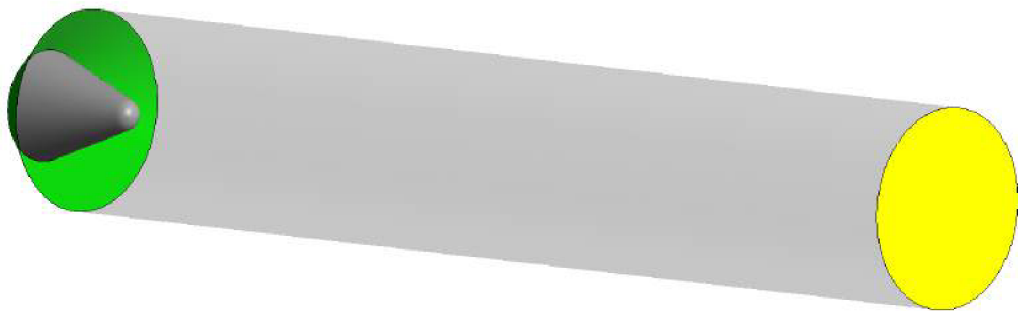
Fig. 5.85: *Inlet tube with the nut.*

Spiral case (**3**) is another absolute non-moving domain in the whole computational model. It contains outlet boundary condition, visualized by the blue surface in fig. 5.84. Such boundary condition was defined by the mass flow rate Q_m $[kg/s]$, which was computed using known density of the water $\rho = 997 \ kg/m^3$ (this is the default setting in ANSYS CFX commercial software). Total number of the six operational points (OP) was numerically simulated and for the purpose of the mutual comparison also examined - all points are summarized in table 5.17 with both, mass flow rate Q_m and flow rate Q.

Tab. 5.17: *Values of the flow rate for simulated operation points (OP).*

	Flow rate Q $[m^3/s]$	**Mass flow rate** Q_m $[kg/s]$
OP1	0.0015	1.496
OP2	0.003	2.991
OP3	0.006	5.982
OP4 (optimal flow rate)	0.007	6.979
OP5	0.008	7.976
OP6	0.01	9.97

The last domain is the pump impeller (**2**). It is the relative rotating computational domain with the hub, the shroud and the blades, which rotate with RPM set according the table describing requested parameters (tab. 5.15). Figures 5.84 and 5.85 also include green surfaces - they are domain interfaces between stationary and rotating parts of the complete pump computational model (for unsteady simulations are in ANSYS CFX called the transient rotor-stator type of the interfaces).

Wall y+ overview

Table 5.18 summarized wall $y+$ $[-]$ of every computational domain, which was employed in URANS CFD simulations. Exact wall $y+$ $[-]$ values were evaluated in the optimal flow rate defined by the table 5.15.

Tab. 5.18: *Wall y+ overview.*

	Area-average value of $y+$ $[-]$
Inlet tube	≈ 18
Original impeller	≈ 13
Optimized impeller	≈ 28
Spiral case	≈ 40

It must be noted that only **one** impeller design was created (optimized) using only the linear change of β angle, mainly because the unsuitable and the unstable tool behaviour during its run, while exploiting the inflection point approach → the optimization tool cyclically frozen in the phase of the random generation of the impellers; it cannot create suitable design, which could be afterwards examined via the numerical simulation. Such unstable behaviour is most likely caused by the long and narrow shape of the meridional flow passage of the pump, where even small changes of the β angle significantly change (deform) the blades. From this perspective, such created impeller is called in following sections the **Optimized impeller** and is compared with so-called **Original impeller** (with thick trailing edges and narrow flow channels), which was designed at OFIVK. The comparison is done only on the CFD simulations base.

5.2.5 Optimized design and complete results comparison

Blades of the optimized impeller (design)

As it was mentioned, only the **linear change** of the β angle was utilized to design the impeller of the low specific speed pump, mainly due to the unstable behaviour of the shape optimization tool, while exploiting inflection point approach mentioned in [26]. The shape optimization tool struggle revolved mainly around the random creation of the impellers in the beginning of the MOPSO algorithm - it did not manage to create suitable designs, so the optimization algorithm could not continue.

The optimized impeller is portrayed by figures 5.86 and 5.87. Fig. 5.86 introduces the optimized design by using two different views - the top and side look. On the other hand, fig. 5.87 is focusing in more detail on the impeller inlet and the leading/trailing edge of the blades.
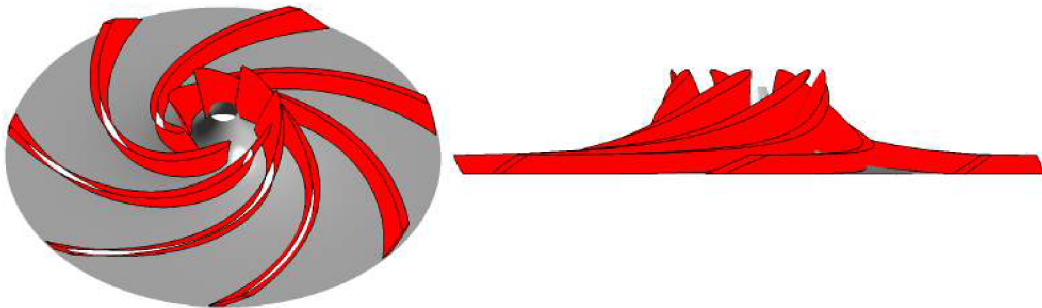
Fig. 5.86: *Geometry of the optimized impeller.*

The optimized design is characteristic for its blade length, the mild curvature of the leading edge and the sloped trailing edge.
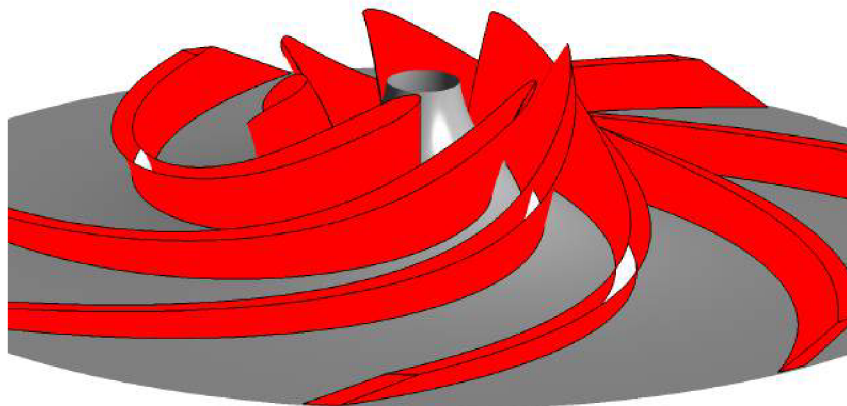
Fig. 5.87: *Geometry of the optimized impeller - detail.*

Figure 5.88 outlines the β angle development along the length of the blade. The inlet angles are sorted by the values in the descending order from the hub to the shroud. The outlet angles are the other way around, with the highest angle magnitude near the shroud and the lowest near the hub. Interestingly, all the β angle shapes (developments) intersect in 60 % of the blade length.
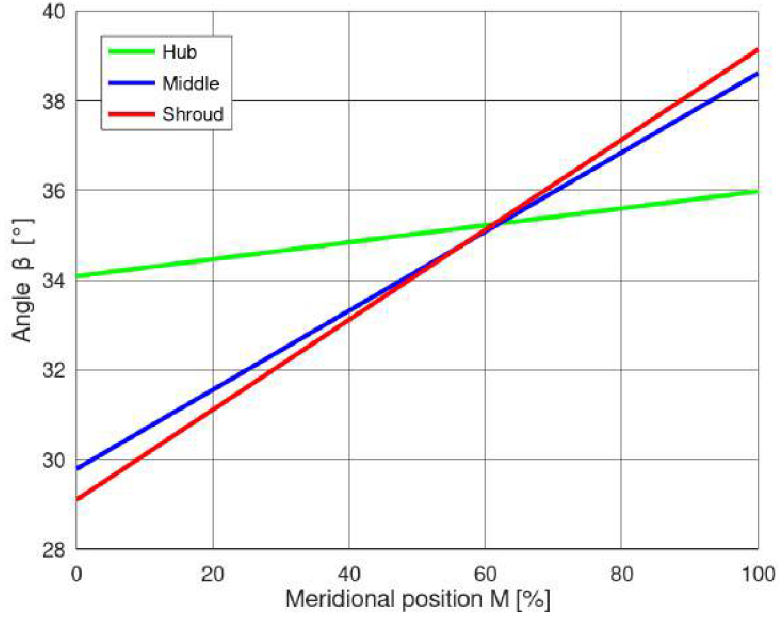
Fig. 5.88*: Developments of the β angle of the optimized impeller.*

The higher difference between the β_1 values (especially while comparing values near the hub and on the middle streamline) creates the slight curvature along the length of the blade - it is noticeable in the detail perspective of the optimized impeller portrayed by fig. 5.87.

Computed parameters - comparison
Following table (tab. 5.19) united and afterwards compares the main parameters of the optimized impeller of the pump. The β angles were evaluate only on the **middle streamline**. The hydraulic efficiencies are computed only for the impeller and only for the optimal flow rate.

Tab. 5.19*: Computed pump parameters - optimized impeller.*

	Design	1. method	2. method	3. method	4. method
Hydr. efficiency η_H [%]	90.32	55.96 [74]	79.76 [72]	51.28 [71]	69.83 [26]
Inlet angle β_1 [^{o}]	29.79	NaN [71]	24 [90]	12 [26]	-
Outlet angle β_2 [^{o}]	38.62	42 [27]	25 [71]	32 [26]	-

The hydraulic efficiency comparison between the CFD simulation and the 1D methodology described in sections above shows only how significant the disk friction losses are in the low specific speed pumps ($10 - 35$ % decrease in the hydraulic efficiency). The best estimation of the inlet β_1 angle brings the second computational approach [90]. The best β_2 angle guess is done by the first approach, which is based on the methodology of Haluza [27]. Also must be clarified the "NaN" acronym by the 1. method [71], while inspecting the inlet β_1 angle. This methodology failed in the computation of the β angle, to be more

140

accurate, it evaluated the c_{m1} velocity in such methodology as a complex number, which is strongly unsuitable in further computation.

Tab. 5.20: *Computed pump parameters - impeller comparison.*

	Original impeller	Optimized impeller
Hydraulic efficiency (CFD) η_H [%]	86.97	90.32
Inlet angle β_1 [^{o}]	-	29.79
Outlet angle β_2 [^{o}]	63	38.62

The optimized design managed to acquire the better/higher hydraulic efficiency of the impeller in the optimal flow rate and also it managed to reduce the outlet β angle from 63° to 39° (see table 5.20).

Blades comparison

The original impeller and the optimized impeller could be compared from the geometrical point of view. This fact is done in a well arranged way in fig. 5.89, where on the left with the green color are characterized thick blades of the original design and on the right are blades designed by the MOPSO algorithm, which was employed in the shape optimization tool.
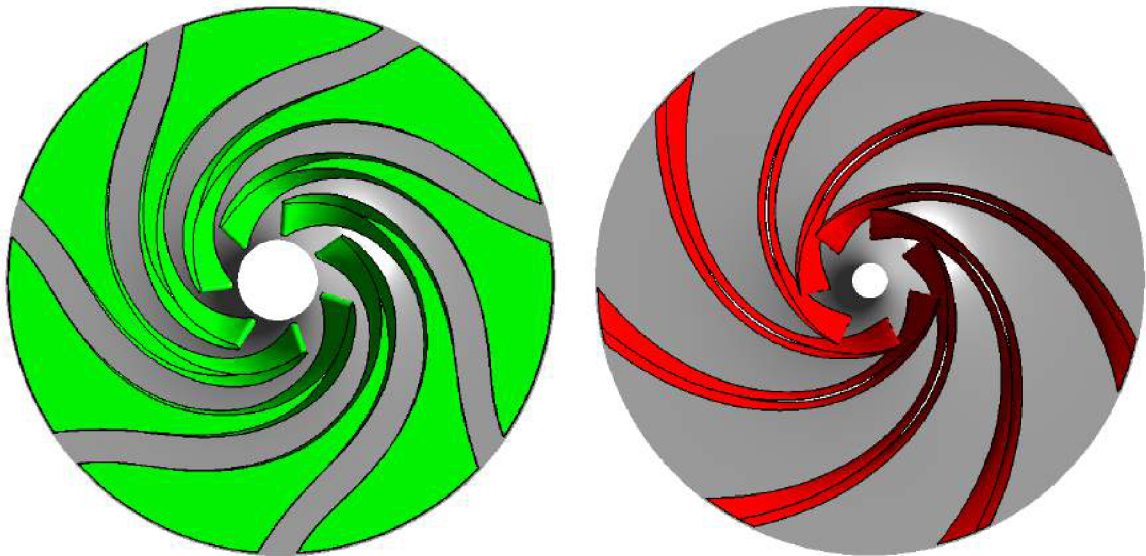
Fig. 5.89: *Design comparison.*

From such perspective (view in fig. 5.89), it is strongly noticeable a crucial geometrical difference between those two impellers. The original design has thick blades especially towards the trailing edge to ensure narrow flow channels, which should better guide water in the small flow rates. The optimized design exploited the traditional blade modelling with the constant blade thickness, which was set to $\Delta = 6\ mm$ [26].

Performance characteristics

Four main performance characteristics were constructed from the six operational points (see table 5.17) for both, the original design (portrayed by the green color) and the optimized one, which is coloured red. Each individual performance dependency is always pictured in one comparative figure to uncover possible similarities or differences.

First performance characteristic is the $H - Q$ dependency (fig. 5.90), with the design point marked as a black cross. From the chosen numerical simulation point of view, the original design did not reach requested head $H = 32\ m$. On the other hand, the optimized design strongly overestimated required head in flow rate $Q = 0.00694\ m^3/s$.
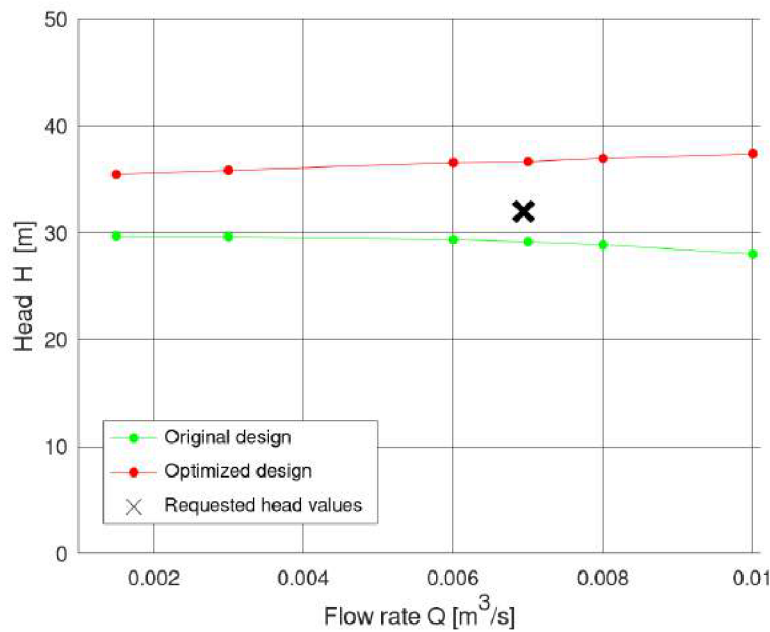
Fig. 5.90: $H - Q$ dependency comparison.

An interesting phenomenon could be observed in the $H - Q$ dependency, while focusing on the optimized impeller. The head values have a rising tendency from the smaller flow rates to the higher magnitudes - this fact is quite unusual for the $H - Q$ dependency in the radial centrifugal field of area with the outlet angle $\beta_2 \approx 40^o$ (see section 5.2.2). It is the head instability, probably caused by the very dissipative and turbulent flow inside the impeller and the spiral case, thanks to the global small flow rates, which are characteristic for the low specific speed pumps.

The second evaluated performance characteristic is the $\eta_H - Q$ dependency - fig. 5.91. Both designs do not have the highest possible value of the hydraulic efficiency in the design point defined by the flow rate $Q = 0.00694\ m^3/s$ - maxima are shifted towards larger flow rates, where the optimized impeller excels with the higher efficiency magnitudes.
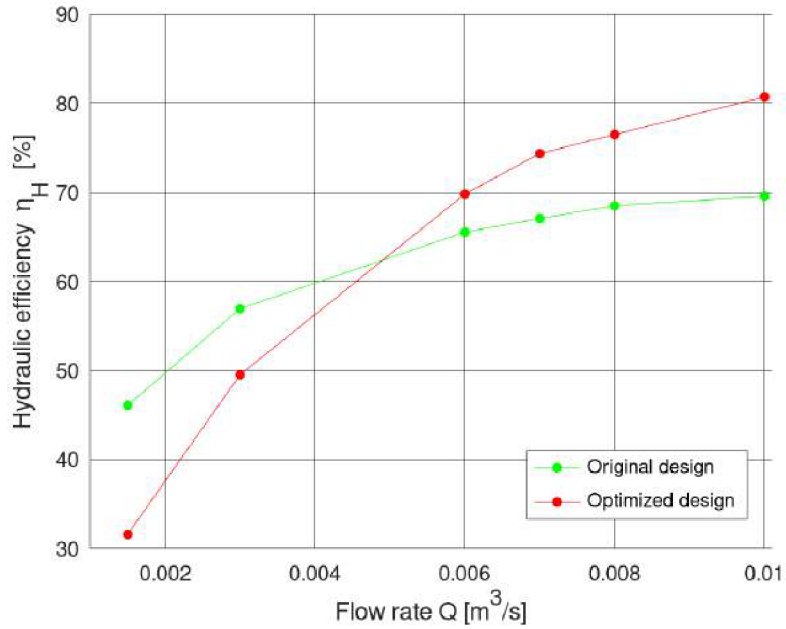
Fig. 5.91: $\eta_H - Q$ dependency comparison.
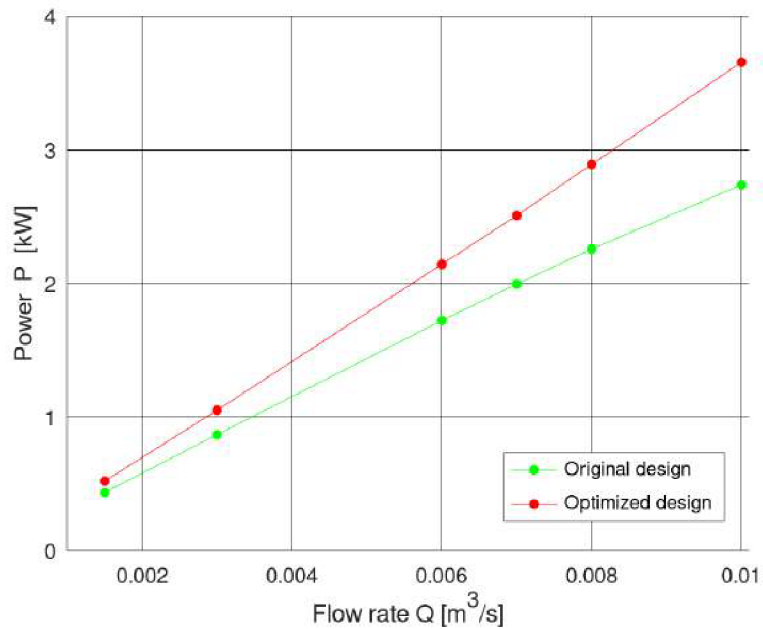
Fig. 5.92: $P - Q$ dependency comparison.

P - Q dependency (fig. 5.92) uncovers the higher power consumption of the optimized

design, which goes hand in hand with the higher values of the pump head and the hydraulic efficiency.
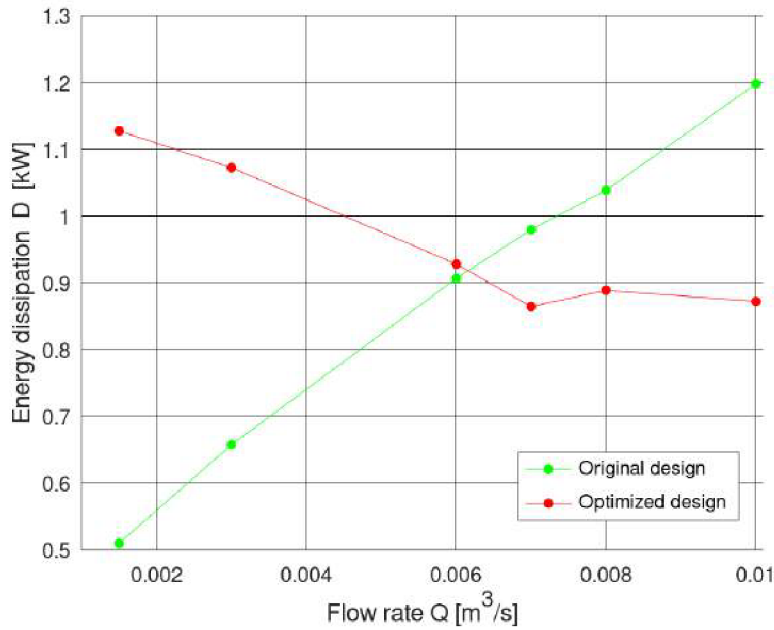
Fig. 5.93: $D - Q$ *dependency comparison.*

The last observed performance characteristic of the low specific speed centrifugal pump impellers in this section is the dependency of the energy dissipation D $[W]$ on the current flow rate Q $[m^3/s]$ - fig. 5.93. Both designs show unusual and strongly deformed developments of such dependency, which has commonly a shape as the quadratic function with the minimum around the value of the highest hydraulic efficiency. Mentioned deformation could be caused by the thick blades in the case of the original design and in the case of the optimized design it is a strong shift of the highest hydraulic efficiency values towards the higher values of the flow rate.

144

Pressure and velocity distributions - meridional view

In this section are first examined pressure (fig. 5.94) and afterwards velocity distributions (fig. 5.95) in the meridional point of view, with the original design on the left of and the optimized design on the right.

Figure 5.94 displays the contours of the average static pressure inside the impellers for a clipped range $\langle -40000\ Pa,\ 300000\ Pa \rangle$. Both designs indicate the gradual change of the average static pressure from the low values near the pump impeller inlet to the high values, which lie at the impeller outlet.
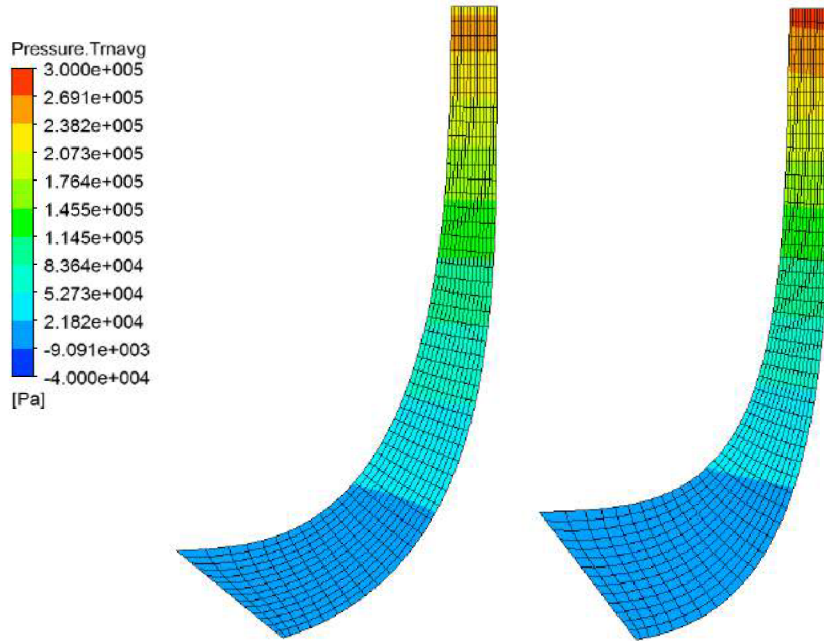
Fig. 5.94: *Avg. static pressure distribution in the meridional point of view (optimal Q).*
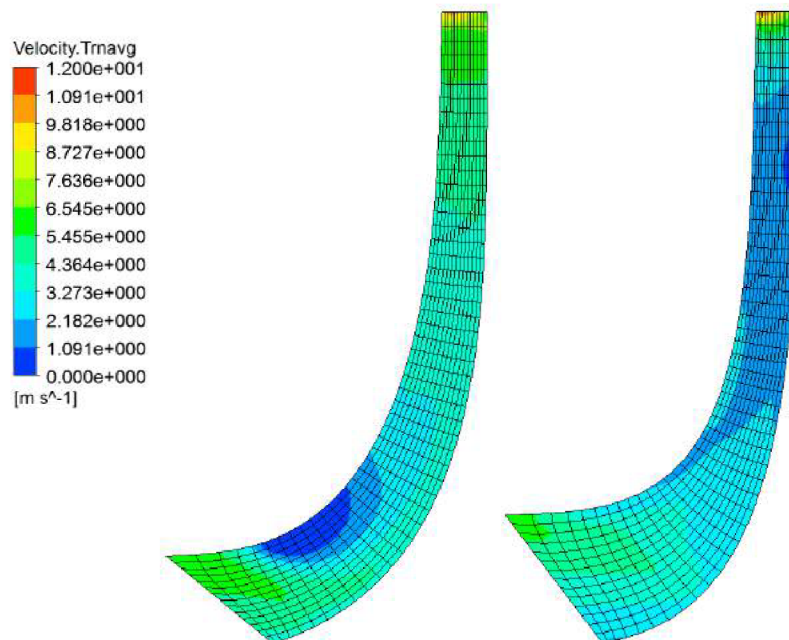
Fig. 5.95: *Avg. velocity distribution in the meridional point of view (optimal Q).*

145

The average velocity distributions in fig. 5.95 uncover recirculation passages inside both impellers → sudden drops in the velocity, captured by the dark blue color. The original impeller has the local recirculation near the inlet, where the leading edge of the blade is. On the other hand, in the optimized impeller the local eddies developed further in the flow passage - in the middle section towards the impeller outlet. These facts are also confirmed in figures 5.107 and 5.108.

Pressure and velocity distributions - blade-to-blade view

Both designs indicate the gradual change of the average static pressure from the leading edge to the trailing edge - fig. 5.96 and 5.97. While focusing on the original design, to be more accurate on the leading edge near the hub and on the middle streamline, there is the mild pressure drop caused by the improper water inflow into the impeller's passage (dark blue color). The same phenomenon is observable on the leading edge of the optimized impeller, but this time is located near the shroud.
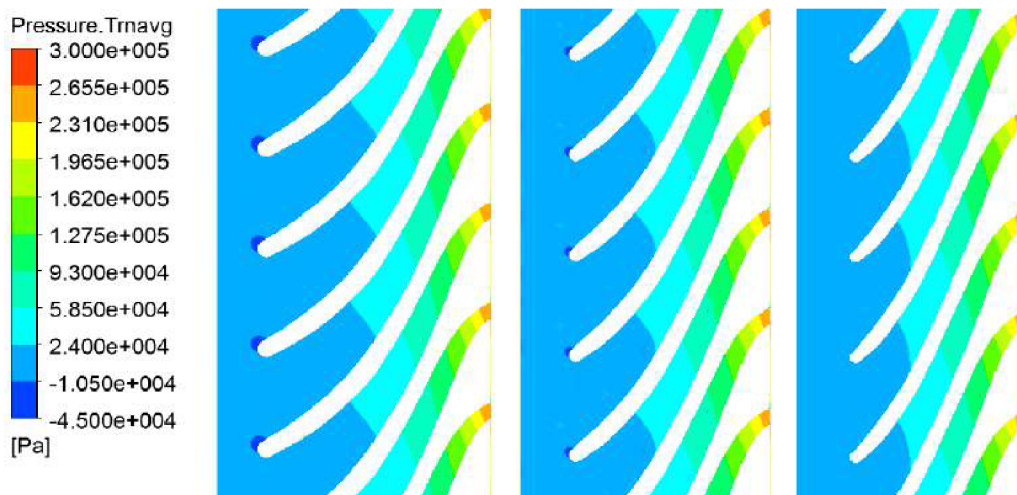
Fig. 5.96: *Avg. static pressure (hub, middle, shroud) - original design (optimal Q).*
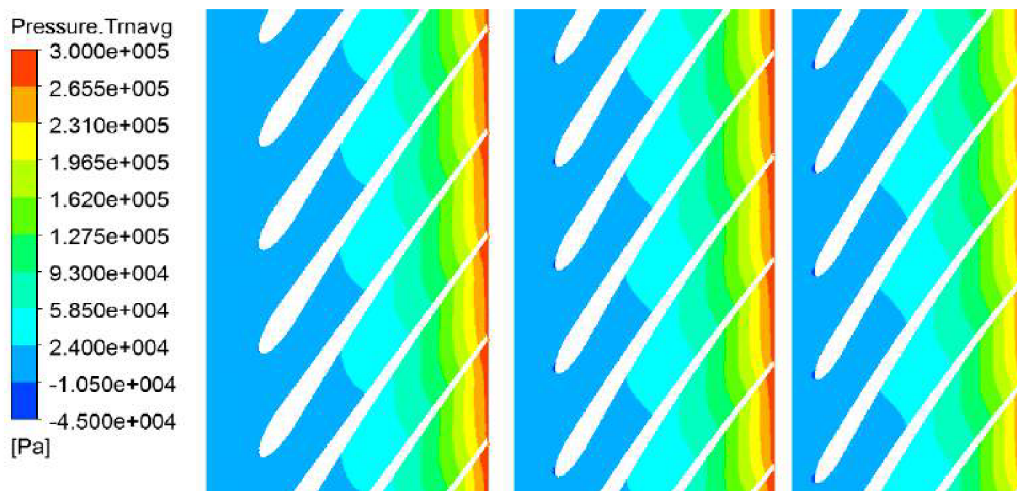
Fig. 5.97: *Avg. static pressure (hub, middle, shroud) - optimized design (optimal Q).*

146

Pressure and velocity distributions - blade loading

The last comparison in the area of the pressure distributions is focused on the blade loading of each design. The average static pressure along the length of the blade has usual development for the original and the optimized design - the pressure side of the blade has the higher values than the suction side. A major instability shows the original design. It is located on the trailing edge → massive pressure change caused by the thick trailing edge interaction with the volute cutwater (tongue of the volute).
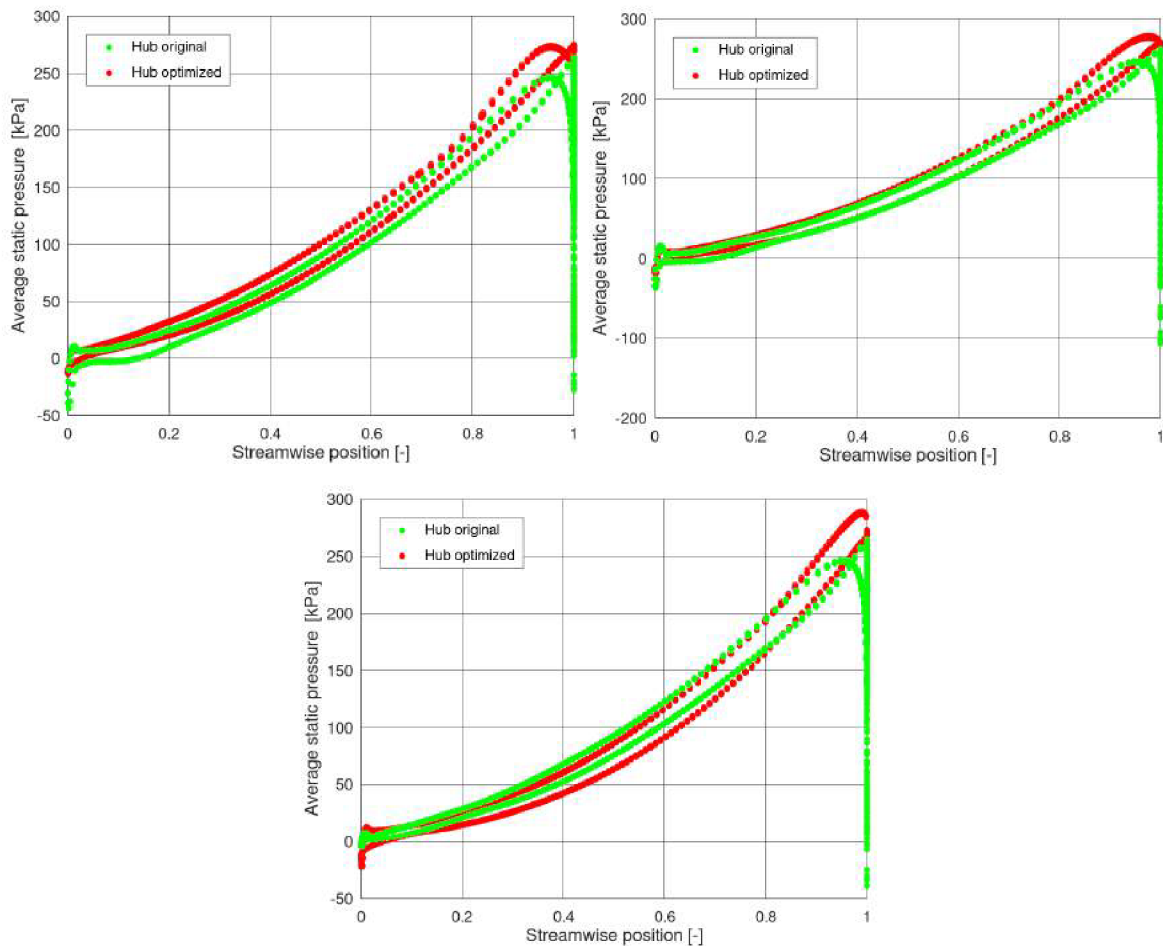
Fig. 5.98: *Blade loading - design comparison (optimal Q).*

From the global perspective, both designs share similar average pressure blade distribution along the length of the blade (except the pressure drop in the original design mentioned above).

Velocity vectors - blade-to-blade view

Figures 5.99-5.101 capture the vectors of the average velocity in the flow passages of the original design. First is outlined the flow near hub - fig. 5.99. The mild water shock is observable in the near hub region, with no flow recirculation areas across the whole flow channel.

147
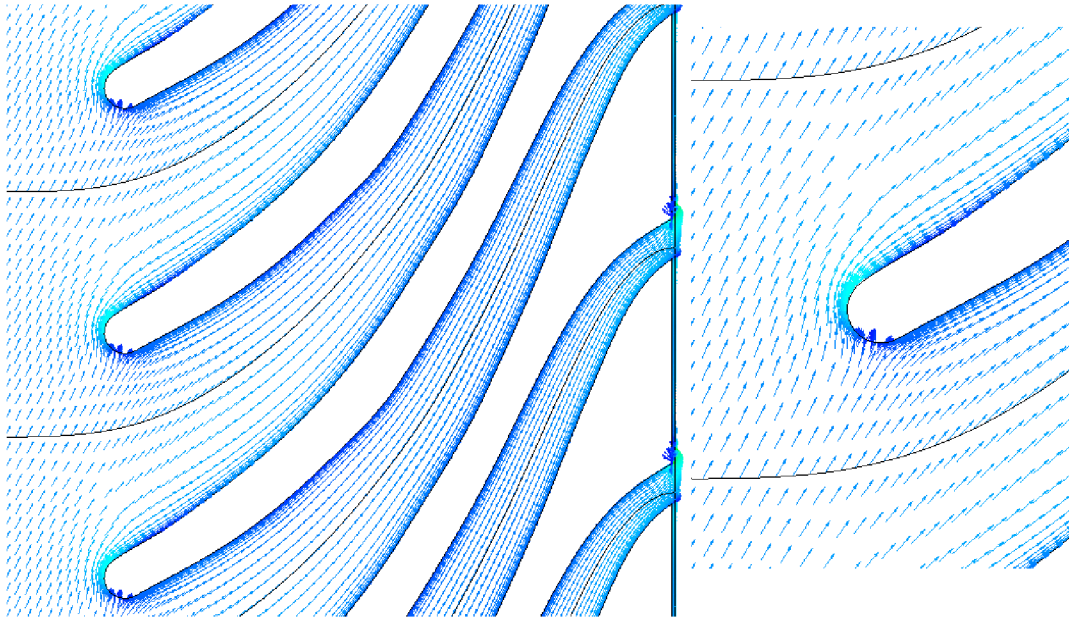
Fig. 5.99: *Avg. velocity vectors near hub - original design (optimal Q).*

Figure 5.100 focuses on the flow in the middle streamline. Once again the mild water shock is observable, while inspecting a detail of the leading edge. The small flow recirculation area is starting to be formed in the first third of the length of the blade, which propagated itself up to the impeller's shroud (fig. 5.101).
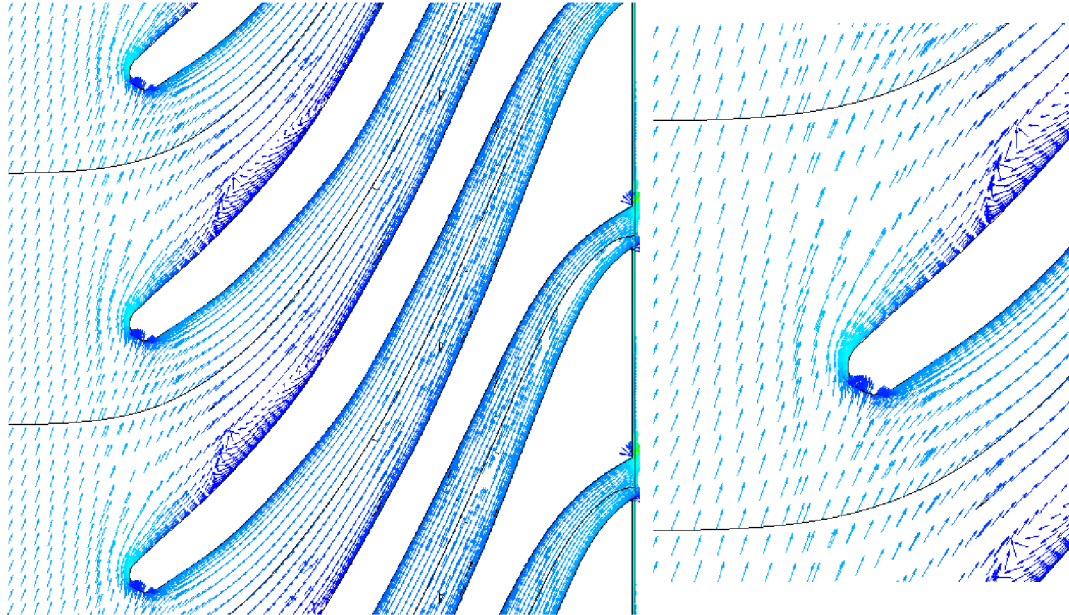
Fig. 5.100: *Avg. velocity vectors on middle streamline - original design (optimal Q).*

Near the shroud area of the original design is evaluated in fig. 5.101. The crucial unsuitable phenomenon here is the huge local eddy, which blocks almost the whole area between each individual leading edge. Such local eddy negatively influences performance characteristics of this design of the low specific speed pump.
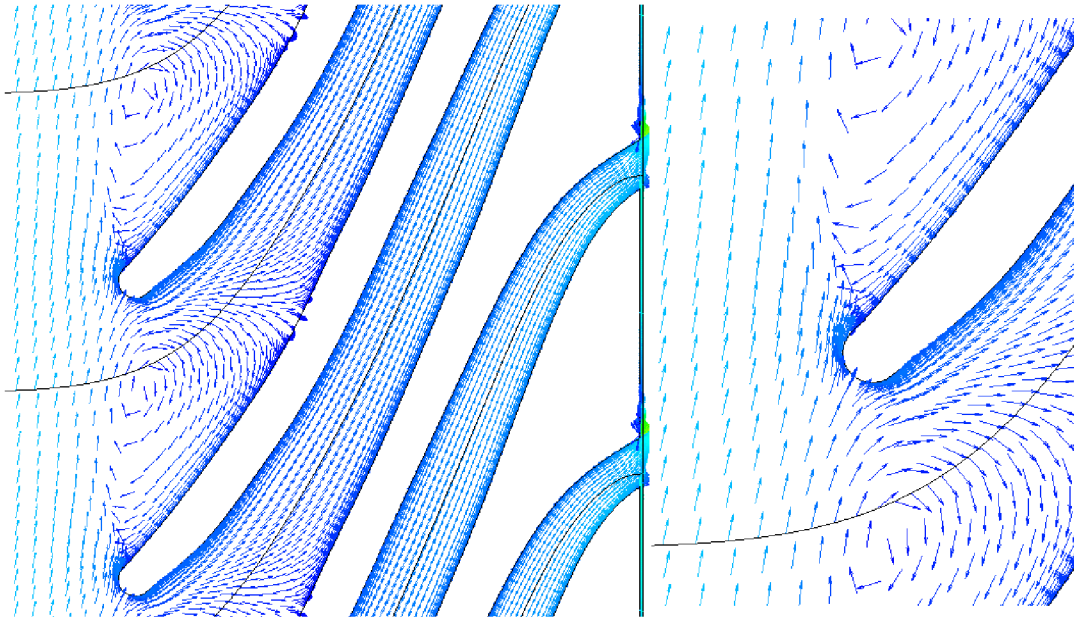
Fig. 5.101: *Avg. velocity vectors near shroud - original design (optimal Q).*

Last three figures in this section 5.102-5.104 orient towards the optimized design and flow inside impeller's passages. Common attribute for this design is the local eddies, which are formed in the second half of each flow channel and created the unsuitable flow patterns along the length of the blade (confirmed by fig. 5.108).
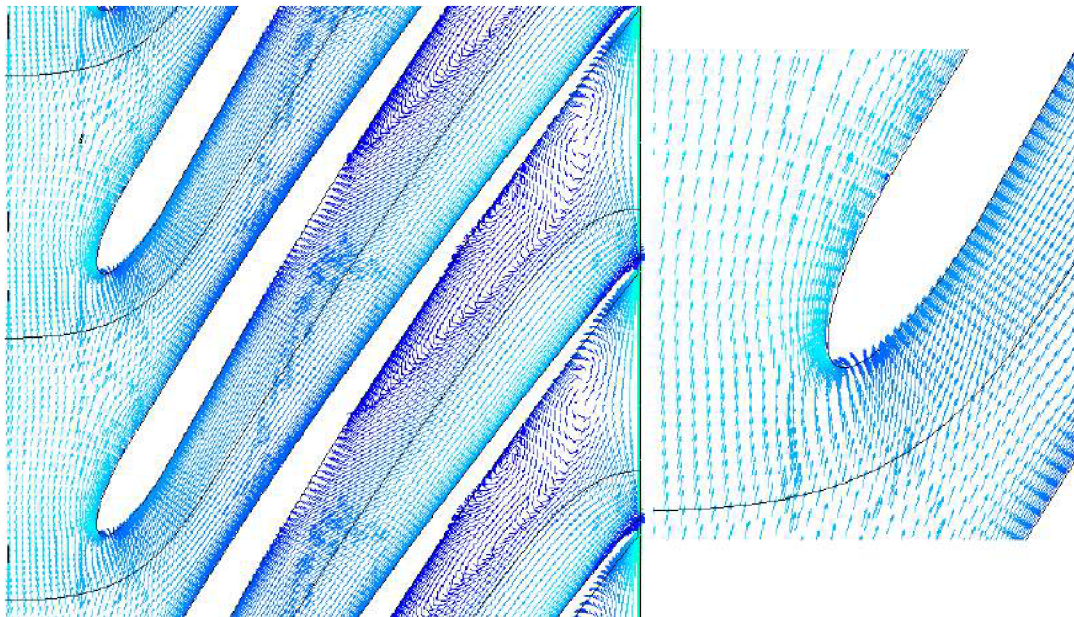
Fig. 5.102: *Avg. velocity vectors near hub - optimized design (optimal Q).*
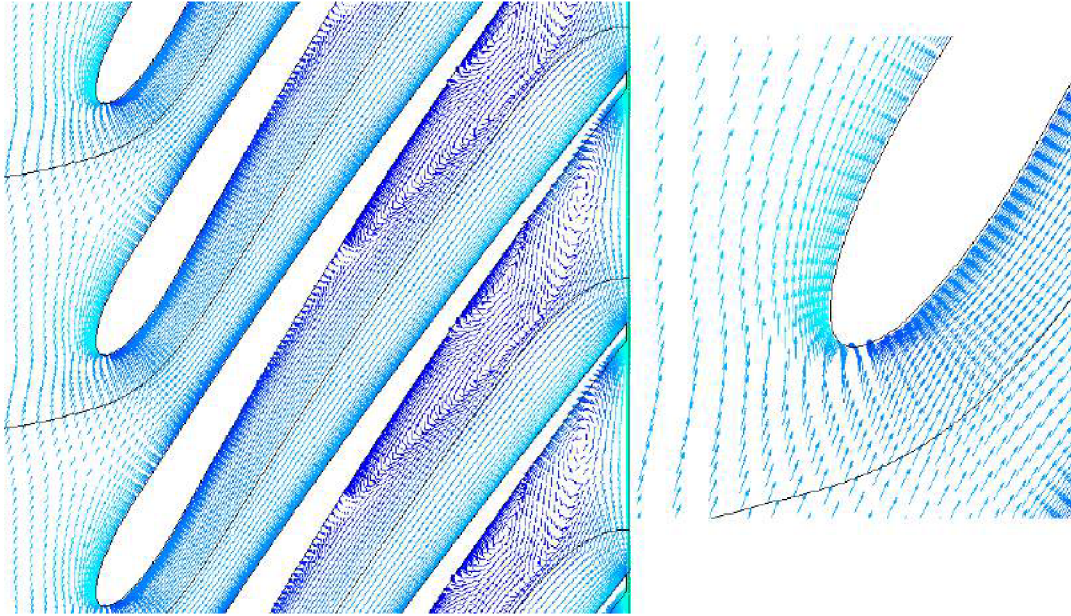
Fig. 5.103: *Avg. velocity vectors on middle streamline - optimized design (optimal Q).*
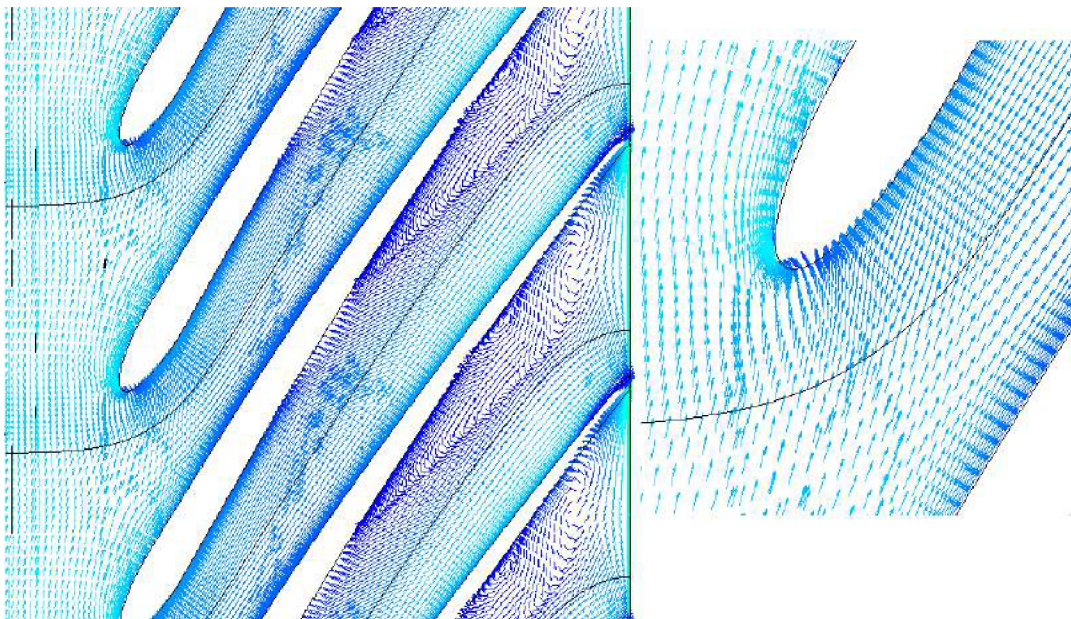
Fig. 5.104: *Avg. velocity vectors near shroud - optimized design (optimal Q).*

Focusing on the unproblematic water entry inside the flow channel of the optimized design - water imperfectly flow around the leading edge on the all three visualized streamlines (near the hub in fig. 5.102, on the middle streamline in fig. 5.103 and near the shroud in fig. 5.104).

Surface streamlines

Figures 5.105 and 5.106 illustratively indicate the streamlines projected on to the each individual blade of both, the original an the optimized impellers. In the original design are confirmed the recirculation passages near the leading edge. On the other hand, while

inspecting the optimized design - the local eddies further in the pump's flow channel are also affirmed.
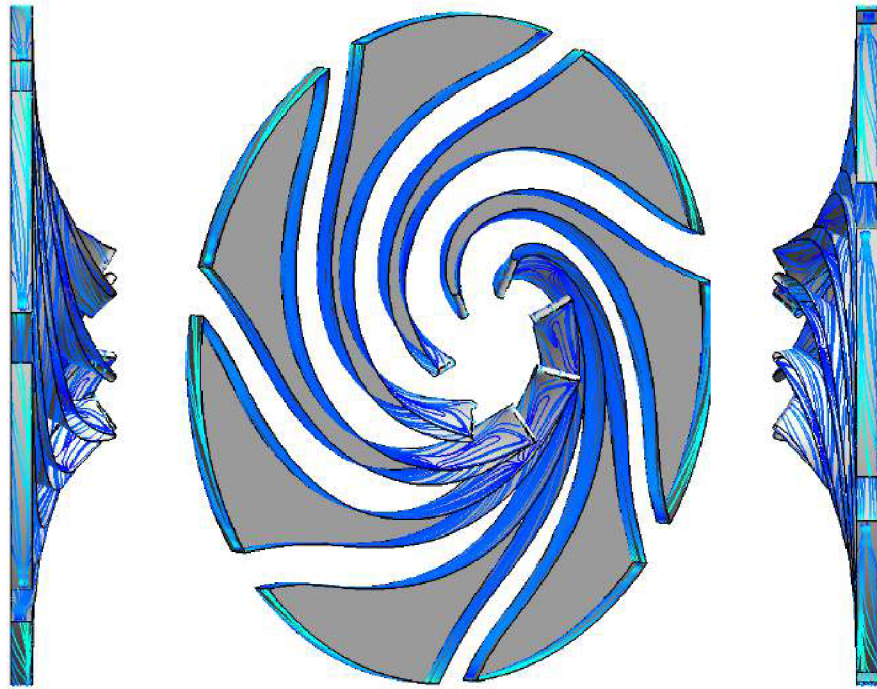
Fig. 5.105: *Surface streamlines - original impeller (optimal Q).*
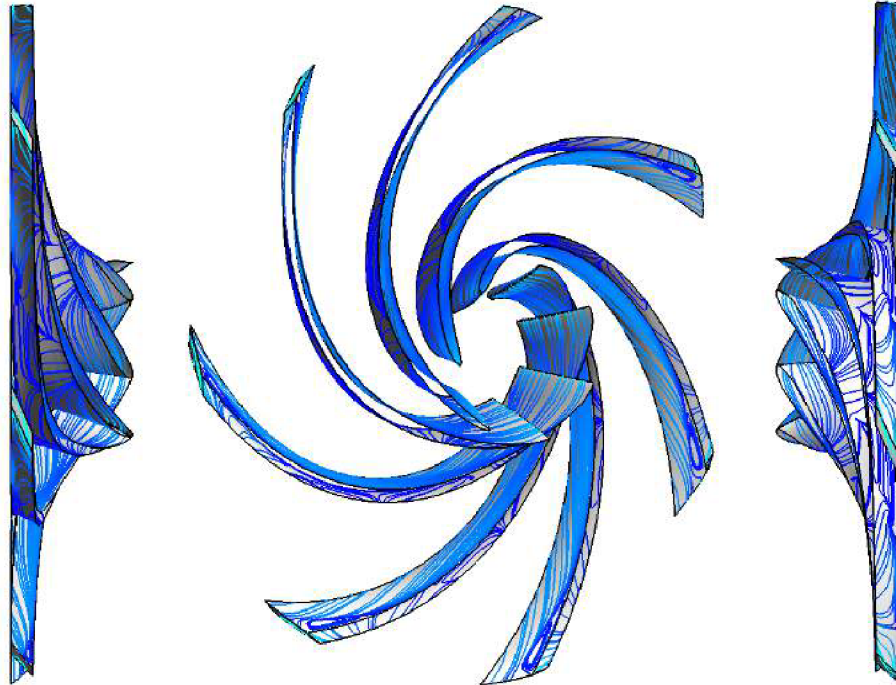
Fig. 5.106: *Surface streamlines - optimized impeller (optimal Q).*
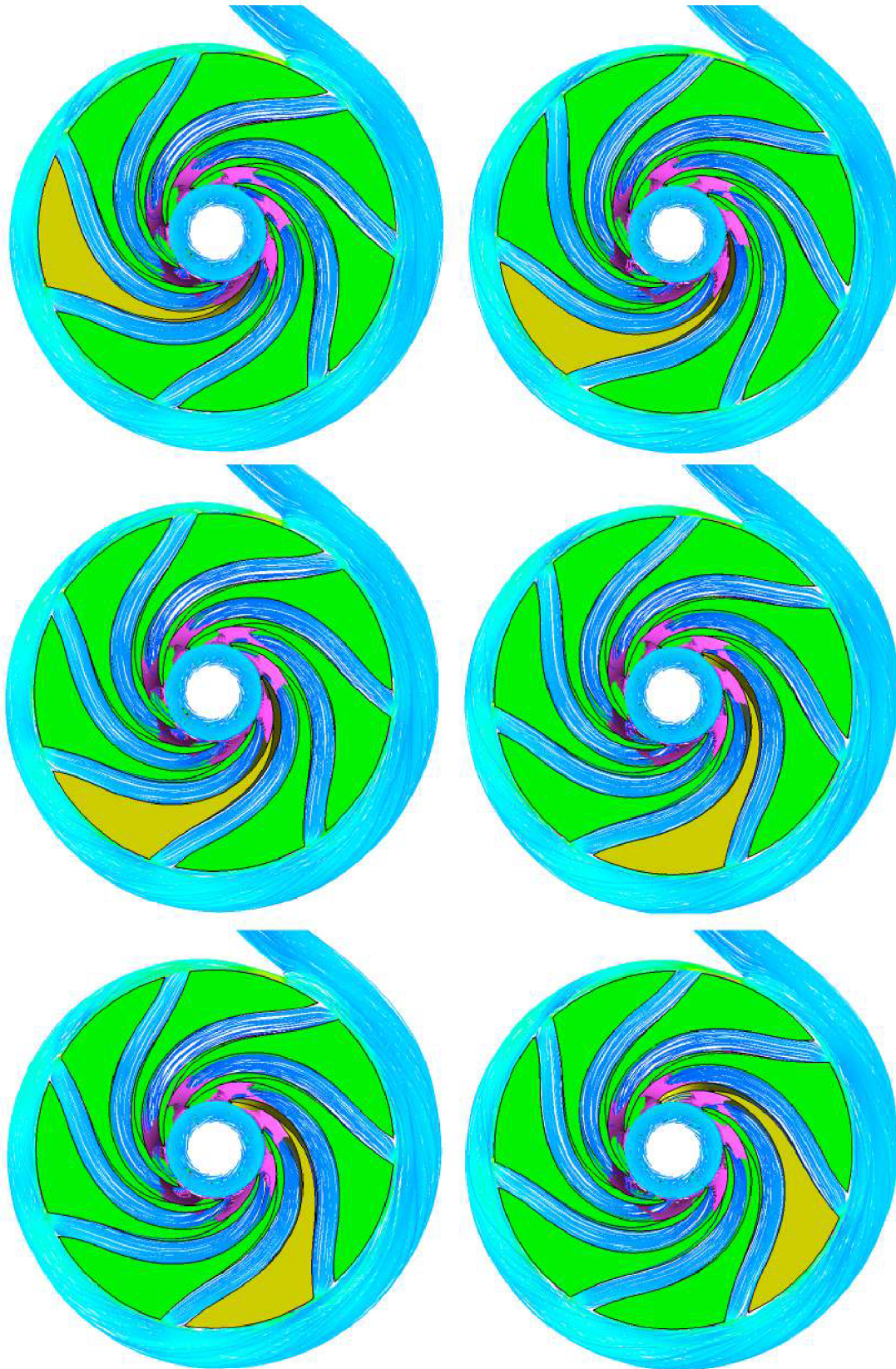
Fig. 5.107: *Streamlines inside of the original impeller (optimal Q).*

Fig. 5.108: *Streamlines inside of the optimized impeller (optimal Q).*

The crucial fault of the low specific speed centrifugal pumps is the formation of the local

eddies, mainly due to the globally small values of the flow rate, which are strongly characteristic for this pump type area. Figures 5.107 and 5.108 focus and afterwards display mentioned local eddies inside the flow channels of both, the original an the optimized design, with 3D streamlines and pink isosurfaces of the small values of the velocity - this fact is captured on the quarter of the one pump revolution. In the case of the original impeller, the recirculation passages formed near the leading edges of the blades, on the other hand, the optimized design shows the local eddies further inside the pump's flow channel. While comparing both mentioned figures, an idea behind the design with the thick blades is strongly noticeable - such blades try to "copy" positions of the created local eddies, presented in the optimized design for the purpose of the unproblematic water flow along the length of the blades.

Partial conclusion - low specific speed pump

The created shape optimization tool, illustratively described in subsections above, was applied on the problem of the creation of the proper design of the very low specific speed centrifugal pump ($n_s = 33 \ min^{-1}$). Such pumps suffer with several unsuitable flow and behaviour phenomena, which directly and negatively influence the proper run of the pump. Among them primarily belong: the formation of the local eddies, the pressure fluctuations or the structural vibrations. Several methods of "how to properly design blades" emerged in past few years, mainly the thick trailing edge approach or the splitter blade approach is worth mentioning. But in this doctoral thesis was utilized only the "classical" approach with the constant blade thickness, which is very characteristic for the centrifugal pump field of area. Such approach was exploited for a purpose of the possible local eddy or pressure fluctuation elimination.

The shape optimization tool possesses two different procedures, how to model the β angle development, which is strongly connected with the shape of the pump's blade. The first approach utilizes the pure linear change of the β from the leading to the trailing edge of the blade on the all exploiting streamlines. On the other hand, the second approach uses the inflection point within the β development, which creates the mild β angle change near the leading and the trailing edge of the blade. Here must be noted that only the linear change was fully exploited, mainly due to the unsuitable behaviour of the shape optimization tool, while exploring the inflection way of the blade modelling. The software struggled in the creation of the random pump impeller designs, which took place in the beginning of the MOPSO algorithm.

A tool set-up was identical as in the case of the **Design C** (displayed in the pump turbine sections of this thesis), with the widest possible change of the inlet angle and smallest possible change of the outlet angle. Once again, only **TEN** particles were employed during the shape optimization process and for the ending criterion was chosen finite number of iterations → **25 iterations**. As it was been several times mentioned, only one approach was utilized in this section, so from this perspective it was created only one design (the **optimized design**), which was compared with the thick trialling edge design developed in OFIVK in Brno University of Technology (the **original design**).

The optimized design is characteristic for its excessive blade length, the mild curvature

of the leading edge and the sloped trailing edge. The impeller possesses the constant blade thickness along the length of the blade - $\Delta = 6\ mm$. The inlet β angles are sorted by the values in the descending order from the hub to the shroud. On the other hand, the β outlet angles are the other way around, with the highest angle magnitude near the shroud and the lowest near the hub. Interestingly, all the β angle shapes (developments) intersect around 60 % of the blade length.

From the performance characteristic point of view (the main pump dependencies on the flow rate), the optimized design has the overall higher efficiency and also power values. The highest value of the hydraulic efficiency is shifted towards the higher values of the flow rate. The optimized design overestimated the requested pump head, which is defined by the value $H = 32\ m$. The shape optimization tool did not manage to eliminate the main flaws of the low specific speed centrifugal pump - in the flow channels of the optimized design are presented noticeable local eddies, which are the main contributors in the pressure pulsation (structural vibrations) and unsuitable (low) values of the hydraulic efficiency. The local eddies were confirmed by the 3D visualisation of the streamlines inside the pump flow channel, together with the highlighting of the smaller values of the fluid velocity. The pressure pulsations of the optimized (red) and the original design (green) are outlined in fig. 5.109, where the total pressure difference between the outlet and inlet boundary conditions in the optimal flow rate are depicted.
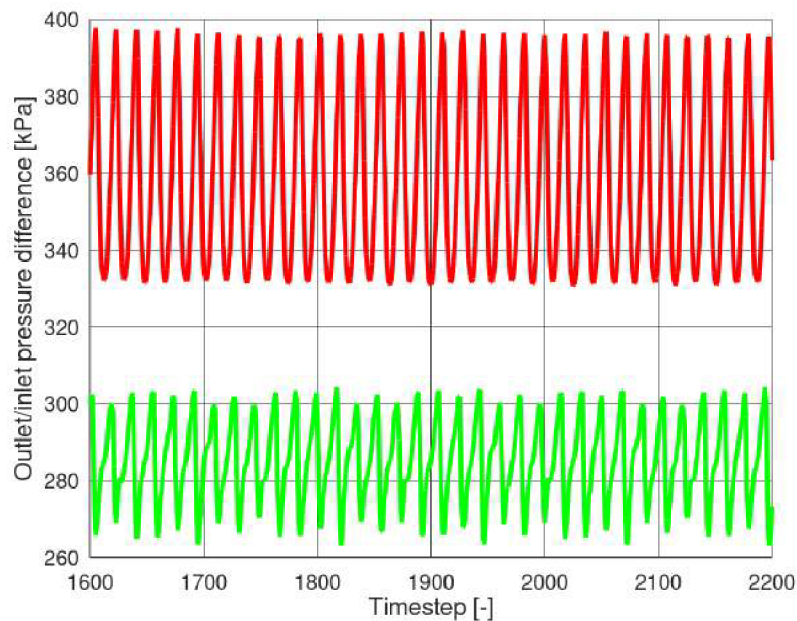
Fig. 5.109: *Total pressure pulsation comparison.*

The optimized design has in certain time passages almost $1.6 \cdot 10^5\ Pa$ pressure difference compared to $0.4 \cdot 10^5\ Pa$ pressure difference delivered by the original design. This fact negatively influenced pump head characteristic, with the strongly inconsistent deliver of the pump head values along the examined time period.

With the formation of the local eddies in the flow passages of the pump goes hand in hand the pulsation of the examined torque, which consists of the torque from the pump

blade, the shroud and the hub. Figure 5.110 compares the torque data of the green original and the red optimized design in the optimal flow rate - the optimized design shows the major periodical torque pulsation with the higher differences than the original design. This phenomenon had the lead role in the strong value inconsistency of the hydraulic efficiency during examined time period, which led even to non-physical values of such examined variables.
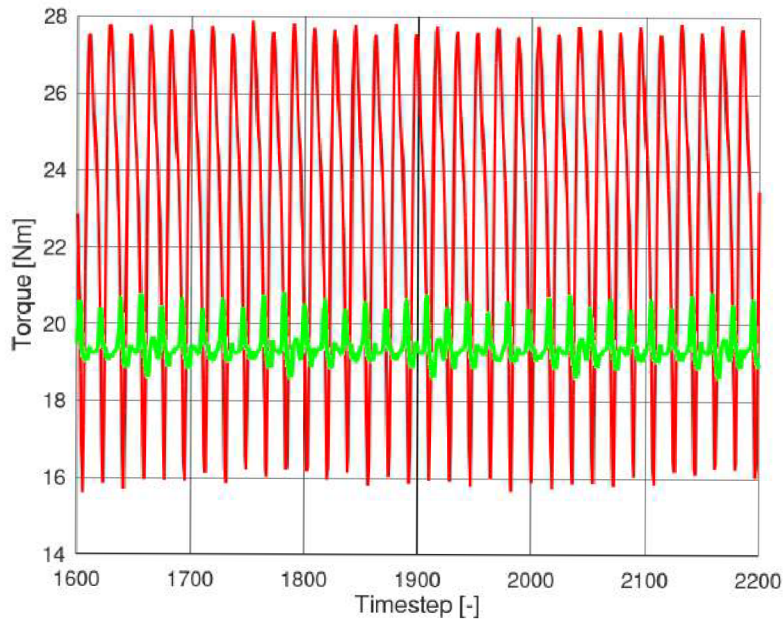
Fig. 5.110: *Torque comparison.*

From the overall perspective, the optimized impeller should be marked as the **unsuitable design**, mainly for its greater flaws, which were described in the text above.

156

6 CONCLUSION

This doctoral thesis aims to contribute to the study in the field of the shape optimization in the hydraulic machinery, to be more accurate in the field of the shape optimization of the radial centrifugal pumps. The thesis and author's work is focused on the creation of the shape optimization tool based on the **Particle Swarm Optimization** algorithm (PSOA). Such algorithm is strongly influenced by the social behaviour of the miscellaneous animals, such as birds or ants - it means that the algorithm run is population based (stochastic nature). Each individual member of the current population carries the information about the actual design features, the best achieved design so far and the velocity, which helps the member to properly move in the given computational area. PSOA together with the Pareto principles forms a strong alliance, which is suitable for the exploitation in the multi-objective shape optimization $\rightarrow$ introducing of the **Multi-objective Particle Swarm Optimization** (MOPSO).

The created shape optimization tool extensively exploited the commercial ANSYS software package, which was fully and autonomously controlled and handled by the **master code** - the complex code within the MOPSO algorithm written in the **MATLAB** programming language and compiled using free licensed **GNU Octave** software. For the impeller designs was exploited **BladeGen** tool (software for the pump/turbine model generation), the fully hexahedral mesh with the high cell resolution near walls was created in **TurboGrid** (here lies a tight bond with BladeGen) and pre-/post-processing and CFD RANS simulations were done in **ANSYS CFX**, which excels in the flow capturing inside the rotary hydraulic machines. All mentioned tools and software from the ANSYS family were handled by the text files, which used only one periodical flow channel of the radial pump for the purpose of time saving and run in the **batch mode** = the application run without the graphical interface (software run in the background of the Windows/Linux operating system). It must be noted that all the RANS simulations were performed remotely using the department's computational cluster **KAPLAN**. For this purpose were created the **shell scripts**, which had the task of the securing the mutual communication and the data transfer between the local PC with the master code and a disk space located in the presence of the KAPLAN cluster.

The crucial development of the shape optimization tool has been supported by three scientific articles, which laid a proper foundation to this academic task:

- MORAVEC, Prokop and Pavel RUDOLF. *Application of a particle swarm optimization for shape optimization in hydraulic machinery.* [63]
- MORAVEC, Prokop and Pavel RUDOLF. *Combination of Particle swarm optimization and Neder-Mead algorithm in diffuser shape optimization.* [64]
- POCHYLÝ, František, RUDOLF, Pavel, ŠTEFAN, David, MORAVEC, Prokop, STEJSKAL, Jiří and Aleš SKOTÁK. *Design of a pump-turbine using a quasi-potential flow approach, mathematical optimization and CFD.* [75]

The complete doctoral thesis is illustratively divided into the six main sections. In the beginning of this thesis is shortly summarized current state of art of the shape optimization methods, which are connected with the hydraulic flow parts and computational

fluid dynamics (CFD). Such optimization methods are here separated into three groups, starting with the most basic trial and error method, continuing with the exploitation of the commercial or non-commercial software and ending with utilization of correct optimization algorithms. The following main section is the theory section, which covers the basic theoretical basis around the shape optimization, Bézier curves, chosen Particle swarm optimization method and its multi-objective modification. Afterwards, 1D pump design section briefly explains chosen procedures and techniques, which are behind the proper design of the radial pump - such knowledge is then employed for the "starting" design in presented shape optimization problems. In the end of the work are the two main applications of the shape optimization tool - the case of the shape optimization of the **pump turbine** impeller and the shape optimization of very l**ow specific speed pump**. Final results from this optimization were compared with comparative CFD simulations and in the case of the pump turbine are also compared with the proper measurements performed by ČKD Blansko Engineering (grant **TH01020982** - *Zefektivnění akumulace energie a zajištění stability rozvodné sítě rozšířením provozního pásma přečerpávacích vodních elektráren*).

Mentioned case of the pump turbine impeller was extensively explored in this thesis, mainly thanks to the creation of three different impeller designs (**design A, B, C**), which heavily differed with β angle modelling approach. The design A, which was strongly influenced by another shape optimization software (based on the quasi-potential flow), was also manufactured as a model and afterwards measured for the purpose of the comparative CFD simulations. Design B explored the pure linear change of the β angle along the length the blade and design C utilized the inflection point within β development to ensure the mild change of the angle near the leading and the trailing edge of the blade. All optimized designs were inspected from several points of view - starting with the main performance characteristics and ending with the flow patterns inside each individual design. It must be noted that not only the one phase URANS simulations were exploited here, but also the two-phase URANS simulation were carefully utilized in the case of the pump turbine to successfully create another type of design comparison $\rightarrow$ the cavitation qualities were extensively explored (but out of the optimization procedure).

The second investigated test case for the presented shape optimization tool was the task of finding the proper shape of the very low specific speed centrifugal pump ($n_s = 33 \ min^{-1}$). Such types of the pumps suffer with a lot of unfavourable/unsuitable flow phenomena, namely: the formation of the local eddies, the pressure pulsations or the overall structural vibrations. Several modelling methods emerged in past few years to successfully eliminate these flow instabilities, but in this thesis was pursued the "classical" type of blade shape modelling with constant blade thickness along the length of the blade. It must be noted that the presented shape optimization tool cannot fully exploit its great potential here, meaning that the inflection approach in β angle modelling was not used $\rightarrow$ the tool struggled with the initial random impeller creation, mainly due to the uncharacteristic shape of the meridional flow channel of the very low specific speed centrifugal pump.

The main thesis outcome:
- The successful creation of the shape optimization tool, which in the unique way merged the MOPSO algorithm, the chosen ANSYS software and remote computation on the cluster KAPLAN.
- The confirmation of the suitable properties of the stochastic (population based) optimization algorithm in the hydraulic machinery field of interest.
- The basic outline of the suitable design of the radial centrifugal pump - with the gradual change of the average static pressure in the meridional view; the descending order of β angle inlet values (from the hub to shroud) with the overall simple β angle development or the mild β angle change near the leading an the trailing edge for the purpose of the reducing of the blade loading, which bring the favourable advantage in the cavitation qualities of the current optimized impeller.

LITERATURE

[1] ACKLEY, D.H.. *A connectionist machine for genetic hillclimbing.* United States, 1987.

[2] AGGIDIS, George A. and Audrius ŽIDONIS. *Hydro turbine prototype testing and generation of performance curves: Fully automated approach.* Renewable Energy, 2014, pp. 433-441 [cit. 2017-05-10]. Available: `http://www.sciencedirect.com/science/article/pii/S0960148114003048`.

[3] ALFONSI G. *Reynolds-Averaged Navier–Stokes Equations for Turbulence Modeling.* ASME. Appl. Mech. Rev. 2009;62(4):040802-040802-20. doi:10.1115/1.3124648.

[4] ANSYS FLUENT 19.1 Manual.

[5] AMPELLIO, Enrico, et al. *Turbomachinery design by a swarm-based optimization method coupled with a CFD solver.* Advances in aircraft and spacecraft science, 2016, pp. 149-170[cit. 2017-05-10].

[6] ARDIZZON, Guido, Giovanna CAVAZZINI and Giorgio PAVESI. *Adaptive acceleration coefficients for a new search diversification strategy in particle swarm optimization algorithms.* Information Sciences [online]. Elsevier, 2015, 299, 337-378 [cit. 2017-05-10]. DOI: 10.1016/j.ins.2014.12.024. ISSN 0020-0255. Available: `http://www.sciencedirect.com/science/article/pii/S0020025514011669`.

[7] AUDET, C. and J.E. DENNIS, Jr. *Mesh adaptive direct search algorithms for constrained optimization.* SIAM Journal on Optimization, 17(1), pp:188–217, 2006.

[8] BAHRAMI, Salman, Christophe TRIBES, Sven VON FELLENBERG, Thi C. VU and François GUIBAULT.*Physics-based Surrogate Optimization of Francis Turbine Runner Blades, Using Mesh Adaptive Direct Search and Evolutionary Algorithms.* International Journal of Fluid Machinery and Systems [online]. Turbomachinery Society of Japan, Korean Fluid Machinery Association, Chinese Society of Engineering Thermophysics, IAHR, 2015, 8(3), 209-219 [cit. 2018-02-10]. DOI: 10.5293/IJFMS.2015.8.3.209. ISSN 1882-9554

[9] BAHRAMI, S., C. TRIBES, C. DEVALS, T.C. VU and F. GUIBAULT. *Multifidelity shape optimization of hydraulic turbine runner blades using a multi-objective mesh adaptive direct search algorithm.* Applied Mathematical Modelling [online]. Elsevier, 2016, 40(2), 1650-1668 [cit. 2017-05-10]. DOI: 10.1016/j.apm.2015.09.008. ISSN 0307-904X. Available: `http://www.sciencedirect.com/science/article/pii/S0307904X1500493X`.

[10] BLAZEK, J. *Computational fluid dynamics: principles and applications.* Amsterdam: Elsevier, 2005, 440 s. : il. 1 CD-ROM. ISBN 0-08-043009-0

[11] BOWERMAN, R.D. and A.J. ACOSTA. *Effect of the Volute on Performance of a Centrifugal-Pump Impeller.* ASME. 1957. pp. 1057-1069.

[12] BROYDEN, C. G. *The convergence of a class of double rank minimization algorithms: The new algorithm.* J. Inst. Math. Appl., 6 (1970), pp. 222–231 [cit. 2017-05-10]. Available: `http://www.math.unm.edu/~vageli/courses/Ma576/Broyden2.pdf`.

[13] BURGREEN, Greg W. and James F. ANTAKI. *CFD-based design optimization of a three-dimensional rotary blood pump.* Symposium on Multidisciplinary Analysis and Optimization. Bellevue, 1996, p. 1-6 [cit. 2017-05-10]. DOI: 10.2514/6.1996-4185. Available: `https://www.researchgate.net/profile/Greg_Burgreen/publication/245633724_CFD-Based_Design_Optimization_of_a_Three-Dimensional_Rotary_Blood_Pumps/links/56edb51208aed17d09f74ed5.pdf`.

[14] COELLO, C.A.C. and M. S. LECHUGA. *MOPSO: A proposal for multiple objective particle swarm optimization..* In Proc. Congr. Evolutionary Computation (CEC'2002), vol. 1, Honolulu, HI, May 2002, pp. 1051–1056 [cit. 2017-04-10]. Available: `http://ieeexplore.ieee.org.ezproxy.lib.vutbr.cz/document/1004388/`.

[15] COELLO, C.A.C., G.T. PULIDO and M.S. LECHUGA. *Handling multiple objectives with particle swarm optimization.* Evolutionary Computation, IEEE Transactions on [online]. USA: IEEE, 2004, 8(3), pp. 256-279 [cit. 2017-04-10]. DOI: 10.1109/TEVC.2004.826067. ISSN 1089778X1089778X. Available: `http://ieeexplore.ieee.org/document/1304847/`.

[16] ČERKASSKIJ, V. M. *Nasosy, ventiljatory, kompressory.* Moskva: Eněrgoatomisdat, 1984. str. 405.

[17] DERAKHSHAN, Sh. and A. MOSTAFAVI. *Optimization of GAMM Francis turbine runner.* World Acad. Sci. Eng. Technol, 2011, pp. 717-723 [cit. 2017-04-11].

[18] DERAKHSHAN, Shahram, et al. *Numerical shape optimization of a centrifugal pump impeller using artificial bee colony algorithm.* Computers and Fluids, 2013, pp. 145-151 [cit. 2017-05-10]. Available: `http://www.sciencedirect.com/science/article/pii/S0045793013001588`.

[19] DERAKHSHAN, Shahram, et al. *Numerical Shape Optimization of a Wind Turbine Blades Using Artificial Bee Colony Algorithm.* ASME. J. Energy Resour. Technol. 2015; 137(5):051210-051210-12. doi:10.1115/1.4031043.

[20] EBERHART, R. and J. KENNEDY. *A new optimizer using particle swarm theory.* In: Micro Machine and Human Science, 1995. MHS '95., Proceedings of the Sixth International Symposium on [online]. Nagoya: IEEE Publishing, 1995, pp. 39-43 [cit. 2017-04-11]. DOI: 10.1109/MHS.1995.494215. ISBN 0-7803-2676-8. Available: `http://ieeexplore.ieee.org.ezproxy.lib.vutbr.cz/document/494215/`.

[21] EISNER, R. and A. RUPRECHT. *Automatic shape optimization of hydro turbine components based on CFD.* Institute of Fluid Mechanics and

Hydraulic Machinery University Stuttgart. 2001 [cit. 2017-04-10]. Available: `http://kwk.ihs.uni-stuttgart.de/fileadmin/IHS-Startseite/veroeffentlichungen/v2001_05.pdf`.

[22] FLETCHER, R. *A new approach to variable metric algorithms.* Computer J., 13 (1970), pp. 317–322 [cit. 2017-05-10]. Available: `https://academic.oup.com/comjnl/article/13/3/317/345520/A-new-approach-to-variable-metric-algorithms`.

[23] GARY WANG, G., Zuomin DONG a Peter AITCHISON. *Adaptive response surface method - A global optimization scheme for approximation-based design problems.* Engineering Optimization [online]. Taylor, 2001, 33(6), 707-733 [cit. 2018-05-21]. DOI: 10.1080/03052150108940940. ISSN 0305-215X.

[24] GOLDFARB, D. *A family of variable metric methods derived by variational means.* Math. Comp., 24 (1970), pp. 23–26 [cit. 2017-05-10]. Available: `https://www.jstor.org/stable/2004873?seq=1#page_scan_tab_contents`.

[25] GRAMAZINI, Joe-Ray. *Adjoind-based airfoil shape optimization in transonic flow.* Missouri, 2015. A thesis [cit. 2017-05-11]. Missouri University of Science and Technology. Supervisor Dr. Serhat Hosder.

[26] GÜLICH, Johann Friedrich. *Centrifugal pumps.* 3rd edition. Heidelberg: Springer, 2014, xli, p. 1116. ISBN 978-3-642-40113-8.

[27] HALUZA, Miloslav. *Tekutinové stroje I.* Lectures notes. Brno: University of Technology. Faculty of mechanical engineering. 2013.

[28] HALUZA, Miloslav and Pavel Zubík. *Porovnání výpočtu a měření metodou PIV radiálního oběžného kola čerpadla.* [cit. 2018-16-04] Brno: University of Technology. Available: `http://www.fce.vutbr.cz/VST/zubik.p/PIV5.pdf`.

[29] HARBECK, Michael and Antony JAMESON. *Exploring the limits of shock-free transonic airfoil design.* In: 43rd AIAA Aerospace Sciences Meeting and Exhibit. 2005, p. 1041 [cit. 2017-05-11]. Available: `http://aero-comlab.stanford.edu/Papers/harbeck.aiaa.05-1041.pdf`.

[30] HASMATUCHI, Vlad, François AVELLAN and Mohamed FARHAT. *Hydrodynamics of a Pump-Turbine Operating at Off-Design Conditions in Generating Mode.* EPFL (Lausanne), 2012. DOI: 10.5075/epfl-thesis-5373.

[31] HILL, William J. and William G. HUNTER. *A Review of Response Surface Methodology: A Literature Survey.* Technometrics, vol. 8, no. 4, 1966, pp. 571–590. JSTOR. vailable: `www.jstor.org/stable/1266632`.

[32] HLINÍK, Juraj. *Tvarová optimalizace difuzoru vodní turbíny.* Brno: University of Technology. Faculty of mechanical engineering. Institute of mathematics. Bachelor's thesis. Supervisor Pavel Rudolf, 2015 [cit. 2017-04-10]. Available: `http://hdl.handle.net/11012/40872`.

[33] HU, X. and R. EBERHART. *Adaptive particle swarm optimization: detection and response to dynamic systems.* Evolutionary Computation, 2002. CEC '02. Proceedings of the 2002 Congress on Honolulu, 2002, pp. 1666-1670 [cit. 2017-04-10]. Available: `http://ieeexplore.ieee.org/document/1004492/`.

[34] CHEN, Hongxun et al. *Impellers of low specific speed centrifugal pump based on the draughting technology.* IOP Conference Series: Earth and Environmental Science [online]. 2010, 12(1), 012018 [cit. 2018-05-25]. DOI: 10.1088/1755-1315/12/1/012018. ISSN 1755-1307.

[35] CHEN, Xi, Matteo DIEZ, Manivannan KANDASAMY, Zhiguo ZHANG, Emilio F. CAMPANA a Frederick STERN. *High-fidelity global optimization of shape design by dimensionality reduction, metamodels and deterministic particle swarm.* Engineering Optimization [online]. Taylor, 2014, , 1-22 [cit. 2018-02-12]. DOI: 10.1080/0305215X.2014.895340. ISSN 0305-215X

[36] CHONG, Edwin K. P and Stanisław H. ŻAK. *An introduction to optimization.* 2nd ed. New York: John Wiley, 2001, xv, p. 476, ISBN 0-471-39126-3.

[37] CHROMEK, L. *Vliv konečného počtu lopatek u hydrodynamických čerpadel.* Brno: University of Technology, Faculty of mechanical engineering, 2010. Bachelor thesis, p. 39.

[38] JACOB, H. G. *Rechnergestützte Optimierung statischer und dynamischer Systeme.* Springer-Verlag. 1982. DOI: 10.1007/978-3-642-95409-2. ISBN 9783540116417.

[39] JAMESON, Antony, et al. *Aerodynamic shape optimization of complete aircraft configurations using unstructured grids.* In: 42nd AIAA Aerospace Sciences Meeting and Exhibit. 2004. p. 533 [cit. 2017-05-11]. `https://arc.aiaa.org/doi/10.2514/6.2004-533`.

[40] JIN, Jie, Ying FAN, Wei HAN a Jiaxin HU. *Design and Analysis on Hydraulic Model of The Ultra -low Specific-speed Centrifugal Pump.* Procedia Engineering [online]. Elsevier, 2012, 31(C), 110-114 [cit. 2019-05-06]. DOI: 10.1016/j.proeng.2012.01.999. ISSN 1877-7058.

[41] KARABOGA, D. and B. BASTURK. *A Powerful and Efficient Algorithm for Numerical Function Optimization: Artificial Bee Colony (ABC) Algorithm..* Journal of Global Optimization, Volume:39, Issue: 3, pp:459-171, November 2007, ISSN:0925-5001, doi: 10.1007/s10898-007-9149-x. Available: `http://link.springer.com/article/10.1007/s10898-007-9149-x`.

[42] KENNEDY, J. and R. EBERHART. *Particle swarm optimization.* In: Neural Networks, 1995. Proceedings., IEEE International Conference on [online]. Perth: IEEE Publishing, 1995, 4, pp. 1942-1948 [cit. 2017-04-11]. DOI: 10.1109/ICNN.1995.488968. ISBN 0-7803-2768-3. Available: `http://ieeexplore.ieee.org/document/488968/`.

[43] KENNEDY, J. and R. MENDES. *Population structure and particle swarm performance.* In: Evolutionary Computation, 2002. CEC '02. Proceedings of the 2002 Congress on [online]. Honolulu: IEEE, 2002, 2, pp. 1671-1676 [cit. 2017-04-11]. DOI: 10.1109/CEC.2002.1004493. ISBN 0780372824. Available: `http://ieeexplore.ieee.org.ezproxy.lib.vutbr.cz/document/1004493/`.

[44] KIM, Sangho, ALONSO, Juan, JAMESON, Antony. *Two-dimensional high-lift aerodynamic optimization using the continuous adjoint method.* In: 8th Symposium on Multidisciplinary Analysis and Optimization. 2000. p. 4741 [cit. 2017-05-11]. Available: `http://aero-comlab.stanford.edu/Papers/AIAA-2000-4741-945.pdf`.

[45] KIM, Sangho, ALONSO, J., JAMESON, Antony. *Design optimization of high-lift configurations using a viscous continuous adjoint method.* In: 40th AIAA Aerospace Sciences Meeting and Exhibit. 2002. p. 844 [cit. 2017-05-11]. `https://pdfs.semanticscholar.org/7c07/566672cf31d3441fc5c7e64a321f1ef57efb.pdf`.

[46] KIM, Sung, Ung-Been JEONG, Kyoung-Yong LEE, Jin-Hyuk KIM, Joon-Yong YOON and Young-Seok CHOI. *Multi-objective optimization for mixed-flow pump with blade angle of impeller exit and diffuser inlet.* Journal of Mechanical Science and Technology [online]. Seoul: Korean Society of Mechanical Engineers, 2017, 31(11), 5099-5106 [cit. 2018-05-21]. DOI: 10.1007/s12206-017-1003-6. ISSN 1738-494X.

[47] KLAMMER, M., DYBOWSKI, J.N., HOFFMANN, D. and C. SCHAAB. *Pareto Optimization Identifies Diverse Set of Phosphorylation Signatures Predicting Response to Treatment with Dasatinib.* PLOS ONE, 2015, Volume 10, pp. 1-16 [cit. 2017-04-11]. Available: `https://doi.org/10.1371/journal.pone.0128542`.

[48] KLAPKA, J., DVOŘÁK, J.and P. POPELA. *Metody operačního výzkumu.* ISBN 80-214-1839-7, (2001), VUTIUM Brno.

[49] KLAS, R., F. POCHYLÝ and P. RUDOLF. *Analysis of novel low specific speed pump designs.* IOP Conference Series: Earth and Environmental Science [online]. 2014, 22(1), 012010 [cit. 2017-08-30]. DOI: 10.1088/1755-1315/22/1/012010. ISSN 1755-1307.

[50] KLAS, R., F. POCHYLÝ and P. RUDOLF. *Influence of low-specific speed pump modifications on stability of Y-Q curve.* EPJ Web of Conferences [online]. Les Ulis: EDP Sciences, 2015, 92 [cit. 2017-08-30]. DOI: 10.1051/epjconf/20159202033. ISSN 21016275.

[51] KYRIACOU, S. A. *Optimization of hydraulic machinery by exploiting previous successful designs.* IOP Conference Series: Earth and Environmental Science [online]. 2010, 12(1), 012031 [cit. 2017-06-05]. DOI: 10.1088/1755-1315/12/1/012031. ISSN 1755-1307. Available: `http://iopscience.iop.org/article/10.1088/1755-1315/12/1/012031/pdf`.

[52] LE DIGABEL, Sébastien. *Algorithm 909: NOMAD: Nonlinear Optimization with the MADS Algorithm.* ACM Transactions on Mathematical Software (TOMS) [online]. ACM, 2011, 37(4), 1-15 [cit. 2017-05-10]. DOI: 10.1145/1916461.1916468. ISSN 0098-3500. Available: `http://dl.acm.org/citation.cfm?id=1916468`.

[53] LE DIGABEL, Sébastien, TRIBES, Christophe and Charles AUDET. *NOMAD user guide.* 2017.

[54] LEMU, Hirpa and G WANG. *CFD-Driven Valve Shape Optimization for Performance Improvement of a Micro Cross-Flow Turbine.* Energies [online]. Basel: MDPI, 2018, 11(1), 248 [cit. 2019-08-28]. DOI: 10.3390/en11010248. ISSN 19961073. Available: `http://search.proquest.com/docview/2002774975`.

[55] LI, Yu, Liang LI, Tong ZHAO a Jun LI. *Aerodynamic optimisation of a low-pressure multistage turbine using the response-surface method.* Journal of Mechanical Science and Technology [online]. Heidelberg: Springer Science, 2013, 27(8), 2537-2546 [cit. 2018-05-21]. DOI: 10.1007/s12206-013-0638-1. ISSN 1738494X.

[56] MA, Rong, et al. *Multi-objective optimization design of low-Reynolds-number airfoils S1223.* In: 27th International Congress of the Aeronautical Sciences. 2010. p. 1-10.

[57] MACH, Jiří. *Optimalizace sací trouby násoskové vírové turbíny [online].* Brno: University of Technology. Faculty of mechanical engineering. Energy institute. Master's thesis. Supervisor Pavel Rudolf, 2016 [cit. 2017-04-10]. Available: `http://hdl.handle.net/11012/59701`.

[58] MACHALOVÁ, Jana and Horymír NETUKA. *Numerické metody nepodmíněné optimalizace.* 1. ed. Palacký University Olomouc, 2013, p. 142. ISBN 978-80-244-3403-2.

[59] *Matematika online.* 2017. Available: `http://mathonline.fme.vutbr.cz/`.

[60] MIAO, Fuqing, Hong-Seok PARK, Cholmin KIM and Seokyoung AHN. *Swarm intelligence based on modified PSO algorithm for the optimization of axial-flow pump impeller.* Journal of Mechanical Science and Technology [online]. Seoul: Korean Society of Mechanical Engineers, 1511, 29(11), 4867-4876 [cit. 2017-05-11]. DOI: 10.1007/s12206-015-1034-9. ISSN 1738-494X. Available: `http://link.springer.com/article/10.1007/s12206-015-1034-9`.

[61] MORAVEC, Prokop. *Návrh oběžného kola odstředivého čerpadla pro dané parametry [online].* Brno: University of Technology. Faculty of mechanical engineering. Energy institute. Master's thesis. Supervisor doc. Ing. Pavel Rudolf Ph.D., 2014 [cit. 2017-04-10]. Available: `http://hdl.handle.net/11012/32448`.

[62] MORAVEC, Prokop, HLINÍK, Juraj and Pavel RUDOLF. *Optimization of hydraulic turbine diffuser.* EPJ Web of Conferences. DOI: 10.1051/epjconf/201611402079. 2016. p. 1-7. ISSN: 2100-014X. Available: `http://www.epj-conferences.org/articles/epjconf/abs/2016/09/epjconf_efm2016_02079/epjconf_efm2016_02079.html`.

[63] MORAVEC, Prokop and Pavel RUDOLF. *Application of a particle swarm optimization for shape optimization in hydraulic machinery.* In EPJ Web of Conferences. EPJ Web of Conferences. 2017. p. 1-11. ISSN: 2100-014X.

[64] MORAVEC, Prokop and Pavel RUDOLF. *Combination of Particle swarm optimization and Neder-Mead algorithm in diffuser shape optimization.* 2018. Advances in Hydroinformatics. Springer Singapore, Singapore. p. 997-1012. ISBN: 978-981-10-7218-5.

[65] MYERS, Raymond H. a Douglas MONTGOMERY. *Response surface methodology: process and product optimization using designed experiments.* 2nd ed. New York: Wiley-Interscience 2002, 2002, 798 s. ISBN 0471412554.

[66] NELDER, J.A. and R. MEAD. *A Simplex Method for Function Minimization.* 1965. The Computer Journal. 7(4): pp. 308-313. DOI: 10.1093/comjnl/7.4.308. ISSN 0010-4620. Available: `http://comjnl.oxfordjournals.org/cgi/doi/10.1093/comjnl/7.4.308`.

[67] NEMEC, M. and D. W. ZINGG. *Newton - Krylov Algorithm for Aerodynamic Design Using the Navier-Stokes Equations.* AIAA Journal, Vol. 40, No. 6, June 2002, pp. 1146-1154.

[68] NOSKIEVIČ, Jaromír. *Kavitace v hydraulických strojích a zařízeních.* Praha: SNTL - Nakladatelství technické literatury, 1990, pp. 333, ISBN 80-03-00206-0.

[69] Official home page of EASY, the Evolutionary Algorithms SYstem. 2017. Available: `http://velos0.ltt.mech.ntua.gr/research/easy.html`.

[70] *Original vs. optimized design.* Figure: Opt2-1024x421.jpg [online], [cit. 2017-04-10]. Available: `http://www.enmodes.de/wordpress/wp-content/uploads/2014/09/Opt2-1024x421.jpg`.

[71] PACIGA, A., STRÝČEK, O. and M. GANČO. *Čerpacia technika.* Bratislava: Alfa Bratislava – SNTL Praha, 1984. p. 224, 63-557-84.

[72] PECK, J. F. *Design of Centrifugal Pumps with Computer Aid..* Proceedings of the Institution of Mechanical Engineers 1968. Volume 183, pp. 321-351. `http://journals.sagepub.com/doi/abs/10.1243/PIME_PROC_1968_183_030_02`.

[73] PETROVIČ, Matej. *Optimization of hydraulic parts using adjoint optimization.* Perspectives in Science [online]. Elsevier, 1603, 7, pp. 337-340 [cit. 2017-05-10]. DOI: 10.1016/j.pisc.2015.12.005. ISSN 2213-0209. Available: `http://www.sciencedirect.com/science/article/pii/S2213020915001019`.

[74] POCHYLÝ, František. *Poznámky z osobních konzultací.* 2018.

[75] POCHYLÝ, František, RUDOLF, Pavel, ŠTEFAN, David, MORAVEC, Prokop, STEJSKAL, Jiří and Aleš SKOTÁK. *Design of a pump-turbine using a quasi-potential flow approach, mathematical optimization and CFD.* 2018. IAHR KYOTO 2018.

[76] RAABE, Joachim. *Hydro power.* Diesseldorf: VDI-Verlag, 1985, p. 684.

[77] REYES-SIERRA, M. and C.A.C COELLO. *Multi-Objective Particle Swarm Optimizers: A Survey of the State-of-the-Art.* INTERNATIONAL JOURNAL OF COMPUTATIONAL INTELLIGENCE RESEARCH [online]. 2006, Volume 2, pp. 287-308 [cit. 2017-04-10]. Available: `http://citeseerx.ist.psu.edu/viewdoc/summary?doi=10.1.1.138.1829`.

[78] ROSENBROCK, H. H. *An Automatic Method for Finding the Greatest or Least Value of a Function.* The Computer Journal, Volume 3, Issue 3, 1960.

[79] RUDOLF, Pavel. *Studie smykových vrstev k optimalizaci sací trouby vírové turbiny.* Brno: University of Technology. Faculty of mechanical engineering. PhD thesis, 2004, p. 147.

[80] RUSSENSCHUCK, Stephan. *Field Computation for Accelerator Magnets: Analytical and Numerical Methods for Electromagnetic Design and Optimization.* ISBN: 978-3-527-40769-9, p. 778, March 2010.

[81] SAFIKHANI, H., A. KHALKHALI and M. FARAJPOOR. *Pareto Based Multi-Objective Optimization of Centrifugal Pumps Using CFD, Neural Networks and Genetic Algorithms.* Engineering Applications of Computational Fluid Mechanics [online]. Taylor, 2011, 5(1), 37-48 [cit. 2017-05-11]. DOI: 10.1080/19942060.2011.11015351. ISSN 1994-2060. Available: `http://www.tandfonline.com/doi/abs/10.1080/19942060.2011.11015351`.

[82] SATOH, Hiroshi, Kazuo UCHIDA and Yinchun CAO. *Designing An Ultra-Low Specific Speed Centrifugal Pump.* Texas AM University. Turbomachinery Laboratories. Available: `https://pdfs.semanticscholar.org/52ee/cd035f7767e9efb200f43fbc8a9923471167.pdf`.

[83] SHANNO, D. F. *Conditioning of quasi-Newton methods for function minimization.* Math. Comp., 24 (1970), pp. 647–650 [cit. 2017-05-10]. Available: `http://www.ipgp.fr/~tarantola/exercices/chapter_04/SquareRoot/PDFS/Shanno.pdf`.

[84] SHI, Y. and R. EBERHART. *A modified particle swarm optimizer.* In: Evolutionary Computation Proceedings, 1998. IEEE World Congress on Computational Intelligence., The 1998 IEEE International Conference on [online]. Anchorage: IEEE Publishing, 1998, pp. 69-73 [cit. 2017-04-11]. DOI: 10.1109/ICEC.1998.699146. ISBN 0-7803-4869-9. Available: `http://ieeexplore.ieee.org.ezproxy.lib.vutbr.cz/document/699146/`.

[85] SHI, Y. and R. EBERHART. *Empirical Study of Particle Swarm Optimization.*Proceedings of the 1999 Congress on Evolutionary Computation-CEC99 (Cat. No. 99TH8406), Washington, DC, 1999, Vol. 3., doi: 10.1109/CEC.1999.785511, pp. 1945-1950 [cit. 2017-04-11]. Available: `http://ieeexplore.ieee.org/document/785511/`.

[86] SKOTAK, Ales, Josef MIKULASEK a Jiri OBROVSKY. Development of The New High Specific Speed Fixed Blade Turbine Runner. International Journal of Fluid Machinery and Systems [online]. Turbomachinery Society of Japan, Korean Fluid Machinery Association, Chinese Society of Engineering Thermophysics, IAHR, 2009, 2(4), 392-399 [cit. 2018-02-12]. DOI: 10.5293/IJFMS.2009.2.4.392. ISSN 1882-9554.

[87] SLOUPENSKÝ, Zdeněk. *Design of centrifugal pump using differential geometry methods.* Brno: University of Technology. Faculty of mechanical engineering. PhD thesis, 2011, p. 112.

[88] STAREČEK, Jakub. *Návrh axiálního čerpadla pro zadané parametry.* Brno: University of Technology. Faculty of mechanical engineering. Energy institute. Master's thesis. Supervisor doc. Ing. Miloslav Haluza CSc., 2015 [cit. 2017-05-10]. Available: `http://hdl.handle.net/11012/40361`.

[89] STEJSKAL, J. *Analysis of the velocity and pressure fields of the liquid using curvilinear coordinates.* Brno: University of Technology. Faculty of mechanical engineering. PhD thesis, 2017.

[90] STRÝČEK, O. and M. GANČO. *Čerpadla (hydraulický výpočet a konstrukce).* Bratislava, 1978.

[91] SVOZIL, Jan. *Optimalizace potrubních tvarovek.* Brno: University of Technology. Faculty of mechanical engineering. PhD thesis, 2012, p. 306 [cit. 2017-05-11]. Available: `http://hdl.handle.net/11012/6302`.

[92] ŠTEFAN, David, MORAVEC, Prokop, RUDOLF, Pavel and František POCHYLÝ. *Tvarová optimalizace oběžného kola reverzní Francisovi turbíny FR125.* Research report. 2018.

[93] THÉVENIN, Dominique and Gábor JANIGA. Optimization and computational fluid dynamics. Berlin: Springer, 2008, xv, p. 293, ISBN 978-3-540-72153-6.

[94] TZANAKIS, Athanasios. *Duct optimization using CFD software 'ANSYS Fluent Adjoint Solver'.* Gothenburg: Chalmers University of Technology. Department of Applied Mechanics. Division of Vehicle Engineering and Autonomous Systems. Master's thesis. 2014 [cit. 2017-04-10]. Available: `http://publications.lib.chalmers.se/records/fulltext/202020/202020.pdf`.

[95] BINGHAM, Derek. *Virtual Library of Simulation Experiments: Test Functions and Datasets.* Website, last update August 2017 [cit. 2017-01-04]. Available: `http://www.sfu.ca/~ssurjano/optimization.html`.

[96] VOJTEK, J. *Čerpací technika (Návody do cvičení.)* Praha: ČVUT, 1988. p. 110.

[97] WEXLER, Arnold. Vapor pressure formulation for water in range 0 to 100 C. A revision. Journal of Research of the National Bureau of Standards Section A: Physics and Chemistry [online]. 1976, 80A(5 and 6), 775 [cit. 2018-06-20]. DOI: 10.6028/jres.080A.071. ISSN 0022-4332

[98] ZHAN, Z.-H., J. ZHANG, Y. LI, and H. S.-H. CHUNG. *Adaptive Particle Swarm Optimization.* The IEEE Transactions on Systems, Man, and Cybernetics, 2009, vol. 39, pp. 1362-1381 [cit. 2017-04-10]. Available: `http://ieeexplore.ieee.org/document/4812104/`.

[99] ZHU, Baoshan, Xuhe WANG, Lei TAN, Dongyue ZHOU, Yue ZHAO a Shuliang CAO. *Optimization design of a reversible pump–turbine runner with high efficiency and stability.* Renewable Energy [online]. Elsevier, 2015, 81, 366-376 [cit. 2018-04-16]. DOI: 10.1016/j.renene.2015.03.050. ISSN 0960-1481.

[100] ZOGRAFOS, K., F. PIMENTA, M. A. ALVES and M. S. N. OLIVEIRA. *Microfluidic converging/diverging channels optimised for homogeneous extensional deformation.* Biomicrofluidics [online]. 2016, 10(4), 043508 [cit. 2018-02-10]. DOI: 10.1063/1.4954814. ISSN 1932-1058.

[101] ŽIDONIS, Audrius, Alexandros PANAGIOTOPOULOS, George A. AGGIDIS, John S. ANAGNOSTOPOULOS and Dimitris E. PAPANTONIS. *Parametric optimisation of two Pelton turbine runner designs using CFD.* Journal of Hydrodynamics, Ser.B [online]. Elsevier, 1506, 27(3), 403-412 [cit. 2017-05-10]. DOI: 10.1016/S1001-6058(15)60498-X. ISSN 1001-6058. Available: `http://www.sciencedirect.com/science/article/pii/S100160581560498X`.

Figures

[102] *Aerodynamic simulation (CFD) of a Formula 1.* Figure: AjointZZBlogPic.jpg [online], [cit. 2018-08-02]. Available: `https://www.ansys-blog.com/wp-content/uploads/2015/04/AjointZZBlogPic.jpg`.

[103] *Flow separation.* Figure: flowseparation.png [online], [cit. 2018-16-04]. Available: `https://qph.fs.quoracdn.net/main-qimg-9f8eeba7fce5bb683bc56bdc000e9443`.

[104] *Pump cavitation.* Figure: pumpcavitation.jpg [online], [cit. 2018-16-04]. Available: `https://hayespump.com/wp-content/uploads/pumpcavitation.jpg`.

[105] *Pump turbine - ANDRITZ.* Figure: cn-news-picture20170911-hydro-fengning-pump-station-data.jpg.png [online], [cit. 2018-16-04]. Available: `https://www.andritz.com/resource/blob/244170/0749b9c622007bf0c81eef2e2c5e4f62/cn-news-picture20170911-hydro-fengning-pump-station-data.jpg`.

[106] *Pump settings.* Figure: 16.gif [online], [cit. 2019-01-01]. Available: `https://nptel.ac.in/courses/112104117/chapter_8/16.gif`.

[107] *Roulette wheel selection.* Figure: 24A9m.png [online], [cit. 2018-08-02]. Available: `https://i.stack.imgur.com/24A9m.png`.

[108] *Shape optimization diagram.* Figure: meshmorphing01.png [online], [cit. 2018-16-04]. Available: `http://www.enginsoft.com/assets/img/tecnology/cfd/meshmorphing_01.png`.

[109] *Trial and error diagram.* Figure: schema-trial.png, [cit. 2018-16-04]. Available: `http://inc-asean.com/editor-picks/trial-error-british-expat-teaching-young-people-embrace-failure/`.

NOMENCLATURE

Acronym	Unit	Description
α_1	[°]	angle of pre-rotation
β	[°]	angle of blade
β_1	[°]	inlet angle of blade
β_2	[°]	outlet angle of blade
$\beta_i, \beta_{ii}, \beta_{ij}$	[-]	regression coefficients
γ	[-]	contraction parameter
γ	[-]	slip factor
γ_1, γ_2	[-]	loss coefficient
δ_{ij}	[-]	Kronecker delta
Δ	[mm]	blade thickness
Δ_k^m	[-]	mesh size parameter
η	[-]	expansion parameter
η_c	[-]	total efficiency
η_H	[-]	hydraulic efficiency
θ	[°]	angle of blade
κ_w	[-]	Waisser correction
λ	[°]	angle of inclination
ξ	[-]	constant
ρ	[-]	reflection parameter
ρ	$[kg/m^3]$	density
σ	[-]	simplex reduction parameter
σ_b	[-]	constant
τ_{al}	[-]	shear stress
τ_{ij}	$[kg/(m \cdot s^2)]$	Reynolds stress tensor
τ_2	[-]	blade blockage
υ	[-]	relative disk loss
φ_1, φ_2	[-]	flow coefficients
ψ	[-]	vector of adjoint variables
ω	$[rad/s]$	radial velocity
Ω	[-]	set, constraint set
a	[-]	variable
a_0	[mm]	guide vanes opening
A, B, C, D	[-]	points of meridional flow channel
A_1	$[m^2]$	area
b_1, b_2	[m]	pump widths
B_i^n	[-]	Bernstein polynomials
$const_H$	[-]	constant
c^0	[-]	starting point
c_1	[-]	positive constant
c_2	[-]	positive constant
c_{m1}, c_{m2}	$[m/s]$	meridional velocity

Acronym	Unit	Description
c_p	[-]	coefficient of pressure recovery
c_{u0}	$[m/s]$	inlet circumferential component of abs. velocity
c_{u2}	$[m/s]$	outlet circumferential component of abs. velocity
$C++$	[-]	programming language
$C_{pressure}$	[-]	pressure constant
D	[W]	energy dissipation
$d_0, d_1, d_2, d_h, d_{shaft}$	$[m]$	diameters
d^*	[-]	dimensionless diameter
e	[mm]	blade thickness
$f(x)$	[-]	function
f_Ω	[-]	function
g	[-]	index
g	$[m/s^2]$	gravitational acceleration
G	[-]	gradient of objective function
H	[m]	pump head
H_A	[m]	system characteristic
i	[-]	particle index
J	[-]	objective function
k	$[m^2/s^2]$	turbulent kinetic energy
k	[-]	iteration
$k-\epsilon$	[-]	turbulence model
k_n	[-]	blockage
k_{m1}	[-]	constant
k_{m2}	[-]	constant
K	[-]	constant
K_h	[-]	constant
k_z	$[m]$	roughness coefficient
L_{hub}	[m]	length of hub curve
L_{shroud}	[m]	length of shroud curve
m	[-]	exponent
M	[-]	set of acceptable solutions
M_{change}	[-]	constant
n	[-]	space dimension, number of workers (cases)
n	$[min^{-1}]$	revolutions per minute (RPM)
n_s, n_b, n_s, n_{ss}	$[min^{-1}]$	specific speeds
n_D	[-]	finite set of directions, problem dimension
$\mathbf{N}$	[-]	natural number
Ns	[-]	new solution
p_1	[Pa]	pressure at inlet
p_2	[Pa]	pressure at outlet
p_c	[-]	contracted point
p_e	[-]	expanded point

Acronym	Unit	Description
p_{gn}	[-]	position of the global best particle
p_{in}	[-]	best previous position the i-th of particle
p_{max}	[-]	point with the best value of examined function
p_{min}	[-]	point with the worst value of examined function
p_r	[-]	reflected point
$p_{total,0}$	$[Pa]$	inlet total pressure
$p_{total,2}$	$[Pa]$	outlet total pressure
pen_θ	[-]	θ angle penalty
pen_{HQ}	[-]	instability penalty
pen_{hub}	[-]	hub penalty
pen_{shroud}	[-]	shroud penalty
P	$[W]$	power
P_{max}	$[W]$	maximal power
P_1	[-]	best previous position of the particle
$P_1, P_2, P_3, ..., P_i$	[-]	control points
P_z, P_{z1}, P_{z2}	$[W]$	power dissipation
$\mathcal{P}^*$	[-]	Pareto optimal set
$\mathcal{PF}^*$	[-]	Pareto front
Q	$[m^3/s]$	flow rate
Q	[-]	vector of flow variables
Q_{loss}	$[m^3/s]$	flow rate with volumetric losses
Q_m	$[kg/s]$	mass flow rate
Q_{ref}	$[m^3/s]$	referential flow rate
$\mathbf{R}$	[-]	real number
R	[-]	discretized RANS residual vector
R	$[m]$	radius coordinate
Ra	$[\mu m]$	average mean roughness
$rand()$	[-]	random number from interval $(0,1)$
$Rand()$	[-]	random number from interval $(0,1)$
Re	[-]	Reynolds number
rep_n	[-]	leader particle
s	$[m]$	axial sidewall gap
S_k	[-]	set of points
S_{blade}	$[m^2]$	area of the blade
$S_{pressure}$	$[m^2]$	area of the blade with specific pressure
$S1 - S6$	[-]	solution 1 - solution 6
u	[-]	vector
u_0	$[m/s]$	circumferential velocity at pump's inlet
u_2	$[m/s]$	circumferential velocity at pump's outlet
$\overline{v}$	[-]	averaged variable
v'	[-]	fluctuating part of the variable
v_0	$[m/s]$	inlet velocity

Acronym	Unit	Description
v_2	$[m/s]$	outlet velocity
v_i	[-]	reduced point
v_t	$[m^2/s]$	turbulent viscosity
v_{in}	[various]	velocity of the i-th particle (step size)
V_1	[various]	velocity of the particle (step size)
w	[-]	inertia weight
$weight_H$	[-]	head weight
$weight_{surf}$	[-]	surface pressure weight
$weight_\eta$	[-]	efficiency weight
x	[-]	variable
$\overline{x}$	[-]	centroid
x_i	[-]	design variable
$x*$	[-]	variable
x_c	[-]	contracted point
x_e	[-]	expanded point
x_{in}	[-]	current position of the i-th particle
X_D	[-]	vector of design variables
x_r	[-]	reflected point
X_1	[-]	current position of the particle
y_0	$[m]$	inlet height
y_2	$[m]$	outlet height
y	[-]	response
Y	$[J/kg]$	specific energy
z	[-]	number of blades
z	$[m]$	coordinate

Acronym	Description
$1D$	One-dimensional
$3D$	Three-dimensional
ABC	Artificial Bee Colony
$AsBeC$	Artificial super-Bee enhanced Colony
$BFGS$	Broyden–Fletcher–Goldfarb–Shanno algorithm
BEP	Best efficiency point
CAD	Computer-aided design
CFD	Computational Fluid Dynamics
COP	Cavitation operation point
CR	Cavitation resistance
EA	Evolutionary Algorithm
$EASY$	Evolutionary Algorithms System
GA	Genetic Algorithm
$GBEST$	Global best particle
HCI	Hydrodynamic cavitation intensity
$LBEST$	Local best particle
LE	Leading edge
$MADS$	Mesh adaptive direct search
$MOPSO$	Multi-objective particle swarm optimization
$NOMAD$	Nonlinear Optimization by Mesh Adaptive Direct Search
NM	Nelder - Mead
$NPSH$	Net positive suction head
$NPSH_3$	Critical net positive suction head
$OFIVK$	Odbor fluidního inženýrství Viktora Kaplana
OP	Operation point
PSO	Particle swarm optimization
$PSOA$	Particle swarm optimization algorithm
$RANS$	Reynolds-averaged Navier–Stokes equations
RHV	Requested head value
RPM	Revolutions per minute
RSM	Response surface method/methodology
TE	Trailing edge
$URANS$	Unsteady Reynolds-averaged Navier–Stokes equations